

Aerosol-Cloud-Radiation interactions in regimes of liquid water clouds

Von der Fakultät für Physik und Geowissenschaften

der Universität Leipzig

genehmigte

DISSERTATION

zur Erlangung des akademischen Grades

Doktor der Naturwissenschaften
(Dr. rer. nat)

vorgelegt

von M.Sc. Karoline Block

geboren am 08.10.1986 in Haldensleben, Deutschland

Gutachter: Prof. Dr. Johannes Quaas
Prof. Dr. Annica Ekman

Tag der Verleihung: 9. Juli 2018

Bibliographische Beschreibung

Block, Karoline

Aerosol-Cloud-Radiation interactions in regimes of liquid water clouds

Universität Leipzig , Dissertation

154 S., 221 Lit., 62 Abb., 13 Tab.

Referat:

Trotz enormer Bestrebungen und jahrzehntelanger Forschung, ist das wissenschaftliche Verständnis um das Wirken von Aerosolen auf das Klima durch Modulierung mikrophysikalischer Wolkeneigenschaften sehr klein, und Abschätzungen des implizierten Strahlungsantriebs (RF_{aci}) variieren mit einer grossen Schwankungsbreite. Dennoch ist es wichtig die Interaktionen zwischen Aerosolen und Wolken (ACI) zu verstehen und ihren Strahlungsantrieb quantifizieren zu können, da eine anthropogene Störung dieses Systems mit einer Reduzierung der globalen Erwärmung assoziiert wird.

Bisherige Studien empfehlen umfassende simultane Messungen und beobachtungsgetriebene Modelle als eine Möglichkeit die ACI besser zu verstehen und damit die Schwankungsbreite des RF_{aci} einschränken zu können. In der vorliegenden Dissertation wird eine Methodik genutzt, in der Satelliten- und Reanalysedaten zusammenwirken. Durch eine kontinuierlich aufbauende Herangehensweise von der Basis an, können Lücken zwischen Satellitenbeobachtungen und Modellsimulationen geschlossen und die Vorzüge beider Seiten genutzt werden. In diesem methodischen Ansatz werden ein beobachtungsgetriebenes Aerosolmodell, verschiedene simultane und miteinander vernetzte Satellitenmessungen, eine moderne Parameterisierung zur Aktivierung von Aerosolen sowie ein Strahlungsmodell miteingebunden.

Es wird gezeigt, dass diese Herangehensweise nützlich ist um quantitative als auch qualitative Aussagen über ACI treffen zu können und um das RF_{aci} bestimmen zu können. Ein Ergebnis dieser Studie ist eine 10-Jahre lange Klimatologie von Wolkenkondensationskeimen (CCN), aus denen sich Wolkentropfen formen können. Diese wird hier vorgestellt und evaluiert. Das ist eine bislang einzigartige Klimatologie, die CCN Konzentrationen für verschiedene Übersättigungen und Aerosoltypen weltweit in 3-D bereitstellt und damit für Evaluierungen von Modellen und anderen ACI Studien geeignet ist. Weiterhin werden in dieser Studie die Verteilung und Variabilität von Wolkentropfenanzahlkonzentrationen (CDNC) und deren Anfälligkeit für Aerosoländerungen untersucht und mit bisherigen Ergebnissen abgeglichen. In diesem Kontext hat sich eine Analyse unter Einbezug von Wolkenregimen als förderlich erwiesen. Nicht zuletzt stellt die Analyse des regime-basierenden RF_{aci} unter heutigen Bedingungen einen finalen Schluss dieser aufwendigen Methodik dar.

Insgesamt betrachtet liefert die vorliegende Dissertation eine umfangreiche Begutachtung von Interaktionen und Unsicherheiten in Bezug auf Aerosole, Wolken und Strahlung in Regimen von Flüssigwasserwolken und trägt dazu bei, das wissenschaftliche Verständnis dieser Prozesse zu erhöhen.

Bibliographic Description

Block, Karoline

Aerosol-cloud-radiation interactions in regimes of liquid water clouds

Universität Leipzig , Dissertation

154 pp., 221 bibliog., 62 fig., 13 tab.

Abstract:

Despite large efforts and decades of research, the scientific understanding of how aerosols impact climate by modulating microphysical cloud properties is still low and associated radiative forcing estimates (RF_{aci}) vary with a wide spread. But since anthropogenically forced aerosol-cloud interactions (ACI) are considered to oppose parts of the global warming, it is crucial to know their contribution to the total radiative forcing in order to improve climate predictions.

To obtain a better understanding and quantification of ACI and the associated radiative effect it has been suggested to use concurrent measurements and observationally constrained model simulations. In this dissertation a joint satellite-reanalysis approach is introduced, bridging the gap between climate models and satellite observations in a bottom-up approach. This methodology involves an observationally constrained aerosol model, refined and concurrent multi-component satellite retrievals, a state-of-the-art aerosol activation parameterization as well as radiative transfer model.

This methodology is shown here to be useful for a quantitative as well as qualitative analysis of ACI and for estimating RF_{aci} . As a result, a 10-year long climatology of cloud condensation nuclei (CCN) (particles from which cloud droplets form) is produced and evaluated. It is the first of its kind providing 3-D CCN concentrations of global coverage for various supersaturations and aerosol species and offering the opportunity to be used for evaluation in models and ACI studies. Further, the distribution and variability of the resulting cloud droplet numbers and their susceptibility to changes in aerosols is explored and compared to previous estimates. In this context, an analysis by cloud regime has been proven useful. Last but not least, the computation and analysis of the present-day regime-based RF_{aci} represents the final conclusion of the bottom-up methodology.

Overall, this thesis provides a comprehensive assessment of interactions and uncertainties related to aerosols, clouds and radiation in regimes of liquid water clouds and helps to improve the level of scientific understanding.

Contents

Bibliographische Beschreibung	I
Bibliographic Description	III
List of Figures	VII
List of Tables	IX
List of Symbols	XI
List of Acronyms	XIII
1 Introduction	1
1.1 Motivation	1
1.2 Context	3
1.3 The scientific challenge	6
1.4 The chapter roadmap	7
2 Fundamentals	9
2.1 Tropospheric aerosols	9
2.2 Droplet nucleation theory	12
2.3 Clouds and their relevance for climate	16
3 A climatology of cloud condensation nuclei derived from the MACC-II aerosol reanalysis	23
3.1 Abstract	23
3.2 Introduction	23
3.3 Data and Methods	25
3.3.1 The ECMWF IFS aerosol model	26
3.3.2 The data assimilation apparatus	27
3.3.3 Previous evaluation of MACC-II AOD and aerosol mass	28
3.3.4 Evaluation of CCN relevant aerosol mass from MACC-II reanalysis with IMPROVE data	31
3.3.5 Computing the MACC-II reanalysis CCN	32
3.3.6 CCN evaluation with ARM data	35
3.4 Results and Discussions	37
3.4.1 The CCN climatology	37
3.4.2 Validation	42
3.5 Conclusions	51
4 Analysis of parameterized cloud droplet number concentrations and their susceptibilities in regimes of liquid water clouds	53
4.1 Abstract	53
4.2 Introduction	54

4.3	Data and Methods	56
4.3.1	The Joint Satellite-Reanalysis Approach	56
4.3.2	The CCCM dataset	57
4.3.3	The aerosol activation parameterization	62
4.3.4	Cloud regimes and updraft experiments	65
4.3.5	Comparison with MODIS retrieved CDNC and CDNC sensitivity . . .	70
4.4	Results and Discussions	72
4.4.1	Assessment of regime-based supersaturations	72
4.4.2	Assessment of regime-based CDNC	75
4.4.3	Assessment of regime-based CDNC sensitivity to aerosol changes . . .	81
4.5	Conclusions	88
5	A cloud regime based assesment of the cloud albedo effect	91
5.1	Abstract	91
5.2	Introduction	91
5.3	Data and Methods	93
5.4	Results and Discussions	97
5.4.1	Experimental setup 1: Constant CDNC and fixed anthropogenic fractions	97
5.4.2	Experimental setup 2: Variable CDNC and fixed anthropogenic fractions	99
5.4.3	Experimental setup 3: Variable CDNC and variable anthropogenic frac- tions	100
5.5	Conclusions	103
	Bibliography	105
	Appendix A Supplement: Cloud Condensation Nuclei	127
A.1	Validation of CCN relevant aerosol mass	127
A.2	Seasonal variability of CCN contributions	129
A.3	Bias distributions of CCN relevant aerosol masses	130
	Appendix B Supplement: Cloud Droplet Number Concentration	131
B.1	Satellite retrieved cloud and aerosol microphysical properties	131
B.1.1	Satellite retrieved cloud microphysical properties determining CDNC .	131
B.1.2	Satellite retrieved aerosol microphysical properties determining CDNC sensitivity	136
B.2	The supersaturation balance equation	138
B.3	Regime-based cloud base parameters	140
B.4	Global distribution of regime-based maximum supersaturations	144
	Appendix C Supplement: Radiative Forcing	147
C.1	RF_{aci} with fixed anthropogenic fraction	147
C.2	RF_{aci} with full anthropogenic fraction distribution	149
	Acknowledgements	153

List of Figures

1.1	Overview of RF estimates	2
1.2	Effect of PD aerosol forcing on temperature projections	3
1.3	Aerosol-Cloud interactions (ACI)	4
2.1	Aerosol modes	10
2.2	Köhler Curves	15
2.3	Global cloud properties	17
2.4	ISCCP cloud classification	18
3.1	IMPROVE stations	32
3.2	CCN load and vertical distribution	37
3.3	Aerosol species contribution to CCN	38
3.4	CCN aerosol species	39
3.5	Time series of CCN species	40
3.6	Seasonal variability of CCN load with latitude	40
3.7	Seasonal variability of CCN species	41
3.8	MACC vs IMPROVE MCONC Joint Histograms	43
3.9	MACC vs IMPROVE MCONC probability density functions	44
3.10	Increase of R with $m_{IMPROVE}$	45
3.11	MACC vs ARM CCN data	47
3.12	MACC CCN species contribution at ARM sites	47
3.13	MACC vs ARM CCN probability density functions	48
4.1	Literature review of ACI estimates	55
4.2	The A-Train constellation	58
4.3	The CCCM ground coverage	59
4.4	The CCCM cloud grouping	60
4.5	Cloud regimes	66
4.6	Updraft PDFs	67
4.7	Regime-based S_{max} as a function of w	72
4.8	Regime-based S_{max} for the various updraft experiments	73
4.9	Global distribution of regime-based S_{max}	74
4.10	Experiment differences in global distribution of regime-based S_{max}	74
4.11	Regime-based median CDNC	75
4.12	Global distribution of median CDNC	76
4.13	Aerosol species contribution to total CDNC	80
4.14	MODIS CDNC-AOD sensitivity	81
4.15	MODIS CDNC-CCN sensitivity	83
4.16	MACC derived CDNC sensitivity	84
4.17	Regime-based MACC CDNC sensitivity	87
5.1	Anthropogenic AOD fraction	94
5.2	Regime-based RFO weighted total cloud cover	97

5.3	SW fluxes for globally fixed CDNC and anthropogenic fraction	98
5.4	RF_{aci} for globally fixed CDNC and anthropogenic fraction	99
5.5	RF_{aci} for regime-based CDNC (Exp3) and fixed anthropogenic fraction	100
5.6	RF_{aci} for regime-based CDNC (Exp3)	101
5.7	Difference of RF_{aci} from full to fixed anthropogenic fraction	102
A.1	MACC vs IMPROVE MCONC Bias Joint Histograms	127
A.2	Maps of Mass Correlation Coefficients	128
A.3	Zonal and seasonal means of CCN contributions	129
A.4	Joint PDF of MACC MCONC bias distributions	130
B.1	Reflection function	132
B.2	References of global CDNC distributions	135
B.3	Regime-based cloud base temperature	140
B.4	Regime-based cloud base pressure	141
B.5	Regime-based cloud base pressure	142
B.6	Regime-based CCN at 0.2% S_{sat} near cloud base	142
B.7	Regime-based total cloud cover	143
B.8	Experiment 1: Global distribution of regime-based S_{max}	144
B.9	Experiment 2: Global distribution of regime-based S_{max}	145
B.10	Experiment 3: Global distribution of regime-based S_{max}	146
C.1	RF_{aci} for regime-based CDNC (Exp1) and fixed anthropogenic fraction	147
C.2	RF_{aci} for regime-based CDNC (Exp2) and fixed anthropogenic fraction	148
C.3	RF_{aci} for regime-based CDNC (Exp1)	149
C.4	RF_{aci} for regime-based CDNC (Exp2)	150

List of Tables

2.1	Key aerosol properties	11
3.1	Aerosol physical and optical properties	33
3.2	ARM validation data	36
3.3	MCONC validation with IMPROVE data	46
3.4	CCN validation with ARM data	47
3.5	CCN-AOD correlation	49
3.6	MCONC bias propagation	50
4.1	Cloud regimes	65
4.2	Updraft experiments	67
4.3	Regime-based σ_w references	69
5.1	RF _{aci}	102

List of Symbols

Symbol	Units	Description
α_e	$m^2 g^{-1}$	mass extinction coefficient
A		curvature parameter
B		hygroscopicity parameter
c_p	$1004 J K^{-1} kg^{-1}$	specific heat capacity at constant pressure
c_v	$717 J K^{-1} kg^{-1}$	specific heat capacity at constant volume
D_v	$cm^2 sec^{-1}$	diffusivity of water vapor
D_p	μm	diameter of water or cloud droplet
D_s	μm	diameter of dry aerosol particle
e	Pa	partial water vapor pressure
e_s	Pa	saturation water vapor pressure
ε		mass fraction of soluble material in a solution
f_{anth}	%	anthropogenic fraction (related here to τ or N_d)
$f_{cld,liq}$	%	liquid cloud cover fraction
F_{SW}	$W m^{-2}$	net TOA all-sky shortwave radiative flux
G		growth coefficient of droplets
g	$9,81 m s^{-2}$	constant of gravity
Γ	$-0.098 K m^{-1}$	dry adiabatic lapse rate
Γ_s	$K m^{-1}$	moist adiabatic lapse rate
γ_w		activity coefficient
H_{cb}	m	cloud base height
K_a	$J m^{-1} sec^{-1} K^{-1}$	thermal conductivity
L_e	$44 kJ mol^{-1} (25^\circ C)$	latent heat of evaporation
M_s	$g mol^{-1}$	molecular weight of aerosol particle
M_w	$18.01 g mol^{-1}$	molecular weight of water
M_d	$28.96 g mol^{-1}$	molecular weight of dry air
M_p	g	average mass per aerosol particle
m	$g kg^{-1}$	aerosol mass mixing ratio
m_s	kg	mass of solute
m_w	$g kg^{-1}$	water vapor mass mixing ratio
N_a	cm^{-3}	aerosol number concentration
N_d	cm^{-3}	droplet number concentration (CDNC)
$N_{d,anth}$	cm^{-3}	anthropogenic droplet number concentration (CDNC)
n_s		number of water moles within a solution
n_w		number of solute moles within a solution
ν		number of dissociated ions
ν_s	m^3	partial molar volume of water within a solution
ν_w	m^3	partial molar volume of the solute within a solution
ω		single scattering albedo
$\omega_{500,700}$	Pa	vertical velocity (at 500/700 hPa)
p	Pa	pressure

p_0	1013.25 mb	reference pressure
p_{surf}	Pa	surface pressure
p_s	Pa	saturation pressure
p_w	Pa	equilibrium water vapor pressure over a pure water droplet
p_w°	Pa	equilibrium vapor pressure over a flat surface of pure water
p_s°	Pa	equilibrium vapor pressure over a flat surface of a solution
ϕ_s		osmotic coefficient
q	$g\ kg^{-1}$	specific humidity
R		linear Pearson correlation coefficient
R_G	$8,31\ J\ K^{-1}\ mol^{-1}$	universal gas constant
R_v	$462\ J\ K^{-1}\ kg^{-1}$	specific gas constant for water vapor
R_d	$287\ J\ K^{-1}\ kg^{-1}$	specific gas constant for dry air
RH	%	relative humidity, equivalent to the saturation ratio S_{sat}
r_s	μm	radius of dry aerosol particle
r_0	μm	count median radius or mode radius in aerosol size distribution
r_c	μm	critical radius of activation
r_{eff}	μm	effective radius of droplet distribution
ρ_s	$kg\ m^3$	dry aerosol density
ρ_a	$kg\ m^3$	dry air density
ρ_w	$1000\ kg\ m^3$	density of liquid water
ϱ		asymmetry parameter
S_{sat}	%	saturation ratio, equivalent to the relative humidity RH
S_c	%	critical supersaturation
S_0	%	mode critical supersaturation
S_{max}	%	maximum supersaturation
σ_g	μm	geometric standard deviation in aerosol size distribution
σ_m	%	relative measurement uncertainty
$\sigma_{w/a}$	$\sim 0.07\ J\ m^{-2}$	surface tension parameter
σ_w	$m\ s^{-1}$	standard deviation of updraft PDF
T	K	temperature
T_0	$273.15\ K$	reference temperature
τ		aerosol optical depth (AOD)
τ_c		cloud optical depth
V_{Htop}	%	variability of cloud top heights
w	$m\ s^{-1}$	cloud-scale updraft
W	$g\ kg^{-1}$	liquid water mass mixing ratio
x_w		mole fraction of water in a solution

List of Acronyms

Acronym	Description
ACI	Aerosol-Cloud-Interactions
ARI	Aerosol-Radiation-Interactions
RF	Radiative Forcing
ERF	Effective Radiative Forcing
RF _{aci}	Radiative Forcing due to aerosol-cloud-interactions (here, the cloud albedo effect)
CRE	Cloud Radiative Effect
SWCRE	short-wave CRE
LW	long-wave
SS	sea salt aerosol
SSl	large mode sea salt aerosol
SSm	medium mode sea salt aerosol
SSs	small mode sea salt aerosol
DU	mineral dust aerosol
DUI	large mode dust aerosol
DUm	medium mode dust aerosol
DU _s	small mode dust aerosol
SO ₂	sulfur dioxide
SU, SO ₄	sulfate aerosol
BC	black carbon aerosol
BCh	hygroscopic black carbon
BCn	non-hygroscopic black carbon
OM	organic matter aerosol
OMh	hygroscopic organic matter
OMn	non-hygroscopic organic matter
POA	particulate organic matter
SOA	secondary organic matter
NC	aerosol number concentration
CCN	cloud condensation nuclei
IN	ice nuclei
CDNC	cloud droplet number concentration
AOD	aerosol optical depth (τ)
AI	aerosol index
FMF	fine-mode fraction
IQR	interquartile range, range between 25th and 75th percentile
Q ₂₅	25th percentile of a given distribution
Q ₅₀	median of a given distribution
Q ₇₅	75th percentile of a given distribution

AVHRR	Advanced Very High Resolution Radiometer
CPR	Cloud Profiling Radar
MODIS	Moderate resolution Imaging Spectroradiometer
CALIOP	Cloud-Aerosol Lidar with Orthogonal Polarization
CALIPSO	Cloud-Aerosol Lidar and Infrared Pathfinder Satellite Observations
CERES	Clouds and the Earth's Radiant Energy System
CCCM	CERES-CALIPSO-CloudSat-MODIS (merged satellite data product)
AERONET	Aerosol Robotic Network
IMPROVE	Interagency Monitoring of Protected Visual Environments network
ARM	Atmospheric Radiation Measurement network
ISCCP	International Satellite Cloud Climatology Project
MACC	Monitoring Atmospheric Composition and Climate
MACC-II	MACC – Interim Implementation
IFS	Integrated Forecasting System
IFS-LMD	extended IFS which follows the aerosol treatment in the LMD-Z model
ECMWF	European Centre for Mediumrange Weather Forecast
CAMS	European Copernicus programme
GMES	Global Monitoring for Environment and Security)
NWP	Numerical Weather Prediction
GCM	General Circulation Model
GLOMAP	Global Model of Aerosol Processes
LMD-Z	“Laboratoire de Météorologie Dynamique - Zoom” GCM
AeroCom	Aerosol Comparisons between Observations and Models
RRTM	Rapid Radiative Transfer Model
LBLRTM	Line-By-Line Radiative Transfer Model
ITCZ	Intertropical Convergence Zone
LCL	Lifting Condensation Level
LTS	Lower tropospheric stability
EIS	Estimated inversion stability
SLPA	Sea level pressure anomalies
RFO	relative frequency of occurrence
PD	present-day
PI	pre-industrial
St_{low}	regime of stratiform (homogeneous) low liquid clouds
St_{med}	regime of stratiform (homogeneous) medium high liquid clouds
St_{high}	regime of stratiform (homogeneous) high liquid clouds
Cu_{low}	regime of cumuliform (inhomogeneous) low liquid clouds

<i>Cu_{med}</i>	regime of cumuliform (inhomogeneous) medium high liquid clouds
<i>Cu_{high}</i>	regime of cumuliform (inhomogeneous) high liquid clouds
<i>All</i>	all cloud regimes taken together
<i>All_{regime}</i>	all cloud regimes taken together and weighted by their relative frequency of occurrence
ci	Cirrus
cs	Cirrostratus
cb	Cumulonimbus
ac	Alto-Cumulus
as	Alto-Stratus
ns	Nimbostratus
cu	Cumulus
sc	Stratocumulus
st	Stratus

Introduction

1.1 Motivation

Over the last century, the climate of the earth has changed dramatically which has been internationally recognized as one of the main concerns of humankind, leading to a series of political and economical treaties to take action starting from the United Nations Framework Convention on Climate Change in 1992, over the Kyoto Protocol in 1997 (entered into force 2005) leading up to the Paris Agreement in 2015.

With a wide consensus between scientists, it has been shown that global warming is occurring at the present and that it is extremely likely human-made and not a result of natural variability. The main reason for global warming are anthropogenic activities perturbing the radiative budget of the earth by extensive emissions of greenhouse gases such as CO_2 and CH_4 (Stocker et al., 2013).

The change of energy fluxes caused by these climate drivers relative to preindustrial times (1750) is referred to as the radiative forcing (RF). It is a measure of the influence a factor has on the balance of incoming and outgoing radiation in the Earth-atmosphere system and is an index of the importance of that factor as a potential climate change mechanism (Solomon et al., 2007). An overview of RF estimates for the main drivers of climate change is given in Figure 1.1. In case of the global climate change as it happens now, the RF is positive meaning that the climate system is forced to take up more energy than it naturally does in a state of equilibrium.

This leads to an overall warming, which is most recognized by the increase of global mean surface temperatures ($\sim 0.85\text{ K}$ from 1880 to 2012, with each decade being warmer than the previous), the reduction of Arctic sea ice cover (~ 0.45 to 0.51 million km^2 per decade from 1979 to 2012), the ice loss from inland glaciers ($\sim 275\text{ Gt/yr}$ from 1993 to 2009) as well as the global mean sea level rise ($\sim 0.19\text{ m}$ from 1901 to 2010) (Stocker et al., 2013).

However, this warming is influenced by the impact of particles (or aerosols) which can either directly interact with the incoming and outgoing radiation through scattering and absorption (ARI) or indirectly interact with the radiation via clouds (ACI) by which they contribute to a cooling of the earth's surface. Thus, they are associated with a negative RF, as seen from Figure 1.1.

In contrast to the high level of scientific understanding of the impact of long-lived greenhouse gases, the level of scientific understanding on the impact of aerosols on climate, especially of indirect ACI effects, is low (Myhre et al., 2013). The high spatial and temporal

variability of clouds and aerosols, limited observational capabilities with a variety of flaws in retrievals and assumptions as well as a low knowledge of microphysical processes representing ACI in climate models produces one of the largest uncertainties in present-day (PD) forcing estimates (Boucher et al., 2013).

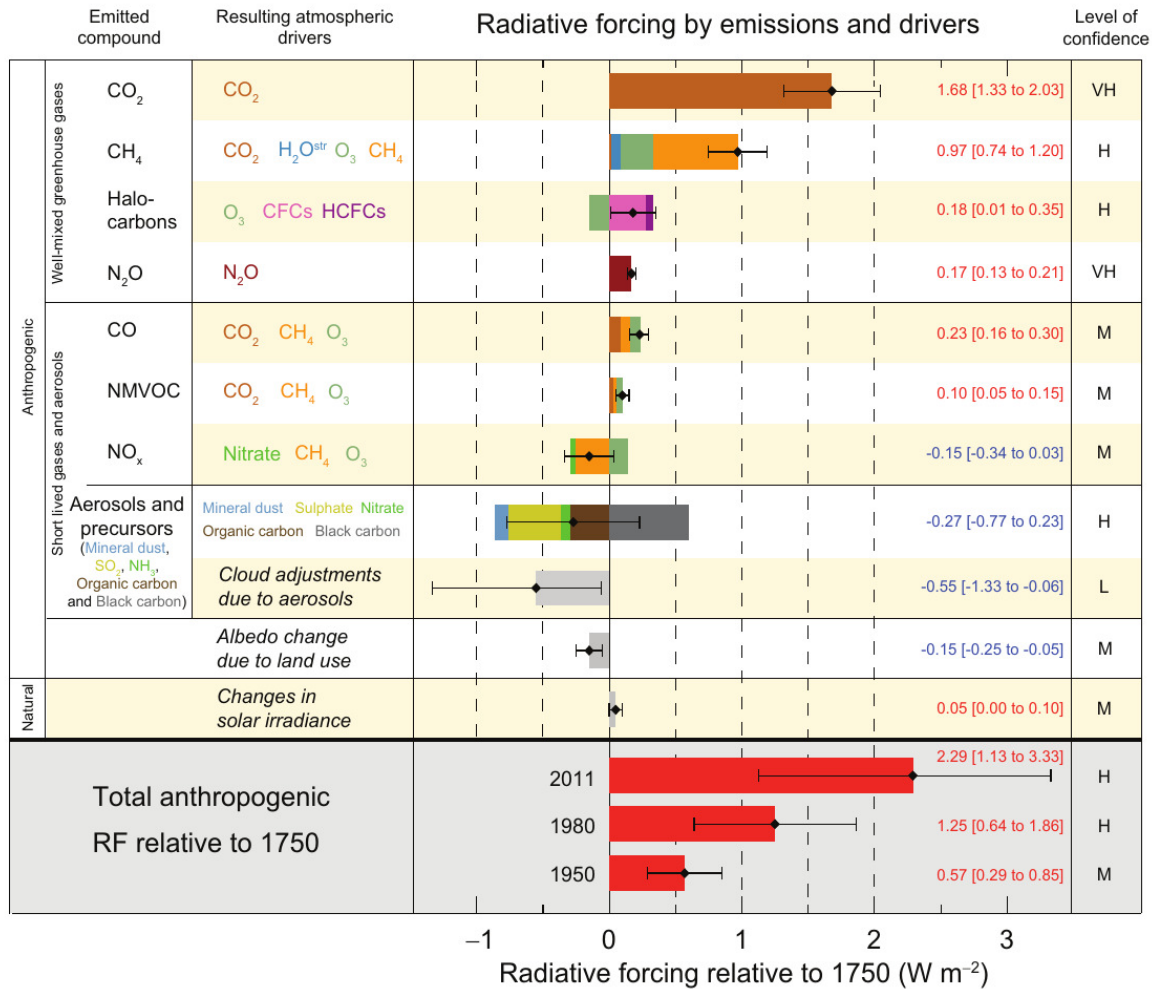


Figure 1.1: Overview of RF estimates and aggregated uncertainties for the main drivers of climate change in 2011 relative to 1750, taken from Stocker et al. (2013). Values are global average RF, partitioned according to the emitted compounds or processes that result in a combination of drivers. The best estimates of the net radiative forcing are shown as black diamonds with corresponding uncertainty intervals; the numerical values are provided on the right of the figure, together with the confidence level in the net forcing (VH – very high, H – high, M – medium, L – low, VL – very low). Albedo forcing due to black carbon on snow and ice is included in the black carbon aerosol bar. Small forcings due to contrails (0.05 Wm⁻², including contrail induced cirrus), and HFCs, PFCs and SF6 (total 0.03 Wm⁻²) are not shown. Concentration-based RFs for gases can be obtained by summing the like-colored bars. Volcanic forcing is not included as its episodic nature makes it difficult to compare to other forcing mechanisms. Total anthropogenic radiative forcing is provided for three different years relative to 1750.

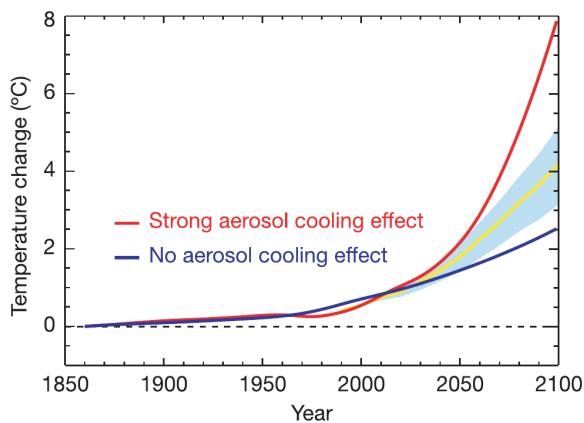


Figure 1.2: Effect of PD aerosol forcing on temperature projections, simulated for the period 1850 to 2100 by Andreae et al. (2005) using a zero-dimensional climate-carbon cycle model. Two extreme cases are shown: strong PD aerosol cooling consistent with forward studies of aerosol effects on climate but with a climate sensitivity not ruled out by observations (red line, $\text{RF}_{\text{total aerosol}} = 1.7 \text{ Wm}^{-2}$), and the case of no aerosol cooling effect (blue line). The shading and the yellow line represent the range and central projection given in IPCC third assessment report. This figure is taken from Andreae et al. (2005).

estimate of -0.7 Wm^{-2}). The IPCC estimates and uncertainty ranges are solely based on climate model computations and their diversities.

Regarding these uncertainties and the implications they have on climate, there is a great need to improve the understanding of aerosol effects, and in particular their interactions with clouds modulating radiation. A reliable quantification of the global mean radiative forcing by anthropogenic aerosols would improve climate projections and contribute to more progressive climate change policy.

1.2 Context

Clouds can significantly decrease incoming solar radiation via reflection (cloud albedo) and also decrease outgoing terrestrial radiation as they absorb and re-emit this energy back to the surface. Depending on the cloud type, the cloud cover, thickness and height these cloud-radiation interactions can vary and thus their impact on climate. Aerosols are able to influence the microstructure of clouds because cloud droplets form on the basis of particles which act as cloud condensation nuclei (CCN). Thus, aerosols are inevitable for the formation of clouds. More on the specifics of aerosols, CCN and clouds are given in Section 2.

Aerosol-Cloud interactions (ACI) can be separated into two main effects (see Figure 1.3), the cloud albedo effect and the lifetime effect, which together determine the effective radiative forcing from aerosols (ERF_{aci}) which are estimated to give -0.55 Wm^{-2} forcing effect with a range of -0.06 Wm^{-2} to -1.33 Wm^{-2} (Boucher et al., 2013). The cloud albedo effect, associated with the first aerosol indirect radiative forcing RF_{aci} , describes the increased cloud

A correct estimate of RF from aerosols is however crucial for better climate predictions, as can be seen in Figure 1.2 from Andreae et al. (2005). They used a simplistic model to show that larger aerosol coolings (stronger PD aerosol forcing and thus smaller net forcings) imply a more sensitive climate leading to larger predicted future warmings. However, smaller or no aerosol coolings (that is a larger net RF) would imply that the 20th century warming can be obtained with a small climate sensitivity, which is defined as the temperature change due to a doubling of CO_2 . For this result a range of PD aerosol forcing between 0 and -1.5 Wm^{-2} was considered which agrees with the uncertainty range of aerosol's ERF given in Myhre et al. (2013) from 0 to -1.2 Wm^{-2} (95% confidence interval) and a best estimate of -0.45 Wm^{-2} (for comparison: Solomon et al. (2007) gives an RF from aerosols of -0.3 to -1.8 Wm^{-2} with a best estimate of -0.7 Wm^{-2}).

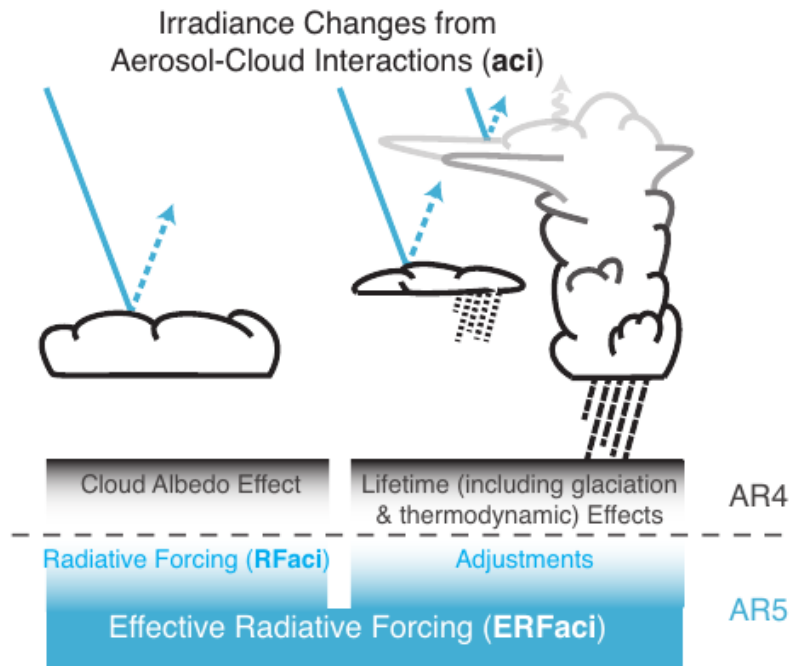


Figure 1.3: Aerosol-Cloud interactions (ACI), illustrating the main effects and their terminology related to the IPCC AR4 and AR5. The blue arrows depict solar radiation and the gray arrows terrestrial radiation. This figure is adopted from (Boucher et al., 2013).

albedo due to more but smaller cloud droplets which is a result of increased CCN supply in the cloud formation process (Twomey, 1974). Assuming a fixed liquid water path, a cloud which can form from many aerosol particles will distribute the available water on a lot of droplets of smaller sizes, while in a macrophysically identical cloud which forms from less particles there will be fewer but bigger droplets. Due to the larger cloud droplet number concentration (CDNC) the overall scattering cross section integrated over the entire cloud is larger and therefore the reflectivity of this cloud is enhanced.

The lifetime effect is a secondary cloud indirect effect and therefore termed as an adjustment to the cloud albedo effect (Boucher et al., 2013). Due to the smaller droplets the precipitation formation can be delayed and thus cloud lifetime prolonged (Albrecht, 1989). This also implies an on average enhanced cloud fraction, larger cloud geometrical thickness and liquid water path (Pincus and Baker, 1994) which leads to an enhanced cloud reflectivity additionally to the cloud albedo effect. The delayed precipitation formation may enable more liquid water reaching the freezing level in convective clouds, and freezing can be delayed to higher altitudes. As a consequence deeper clouds with more intense precipitation may occur (Rosenfeld et al., 2008). This is the thermodynamic effect or convective invigoration effect (Koren et al., 2005) which is also included in the lifetime effect. Contrasting this is the glaciation effect which states that due to the smaller drop sizes glaciation might occur earlier than in an unperturbed state if aerosols are efficient as ice nuclei (IN), precipitation would then also be more efficient and the cloud would dissolve faster (Lohmann, 2002).

The secondary aerosol indirect effects are complex and are very difficult to quantify. However, even though the cloud albedo effect itself seems to be much more easier since it is only

one specific process, the scientific consensus on this is very low leading to the large uncertainty range as seen in Figure 1.1. Therefore, in order to better describe secondary effects a good understanding and quantification of the cloud albedo effect is necessary in the first place.

Previous attempts to quantify ACI processes and to reliably evaluate their impact on radiative forcing have been unsatisfying mostly because of the difference between the scale and accuracy of observation or simulation and the scale and importance of the actual interaction process (e.g. McComiskey and Feingold, 2012; Grandey and Stier, 2010).

Estimates from field campaigns, or small-scale modeling (large-eddy simulations, LES) are limited to specific cases, and the simulations often rely on idealized boundary conditions. Examples from observations come from flight and satellite-based AVHRR observations by Taylor and McHaffie (1994) and Platnick and Twomey (1994) who confirmed higher cloud susceptibility to aerosol changes for lower initial pollution in several stratus scenes, or by Ackerman et al. (2000) who confirmed the Twomey effect by using ship track measurements. The first measurement of Twomey effect with ground based remote sensors has been conducted by Feingold et al. (2003). Werner et al. (2014) found a clear experimental evidence of the Twomey effect for shallow trade wind cumuli near Barbados from helicopter-borne spectral cloud-reflected radiance measurements (ACTOS) and collocated in situ observations. On the one hand these observations may ensure a large certainty degree concerning the observed processes but on the other hand only very specific ACI processes may be detected which may not represent a major contribution to the global mean forcing in a large-scale context.

The large-scale context is provided by satellite observations and global models, which however suffer from other restrictions. Satellite estimates may be flawed due to various retrieval problems (see Appendix B, Section B.1) or a joint variability not reflecting a cause-effect relationship (e.g. Gryspeerd et al., 2016). Furthermore, even though they can achieve resolutions of less than or about 1 km, the variability of ACI processes can occur below that restricting satellite estimates to be rather a statistical representation of large-scale average effects. Examples are the studies of Boers et al. (2006) who found a clear correlation of MODIS retrieved cloud albedo to droplet concentration for a selected region near Tasmania in the South Pacific, or the review on estimates from satellite retrievals and model simulations by Quaas et al. (2009b) who showed generally positive correlations of CDNC to aerosol optical depth (AOD) with models overestimating this effect over land.

Global models have coarse resolutions and need to rely on statistical formulations to simulate aerosol effects. These often involve empirically based parameterizations which may not be very reliable. However, only models allow us to compute anthropogenic forcing estimates relating PD to PI aerosol effects, while observations from satellites can distinguish only the PD natural and anthropogenic aerosol effects at most, also relying on broad assumptions.

Recent model studies on ACI effects and associated forcing estimates focus on a variety of different aspects. Bellouin et al. (2011) is one of the studies which confirm the importance of aerosols influencing the Earth's climate, albeit with a reduced impact in the future, using HadGEM2-ES. However, they focus on the impact of aerosol species and emission scenarios and suggest that nitrate aerosols will partially replace sulphate aerosols to become an

important anthropogenic species in the remainder of the 21st century.

Meanwhile there are studies who discuss the overall role of aerosols on climate change in comparison to other climate drivers. Stevens (2013) argued on the basis of a publication by Carslaw et al. (2013) that the climate forcing by natural aerosols in the pristine pre-industrial climate may have been of large relevance but is too poorly constrained to be estimated correctly, while in a today's atmosphere anthropogenic aerosol forcing might be irrelevant for climate forcing since the effect is buffered from the high levels of pollution and CO₂ is dominating the climate forcing instead. To this end, Anderson et al. (2003) argued that the magnitude and uncertainty of aerosol forcing may affect the magnitude and uncertainty of total forcing to a degree that has not been adequately considered in climate studies at all.

Other studies like the one from West et al. (2014) are digging deeper into the representation of aerosols and their interaction with clouds in climate models. They explored the range of uncertainty in ACI estimates attributable to the choice of parameterization of the sub-grid-scale variability of vertical velocity in HadGEM-UKCA and demonstrate that the use of a characteristic vertical velocity cannot replicate results derived with a distribution of vertical velocities.

Then there are studies looking into models as a way to understand the variability of observations better. Stier (2015) uses a fully self-consistent global model (ECHAM-HAM) and shows that common assumptions used in satellite studies on the relationship between aerosol radiative properties and cloud condensation nuclei are violated for a significant fraction of the globe, hinting to the potential of vertically resolving remote sensing techniques as one way to improve this.

Satellite observations and modeling studies have something in common despite their different assumptions, schemes, scales and processes they cover. Because clouds and ACI occur on finer spatiotemporal scales than can be resolved, satellites as well as models comprise a whole variety of processes which can occur in addition to aerosol effects and also oppose one another.

ACI retrievals at large scales then suffer from buffering effects from clouds, from high levels of pollution and unresolved processes as well as from averaging over different aerosol-cloud regimes leading to a rather low signal-to-noise ratio. This makes it difficult to disentangle various pathways and impacts of aerosol-cloud-climate forcings, which is very low (less than 2%) compared to the natural short-wave cloud radiative effect of about -50 Wm^{-2} .

In conclusion, a reliable global-mean quantification of aerosol-cloud-radiation effects is difficult to obtain. ACI and RF_{aci} estimates from process-scale modeling or field observations are limited to very specific and often idealized cases while satellite observations and global climate models are restricted by the too coarse resolution and confounding effects.

1.3 The scientific challenge

The goal of this study is to quantify interactions between aerosols and clouds at a global scale and to estimate the associated RF_{aci} . This is an exploratory thesis, in which a new approach with latest datasets and methodologies is used to improve existing estimates and analyses on aerosol-cloud-radiation-interactions. The gap between models and observations should be bridged by using multi-sensor satellite observations together with a model which is con-

strained by satellite retrievals, using the strength of both sides. The joint satellite-reanalysis approach is further advanced as the impacts of different aerosol species, cloud regimes and nucleation assumptions is taken into consideration.

This study should help to

- improve the level of understanding on aerosol-cloud-climate effects,
- disentangle important and less important pathways of aerosol effects on clouds,
- quantify ACI and RF_{aci} within a reliable uncertainty range,
- overcome the problem of the buffering effects from averaging over regimes,
- retrieve a higher signal-to-noise ratio by filtering out error-prone sources in the observations.

1.4 The chapter roadmap

This thesis starts out describing the fundamental elements and processes involved in aerosol-cloud-radiation interactions. This is done in Chapter 2 which describes how a cloud is formed, what a cloud condensation nuclei (CCN) is and what supersaturation has to do with it.

Then in Chapter 3 a CCN climatology is derived on the basis of the ECMWF MACC-II aerosol reanalysis. The model and the assimilation is described and the relevant aerosol masses and numbers are validated. This is important as the resulting CCN are used in the following analyses.

In Chapter 4 the satellite-reanalysis approach is introduced combining the MACC-II reanalysis with merged multi-sensor satellite retrievals from NASA. This chapter has a comprehensive methodological part (including the Appendix B) in which the approach, the ingoing observations, the related uncertainties and assumptions, the droplet activation parameterization and the cloud regimes as well as updraft experiments is explained and validated as far as possible. The results of this chapter illuminate supersaturations, cloud droplet numbers (CDNC) and their susceptibility to aerosol (CCN) changes for different cloud regimes in a set of systematic parameterization experiments.

The last chapter (Chapter 5) uses the results from the previous chapters to calculate a present-day radiative forcing due to aerosol-cloud-interactions RF_{aci} , using a stand-alone radiative transfer scheme and estimates of PD anthropogenic aerosol fractions used in CAMS provided from Nicolas Bellouin on the basis of his study Bellouin et al. (2013). The resulting RF_{aci} is not related to the change from the preindustrial era, but is rather an estimate of the difference of today's anthropogenic contributions over purely natural ones. Again, this is evaluated for different cloud regimes and updraft experiments giving this estimate a range of uncertainty.

The chapters are successive but still so different that each of them has an abstract, an introduction, a methodology part, results and discussion and a conclusion. The overall summary is given in the bibliographic description.

Fundamentals

To understand how aerosols interact with clouds, the characteristics of both elements have to be examined individually. In this Section, the properties and the relevance of aerosols are investigated and the question of what makes an aerosol a good CCN is discussed. Then the fundamental principles of droplet nucleation and cloud formation is reviewed and the properties of clouds and their role in the climate system is briefly described.

2.1 Tropospheric aerosols

Aerosols are defined as a suspension of solid or liquid particles in the air with sizes in the order of a few nanometers to tens of micrometers in diameter D_s (assuming they are spherical particles). Particles are distinguished between primary aerosols, which are directly emitted as such from the surface, and secondary aerosols which form via gas-to-particle conversion processes in the air or within clouds. Their origin can be of natural kind, such as wind-borne sea spray, dust, or volcanoes, or they can stem from anthropogenic activities, such as combustion of fuels (Ghan and Schwartz, 2007; Kaufman et al., 2002).

Aerosols can change their size and composition by various processes, e.g. by hygroscopic growth, coagulation, chemical reactions (aging or coating) or by activation to form a cloud droplet. Therefore, their size distribution is usually divided into modes, as shown in Figure 2.1. The number concentration distinguishes between the nucleation mode ($D_s \lesssim 0.01 \mu m$), which contains fresh aerosols nucleated from the gas phase, and the Aitken mode (from ~ 0.01 to $\sim 0.1 \mu m$) which contains primary particles on which very often secondary material condenses on. They typically dominate the rural and the urban areas. Particles larger than $\sim 0.1 \mu m$ are small in numbers, while for the volume (mass) distribution they are considerable. The volume distribution basically consists of the accumulation mode (from ~ 0.1 to $\sim 2 \mu m$) and the coarse mode (from ~ 2 to $\sim 50 \mu m$).

Accumulation-mode particles arise from primary emissions; condensation of secondary sulfates, nitrates, and organics from the gas phase; and coagulation of smaller particles. Particles in the coarse mode are usually produced by mechanical processes such as wind or erosion (dust, seasalt, pollen, etc.) and are therefore primary, but can also stem from secondary sulfates or nitrates (Seinfeld and Pandis, 2006).

As the range in aerosol size goes over several orders of magnitudes, it is common to describe ambient aerosols by a log-normal distribution function. This has been shown to be a good fit to observed size distributions (e.g. Heintzenberg, 1994; Heintzenberg et al., 2011; Asmi et al., 2011).

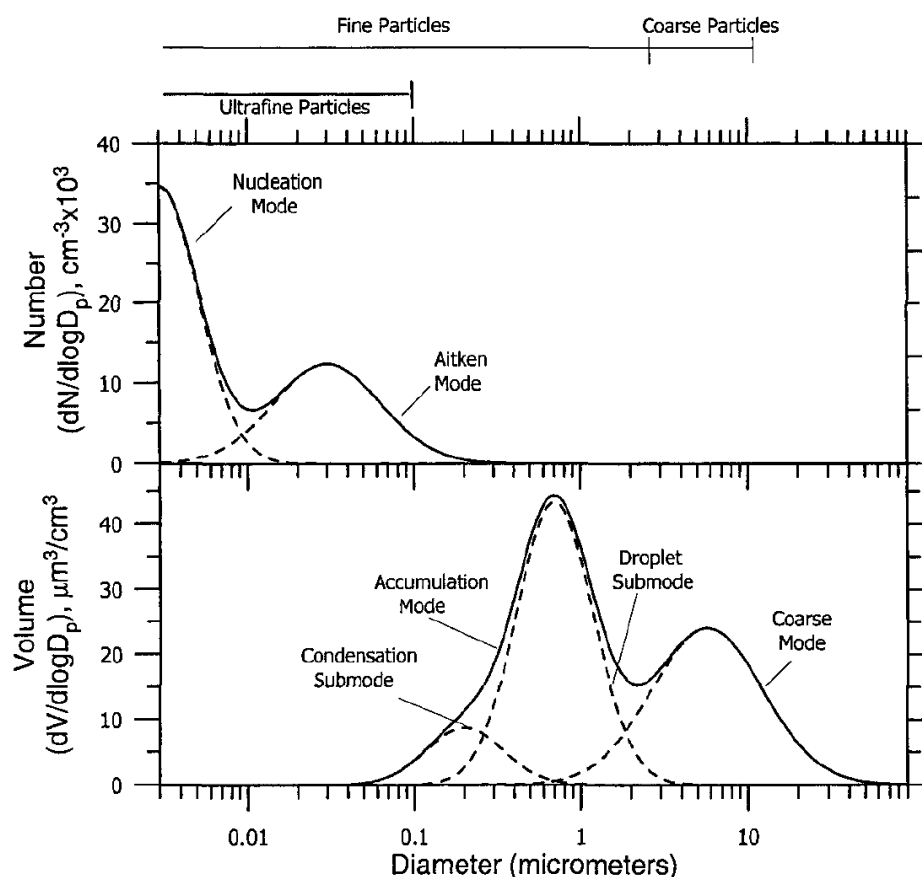


Figure 2.1: Aerosol modes - showing the typical number and volume distributions of tropospheric aerosols. This Figure is taken from Seinfeld and Pandis (2006).

Aerosols are removed from the atmosphere after a relatively short lifetime from a few days up to about one week by either dry deposition or wet deposition/scavenging. Resulting from the short lifetime and a highly non-uniform geographic distribution of sinks and sources the concentration and composition of aerosols varies widely over the globe (Seinfeld and Pandis, 2006; Ghan and Schwartz, 2007; Kaufman et al., 2002).

As was described in Section 1.2, aerosol effect our climate in two ways, via ARI and via ACI. An overview of the key properties of the main aerosol species is given in Table 2.1.

For ACI it is necessary that aerosols are capable of initiating drop formation at a given supersaturation (Pruppacher and Klett, 1997), that is that they serve as cloud condensation nuclei (CCN). To become a CCN an aerosol has to fulfill specific conditions.

First, the aerosols hygroscopicity plays an important role. Hygroscopicity describes the ability to attract, absorb, adsorb or release water molecules. It also refers to the change in diameter, volume and mass of particles when exposed to water vapor. Hygroscopic aerosols can swell as water molecules become suspended between the substance's molecules. This is the case for e.g. sea salt, sulfate or nitrate. For this it might be useful for the aerosol to be of hydrophilic nature, that is it can bond with water on a molecular level and thus is soluble in water. For hydrophilic compounds, the reaction with water might lead to the transformation

Table 2.1: Key aerosol properties of the main aerosol species in the troposphere. This table is adapted from Boucher et al. (2013).

Aerosol Species	Size Range	Main Sources	Main Sinks	Tropospheric Lifetime	Key Climate Relevant Properties
Sulfate (SU, SO_4)	fine modes	Primary: marine & volcanic emissions; Secondary: mostly by oxidation of SO_2	wet & dry deposition	~ 1 week	light scattering, very hygroscopic, enhances absorption when coated on BC, CCN active
Nitrate (NO_3)	accumulation & coarse modes	oxidation of NO_x	wet & dry deposition	~ 1 week	light scattering, hygroscopic, CCN active
Black Carbon (BC)	freshly emitted: ultrafine modes, aged: accumulation mode	combustion of fossil fuels, biofuels & biomass	wet & dry deposition	~ 1 week to 10 days	large mass absorption efficiency in the shortwave, CCN active when coated, may be good ice nuclei
Organic Matter (OM)	POA: aitken & accumulation modes, SOA: fine modes, aged: accumulation mode	combustion of fossil fuel, biofuel & biomass, terrestrial & marine biogenic ecosystems	wet & dry deposition	~ 1 week	light scattering, enhances absorption when coated on BC, CCN active (depending on aging, time and size)
Mineral Dust (DU)	coarse modes & small accumulation mode	wind erosion, soil resuspension, some agricultural practices & industrial activities	sedimentation, wet & dry deposition	~ 1 day to 1 week depending on size	light scattering & absorption, greenhouse effect, good ice nuclei
Sea Salt (SS)	coarse & accumulation modes	breaking of air bubbles induced by e.g. wave breaking, wind erosion	sedimentation, wet & dry deposition	~ 1 day to 1 week depending on size	light scattering, very hygroscopic, CCN active, can include POA in smaller size ranges

into another species, so that if the water evaporates from a solution, different aerosols are released than were dissolved. Hydrophobic aerosols, such as carbonaceous compounds, do not attract water vapor or are soluble in water. Thus, they cannot be CCN active when freshly emitted. The same is valid for fresh mineral dust (including calcium carbonate ($CaCO_3$), Arizona Test Dust (ATD), Illite, Kaolinite or Montmorillonite), which has a low hygroscopicity, and thus a low CCN activity (Tang et al., 2016). However, these aerosols can turn into CCN active species by aging or when they get coated by secondary more soluble compounds on their way through the atmosphere (Andreae and Rosenfeld, 2008). These chemical processes and different pathways are complicated to understand and to measure and are therefore still debated in the literature (Tang et al., 2016). This is one reason why in aerosol models they are still not properly described, but rather very much simplified or even totally neglected (Andreae and Rosenfeld, 2008).

Secondly, CCN are defined for a specific environmental supersaturation S_{sat} of water vapor. That means, that the number of particles from a given aerosol population that can act as CCN is a function of the water supersaturation and can only activate from a certain size on (see Section 2.2). In summary, size and chemical properties determine if an aerosol can act as a CCN or not. Given that the average lifetime of a CCN is about 1 week (Figure 2.1, Table

2.1), an average CCN is expected to experience 5 to 10 cloud activation/cloud evaporation cycles before actually being removed from the atmosphere by precipitation (Seinfeld and Pandis, 2006).

2.2 Droplet nucleation theory

The theory of heterogeneous droplet nucleation is founded on the work of Hilding Köhler (Köhler, 1936) who determined the equilibrium radius of particles as a function of dry radius r_s and relative humidity RH (Seinfeld and Pandis, 2006). We refer to the formulation of this relationship as the Köhler equation, which is explained further in this Section.

For the formation of a cloud droplet, the thermodynamic equilibrium between the gas and liquid phase needs to be reached. The condition for this equilibrium takes into account two effects, the curvature of the particles and the formation of aqueous solutions. These are the two pillars on which the Köhler equation is based on.

The curvature effect is described by the Kelvin equation which relates the equilibrium water vapor pressure p_w over a pure water droplet of diameter D_p to the equilibrium vapor pressure over a flat surface p_w° at the same temperature (Seinfeld and Pandis, 2006).

$$\frac{p_w(D_p)}{p_w^\circ} = \exp\left(\frac{4M_w\sigma_{w/a}}{R_G T \rho_w D_p}\right) \quad (2.1)$$

with the surface tension parameter $\sigma_{w/a}$, the universal gas constant R_G , temperature T , the molar mass of water M_w and the water density ρ_w .

It shows that at any given temperature the equilibrium vapor pressure over a curved interface exceeds that of the same substance over a flat surface. This can be explained in a more illustrative way. To bring a water molecule from the liquid to the gas phase, a certain energy is needed to overcome the attractive forces exerted by its neighbors. At a curved interface, as in a small droplet, there are fewer molecules immediately adjacent to a molecule on the surface than when the surface is flat. This makes it easier for a molecule to escape and the energy needed is smaller. Therefore it is possible that in an equilibrium between the liquid and the gas phase, the vapor pressure over the curved interface is higher than that over a plane surface, and even more so the smaller the droplet is (Seinfeld and Pandis, 2006).

The degree of saturation of a substance in air at temperature T is defined by its saturation ratio $S_{sat} = p/p_s(T)$ (Seinfeld and Pandis, 2006), where p is the partial pressure of the substance and $p_s(T)$ is the saturation pressure of the substance in the gas phase which is in equilibrium with its liquid phase at temperature T . For water vapor, we can write $p_w(D_p)/p_w^\circ = e(D_p)/e_s(T) = S_{sat}$, with the relation of e being the partial water vapor pressure and e_s being the saturation water vapor pressure, defining the saturation ratio or equivalently RH . For $S_{sat} < 1$, the parcel is then sub-saturated, for $S_{sat} = 1$ it is saturated and for $S_{sat} > 1$ the air is supersaturated. Now, Equation 2.1 can be written as

$$S_{sat} = \frac{e(D_p)}{e_s} = \exp\left(\frac{4M_w\sigma_{w/a}}{R_G T \rho_w D_p}\right). \quad (2.2)$$

Thus, the Kelvin equilibrium requires an environmental supersaturation S_{sat} of water vapor

($S_{sat} = (e/e_s) > 1 = (e/e_s) - 1 > 0$) in order to let a forming droplet form by diffusion in thermodynamic equilibrium. For the equilibration of a large pure water droplet, a modest S_{sat} is necessary, but a large S_{sat} is necessary for a small droplet.

Theoretical supersaturations required to form a droplet of pure water are very high (> 10%), but observations find supersaturations over liquid water to be typically less than 1% (Seinfeld and Pandis, 2006), which makes the formation of pure water droplets practically not possible in natural atmospheric conditions.

However, droplets in the atmosphere never consist exclusively of water; each droplet contains a dissolved compound - an aerosol particle. The effect of the solution is the one making droplet nucleation in natural atmospheric conditions possible. A solution causes a reduction of the water equilibrium vapor pressure over the solution p_s° in comparison to that over pure water p_w° and is described by Raoult's law (Seinfeld and Pandis, 2006)

$$p_s^\circ = x_w \gamma_w p_w^\circ \quad (2.3)$$

with $x_w = n_w / (n_w + n_s)$ being the mole fraction of water in a solution consisting of n_w water moles and n_s solute moles, and γ_w being the activity coefficient. The number of moles in a solution, n_s , depends on the number of ions ν that a molecule dissociated into when dissolved in water. A dissociated molecule that has dissociated into n ions is treated as n molecules, whereas an undissociated molecule is counted only once. Therefore, the reduction in water vapor pressure is strongly dependent on the type of solute, as it is more reduced by solutes that dissociate (e.g. salts) than those that don't (e.g. carbon).

Combining Equations 2.1 and 2.3, a relationship of the equilibrium water vapor pressure over a pure water droplet of diameter D_p to that over a solution (p_s°) can be found

$$\frac{p_w(D_p)}{p_s^\circ} = \frac{p_w(D_p)}{p_w^\circ} \frac{p_w^\circ}{p_s^\circ} = \frac{p_w(D_p)}{x_w \gamma_w p_w^\circ} = \exp\left(\frac{4M_w \sigma_w / a}{R_G T \rho_w D_p}\right). \quad (2.4)$$

Regarding that $\frac{1}{6} \pi D_p^3 = n_w \nu_w + n_s \nu_s$ with ν_w and ν_s being the partial molar volumes, and using this in combination with $1/x_w$ we obtain

$$\frac{p_w(D_p)}{\gamma_w p_w^\circ} \left(1 + \frac{n_s \nu_s}{\frac{\pi}{6} D_p^3 - n_s \nu_s}\right) = \exp\left(\frac{4M_w \sigma_w / a}{R_G T \rho_w D_p}\right), \quad (2.5)$$

which further evolves into

$$\ln\left(\frac{p_w(D_p)}{p_w^\circ}\right) = \frac{4M_w \sigma_w / a}{R_G T \rho_w D_p} + \ln(\gamma_w) - \ln\left(\frac{n_s \nu_s}{\frac{\pi}{6} D_p^3 - n_s \nu_s}\right). \quad (2.6)$$

For a dilute solution, it can be assumed that $\frac{\pi}{6} D_p^3 \gg n_s \nu_s$ and $\gamma_w \rightarrow 1$, and approximating $\ln(1+x) \simeq x$ as $x \rightarrow 0$ we can write Equation 2.6 as (Seinfeld and Pandis, 2006)

$$\ln\left(\frac{p_w(D_p)}{p_w^\circ}\right) = \frac{4M_w \sigma_w / a}{R_G T \rho_w D_p} - \frac{6n_s M_w}{\pi \rho_w D_p^3} = \frac{A}{D_p} - \frac{B}{D_p^3}, \quad (2.7)$$

$$\text{with } A = \frac{4M_w \sigma_w / a}{R_G T \rho_w} \quad \text{and} \quad B = \frac{6n_s M_w}{\pi \rho_w}$$

being the curvature parameter and the hygroscopicity parameter, respectively. Regarding the number of moles n_s also the number of dissociated ions ν of one solute molecule are

considered for a complete dissociation, thus writing $n_s = \nu m_s / M_s = (\nu \pi \rho_s D_s^3) / 6 M_s$ (Seinfeld and Pandis, 2006). Using this, the hygroscopicity parameter B can also be written as

$$B = \frac{\nu M_w \rho_s}{M_s \rho_w} D_s^3, \quad (2.8)$$

with D_s being the dry aerosol diameter. As was done for Equation 2.2, $\ln(p_w(D_p)/p_w^\circ)$ can be written as $\ln S_{sat} = \ln(e(D_p)/e_s)$ which is nothing more than the change in relative humidity $RH = e/e_s \cdot 100\%$ as a function of the aerosols' dry diameter and its hygroscopicity.

Equation 2.7 is already one form of the Köhler equation, in which is assumed that all of the aerosol mass in the solution is soluble and that the solution itself is very dilute.

To account for deviations of these assumptions, Equation 2.7 can be extended by including ε , the mass fraction of soluble material, and the osmotic coefficient ϕ_s , which is based on the molality - the number of moles of salt dissolved in 1 kg of water. ϕ_s depends on the concentration of the solute and its chemical properties. Both factors approach 1 for a more and more dilute solution. Adjusting Equation 2.7 to a more general form including ε and ϕ_s (similar as in Pruppacher and Klett (1997)), we get

$$\ln S_{sat} = \frac{4M_w \sigma_{w/a}}{R_G T \rho_w D_p} - \frac{\phi_s \varepsilon \nu \rho_s M_w D_s^3}{\rho_w M_s D_p^3} = \frac{A}{D_p} - \frac{B}{D_p^3} \quad (2.9)$$

with

$$A = \frac{4M_w \sigma_{w/a}}{R_G T \rho_w} \quad \text{and} \quad B = \frac{\phi_s \varepsilon \nu \rho_s M_w}{\rho_w M_s} D_s^3 = K D_s^3.$$

This is the form of the Köhler equation that will be applied later in Chapter 3, Section 3.3.5 and also in Chapter 4, Section 4.3.3. Equation 2.9 gives the supersaturation at a specific temperature at which a droplet is in equilibrium with its environment as a function of the wet droplet diameter D_p , the dry aerosol particle diameter D_s and the hygroscopicity of the aerosol particle. Dependent on these parameters, the Köhler function can vary in shape as shown in Figure 2.2.

The two terms of Equation 2.9 express the two effects that determine the vapor pressure over an aqueous solution droplet - the Kelvin effect that tends to increase vapor pressure and the solute effect that tends to decrease vapor pressure (Seinfeld and Pandis, 2006). For a pure water droplet $B \rightarrow 1$ as $D_s \rightarrow 0$, and the Köhler equation is merely dependent on the curvature effect.

From Equation 2.2 we have seen that the water vapor pressure of a pure droplet is always larger than the saturation vapor pressure ($e > e_s$), whereas now the vapor pressure of an aqueous solution drop can be larger or smaller than the saturation vapor pressure over a pure water surface depending on the magnitude of the solute effect term relative to the curvature term. That is, for a sub-saturated environment the droplet can also be in equilibrium if $D_p^2 A < B$.

For small droplets, the solute effect dominates and the various curves rise steeply, but as droplets increase in size the curvature effect becomes more and more dominant. For very large diameters, the solute concentration is so small that the droplet can almost be regarded as pure water so that all curves approach the Kelvin equation and differ no more.

From Figure 2.2, it can be seen that most curves pass through a maximum. For an aerosol

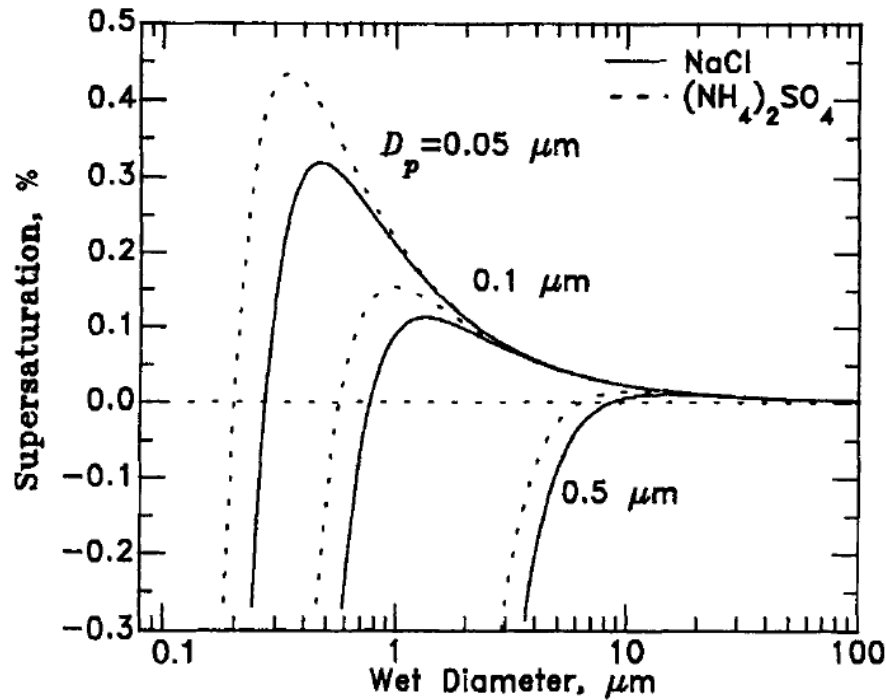


Figure 2.2: Köhler curves for $NaCl$ and $(NH_4)_2SO_4$ particles with dry diameters 0.05, 0.1, and 0.5 μm at 293 K (assuming spherical dry particles). The supersaturation is defined as the saturation minus one. This figure is taken from Seinfeld and Pandis (2006). Please note that the dry diameter is noted here as D_p whereas elsewhere it is stated as D_s .

of dry diameter D_s , we can find this Köhler maximum ($d \ln S_{sat}(D_p) / d D_p = 0$) at a critical wet diameter D_c of

$$D_c = \sqrt{\frac{3B}{A}} = \sqrt{\frac{3K D_s^3}{A}}, \quad (2.10)$$

and critical supersaturation S_c of

$$\ln S_c = \sqrt{\frac{4A^3}{27B}} = \sqrt{\frac{4A^3}{27K D_s^3}} = \frac{2}{\sqrt{K}} \left(\frac{A}{3D_s} \right)^{\frac{3}{2}}. \quad (2.11)$$

As the equilibrium behavior of the solution droplet depends on the type of solute, distinct differences in the curves of $NaCl$ and $(NH_4)_2SO_4$ can be observed due to differences in M_s . That is the reason why the curves of $(NH_4)_2SO_4$ lie above $NaCl$.

The critical diameter marks the onset of the cloud drop formation. For diameters smaller than the critical diameter, a solution droplet being in equilibrium with its environment is in a stable state as long as the atmospheric saturation is constant. Following the equilibrium line, any small perturbation it may experience in size is repelled by the difference in saturation to the fixed atmospheric saturation so that it will return to its original size. Here droplet growth can only occur in response to an increase in RH .

If the ambient saturation ratio S_{sat} exceeds the critical supersaturation S_c , the droplet can exceed the critical diameter D_c , where it enters an unstable equilibrium state. Following the equilibrium line in this region of the Köhler formulation, a small increase in size corresponds to

a decrease in saturation so that it will be lower than the fixed atmospheric saturation. Thus, as already described for the Kelvin effect, the droplet will grow further to become a cloud drop of $10\ \mu\text{m}$ or more in diameter, as long as S_{sat} stays higher than equilibrium saturation ratio of the drop. Conversely, a small decrease in size leads to a higher equilibrium vapor pressure than the ambient and the droplet will evaporate until it intersects the ascending branch of the Köhler curve and is back in a stable equilibrium.

In summary, a diameter larger than D_c is needed to activate a particle. Corresponding to that, an ambient saturation ratio S_{sat} larger or equal to S_c is also needed. Imagine a particle at D_c . A small increase in size will lead to a smaller saturation ratio than in the environment if $S_{sat} > S_c$ and the particle can be activated. For $1 < S_{sat} < S_c$, the conditions for activation are not fulfilled. Instead there would be two equilibrium states, with one being stable and the other unstable. A particle in the stable state can only grow up to S_{sat} but cannot be activated as it does not reach the required S_c , thus D_c . These particles are called haze particles or interstitial aerosols. A particle in the unstable state, which already has fulfilled the conditions for activation can now either grow further or evaporate, and thus transfer into the stable state. Thus, a transfer between the two states is only possible in case of evaporation, but not for condensation.

These behaviors are important to understand, as the ambient S_{sat} during a cloud formation can vary in time, e.g. when the air parcel mixes with drier air (entrainment), or the updraft velocity changes so that cooling is reduced. Further information on S_{sat} is given in the next Section.

2.3 Clouds and their relevance for climate

The American philosopher, anthropologist and natural science writer Loren C. Eiseley once wrote "If there is magic on this planet, it is contained in water" (Eiseley, 1953). In fact, without water in all its diversity life on earth would hardly be possible nor as fascinating as we know it.

More than $\sim 97\%$ of Earth's water is stored in the oceans, $\sim 2.1\%$ in solid form in the polar ice caps and $\sim 0.6\%$ exists as ground water. Only $\sim 0.001\%$ is contained in the atmosphere where it exists in all three phases (Seinfeld and Pandis, 2006). Via transport and phase changes induced by varying pressures and temperatures, this tiny amount of water shapes our weather and climate tremendously. In the gas phase, water plays a major role for the energy balance of the earth acting as a greenhouse gas. But also in liquid or solid form - as clouds - water has a large impact on the energy budget, as clouds reflect solar radiation (short-wave cloud radiative effect (SWCRE) of about $-50\ \text{W m}^{-2}$) and absorb and re-emit outgoing terrestrial radiation (long-wave cloud radiative effect (LWCRE) of about $+30\ \text{W m}^{-2}$), thereby exerting cooling and warming effects on the planet depending on the cloud's properties. The global mean net cloud radiative effect (CRE) is about $-20\ \text{W m}^{-2}$, implying that clouds have a net cooling effect on the Earth's surface in the current climate state (Loeb et al., 2009; Boucher et al., 2013).

But what exactly determines a cloud and what are typical characteristics of clouds?

The WMO International Cloud Atlas (WMO, 1975) gives the following definition: "A cloud is a hydrometeor consisting of minute particles of liquid water or ice, or of both,

suspended in the free air and usually not touching the ground. It may also include larger particles of liquid water or ice as well as non-aqueous liquid or solid particles such as those present in fumes, smoke or dust.” Further they state that “the appearance of a cloud is determined by the nature, sizes, number and distribution in space of its constituent particles; it also depends on the intensity and color of the light received by the cloud and on the relative positions of observer and source of light (luminary) with respect to the cloud.”

In other words, clouds are an accumulation of air-suspended cloud droplets or ice crystals which have formed from cloud-active aerosols and water vapor. And just like aerosols, clouds and their characteristics are highly variable in space and time. The detection of a cloud and observation of its properties depends on the sensitivity and resolution of the observing system. Even if invisible to the human eye, very thin clouds (such as sub-visible cirrus or ground-near mist) can still be detected by remote sensing techniques measuring in the infrared region of the electromagnetic spectrum.

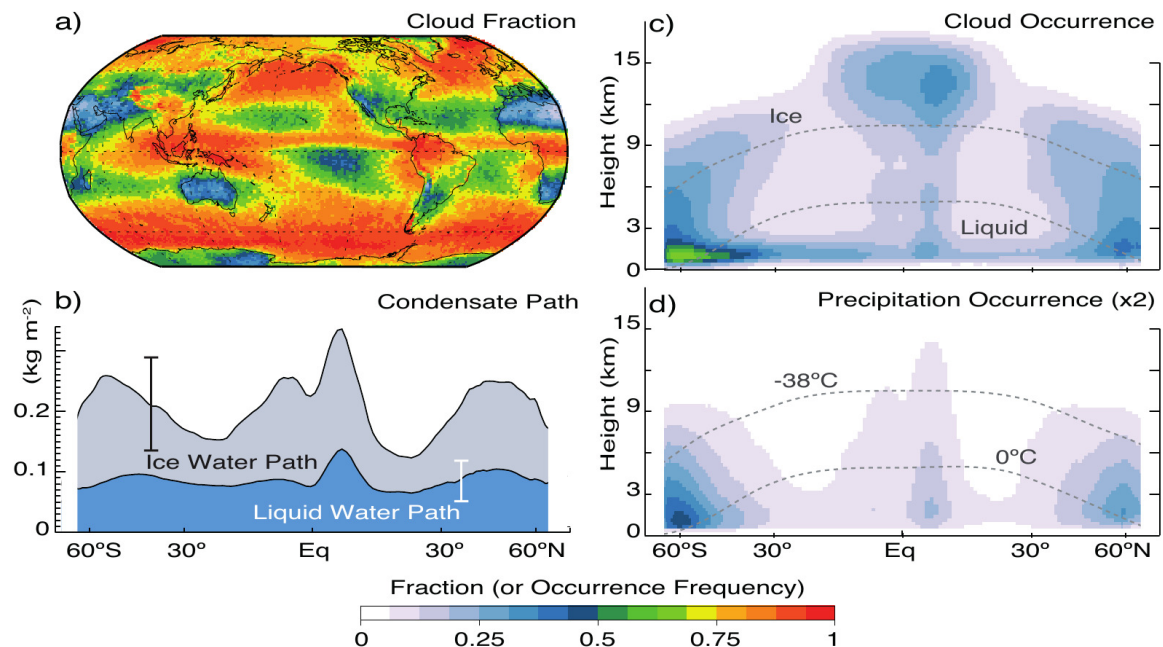


Figure 2.3: Global cloud properties, a) annual mean cloud fractional occurrence (CloudSat/CALIPSO 2B-GEOPROF-LIDAR data set for 2006-2011; Mace et al. (2009)) ; b) Annual zonal mean liquid water path (blue shading, microwave radiometer data set for 1988-2005; O’Dell et al. (2008)) and total water path (ice path shown with gray shading, from CloudSat 2C-ICE data set for 2006-2011 over oceans; Deng et al. (2010)), with 90% uncertainty ranges indicated by the error bars; c-d) latitude-height sections of annual zonal mean cloud occurrence and precipitation occurrence (2B-GEOPROF-LIDAR data set, attenuation-corrected radar reflectivity > 0 dBZ). The latter has been doubled to make use of a common color scale. The dashed curves show the annual mean 0°C and -38°C isotherms. This figure is taken from Boucher et al. (2013).

Satellites have contributed much to our understanding of the structure and occurrence of clouds. Especially active sensors, such as the Cloud Profiling Radar (CPR) on the CloudSat satellite (Stephens et al., 2002, 2008) and the Cloud-Aerosol Lidar with Orthogonal Polarization (CALIOP) on board the Cloud-Aerosol Lidar and Infrared Pathfinder Satellite Observations (CALIPSO) satellite (Winker et al., 2004, 2007, 2009) have significantly improved the quantification of vertical profiles of cloud occurrence and water content, and complement the detection capabilities of passive multispectral sensors, such as the Moderate resolution

Imaging Spectroradiometer (MODIS) on board of the Aqua and Terra Satellites (King et al., 1992, 1998).

From these satellite observations it is known that clouds roughly cover about two third of the globe, with varying values depending on the optical depth threshold used to define a cloud and the spatial scale of measurement (Wielicki and Parker, 1992; Stubenrauch et al., 2013; Boucher et al., 2013). The global distribution of cloud fraction, occurrence, water and ice content and precipitation occurrence as derived from satellite measurements is shown in Figure 2.3. High cloud fraction can be found in the Intertropical Convergence Zone (ITCZ), in the oceanic storm track regions and in regions of preferred stratocumulus occurrence, e.g. along the westcoast of South America and South Africa. Less cloudy regions are the central subtropical oceans and the continental desert regions.

The vertical distribution reveals that a large fraction of the clouds in the ITCZ are ice clouds (cirrus anvils) which develop from high rising convective clouds (cumulus congestus/ cumulonimbus). A large part of the storm track clouds are of mixed phase, and only a very small part is purely liquid. In the subtropics, where cloud fraction and cloud occurrence is low, most of the clouds are purely liquid. In this categories fall e.g. the stratocumulus decks. The condensate path shows that the mass of ice is in general twice as large as the mass of water contained by all of the clouds together, zonally averaged. This confirms that a large part of the cloud occurs in the mixed or ice phase.

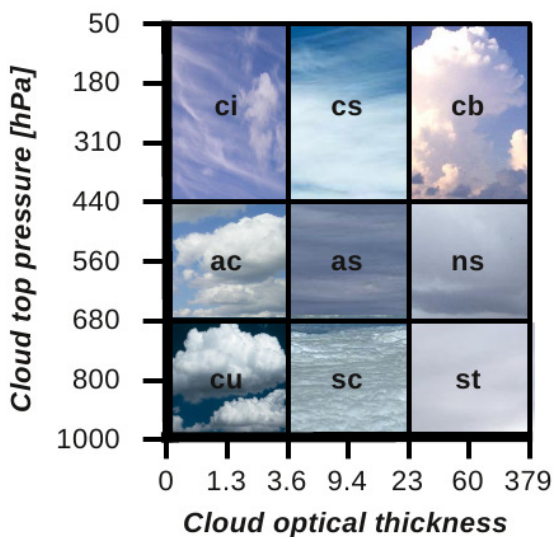


Figure 2.4: ISCCP cloud classification, distinguishing cloud types by top pressure and optical thickness. This figure is adjusted from Rossow and Schiffer (1999), by using cloud pictures from the Karlsruher cloud atlas (www.wolkenatlas.de). For abbreviations please see the List of Symbols.

The precipitation occurrence is related to these two pictures (Figure 2.3b and c), as most of the precipitation occurs for latitudes with a lot of clouds in the mixed or ice phase. Only a small fraction comes from warm liquid water clouds. This behavior has recently been confirmed and extended by findings of Mülmenstädt et al. (2015), who showed that most of the precipitation over the tropical oceans outside the ITCZ is warm rain defined as rain produced via the liquid phase only, while cold rain produced via the ice phase dominates the precipitation occurrence over the midlatitude oceans and continents. According to his findings, the scarcity of warm rain over land might be explained by smaller cloud drops in continental clouds which delay the onset of precipitation. In comparison to the cloud occurrence, the precipitation occurrence is much lower. This indicates that clouds form and evaporate repeatedly.

Only a small fraction ($\sim 10\%$) of all clouds actually generate precipitation which likely reaches the surface (Seinfeld and Pandis, 2006; Stephens et al., 2008). In most cases the cloud will evaporate without forming rain droplets, or the raindrops evaporate on their way to the surface.

Besides the distribution of clouds, the cloud type is an important feature to notice since it gives information on the environment the cloud has developed in. In the approach suggested by Rossow and Schiffer (1999), using data from the International Satellite Cloud Climatology Project (ISCCP), clouds can be roughly sorted into 9 categories, depending on their optical thickness and their top pressure (Figure 2.4). This already indicates that the amount and structure of clouds might be dependent on meteorological conditions, heat fluxes and surface coupling. The typing can however vary with the criteria chosen to categorize clouds. The environmental conditions also determine the ambient supersaturation under which a cloud can form by nucleation of aerosol particles. Therefore the ambient, or maximum supersaturation S_{max} might be described dependent on cloud regime. More on this topic will be discussed in Chapter 4.

We have seen from the previous Section how particles become activated in dependence of their size, chemical characteristics and the maximum supersaturation. But what determines S_{max} , and how can an air parcel achieve supersaturation?

The saturation vapor pressure e_s marks the ability of an air parcel to hold water vapor as a function of temperature and is given by the Clausius-Clapeyron relation, which can be approximated as (Pruppacher and Klett, 1997)

$$\frac{d \ln e_s}{dT} \approx -\frac{L_e}{R_G T^2}, \quad (2.12)$$

with L_e being the latent heat of evaporation. Equation 2.12 shows that the saturation vapor pressure decreases exponentially with temperature. Together with the ideal gas equation for water vapor $e = \rho_v R_v T$ we find the conditions for evaporation ($e < e_s$; $RH < 1$), for condensation ($e > e_s$; $RH > 1$) and for saturation ($e = e_s$; $RH = 1$).

In order to form a cloud, it is necessary that the air parcel achieves and exceeds the saturation line. Under natural atmospheric conditions, a moist air parcel exceeds 100% RH usually via two mechanisms, either by isobaric or by adiabatic cooling.

Isobaric cooling is the decrease in temperature of the air parcel under constant pressure. This usually occurs as a result of radiative losses of energy (radiative cooling) or horizontal movement of an airmass over a colder land or water surface or colder air masses and subsequent conduction of heat. Fog and low stratus are typically formed via this process. Here, heat exchange with the environment is the essential driver of this mechanism. Saturation is then reached when the air parcel temperature reduces down to the dew point temperature of the unperturbed parcel.

Adiabatic cooling is an idealized process, for which no heat exchange of the air parcel with its environment is assumed. The cooling occurs by expansion due to decreasing pressure as the air parcel rises in the atmosphere. The formation of convective, orographic and most frontal clouds as well as clouds formed by wave perturbations is typically generated via this process. The thermodynamic behavior of a rising moist air parcel can be described in two steps. First, by the rise of the unsaturated parcel following the dry adiabatic lapse rate $\Gamma = \frac{dT}{dz} = -\frac{g}{c_p}$ up to the Lifting Condensation Level (LCL) near cloud base where it reaches saturation. Secondly, by a lifting beyond the LCL, where the saturated parcel moves along the moist adiabatic lapse rate $\Gamma_s = \frac{dT}{dz} = -\left(\frac{g}{c_p} + \frac{L_e}{c_p} \frac{dm_w}{dz}\right)$. Here, the decrease in the water vapor mass mixing ratio m_w due to condensation and the corresponding release of latent

heat is taken into account. The latent heat release enhances the buoyancy of clouds, but also offsets the cooling from the parcel expansion, so that the air now cools at a lower rate than in the unsaturated state. Thus, the temperature gradient inside a cloud is less than that for cloud-free air ($|\Gamma| > |\Gamma_s|$). We can set $\frac{dm_w}{dz} \propto \frac{dm_w}{dT}$, with $\frac{dm_w}{dT} \propto \frac{d \ln e_s}{dT}$. The moist lapse rate is not a constant like the dry adiabatic lapse rate, but rather a strong function of temperature. Therefore, in a warm atmosphere with lots of water vapor, Γ_s is significantly lower than Γ due to larger derivatives in dm_w/dT . For decreasing temperatures $\Gamma_s \rightarrow \Gamma$. It has been found that in the tropics the moist adiabatic lapse rate is roughly one-third of the dry adiabatic lapse rate, while in the polar regions the difference is minimal (Seinfeld and Pandis, 2006).

For both mechanisms, isobaric and adiabatic cooling, it is assumed that no mass exchange occurs with the environment of the air parcel, so that the specific humidity stays constant, and the parcel can become supersaturated with water vapor upon a little more cooling when it has reached saturation. In reality there is always some heat and mass exchange between the parcel and its environment causing a substantial deviation from adiabaticity, e.g. by entrainment of drier surrounding air making the cloud sub-adiabatic. This is why Γ_s usually overestimates the temperature difference between cumulus clouds and the environment (Seinfeld and Pandis, 2006). A correction for the entrainment rate would increase the lapse rate and would describe cloud formation more realistically. However, this is not easily done, as the entrainment rate depends on the time and length-scale characteristics of the entrainment process as well as on the relative humidity of the environmental air. The difference of time scale of entrainment to that of evaporation is one factor determining the type of turbulent entrainment-mixing process, which can be homogeneous or inhomogeneous and may cause partial or, for the inhomogeneous case, total droplet evaporation. The entrainment of sub-saturated ambient air introduces a broadening in the droplet size distribution - a critical feature determining rain formation and cloud lifetime. Although the conceptual model is well established, these processes are poorly understood and quantified in real conditions and are matter of ongoing scientific work (e.g. Freud et al., 2011; Lu et al., 2013; Tölle and Krueger, 2014).

We imagine now an air parcel that has reached saturation and is in equilibrium with the surrounding environment. The particles have already grown to several times their dry size as a result of water absorption. Upon further cooling, the particles absorb more water vapor, but the cooling rate is too rapid compared to the mass transfer and the air parcel becomes supersaturated. The particles become activated, first the larger ones, later the smaller ones. The rate of growth of droplets by water vapor diffusion onto the particles is inversely proportional to their diameters so smaller droplets grow faster than larger ones. As a result, small droplets catch up in size with larger ones during the growth stage of the cloud (Seinfeld and Pandis, 2006). As more and more particles get activated, the rate of transport of water from the vapor to the particulate phase increases. As a result the supersaturation increase from the cooling is slowly reduced by the consumption of water vapor by the diffusional growth of the droplet. The balance of these two processes determine the rate of change of supersaturation S_{sat} which can be expressed in a simplified form as (Leitch et al., 1986; Pruppacher and Klett, 1997; Abdul-Razzak et al., 1998)

$$\frac{dS_{sat}}{dt} = \alpha w - \gamma \frac{dW}{dt} , \quad (2.13)$$

with α and γ being size-invariant coefficients, w being the cloud-scale updraft velocity (determining the cooling rate) and dW/dt being the condensation rate during the aerosol activation and subsequent growth processes. The velocity of the air parcel is the result of buoyancy forces and the gravitational force due to liquid water. The buoyancy force is proportional to the volume of the air parcel and the density difference between the air parcel and its surroundings. The condensation rate is limited by the mass transport to particles, which in turn depends on the particle size distribution and on their state of activation (Seinfeld and Pandis, 2006). Although the effect of the cooling rate on supersaturation in Equation 2.13 is expressed in terms of updraft velocity, it holds as well (in a more generalized form) for radiative cooling processes which has been shown by Ghan et al. (1993). The maximum supersaturation of the parcel S_{max} is reached for $dS_{sat}/dt = 0$, that is the cooling and condensation rate balance each other. Further details on the saturation balance equation are given in the Appendix B, Section B.2.

A climatology of cloud condensation nuclei derived from the MACC-II aerosol reanalysis

3.1 Abstract

Determining concentrations of cloud condensation nuclei (CCN) is the basis to analyze aerosol-cloud interactions (ACI). Here, we introduce and evaluate a CCN climatology derived from the MACC-II aerosol reanalysis. This climatology is the first of its kind, providing 3-D CCN concentrations of global coverage for various supersaturations and aerosol species from 2003 to 2012, offering the opportunity to be used for evaluation in models and in ACI studies.

As in many previous observational studies on ACI, the resulting CCN have a strong tie to aerosol optical depth (AOD), as this is assimilated in the MACC-II reanalysis to constrain modeled aerosols. While the bulk CCN-AOD relationship is kept, the CCN distribution within the atmospheric column is revised with the help of the ECMWF MACC-II aerosol reanalysis. Therefore, four of the main uncertainties related with AOD as a proxy for CCN are tackled, that is the vertical resolution, the insufficient spatial and temporal coverage, the aerosol speciation as well as the influence by hygroscopic effects.

The effect of these revisions is demonstrated in this study and evaluated with in-situ observations. The simulated total CCN concentrations agree well with surface observations, with correlation coefficient $R = 0.64$. In comparison to AOD with $R = 0.35$, the correlation coefficient almost doubles. This result shows that refining the observed column AOD by a vertical distribution and an aerosol speciation clearly improves estimates of CCN. The bias in total CCN is about +50% compared to surface in-situ observations. Reducing the bias in CCN relevant aerosol mass concentrations does not produce a better outcome. This indicates that besides the emission rates, the vertical distribution and the assumed aerosol size distributions of the model influence the result to a major extent.

3.2 Introduction

Determining concentrations of cloud condensation nuclei (CCN) is the basis to analyze aerosol-cloud interactions (ACI), which still are associated with large uncertainties in their contribution to climate change (Myhre et al., 2013). However, a global exploration of their magnitude, source, temporal and spatial distribution cannot be easily obtained from measurements, which is one the reasons for the low level of scientific understanding in ACI effects.

In-situ observations can detect CCN for various supersaturations, but they only provide sparse and very localized information. For that reason ACI studies often use satellite re-

trievals to get a global picture. However, a detection of CCN with remote sensing is not directly possible, but needs to be derived from optical properties. This is difficult due to the difference in size ranges important for CCN concentrations on one hand, and for light extinction on the other (Andreae, 2009). Nevertheless, aerosol optical properties such as aerosol optical depth (AOD) are commonly used as proxies for CCN in ACI studies (e.g. Kaufman et al., 2005; Quaas et al., 2008, 2009b; Grandey and Stier, 2010; Gryspeerdt and Stier, 2012; Bellouin et al., 2013; Koren et al., 2014). Even though it has been shown that AOD is suitable as a first indicator of CCN concentrations (Andreae, 2009), it suffers from various problems which makes it difficult to get a correct estimate of CCN. First of all, AOD is a bulk property and doesn't provide a vertical resolution of CCN which is needed when interactions with clouds are studied. The variability in the scale height of the vertical aerosol distribution and the existence of aerosol layers aloft can introduce substantial variability in the relationship between column and surface properties. Secondly, AOD can only be retrieved in cloud-free conditions and mostly over dark surfaces, so that larger areas such as the Sahara, the poles or areas with permanent cloud cover such as wide stratocumulus decks are not or insufficiently covered. Therefore, as satellite retrieved AOD does not offer a complete temporal and spatial coverage of the Earth's surface, sampling biases are introduced in its statistics. Third, AOD and also related optical properties such as the aerosol index (AI), cannot provide a specification of the involved aerosol components which matters to determine their chemical suitability as CCN. Furthermore, changes in relative humidity (RH) can result in pronounced variations in AOD due to aerosol swelling, while the actual number of CCN is constant.

Various studies using AI found an improvement in the relationship to CCN (e.g. Nakajima et al., 2001; Kapustin et al., 2006; Liu and Li, 2014) but the problems listed above still remain the same. This is confirmed by the findings of Stier (2015) who analyzed the relationship between AOD and CCN using a fully self-consistent global model (ECHAM-HAM). He found correlation coefficients between CCN at 0.2% at cloud base and AOD to be below 0.5 for 71% of the area of the globe. That means that AOD variability explains only 25% of the CCN variance. He also showed that correlations for alternative aerosol radiative properties proposed as superior proxies of CCN such as fine mode aerosol optical depth, dry aerosol optical depth and aerosol index (AI) do not show significant improvements.

Shinozuka et al. (2015) have examined the relationship between CCN and dry extinction for a variety of airborne and ground-based observations. They also demonstrate that the uncertainty in the CCN-AOD relationship arises not only from the uncertainty in the relationship between CCN and dry extinction, but also from the humidity response of light extinction, the vertical profile, the horizontal-temporal variability and the AOD measurement error. These examples show how important it is to account for these uncertainties related with CCN.

Several attempts exist to give a comprehensive picture on CCN relevant aerosol distribution and variability. Kinne et al. (2013) introduced the MAC-v1 climatology for tropospheric aerosol, which describes optical properties such as AOD, SSA (single scattering albedo) and fine-mode AOD fraction of tropospheric aerosols on monthly timescales and with global coverage. Aerosol mass concentrations are comprehensively assessed in a European aerosol phenomenology, which analyses PM10 and PM2.5 mass concentrations, their chemical composition and aerosol particle size distributions (Van Dingenen et al., 2004; Putaud et al., 2004, 2010). Asmi et al. (2011) have analyzed two years of harmonized aerosol number size distribution data from 24 European field monitoring sites, focusing on near surface aerosol particle

number concentrations and number size distributions between 30 and 500 nm of dry particle diameter, that is relevant for CCN sized aerosols. Winker et al. (2013) focused more on the aerosol vertical distribution, by constructing a monthly global gridded dataset of daytime and nighttime aerosol extinction profiles from Caliop lidar observations, thus introducing an initial global 3-D aerosol climatology. A synthesis of in-situ CCN measurements are provided by Spracklen et al. (2011), who used observations reported in the published literature to produce a worldwide dataset of CCN, which is combined with the GLOMAP global aerosol microphysics model to explore the contribution of carbonaceous combustion aerosol to CCN. Another CCN synthesis is provided by Paramonov et al. (2015), who uses measurements from the European Integrated project on Aerosol Cloud Climate and Air Quality interactions (EUCAARI) framework to analyse CCN activation and hygroscopic properties of the atmospheric aerosols. All of these studies taken together provide a sound foundation of CCN relevant aerosol properties, but most of them do not refer to CCN concentrations themselves, and the ones who do (CCN synthesis) do not give a global coverage nor a vertically resolved picture.

In this study we suggest a new approach to resolve these issues, by computing CCN from an aerosol reanalysis provided by the European Centre for Medium-range Weather Forecast (ECMWF). In contrast to satellite retrievals, a model can simulate the full spatial and temporal distributions of aerosols. On the other side, aerosol distributions and life cycles need to be modeled properly which is very challenging and usually depart distinctly from observations. Deviations can however be reduced by constraining modeled estimates with observations. This is done in the MACC-II reanalysis (Morcrette et al., 2009; Benedetti et al., 2009), in which assimilated AOD from MODIS (Moderate Resolution Imaging Spectroradiometer) is used to constrain total aerosol mass mixing ratio. Thus, a strong relationship between observation and model is kept, while the vertical distribution, the horizontal and temporal coverage, the aerosol speciation and hygroscopic effects are accounted for by the model.

Using the MACC-II reanalysis, we have produced a 10 year long CCN climatology which is presented and evaluated in this study. It consists of total 3-D CCN fields for three different supersaturations, and a 2D CCN field near the surface (at lowest model level) containing the relevant aerosol species involved for 31 S_{sat} ranging from 0.02 % to 1.5 %. The dataset offers the opportunity to be used for evaluation in models and in studies of aerosol-cloud interactions.

3.3 Data and Methods

Within the framework of the European Copernicus program (CAMS), previously known as GMES (Global Monitoring for Environment and Security), the European Centre for Medium-range Weather Forecast (ECMWF) provides an aerosol reanalysis for the Monitoring Atmospheric Composition and Climate (MACC) project. For this, the ECMWF Integrated Forecasting System (IFS) has been extended within the GEMS project (Global and regional Earth-system Monitoring using Satellite and in-situ data) to a near real-time assimilation and forecasting system of aerosols, trace and greenhouse gases (now IFS-LMD). Therefore, this project represents an unprecedented effort to model atmospheric aerosols in the context of operational numerical weather prediction (NWP) taking an advantage of state-of-the-art meteorological information and data assimilation techniques. Operation and improvement of this system was further developed in the Interim Implementation MACC-II.

The MACC-II reanalysis, which is used in this study, is therefore a state-of-the-art aerosol reanalysis covering the years 2003 to 2012, which is based on the ECMWF IFS extended aerosol model fully integrated in the four-dimensional assimilation apparatus employed operationally at ECMWF.

CAMS currently uses a simple bin scheme for its near-real-time forecasts and the reanalysis (IFS-LMD), while implementing a more elaborate modal scheme for the future (IFS-GLOMAP). The IFS-LMD aerosol scheme is the scheme that was introduced to add aerosol modeling to the ECMWF IFS forecasting system. It is currently used for the daily analysis and 5-day forecast and was also used for the MACC-II reanalysis.

3.3.1 The ECMWF IFS aerosol model

The ECMWF IFS has been extended by an aerosol scheme which mainly follows the aerosol treatment in the LMD-Z model (Boucher et al., 2002; Reddy et al., 2005). The resulting IFS-LMD (Morcrette et al., 2009) is a forward model which simulates the mass of five aerosol species: mineral dust (DU), sea salt (SS), sulfate (SU), black carbon (BC) and organic matter (OM).

A bin representation is used for the prognostic aerosols of natural origin, meaning mineral dust and sea salt. Sea salt aerosols are represented by 3 bins, with limits at 0.03, 0.5, 5 and 20 microns. Similarly, the desert dust aerosols are represented by 3 bins with limits at 0.03, 0.55, 0.9, and 20 microns. Further on, these bins will be referred to as small, medium and large modes (e.g. SSs, SSm and SSl). The limits of the three different size classes are chosen so that roughly 10, 20 and 70 % of the total mass of each aerosol type are in the various bins. A bulk representation is chosen for the other species, in which BC and OM are distinguished for being hydrophilic or hydrophobic.

The different aerosol species are assumed to be externally mixed, meaning that the individual species are assumed to coexist in the volume of air considered and to retain their individual optical and chemical characteristics, making it easier to trace them as they undergo model dynamics. In total the model predicts 11 model tracers which go into the IFS vertical diffusion and convection schemes and are advected by the semi-Lagrangian scheme. The IFS-LMD also includes emission sources and various aerosol physical processes, such as interactions of the aerosols with the vertical diffusion and convection, as well as sedimentation, dry deposition and wet deposition.

Mineral dust and sea salt emission is modeled dependent on near-surface wind speeds. Sea-salt production is calculated assuming an 80 % relative humidity, but only the dry mass is added to the respective bin and transported, thus no water is transported via the aerosol. Mass is not transferred between bins because of growth. However, wet density and radius are considered for all the size bins when dealing with dry deposition, sedimentation and radiation. For the other species, emissions are taken from inventories providing annual or monthly mean climatologies, such as the GFED (Global Fire Emission Database), SPEW (Speciated Particulate Emission Wizard) or EDGAR (Emission Database for Global Atmospheric Research). These data sets include sources of organic and black carbon, and sulphate aerosols linked to fire emissions, both natural and anthropogenic, plus emissions from domestic, industrial, power generation, transport and shipping activities. More details on the sources of aerosols are given by Dentener et al. (2006). It should be noted here that emission of aerosols of

volcanic sources are not included. Further, it should be noted that the model only contains tropospheric aerosols, a stratospheric contribution is not included.

The freshly emitted OM is distributed between 50% of hydrophobic and 50% of hydrophilic, while BC is kept as 80% hydrophobic and 20% hydrophilic. Once emitted, both species experience aging from hydrophobic to hydrophilic with a time constant of 1.16 days. The sulfur cycle is represented only as a very simplified version with sulfur dioxide (SO_2) produced at or near the surface which is being transformed into sulfate aerosol (SO_4 , or SU) using a prescribed, latitude dependent e-folding time scale ranging from 3 days at the Equator to 8 days at the poles. Nitrate, as well as secondary organic aerosols (SOA), are not included in the model. DU does not experience any aging or coating and is treated entirely as an insoluble aerosol.

The removal of aerosols is modeled by several processes: by dry deposition including the turbulent transfer to the surface and gravitational settling, or by wet deposition including rainout and washout of aerosol particles in and below the clouds. Wet deposition is modeled separately for convective and large-scale precipitation. The fraction of aerosol included in droplets through dissolution or impaction is set to 0.7 for all CCN relevant aerosol species.

Even though this aerosol model only uses a simplistic 1-moment bulk aerosol scheme, Morcrette et al. (2009) showed that it compares reasonably well with observations, even without assimilation.

3.3.2 The data assimilation apparatus

The IFS aerosol modeling and analysis system is fully integrated in the operational 4-D assimilation apparatus which has been extended to include atmospheric tracers among the control variables (Benedetti et al., 2009). A variational assimilation approach is used which combines model background information with observations to obtain the "best" forecast possible. The method is based on minimization of a cost function which measures the distance between observations and their model equivalent. The minimization is iterated until convergence is achieved within observational and model errors. A control variable is used for optimization of this cost function.

The assimilated observation is the total AOD (with different retrieval algorithms applied over land and ocean (Remer et al., 2005)) at $0.55 \mu m$ from MODIS collection 5 (MODerate resolution Imaging Spectroradiometer) on board of Aqua and Terra satellites, each available once a day over a wide path. AOD is not retrieved in cloud covered locations, nor at high latitudes where the solar illumination is small, nor over bright surfaces (snow covered high latitudes or the desert areas of Sahara and Australia) due to the impact of the surface reflectance on retrieval accuracy. Other factors affecting accuracy such as cloud contamination, assumptions about the aerosol types and size distribution, near-surface wind speed, radiative transfer biases, and instrumental uncertainties are also taken into account and are reviewed by Zhang and Reid (2006).

The assimilation window is 12 h. In this time period, there are around 16,000 data points on average from MODIS on Aqua and Terra satellites that would have to be assimilated. Since this is too much to be processed, the observational data are first subdivided into time slots of 30 min and ingested step-by-step over the window. Secondly, since the analysis is run at a coarser resolution (T159, corresponds to $\sim 120 \times 120 km$) than the original MODIS retrievals are ($\sim 10 \times 10 km$), a thinning is applied on the MODIS AODs to a

grid of $0.5^\circ \times 0.5^\circ$. Then the model aerosol fields are interpolated to the thinned subset of observations. Only afterwards, the observation operator which is used to compute the model equivalent is applied. It should be noted here that the assimilation modifies the modeled field not only at the point of observation but also around it. Regions with no observations because of cloudiness or high surface reflectance will still be improved by the data assimilation, but to a lesser extent than regions close to the location of assimilated data.

Total and component AODs are diagnosed at 17 MODIS correspondent wavelengths ranging from 0.34 to 2.13 microns by using precomputed optical properties, such as mass extinction coefficient α_e , single scattering albedo ω , and asymmetry parameter g (see Sect. 4.2 of Morcrette et al. (2009)). The optical characteristics of the aerosols are computed using Mie theory (Ackerman and Toon, 1981), and are then integrated over the physical size range using the model's prescribed log-normal distributions which are fixed for each tracer (Benedetti et al., 2009). Sea salt and dust AODs are obtained by summing over the individual bin contributions. Optical properties of hygroscopic aerosols are parameterized as a function of relative humidity accounting for the respective growth factors. The total AOD τ at the respective wavelength λ is then calculated as the sum of the single-species AODs,

$$\tau_\lambda = \sum_{i=1}^N \int_{p_{surf}}^0 \alpha_{ei}(\lambda, RH(p)) r_i(p) \frac{dp}{g}, \quad (3.1)$$

with N being the total number of aerosol species, r being the mass mixing ratio, p being the pressure of the model layer, p_{surf} being the surface pressure and g being the constant of gravity (Equation 3.1 is taken from Benedetti et al. (2009)).

The model control variable which is modified according to the outcome of the data assimilation, is the total aerosol mass mixing ratio, defined as the sum of the eleven aerosol species. At each iteration of the minimization, the increments in the total mass mixing ratio derived from the assimilation of MODIS AOD have to be redistributed into the mixing ratios of the single species. Thereby each aerosol component is corrected in proportion of its original contribution to the total aerosol mass, meaning that the modeled speciation is not changed by the assimilation. The total and species aerosol mass needs to be conserved over the assimilation window, meaning that non-conserving processes such as deposition and sedimentation should not be activated during the trajectory run. However, in practice the trajectory run is performed with all aerosol processes switched on. As stated in Benedetti et al. (2009), this still gives a meaningful analysis since most of the dominant physical processes happen over time scales longer than 12 h. For example, the typical residence time for the largest bin of desert dust and sea salt is approximately 1 day, whereas anthropogenic species have a typical residence time of a week.

3.3.3 Previous evaluation of MACC-II AOD and aerosol mass

For an accurate evaluation and monitoring of (anthropogenic) aerosol impacts it is important to combine model and observations. This can be seen clearly as agreement with observations improves when the aerosol data assimilation system is used. Validation of the free-running forecast (DIRECT) and the analysis including assimilation (ASSIM) was mainly done by Benedetti et al. (2009) and Mangold et al. (2011), which should be reassessed here to give a full and comprehensive picture in addition to my own validation which is about to be described and discussed in the following Sections.

To assess the horizontal distribution of modeled AOD, comparisons were carried out with monthly mean optical depths from MODIS and MISR (Multiangle Imaging SpectroRadiometer on board of TERRA satellite). Further, to analyze the temporal variability, time series of optical depths at a number of AERONET sites (ground-based Sun photometer networks) were taken and compared to model behavior.

The comparisons show that the analysis including assimilation has a lower bias and a lower root mean square error (RMSE) for most sites than the free-running forecast without assimilation. The assimilation also improves AOD over sites where the MODIS observations are not available due to the horizontal and vertical spreading of the correction in the assimilation process.

An in-detail validation was carried out for three specific test cases by Mangold et al. (2011). The events covered periods of high and low sea salt production, a large Saharan dust event in March 2004, and the summer heat wave in August 2003 over Europe, characterized by forest fire aerosol and conditions of high temperatures and stagnation, favoring photochemistry and secondary aerosol formation.

For these cases, not only AOD was validated, but also daily means of PM_{2.5} (particulate mass with a diameter lower than 2.5 μm) obtained from the French air quality monitoring network, handled by the French Environment and Energy Management Agency (ADEME). The sampling sites were located at Lille, Calais and Marseille, all being densely populated and industrial areas that provide the main emission sources of anthropogenic aerosols. The model equivalent PM_{2.5} concentrations (or rather fine-mode aerosols) are computed from the sum of the smallest SS size bin, 5% of the second SS size bin (which is 0.5 - 5 μm), the two smallest DD size bins, and all bins of OM, BC, and SU. Additionally, mass concentrations of SS and SU are compared to measurements from the EMEP (European Monitoring and Evaluation Programme) network, as well as from the Mace Head GAW station. This comparison with surface aerosol species concentrations is demanding, since the evaluation is looking into a surface mass concentration, while total AOD is used to correct aerosol column loads. This means that any error in aerosol composition, optical aerosol model and vertical distribution might be amplified (Mangold et al., 2011).

The results show a general overestimation in modeled sea salt AOD and corresponding to that, a significantly overpredicted total sea salt mass concentration.

The general transport and atmospheric dynamics is simulated reasonably well in the model. This was not just shown by comparisons with the CALIPSO cloud-aerosol masks which reveal that the model generally produces the cloud and aerosol in the proper location both horizontally and vertically. Also during the Saharan dust storm event the horizontal locations of the main features of the aerosol distribution were well captured, as well as the timing of the AOD peaks. However, the emission intensity of dust particles in the Sahara seems to be underestimated in the DIRECT version, which is improved by including the assimilation.

Also for the fire plume events, the model simulated the general pattern of areas of elevated fine-mode aerosol reasonably well, even though OM and BC were underrepresented in contrast to the dominating SU.

Sulfate mass concentration was found to be significantly overestimated in the model, although the temporal evolution during the heat wave period was well captured with correlation coefficients ranging from 0.70 to 0.86. During the period of increased sulfate mass (and therefore increased sulfate AOD), total AOD peaks were better matched with the ASSIM version,

compared to lower concentrations before and after the event. In general, one can conclude that fine-mode aerosol, which is dominated by SU, is overestimated in the aerosol model.

Since the assimilation of total AOD does not change the contribution of modeled aerosol specification, it has in principle no effect on correcting a positive (PM_{2.5}, sulfate mass concentration) or negative (desert dust plume AOD) model bias. Therefore, the assimilation of MODIS AOD does not significantly improve the simulation of the mass concentrations of the individual species. In comparison to measured PM_{2.5}, the simulated model equivalent mass agreed best with a correlation coefficient of 0.71, followed by observed AOD ($R = 0.47$) before modeled AOD ($R = 0.40$).

Since the model does not consider biogenic sulfate and organic carbon emissions, it cannot account for significant contributions those species might have on aerosol loadings. But as anthropogenic sulfate is largely overestimated, this can be evaluated somewhat as a compensation for the absence of biogenic component, especially over oceanic locations.

Mangold et al. (2011) offer various possibilities for explaining the results and improving the validation results. First of all, it is important to have a good representation of source functions and emissions, since the model computes AOD from mass extinction coefficients. For example, sea salt concentrations could be improved by refinements in the sea salt source function and wind speed modeling. The inclusion of a contribution by biogenic organic matter in sea spray due to enhanced biological activity in oceanic surface waters, yet unaccounted in the aerosol model, might also have positive effects.

Secondly, the quality of the results depends strongly on the dynamics of the model and the adequacy of the aerosol physical parameterizations. Thus, the discrepancies of modeled and observed PM_{2.5} might not just result from an overestimation of the emitted mass or inadequate emission inventories, but can also result from a too efficient and rapid conversion of SO₂ to SU and too weak dry deposition, or discrepancies in the aerosol vertical profile. Furthermore, the fraction of boundary layer SU might be too large. A more detailed sulfate chemistry scheme or the assimilation of fine-mode AOD might be useful to improve this effects. Another possibility is to make use of the Angstrom parameter which also gives information on the size of the aerosol particulate from observations of optical depth at different wavelengths.

The discrepancies during the fire plume events may result from the smoothed 8 day resolution of the emissions, which does not capture the strength of individual fires. Also, a parameterization of the injection height of fire-produced aerosol is required to properly represent long-range transport of aerosols from fire emissions. The vertical distribution could be improved via a plume model, the assimilation of vertical profiles of the extinction coefficient (using ground-based or spaceborne lidar data), and the introduction of the injection height for smoke aerosols (SEVIRI Fire Radiation Power product).

Finally, a validation of the results also depends on the representativeness of the observation used. The selection of sites is critical, since a strong local aerosol source at a certain station can distort the comparison when not accounted for. Therefore, an in-depth review of the results and comparisons with yet more independent data sets and more high-quality chemical observations might help to facilitate such an evaluation.

All this just shows the complexity and difficulties of modeling the conversion of aerosol species mass concentrations into optical properties. Problems may rise from the vertical distribution of the aerosol species, their optical constants, the crude bulk-bin aerosol size distributions or the spatial scales of the different parameters. To this end, it is important

to note that a new aerosol module "GLOMAP-mode" (Mann et al., 2010, 2012) is being implemented into the IFS, but is not available for the reanalysis yet. This new aerosol microphysics scheme is a 2-moment modal scheme which simulates the evolution of the particle size distribution, with explicit sources and sinks of particle number (e.g., via nucleation and coagulation) as well as mass. The scheme tracks the same tracers as the IFS-LMD but calculates how their composition is distributed across the size range resolving internal mixtures and gas to particle transfer. This will probably improve many points addressed in the validation above.

3.3.4 Evaluation of CCN relevant aerosol mass from MACC-II reanalysis with IMPROVE data

Because the accuracy of the retrieved CCN in this study depends on the accuracy of the simulated CCN relevant aerosol masses, we have extended the previous validation by Mangold et al. (2011) to specifically look at masses from SU, BC, OM and SS from the MACC-II reanalysis. While Mangold et al. (2011) only used specific "short term" test cases, we now have the opportunity to do "long term" analyses within the time period from 2003 to 2012.

The data was taken from the IMPROVE (Interagency Monitoring of Protected Visual Environments) network which is primarily funded by the US Environmental Protection Agency. A detailed description is given in Malm et al. (1994). The IMPROVE monitoring program is a collaborative association initiated in 1988, starting with 36 stations spread over US national parks and wilderness areas. Its goal is to monitor aerosols and visibility, to identify aerosol chemical species and emission sources, as well as to document long-term trends. The major visibility-reducing aerosol species, sulfates, nitrates, organics, light-absorbing carbon, and wind-blown dust are monitored as well as light scattering and extinction. Up to today this network has been widely extended, evaluated and technologically advanced. Even though the network has been extended to include urban locations, still most stations are situated in rural areas (Hand et al., 2011). Therefore, in contrast to the analysis by Mangold et al. (2011), the IMPROVE sites are representative for clean natural regions which are supposed to be not distorted from local anthropogenic aerosol sources.

In our analysis, we use 187 stations (Figure 3.1) from the currently available 220 sites (available at <http://views.cira.colostate.edu/fed/>) which accurately measure CCN relevant aerosol mass more or less continuously between 2003 and 2012. The stations were chosen regarding their data availability.

The IMPROVE version II sampling system (deployed in 2000) consists of four independent sampling modules (A, B, C and D) that collect 24-hour samples every third day. Three modules are fine-particle samplers (PM_{2.5}) while the fourth one samples particles with a diameter less than 10 microns (PM₁₀).

Each module contains a filter substrate specific to the analysis carried out. Module A is equipped with a Teflon filter for measuring gravimetric fine mass, elemental concentration, and light absorption. Module B contains a Nylon filter for detecting the anions sulfate, nitrate, nitrite, and chloride using ion chromatography. Module C works with a quartz fiber filter to measure organic and light absorbing carbon via thermal optical reflectance (TOR). Last but not least, module D utilizes a Teflon filter and a special PM₁₀ inlet to measure gravimetric PM₁₀ aerosol mass concentrations. A detailed description of the aerosol sampling is given in Hand et al. (2011), Chapter 1.

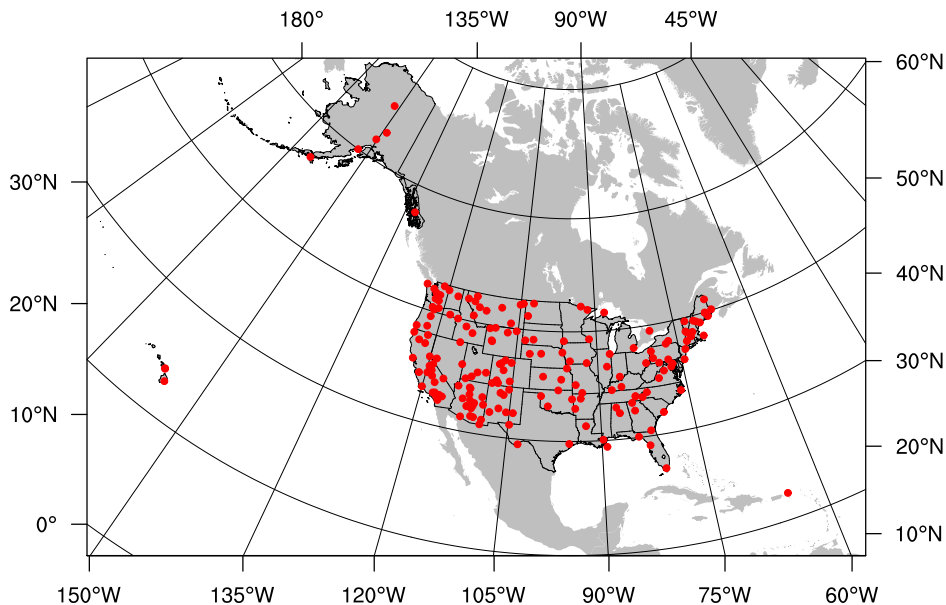


Figure 3.1: IMPROVE stations

To produce reasonable comparisons against CCN relevant aerosol species from MACC-II, we use the following retrievals from the IMPROVE network: Elemental sulfate (SO_4f) measured from Module B and obtained from the IMPROVE aerosol (IMPAERSPED) dataset; elemental carbon (ECf) derived from measured TOR carbon fractions in Module C, particulate organic matter (OMCf) determined as $1.8 \times$ organic carbon also measured with Module C, and fine-mode sea salt (SeaSaltf) computed as $1.8 \times$ chloride, or $1.8 \times$ chlorine if the chloride ion measurement in Module B is below detection limits, missing or invalid. ECf, OMCf and SeaSaltf are obtained from the IMPROVE aerosol calculated dataset (IMPAER-CALC). These species are compared against MACC-II SU, BC and OM (each as the sum of hydrophilic and hydrophobic components) and the first size bin of SS mass, respectively (see Section 3.4.2). The according model values were retrieved from the closest grid cell and compared in terms of daily means.

Uncertainties included in the IMPROVE measurements have been assessed in Hand et al. (2011) via comparisons with collocated stations from the EPA's Chemical Speciation Network (CSN, formally STN). Errors were fairly low for most species except for sea salt, which also had high biases reflecting differences in sampling or analytical techniques. We follow the error assessment from Hand et al. (2011) and assume uncertainties to be 16% for OMCf data, 20.2% for ECf data, 7.5% for SO_4f data (assuming similar errors as for ammonium sulfate) and finally 78.3% for SeaSaltf data.

The results of this comparison are shown and discussed in Section 3.4.2.

3.3.5 Computing the MACC-II reanalysis CCN

Using the MACC-II aerosol reanalysis, we have produced a 10 year long daily mean global 3D CCN field for three different supersaturations (0.2, 0.4 and 1%), and a 2D CCN field near the surface (at the lowest model level) containing the total CCN and CCN from SU, BC, OM and SS computed for 31 different supersaturation (S_{sat}) ranging from 0.02% to 1.5%.

Table 3.1: Aerosol physical and optical properties used in this study, with the count median radius r_0 and geometric standard deviation σ_g going in to the log-normal size distribution. The dry aerosol density ρ_p , as well as the optical properties as the mass extinction coefficient α_e , the single scattering albedo ω and the asymmetry parameter ϱ (all given for 550nm and 50% RH) are going into the aerosol optical depth computation. Furthermore, the aerosol molecular weights M_s are given. Properties are taken from Benedetti et al. (2009), Reddy et al. (2005) and references therein.

aerosol	r_0 [μm]	σ_g	ρ_s [g/cm^3]	M_s [g/mol]	α_e [m^2/g]	ω	ϱ
DU small	0.135	2.0	2.16	250.00	2.6321	0.9896	0.7300
DU medium	0.704	2.0	2.16	250.00	0.8679	0.9672	0.5912
DU large	4.4	2.0	2.16	250.00	0.4274	0.9441	0.7788
SS small	0.125	2.0	2.60	58.443	3.0471	0.9996	0.7394
SS medium	1.6	2.0	2.60	58.443	0.3279	0.9961	0.7703
SS large	10.0	2.0	2.60	58.443	0.0924	0.9916	0.8224
SU	0.0355	2.0	1.84	96.0631	6.609	1.0	0.673
BC	0.0118	2.0	1.80	12.01	9.412	0.206	0.335
OM	0.0355	2.0	1.76	180.00	5.502	0.982	0.655

The prescribed S_{sat} range is taken for the most commonly measured S_{sat} , as in Spracklen et al. (2011).

The CCN are calculated diagnostically in a box model, which once was created to be used for HadGEM3-UKCA (Davies et al., 2005; Mann et al., 2010; Hewitt et al., 2011; O’Connor et al., 2014). It also uses modules from a modified version of ECHAM5-HAM (Stier et al., 2005) and has now been updated to the ECHAM6 version (Stevens et al., 2013). It reads all necessary parameters, such as temperature, pressure, specific humidity and aerosol mass mixing ratios from the MACC-II reanalysis. First the mass mixing ratio is converted to an average aerosol mass concentration per volume via the dry air density ρ_a . In the next step, the mass per aerosol particle M_p is computed as

$$M_p = \frac{4}{3}\pi\rho_s(r_0\beta)^3 \quad \text{with} \quad \beta = 1.5 \cdot \ln^2 \sigma_g, \quad (3.2)$$

using the Hatch-Choate conversion (Hinds, 1998) which relates the count median radius r_0 to the radius of average mass for the prescribed log-normal size distribution with the geometric standard deviation σ_g .

The total aerosol number concentration N_a is then obtained by dividing the average aerosol mass concentration by the mass per aerosol particle. The resulting log-normal number distribution for an aerosol species k can be written as

$$N_{a,k}(r) = N_{a,k} \cdot \frac{1}{\sqrt{2\pi} \cdot \ln \sigma_{g,k}} \cdot \exp \left[-\frac{\ln^2(r/r_{0,k})}{2\ln^2 \sigma_{g,k}} \right]. \quad (3.3)$$

The relevant parameters of the size distribution and aerosol properties used are listed in Table 3.1. Please note that only hygroscopic aerosol species are used for further processing. Even though the total number concentration is computed with all 11 tracers, CCN concentrations result only from hydrophilic BC and OM, SU and SS components. Dust is treated entirely as an insoluble aerosol species and no aging or coating effects are considered in the model.

Once the number concentration is computed for each aerosol species, the Köhler theory (Köhler, 1936; Pruppacher and Klett, 1997; Seinfeld and Pandis, 2006) is applied to compute how

many aerosols act as CCN at a specific supersaturation. The Köhler equation is derived on the basis of a combination of two equations: the Kelvin equation, which governs the increase in water vapor pressure over a curved surface (curvature parameter A); and a modified Raoult's law, which describes the solution effect of the water equilibrium over a flat solution (hygroscopicity parameter B).

For the A and B parameter we follow Equation 2.9, writing them in dependence of the droplets dry radius r_s

$$A = \frac{2M_w\sigma_{w/a}}{R_G T \rho_w} \quad \text{and} \quad B = \frac{\nu\phi_s\varepsilon M_w \rho_s r_s^3}{M_s \rho_w} = K r_s^3, \quad (3.4)$$

with the surface tension parameter $\sigma_{w/a}$, the universal gas constant R_G , temperature T , number of dissociated ions ν , the mass fraction of soluble material ε and the osmotic coefficient ϕ . M_w and M_a are the molecular weights of water and aerosol, respectively; and ρ_w and ρ_s are the densities of liquid water and aerosol particle, respectively. It is assumed that all hygroscopic particles can completely absorb and dissolve in water so that the osmotic coefficient $\phi = 1$ and the fraction of soluble material $\varepsilon = 1$. The number of dissociated ions is assumed to be $\nu = 2$ for SS and SU and $\nu = 1$ for aged or coated OM and BC.

Since we deal with external mixtures, every aerosol species k has its own B parameter, so that $B = B_k$. The A and B parameter are used in the next step to calculate the corresponding radius of activation (critical radius, r_c) for each aerosol species.

Each water soluble particle has a threshold supersaturation. This threshold or critical supersaturation marks the onset of drop formation on a particle, that is, the particle gets activated. At the maximum of the Köhler curve, for a dry aerosol particle of radius r_s the critical supersaturation S_c is given by (Abdul-Razzak et al., 1998)

$$S_c = \frac{2}{\sqrt{K}} \cdot \left(\frac{A}{3r_s} \right)^{\frac{3}{2}}. \quad (3.5)$$

The critical supersaturation of the smallest aerosol particle in an aerosol population being activated is equal to the maximum supersaturation S_{max} of an air parcel rising adiabatically at uniform speed. Its critical radius r_c is then related to S_{max} as (Abdul-Razzak et al., 1998)

$$S_{max} = \frac{2}{\sqrt{K}} \cdot \left(\frac{A}{3r_c} \right)^{\frac{3}{2}}. \quad (3.6)$$

Particles smaller than r_c require a higher S_c than S_{max} and cannot be activated. Particles larger than r_c require a smaller S_c than S_{max} and can principally all activate. CCN can be described as potential CDNC as they are computed at a given supersaturation, meaning the maximum supersaturation is prescribed. For a given set of S_{max} the corresponding critical radii can therefore be computed as

$$r_c = \frac{A}{3K^{\frac{1}{3}}} \cdot \left(\frac{2}{S_{max}} \right)^{\frac{2}{3}}. \quad (3.7)$$

The number concentration of activated aerosols is the number concentration of aerosols larger than the size of the smallest activated aerosol, thus with a dry critical radius of r_c .

The calculation of the activated number fraction from the critical radii is done by transforming the individual log-normal distributions to an error function (Ghan et al., 1993; Khvorostyanov and Curry, 2006) which is then computed cumulatively as in the M7 aerosol microphysics scheme (Vignati et al., 2004).

3.3.6 CCN evaluation with ARM data

The resulting CCN are evaluated with data from the Atmospheric Radiation Measurement (ARM) network. The surface sites measure CCN concentrations at several supersaturations using a Droplet Measurement Technologies (DMT) single-column CCN counter (Roberts and Nenes, 2005).

The instrument steps through several supersaturations in a pyramid-like profile with 7 intervals (0.1, 0.2, 0.4, 0.6, 0.9, 1.1 and 1.2 %) in a cycle of 30 minutes with 5 minutes at each setting. The different supersaturations are obtained by variation of the chamber wall temperature. Additionally to the static calibrated supersaturations, S_{sat} are calculated using a heat transfer and fluid dynamics flow model (Lance et al., 2006). It is recommended to use the calculated S_{sat} since it is more reliable than the static calibrated one (Shi et al., 2013). The instrument’s calibration and uncertainties involved are discussed in Rose et al. (2008). We follow the assumption of Spracklen et al. (2011), who made a synopsis of extensive CCN observations, and found a range of uncertainties from 5-40 % depending on CCN concentration, supersaturation and the type of CCN instrument used. Based on their findings we assume a relative uncertainty of $\pm 40\%$ and a minimum absolute uncertainty of $\pm 20\text{cm}^{-3}$.

We have chosen to use the Aerosol Observing System Cloud Condensation Nuclei Average (AOSCCNAVG) value-added product (VAP) (Shi et al., 2013) because it consolidates the relevant CCN parameters into a single file and averages the data over the 5-minute integration time of each S_{sat} -value. Since the first minute of each S_{sat} -setting is unstable in terms of temperatures and the S_{sat} -value overshoots the setpoint, only the last four minutes are taken into account.

The AOSCCNAVG VAP produces two output datastreams, from which we have chosen to use the c2 output produced from the mentor-edited b1 level input datastreams. The data are taken from 4 land stations. Additionally we have taken AOS CCN data (not VAP) from the Marine ARM GPCI Investigation of Clouds (MAGIC) project which is a ship campaign. The sites, datasets and measurement times used, are listed in Table 3.2.

Stemmler et al. (submitted) found that for the GRW data, there was an abnormal degradation in CCN concentrations from October 2009 to June 2010. The values returned back to normal (in comparison to concentrations from the CN counter) after the instrument was maintained thoroughly. They corrected the data using monthly multiplication factors to obtain a stable ratio between CCN and NC, assuming that the CN counter was correct. In this study we also use the corrected dataset from Stemmler et al. (submitted) (kindly provided by Robert Wood). It significantly improves the validation of MACC CCN in comparison to the original ARM GRW data (not shown).

As in the validation of aerosol mass, we use daily means of quality checked CCN measurements. Special care is taken for the daily mean statistics, which is used to compute CCN at 0.4 % S_{sat} . To ensure a statistically stable result, only CCN data retrieved at at least 4 of the 7 S_{sat} -bins with a minimum of total 96 measurements per day (1/3 of maximum possible data coverage) are taken into account. Further we neglect data which seem to have artifacts

Table 3.2: ARM sites and measurement periods used for CCN validation.

Site/Campaign	Site ID	Dataset	Time period (month/year)
Southern Great Plains: Central Facility, Lamont, OK, USA	SGP	C1	01/2011-12/2012
Cape Cod: Highland Center, Cape Cod, MA, USA	PVC	M1	07-12/2012
Ganges Valley: ARIES Observatory, Nainital, Uttarkhand, India	PGH	M1	06/2011-03/2012
Graciosa Island: Azores, Portugal	GRW	M1	04/2009-12/2010
MAGIC: Los Angeles, CA to Honolulu, HI, USA - container ship Horizon Spirit	MAG	M1	10-12/2012

like a systematic significant increase of NC with supersaturation. This was mainly found for GRW data. Therefore, the corrected dataset from Stemmler et al. (submitted) was only applied on days with good daily statistics.

The comparison to MACC CCN is done for a single supersaturation at 0.4% for reasons of convenience. Were there enough data at 0.4% S_{sat} available, the daily average was simply taken from those measurements. Otherwise, the measured data from the various S_{sat} -bins were converted to CCN_{0.4} as is done in Andreae (2009), using Twomey's power law (Twomey, 1959; Seinfeld and Pandis, 2006)

$$CCN(S_{sat}) = CCN(1\% S_{sat}) \cdot S_{sat}^k. \quad (3.8)$$

Solving Equation 3.8 for k,

$$k = \frac{1}{\ln S_{sat}} \cdot \ln \left(\frac{CCN_{0.4}}{CCN_{1.0}} \right), \quad (3.9)$$

and transforming it to a more general form, regarding that $\ln(S_{sat} = 1\%) = 0$,

$$\ln CCN_2 - \ln CCN_1 = k \cdot (\ln S_{sat_2} - \ln S_{sat_1}), \quad (3.10)$$

one obtains this simple form

$$\ln CCN_{0.4} = k \cdot \ln \left(\frac{0.4}{S_{sat}} \right) + \ln CCN(S_{sat}). \quad (3.11)$$

Taking the exponential of Equation 3.11, we obtain the final form, which is used in this study to convert CCN at any measured S_{sat} to 0.4%

$$CCN_{0.4} = CCN(S_{sat}) \cdot \left(\frac{0.4}{S_{sat}} \right)^k. \quad (3.12)$$

The exponent k is computed from linear regression between logarithmic S_{sat} and the respective CCN. The actual behavior of CCN with S_{sat} is not exactly following the power law. A

demonstration and a possible extension of the formula is given in Cohard et al. (1998). This deviation has been accounted for by the standard deviation of k . But since this only adds about 1-3% uncertainty to $CCN_{0.4}$, it can be neglected compared to the 40% measurement uncertainty. For the $CCN_{0.4}$ validation results, please see Section 3.4.2.

3.4 Results and Discussions

Using the MACC-II reanalysis, a 10 year long daily mean global 3D CCN field for three different supersaturations was created, additionally to a 2D CCN field near the surface (at lowest model level) containing the relevant aerosol species involved for 31 S_{sat} ranging from 0.02% to 1.5%. This dataset offers the opportunity to be used as a CCN climatology, for evaluation in models and in studies of aerosol-cloud interactions.

3.4.1 The CCN climatology

Figure 3.2 shows the global distribution of CCN load [m^{-2}] over the atmospheric column, as well as the vertical distribution of CCN concentration [cm^{-3}] over latitudes. The two hemispheres are very much decoupled through both legs of the Hadley cell. The major CCN load can therefore be found between 30 and 60 degrees south and north, while minimal loads are found in the inter-tropical convergence zone (ITCZ) and near the poles. The CCN load is determined by both, the emission rate and the scavenging rate. Overall, the industrial and developing countries in the northern hemisphere show high CCN loadings due to large aerosol emissions. But those areas with less precipitation and therefore less scavenging have especially high CCN loadings, like China, north and south of the Himalayan, the Middle East as well as the Basin and Range Province in the western USA. Regions with especially low aerosol emission or advection are western Australia and the Weddel Sea. The western Pacific also has very low CCN loadings. This on the other side is probably due to a high scavenging rate as this is the rising arm of the Walker circulation cell and therefore determined by convective precipitation.

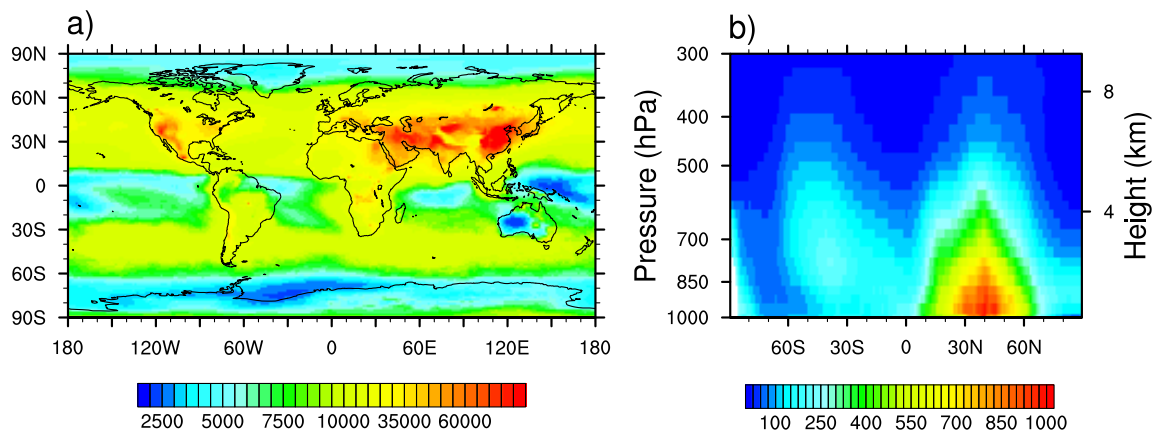


Figure 3.2: CCN load and vertical distribution at 0.4% S_{sat} , averaged from year 2003, for a) global load [m^{-2}], and b) the vertical zonally averaged distribution [cm^{-3}]. The color bar for a) scales from 2.000 to 80.000, with intervals of 500 until 10.000, and 5.000 afterwards. The color bar for b) scales from 25 to 1.000 in steps of 25 CCN.

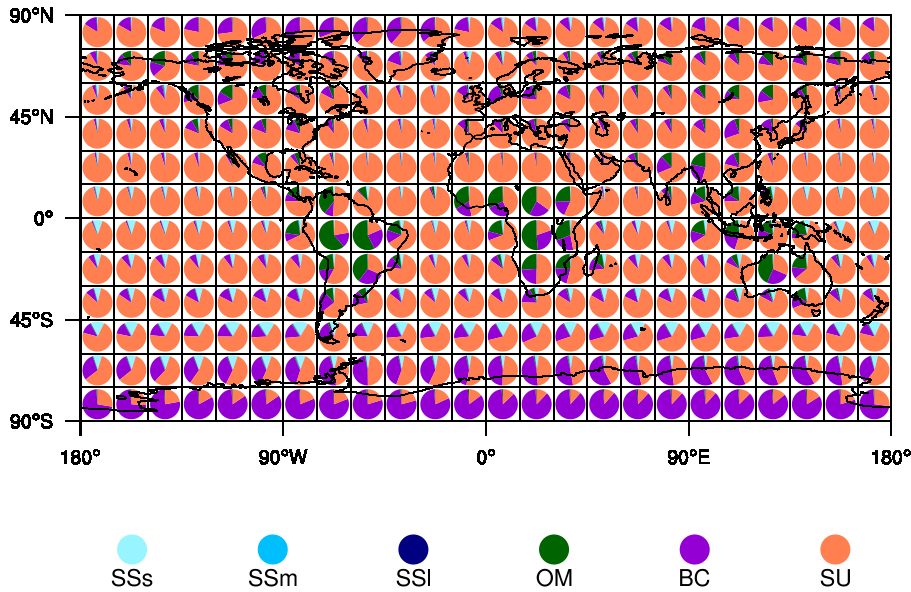


Figure 3.3: Aerosol species contribution to CCN at 0.4% Ssat, averaged from 2003 to 2012. Each piechart is produced of a $15^\circ \times 15^\circ$ average. Shown are small mode, medium mode and large mode sea salt components (SSs,SSm and SSI, respectively), organic matter (OM), black carbon (BC) as well as sulfate (SU).

While the vertical distribution in the NH reveals that CCN concentration stays mostly in the boundary layer and decreases with height, the SH shows increased concentrations aloft between 850 and 700 hPa. Furthermore, it can be seen that the Arctic is much more connected to NH aerosol emissions, while the Antarctic shows concentrations which are decoupled from SH emissions and advectations, probably due to a stronger West Wind Drift.

The aerosol species contributing to total CCN are shown in Figure 3.3. The dominant species worldwide is SU, except for Antarctica where BC is prevalent, and the tropical rainforest areas where OM as well as BC are prevalent. Contributions from SS, resulting mainly from SSs, contributes the least to total CCN. Sea salt CCN are found commonly over the ocean with the strongest contribution over the Southern Ocean.

Figure 3.4 shows the global distributions of total near-surface CCN at 0.4% Ssat and the contributing CCN of the various relevant aerosol species. In contrast to CCN load (Figure 3.2), the near-surface total CCN show a much stronger inter-hemispheric difference and land-ocean difference, because advection and aerosol physical processes don't play as much of a role as emission does. Especially over the NH, total CCN follow the distribution of SU CCN, being the main contributor. The SU CCN pattern shows a clear inter-hemispheric gradient, presenting most of the industrial and therefore SU emissions over the NH continents, with the largest emissions over China.

OM and BC mostly show their impact on total CCN over the tropical rainforests regions in South America, South Africa and South-East Asia. Additionally, BC CCN are increased over industrial areas as e.g. China. Both, continental OM and BC distributions seem to be quite realistic, except for a surprisingly large amount of BC CCN over Antarctica. Since I cannot find a reason why there should be an enhanced BC emission or transport in this region, I

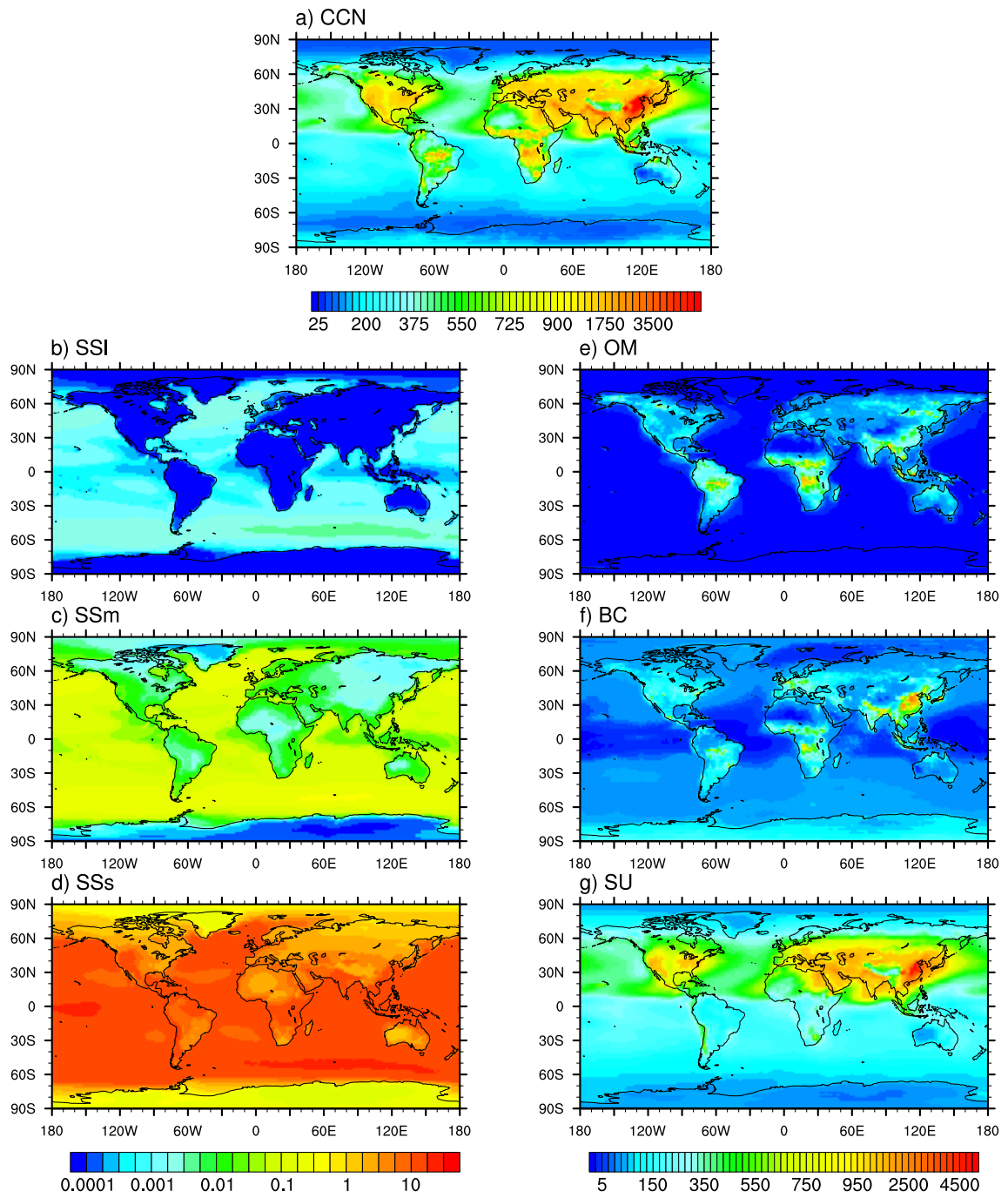


Figure 3.4: CCN aerosol species, at 0.4% Ssat near the surface (lowest model level) averaged from 2003 to 2012 [cm^{-3}]. a) total CCN; b) large mode SS, c) medium mode SS, d) small mode SS, e) OM, f) BC and g) SU. The color bar for left panels (b-d) is logarithmic from 0.0001 to 50 with 4 steps in each order of magnitude. The color bar for right panels (e-g) ranges from 25 to 5,000, with steps of 25 until 1,000, followed by steps of 250.

would recommend not to use BC CCN data south of 60° South.

BC also has larger CCN concentrations over the mid-latitude oceans and seems to be spread out more in comparison to OM. This might result from the smaller count median radius in the BC size distribution as well as from the smaller hydrophilic fraction in the emission.

First, the smaller BC aerosol require larger Ssat than for the OM aerosol to activate, so that it might stay longer in the atmosphere without getting involved in cloud processing.

The second condition can be assessed best with an example. Assuming absolute equal and constant emission rates of BC and OM, there is 50% hydrophilic OM but only 20% hydrophilic BC emitted. Adding to that, comes OM and BC which is converted from the hydrophobic fraction emitted the day before. Assuming that only half of the fraction of the 50% hydrophobic OM and 80% hydrophobic BC will add to the hydrophilic compound, we get 75% OM but only 60% BC aerosols that can act as CCN.

In conclusion, there is more time for BC aerosols to be advected since it can stay longer in the atmosphere before it becomes hydrophilic and undergoes cloud processing and scavenging. Therefore a spread out BC pattern is thinkable. SS CCN have to be analyzed on a totally different scale, as they contribute least to total CCN over the oceans. The SS modes increase by two orders of magnitude, respectively. The large and medium mode SS only attribute noticeable amounts of CCN in large storms, when surface wind speed are high and vertical mixing is enhanced. However, small mode SS CCN are also noticeable in the mean distribution (as seen in Figure 3.3) and can even contribute minor parts over continents, close to coastlines.

The CCN climatology experiences a significant trend (on 95% significance level) in total CCN over the 10 years, from 2003 to 2012 (Figure 3.5. Normalized and de-seasonalized

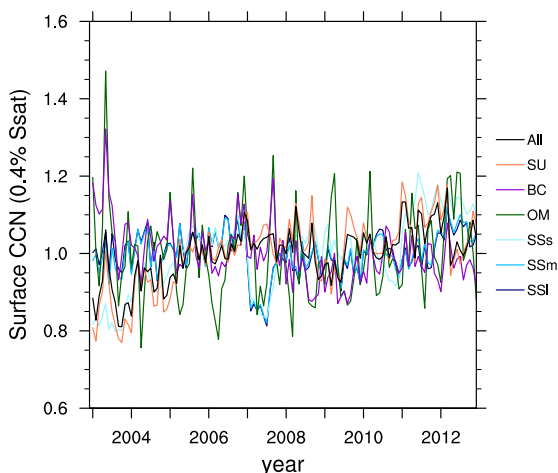


Figure 3.5: Time series of CCN species, at 0.4% Ssat near the surface (lowest model level) in monthly means [cm^{-3}] for total CCN (All), large mode SS (SSl), medium mode SS (SSm), small mode SS (SSs), hydrophilic organic matter (OM) and black carbon (BC), and Sulfate (SU). For better comparison, the CCN are normalized and the seasonal cycle is removed.

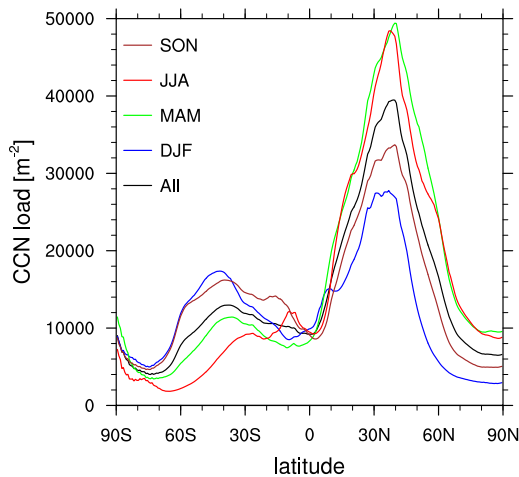


Figure 3.6: Seasonal variability of CCN load [m^{-2}] with latitude, with all seasons (black), DJF (blue), MAM (green), JJA (red) and SON (brown) averaged from 2003 to 2012, at 0.4% Ssat.

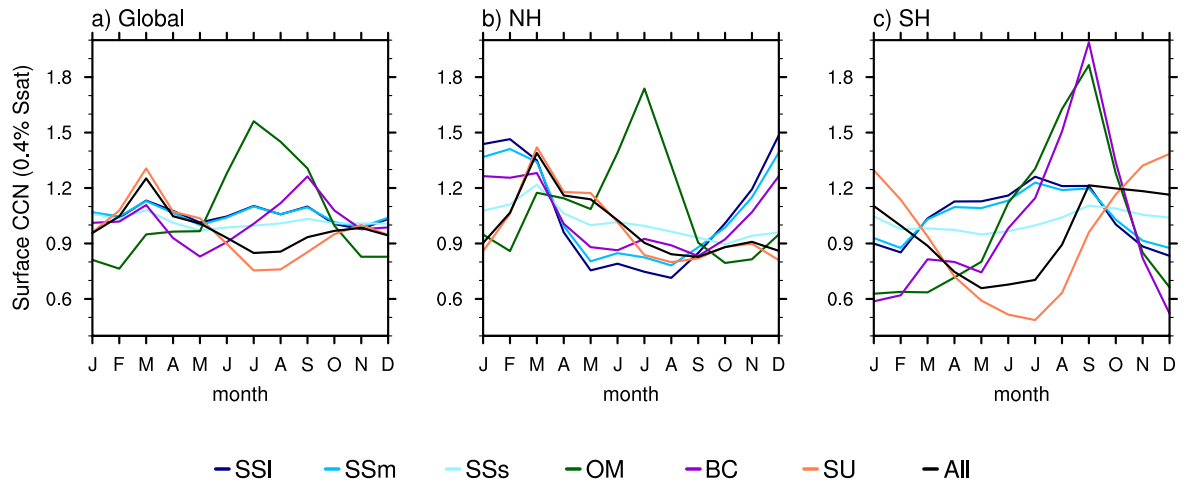


Figure 3.7: Seasonal variability of CCN species, calculated from multi-year (2003-2012) monthly means [cm^{-3}] at 0.4% Ssat near the surface (lowest model level). The seasonal cycle of total CCN (All), large mode SS (SSI), medium mode SS (SSm), small mode SS (SSs), hydrophilic organic matter (OM) and black carbon (BC), and sulfate (SU) is shown as a) global, b) northern hemisphere (NH) and c) southern hemisphere (SH) averages. For better comparison the CCN are normalized and detrended.

near-surface CCN concentrations increase by $0.0012 \pm 0.00014 \text{cm}^{-3}$ ($R^2 = 0.38$). This is accompanied by significant increases in SSs ($0.0019 \pm 0.00018 \text{cm}^{-3}$, $R^2 = 0.5$) and SU ($0.0017 \pm 0.00017 \text{cm}^{-3}$, $R^2 = 0.43$), while BC experiences a significant decrease ($-0.00095 \pm 0.00017 \text{cm}^{-3}$, $R^2 = 0.19$). A closer look on seasonal trends (not shown) reveals that the overall CCN trend mainly is a wintertime phenomena in the NH, which is due to a significant wintertime increase in SU. The decrease in BC is determined by a significant decrease in the summertime SH (DJF). The increase in SSs CCN does not relate to a specific season, but is more of a general trend. Further, even though there is no global overall trend in OM, it shows a significant decrease in wintertime CCN in the respective hemisphere. These time evolutions may be related to changes in the emission inventories, and don't necessarily have to do with changes in the aerosol physical processing, even though this cannot be readily excluded. Further influences on overall trends might also come from spurious trends in the MODIS AOD on board of Terra and Aqua satellites, which result from calibration issues (Zhang and Reid, 2010).

The total CCN load clearly shows a yearly cycle (Figure 3.6), with larger loadings during spring and summer within the respective hemisphere. The near-surface contributions reveal that in absolute values, SU continues to stay the dominant species, followed by BC, OM and finally SS in all seasons (see Appendix, Figure A.3). But the relative change from winter (DJF) to summer (JJA) is driven by different components in the two hemispheres. In the NH, the change from winter to summer (taken as multi-year seasonal means) is about 8%, composed of 12.1% SU and 1.7% OM, while the increase is inhibited mostly by BC with -5.8%. However, in the SH the change behaves the opposite way with wintertime CCN concentrations being larger than summertime concentrations. Here, the change is much larger than in the NH with approximately 20.8%, added up by contributions of about 44% from SU, -12.6% from OM and -10.6% from BC.

This behavior already indicates that the seasonal variability of the different aerosol species is not all naturally driven, but also anthropogenically. This can be further analyzed when looking at the normalized seasonal variability of the different species (Figure 3.7). The total CCN variability is mostly determined by the SU variability, which was already detected in the summer-winter time difference. SU CCN concentrations peak around May and decrease to minimal values around August, globally and in the NH. In the SH however, the seasonal cycle looks very different with minimum values around July and maximum values around December.

That shows, that the inter-hemispheric variability does not behave exactly opposite as one might expect, but is very much influenced by anthropogenic emissions which do not follow a natural seasonal cycle. The same can be seen for BC, which has its major contribution in the NH during wintertime, while in the SH it peaks around September. OM however follows more or less the natural cycle, with large contributions in the summertime, while maximum contributions in the SH shift to around September. It is interesting that there is such a strong seasonal cycle of OM in the SH, regarding that most of the emissions are from the tropical rainforests which do not have pronounced seasons. The most natural aerosol component is SS. While SSs CCN concentrations don't show much seasonal variability in both hemispheres, SS1 and SSm CCN clearly increase in the respective wintertime hemisphere due to enhanced wind speeds in the storm tracks.

3.4.2 Validation

3.4.2.1 Validation of CCN relevant aerosol mass concentrations

Since the CCN are computed based on the models simulated and nudged aerosol mass mixing ratios, it is necessary to validate those first. Any deviations here may pass on to the computed number concentrations, requiring a proper error assessment at this point.

The joint histograms in Figure 3.8 demonstrate a good agreement between MACC-II simulation and IMPROVE observations for BC, OM and SU. Most of the data lies within one range of magnitude with the strongest occurrence very close to the one-to-one line. Correlation coefficients of the logarithmic values are reasonably well with $R = 0.31$ for BC and SU, and $R = 0.46$ for OM. Figure 3.9 shows the PDFs of measured and simulated distributions, the respective values are listed in Table 3.3. Here, it can easily be seen that the CCN relevant mass concentrations are generally overestimated by MACC-II reanalysis. The medians of the log-normal distributions show an overestimation with factors of about 2.6 for BC, 1.2 for OM and 3.8 for SU. The larger bias in SU mass might result from the fact that the model SU also comprises SOA and Nitrate which is not accounted for in the model - but still goes in via the AOD assimilation and the related correction process. Therefore, the actual SU bias might be lower, if observations and model treat the same chemical species.

Through the shift in the medians, higher MACC-II aerosol masses tend to overestimate observations while lower MACC-II aerosol masses more often underestimate them, especially for BC and SU (for joint histograms of the bias, please see Appendix, Figure A.1). However, the widths of the distributions determined by the interquartile range (IQR), are slightly underestimated, showing that the observational variability is not fully covered by the simulation.

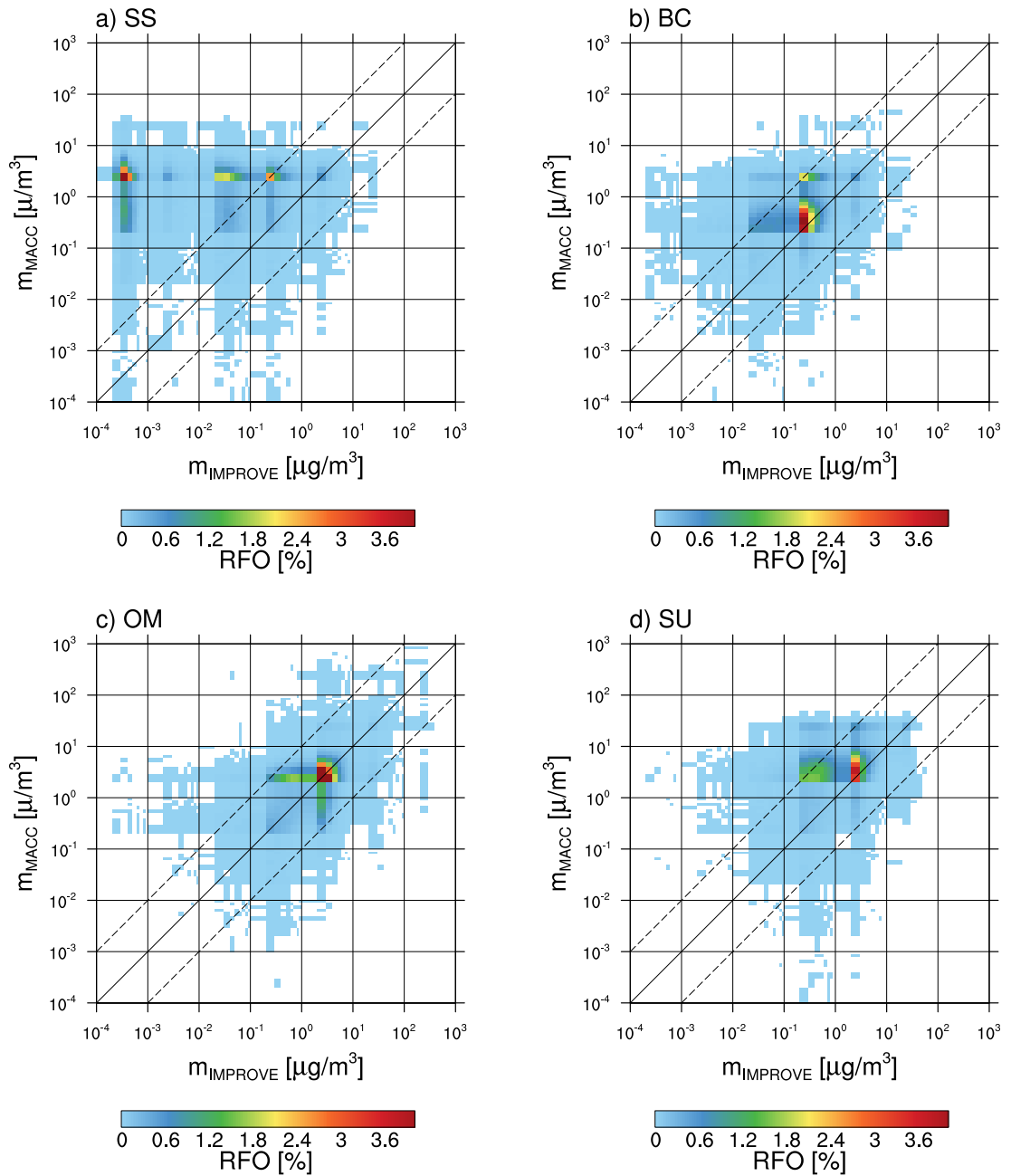


Figure 3.8: MACC vs IMPROVE MCONC Joint Histograms, for a) fine-mode sea salt, b) elemental/black carbon, c) organic matter and d) sulfate.

When comparing correlation coefficients between stations (Figure 3.10; Figure A.2), we find stronger temporal correlations for stations with higher observed aerosol masses. This is valid for sea salt as well as for BC and SU, with correlation coefficients increasing from about 0.1 up to 0.5 for the observed range of mass concentrations. This indicates that the simulation agrees better with observations with higher AOD. This behavior may result from the fact that the analysis is more efficient in increasing rather than reducing the values of AOD within the assimilation procedure (Benedetti et al., 2009). In general, our results agree with results from the previous validation by Mangold et al. (2011), showing a systematic overestimation of near-surface fine-mode mass concentration, especially for SU.

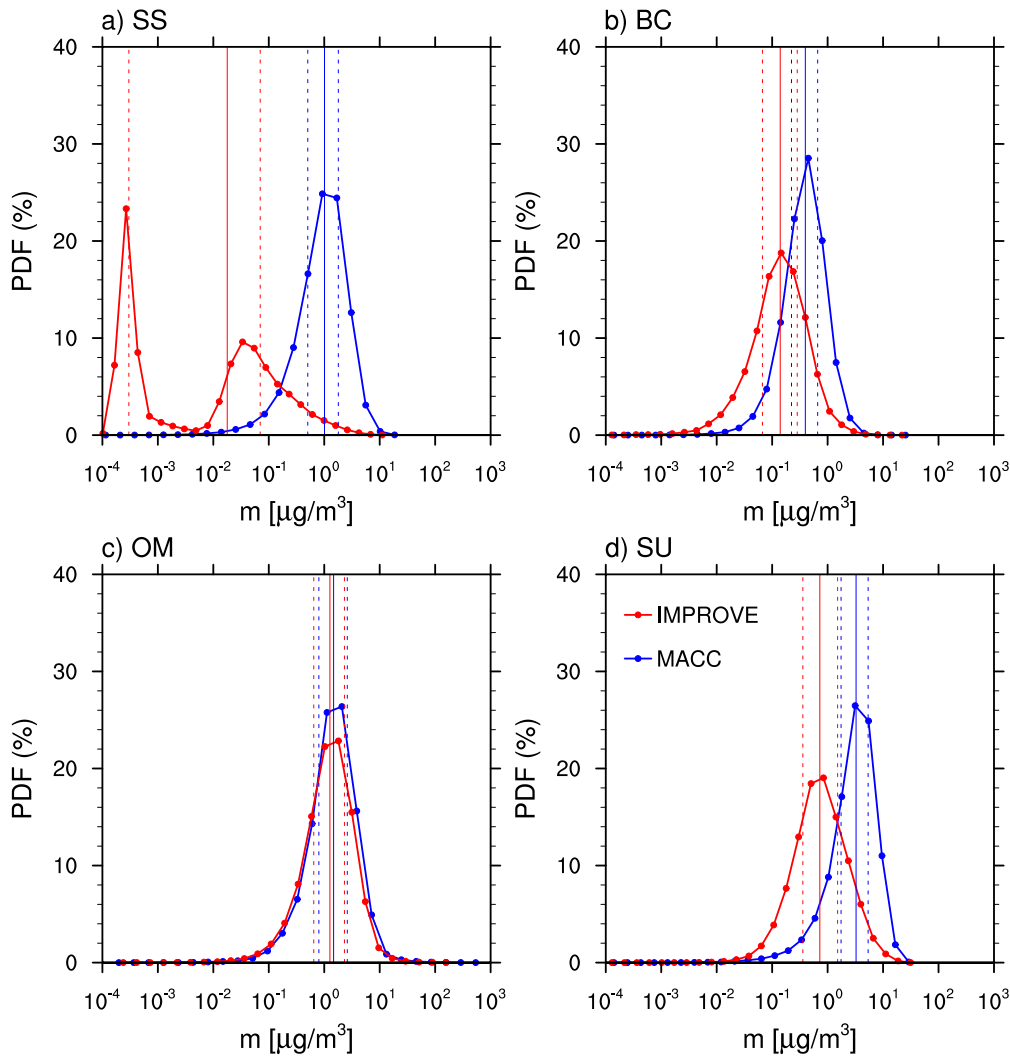


Figure 3.9: MACC vs IMPROVE MCONC probability density functions, with PDFs shown for a) fine-mode sea salt, b) elemental/black carbon, c) organic matter and d) sulfate aerosols. MACC data are plotted in blue and IMPROVE data in red. The vertical lines indicate the medians of the distributions (solid lines), and the dashed lines show the interquartile range (IQR), with one line at the 25th, and the other at the 75th percentile, respectively.

For completeness, the validation results of fine-mode SS are also given in Figure 3.8 and 3.9, as well as in Table 3.3. The results show a huge overprediction with a factor of 74, a large underestimation in variability (0.2), and no correlation between simulation and observations can be found. These results must be taken very carefully, since the measurement uncertainty itself is very high with 78.3% and we deal with continental sea salt measurements, meaning very low concentrations which is difficult for the model to reproduce, even with AOD assimilation. Towards the coast the correlation coefficients slightly increase (from 0 to 0.2) giving hope that the simulation does better over the ocean, which needs to be further evaluated. Nevertheless, this result also agrees with the findings of Mangold et al. (2011).

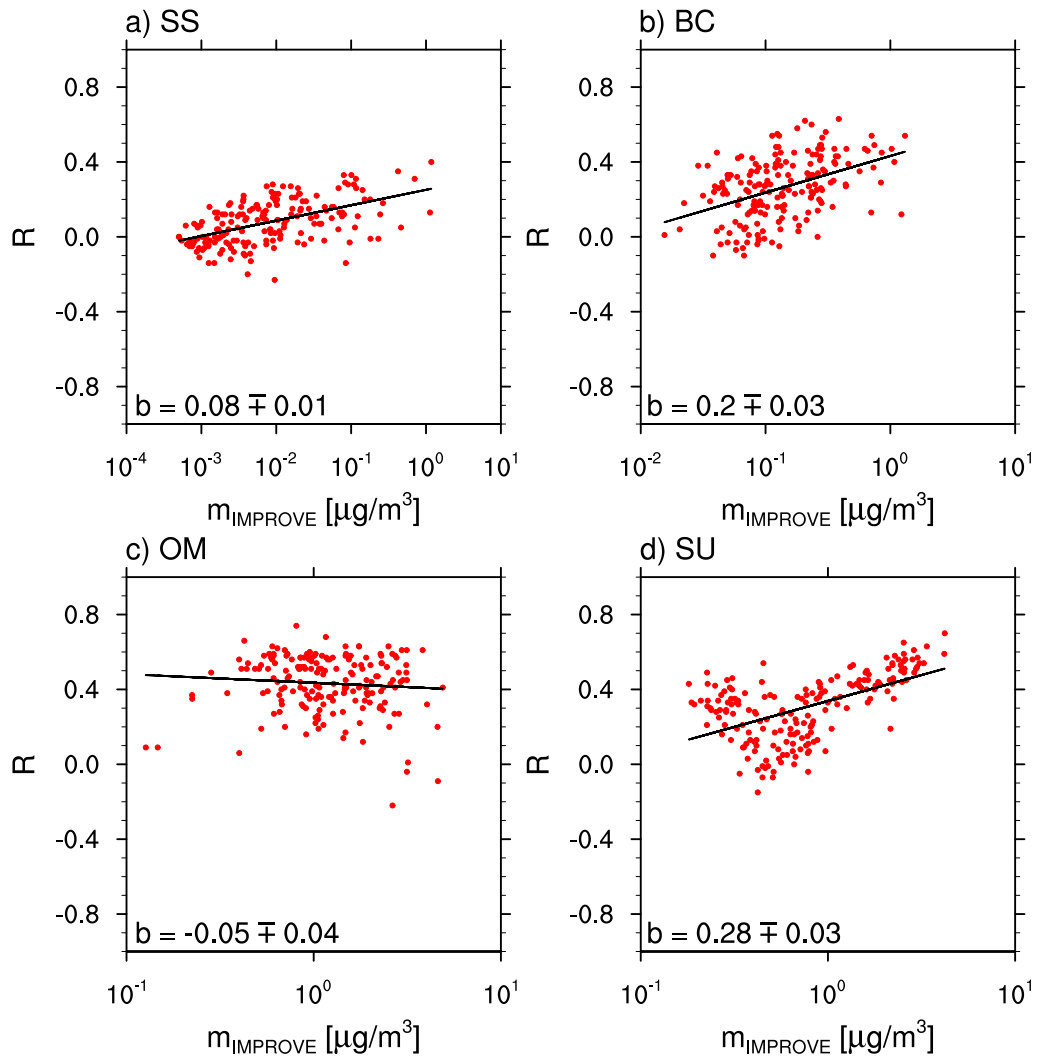


Figure 3.10: Increase of R with m_{IMPROVE} , where R is the linear Pearson correlation coefficient of the logarithmic values of m_{IMPROVE} and m_{MAcc} . Each dot represents the measured average aerosol mass concentration at one IMPROVE station. b indicates the regression slope \pm the standard deviation for a) fine-mode sea salt, b) elemental/black carbon, c) organic matter and d) sulfate.

One question remains for this validation: How can it be that the simulated aerosol mass is systematically overestimated when the reanalysis AOD agrees well with observed AOD?

This question can be answered with the assumed size distribution, on which the optical properties depend and which is used to convert MMR to AOD. Another size distribution would map the same MMR to another AOD. Accordingly, the MMR will be changed by the reverse mapping of the corrected AOD within the assimilation procedure. In conclusion, the AOD would still resemble to assimilated one well, while the MMR may show a totally different picture than before. In other words, the prescribed size distribution determines the magnitude of MMR, and thus MCONC. Therefore, a variable modal size distribution (as in the GLOMAP scheme), which is close to observational data, would be desirable in future model developments and help to reduce the discrepancies of aerosol mass to observations.

Table 3.3: MCONC validation with IMPROVE data, given the measurement uncertainties σ_m in %. The probability distribution characteristics as shown in Figure 3.9 are given by the median Q_{50} , the 25th percentile Q_{25} and the 75th percentile Q_{75} of the mass concentrations in $\mu g m^{-3}$. The bias is computed by dividing MACC MCONC by the IMPROVE measured concentrations. $Q_{50}(\text{bias})$ is then the median of the bias distribution, regarding measurement uncertainties in square brackets. The last column indicates the bias of the IQR.

aerosol	σ_m	Q_{25}	Q_{50}	Q_{75}	$Q_{50}(\text{bias})$	bias(IQR)
$SS_{IMPROVE}$ SS_{MACC}	78.3	0.0003 ± 0.0002 0.504	0.017 ± 0.014 1.01	0.07 ± 0.055 1.793	74.03 [41.52,341.16]	0.23
$BC_{IMPROVE}$ BC_{MACC}	20.2	0.066 ± 0.014 0.223	0.139 ± 0.029 0.396	0.283 ± 0.058 0.661	2.65 [2.20,3.32]	0.75
$OM_{IMPROVE}$ OM_{MACC}	16.0	0.647 ± 0.104 0.8	1.265 ± 0.203 1.47	2.314 ± 0.371 2.6	1.18 [1.02,1.41]	0.93
$SU_{IMPROVE}$ SU_{MACC}	7.5	0.357 ± 0.027 1.747	0.723 ± 0.055 3.258	1.514 ± 0.114 5.375	3.82 [3.55,4.12]	0.78

However, to stay consistent with the model assumptions, we have chosen to use the given size distribution to convert MMR to NC. That way, we keep the proportionality between AOD and the resulting CCN. Any improvement the resulting CCN might reveal over AOD can then only arise from the vertical distribution and the simulated species contribution.

3.4.2.2 Validation of MACC-II reanalysis CCN

The validation of the resulting MACC-II reanalysis $CCN_{0.4}$ with ARM data (Figure 3.11) reveals a good agreement. 99% of the data lies within a factor of 10, that is one order of magnitude. As expected, the lowest CCN concentrations are found for marine settings (GRW and MAG), which are followed by settings with medium concentrations (SGP and PVC). The Indian site (PGH) which is found to be polluted the most from the 5 settings, shows the highest model CCN concentrations. The CCN species contributions of the individual stations are presented in Figure 3.12. As already seen from Figure 3.3, SU is dominating for each of the stations, followed by BC and OM.

The simulated total CCN generally overestimate the observations as can be seen in Figure 3.13. The variability however is slightly underestimated for most stations, except for GRW and PVC. The results are summarized in Table 3.4. For all of the stations taken together, the log-normal distributions have an overall bias of +46% with only a slight underestimation in variability by 9%.

The correlation coefficients clearly show the improvement of MACC-II CCN over AOD (Table 3.5), when compared to near-surface CCN measurements. The overall correlation coefficient increases by a factor of 1.8 when using MACC-II CCN instead of AOD as a proxy for observed CCN. The strongest improvements are found for the GRW and PGH stations. A study of Logan et al. (2014) shows that the Azores (GRW site) experiences a range of aerosol conditions with mixtures of dust, pollution and smoke. They found rather weak correlations between aerosol loading and CCN due to mineral dust influences, while events with sulfate content within volcanic ash and pollution particles showed strong relationship with CCN. Regarding their findings, one reason for the improvement of R might be related to the fact, that DU is neglected here as potential CCN due to its insoluble character, even though this is debatable regarding the findings of Karydis et al. (2011). Furthermore, the vertical resolution

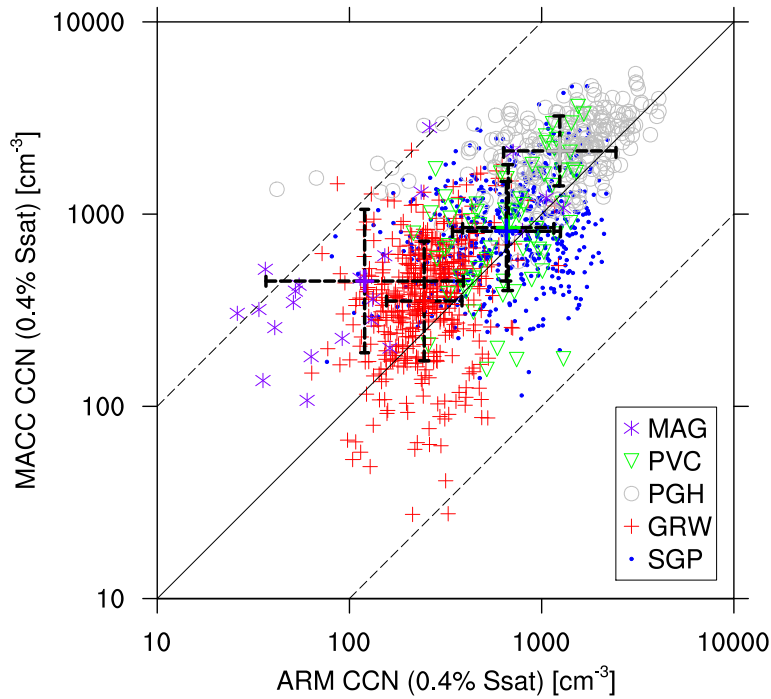


Figure 3.11: MACC vs ARM CCN data, at 0.4% S_{sat} near the surface, shown for the ARM stations listed in Table 3.2. Vertical and horizontal bars indicate the standard deviations from the regression analysis for each station.

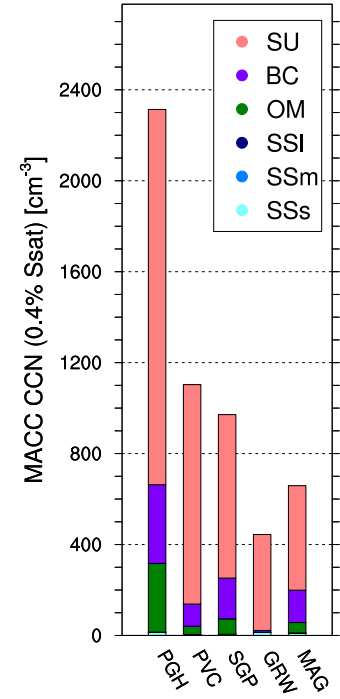


Figure 3.12: MACC CCN species contribution at ARM sites, shown for 0.4% S_{sat} near the surface.

Table 3.4: CCN validation with ARM data, given the measurement uncertainties σ_m in %. The probability distribution characteristics as shown in Figure 3.13 are given by the median Q_{50} , the 25th percentile Q_{25} and the 75th percentile Q_{75} of the CCN concentrations in [cm^{-3}]. The bias is computed by dividing the MACC CCN concentrations by the ARM measured concentrations. $Q_{50}(\text{bias})$ is then the median of the bias distribution, regarding measurement uncertainties, while bias(IQR) is the bias of the interquartile range. The last column indicates the normalized root mean square logarithmic error (NRMSLE) in %. It is calculated from the root mean squared error of logarithmic values, divided by $\log(Q_{50})$ of the observations.

Site ID	days	data	σ_m	Q_{25}	Q_{50}	Q_{75}	$Q_{50}(\text{bias})$	bias(IQR)	NRMSLE
MAG	22	ARM MACC	40.0	41 ± 16 226	102 ± 41 379	162 ± 65 607	3.91 [2.79,6.51]	0.72	33.5
GRW	420	ARM MACC	40.0	182 ± 73 233	244 ± 98 375	323 ± 129 562	1.30 [0.93,2.17]	1.53	15.2
PVC	64	ARM MACC	40.0	427 ± 171 470	696 ± 278 891	1049 ± 420 1528	1.54 [1.10,2.57]	1.31	11.3
SGP	547	ARM MACC	40.0	416 ± 166 553	699 ± 280 808	1089 ± 436 1220	1.55 [1.11,2.58]	0.82	11.8
PGH	252	ARM MACC	40.0	865 ± 346 1634	1440 ± 576 2258	1927 ± 771 2918	1.28 [0.92,2.14]	0.72	11.3
All	1305	ARM MACC	40.0	268 ± 107 411	506 ± 202 740	1058 ± 423 1427	1.46 [1.04,2.43]	0.91	13.2

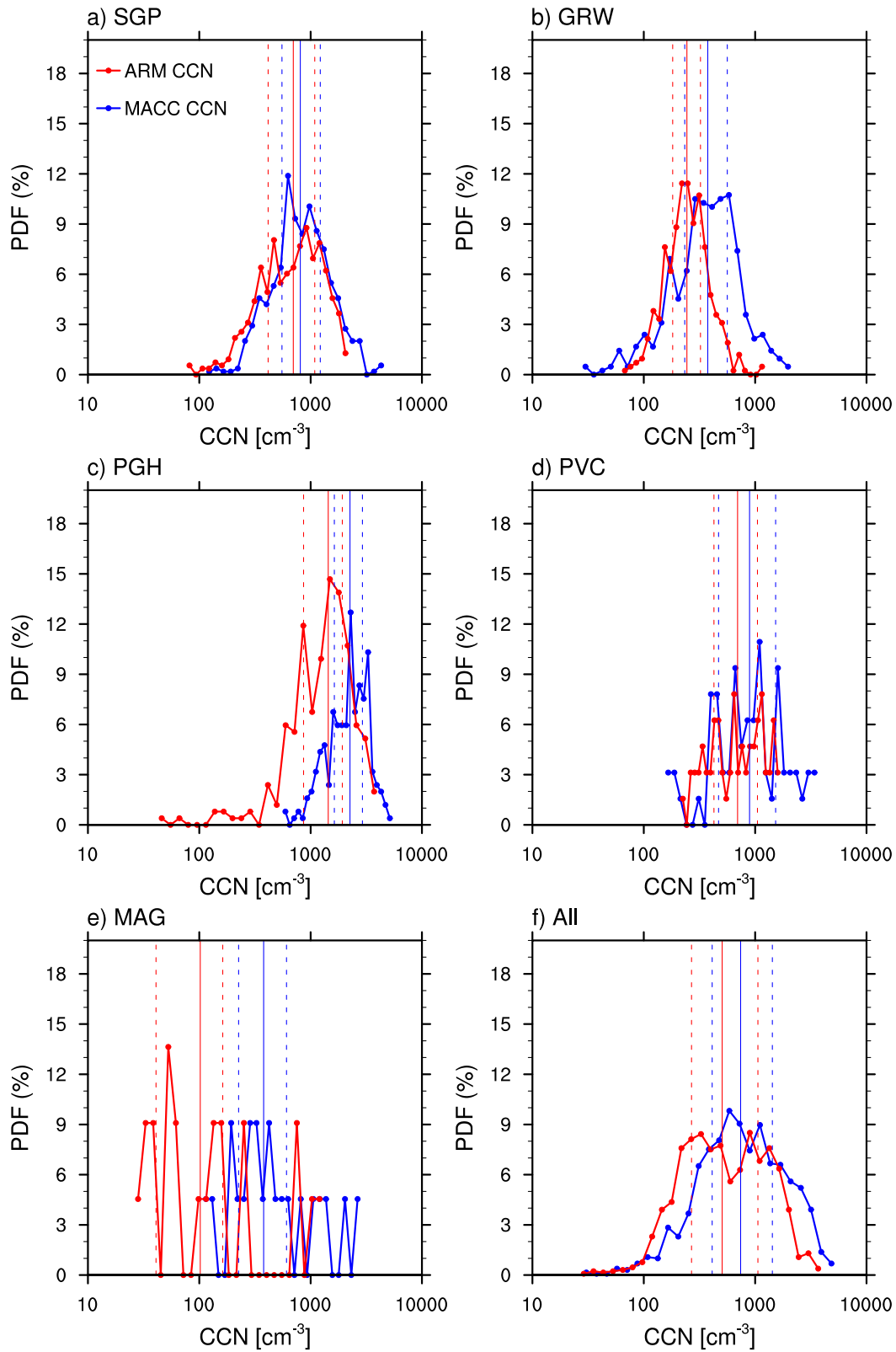


Figure 3.13: MACC vs ARM CCN probability density functions, for CCN taken at 0.4% S_{sat} near the surface. The PDFs are shown for the the ARM sites listed in Table 3.2, with all stations taken together in Panel f). MACC data are plotted in blue and ARM data in red. The vertical lines indicate the medians of the distributions (solid lines), and the dashed lines show the interquartile range (IQR), with one line at the 25th, and the other at the 75th percentile, respectively.

Table 3.5: CCN-AOD correlation. CCN corresponds to $CCN_{0.4}$, either observed (CCN_{ARM}) (CCN_{ARM}) or simulated (CCN_{MACC}). AOD_{MODIS} is the AOD measured from MODIS (collection 6 on board of Aqua) at 550 nm. The Pearson correlation coefficients R is taken of the according logarithmic values. The last row presents the results if all the stations were taken together as in Figure 3.13, f).

Site ID	R (CCN_{MACC} vs CCN_{ARM})	R (AOD_{Modis} vs CCN_{ARM})
MAG	0.71	0.67
GRW	0.23	0.09
PVC	0.45	0.43
SGP	0.29	0.25
PGH	0.43	0.21
All	0.64	0.35

enables filtering aerosol layers from long-range transport. These layers can increase column AOD without actually increasing CCN at the relevant height (in this case near the surface), leading to low correlations. The PGH station in India is more strongly affected by BC and OM (see Figure 3.12) in comparison to the other stations. While AOD is affected by both, hydrophilic and hydrophobic components, the model can distinguish between them, leading to a better assessment of CCN. The highest correlations are found for the remote marine site (MAG), where MODIS AOD is supposed to work best (Remer et al., 2005). Still, even for this site the correlation to observations by MACC CCN is slightly enhanced.

The general correlation of $R = 0.64$ shows that the simulated CCN fit well to the observations. The general overestimation of about 50% results not just from the overestimation in CCN relevant aerosol mass, but is furthermore influenced by assumed aerosol size distribution. The results show that the correlation coefficient to measured CCN almost doubles when using CCN from the reanalysis instead of AOD. This can only result from the resolved vertical distribution and the aerosol speciation in the MACC-II reanalysis.

3.4.2.3 Propagation of uncertainty

Table 3.6 shows how large the bias of MACC CCN over ARM CCN would be, if the bias in simulated MCONC (see Table 3.3) is reduced. The results clearly show that removing the bias in OM almost has no effect on the simulated CCN distribution, since the simulated values change only very slightly. The same can be seen for SS, even though the bias here is very large. But since SS represents a minor contribution to CCN in the model, changing the SS mass doesn't have a profound effect. Eliminating the bias in BC however shows a little more effect, by reducing the overall CCN bias by about 8%. The largest change comes from SU, which is the only component leading to an underestimation of a factor of 0.44. The original bias of 46% is increased in absolute values to 56% in the opposite direction. The strong effect is not surprising regarding that SU presents the major CCN contributor, and also has a high MCONC bias, which is probably overestimated due to reasons described in Section 3.4.2.1.

This result clearly shows, that if one wants to improve the modeled CCN by changing the mass alone, this does not necessarily give the desired outcome. Also the size distribution needs to be improved to retrieve a better result. Therefore a proper size distribution evaluation with

Table 3.6: MCONC bias propagation, indicated by the median of the bias distribution $Q_{50}(\text{bias})$ of MACC CCN compared to ARM CCN. Columns with specified aerosol species give the CCN bias, when only the bias of this specific species is eliminated. Column “ALL” in section $MCONC/Q_{50}(\text{bias})$ gives the CCN $Q_{50}(\text{bias})$ if all the CCN relevant species are divided by their according bias, given in Table 3.3. The last column represents the original CCN $Q_{50}(\text{bias})$, without any bias reduction in MCONC.

Site ID	MCONC/ $Q_{50}(\text{bias})$					original MCONC
	OM	SS	BC	SU	All	All
MAG	3.90	3.71	3.88	1.28	1.05	3.91
GRW	1.30	1.29	1.25	0.45	0.38	1.30
PVC	1.54	1.48	1.52	0.47	0.40	1.54
SGP	1.51	1.54	1.42	0.76	0.57	1.55
PGH	1.28	1.28	1.13	0.58	0.42	1.28
All	1.45	1.44	1.34	0.58	0.44	1.46

observational data is required. Since the size distributions used here are globally fixed, with a wide spread and customized for external mixtures of aerosols, such an evaluation, including an assessment of uncertainty sensitivities, doesn’t make much sense at this point. But further improvements of the aerosol scheme, e.g. in IFS-GLOMAP, using internal mixtures and varying modal modes, may require such an evaluation.

Since the evaluation of MCONC and CCN is done separately for different locations and time periods, a direct error propagation is not possible. But we can make a general estimate by analyzing the uncertainty associated with the MCONC bias distribution. In order to make an assessment of the error resulting from the modeled mass concentration, it is assumed that there is no uncertainty in size distribution. Following the Gaussian Error Propagation Principle, the total propagated uncertainty of MCONC on CCN could be calculated as

$$\begin{aligned}
 \sigma_{CCN}^2 = & \left| \frac{\partial N_{CCN}}{\partial m_{SS}} \right|^2 \sigma_{m_{SS}}^2 + \left| \frac{\partial N_{CCN}}{\partial m_{OM}} \right|^2 \sigma_{m_{OM}}^2 + \left| \frac{\partial N_{CCN}}{\partial m_{BC}} \right|^2 \sigma_{m_{BC}}^2 + \left| \frac{\partial N_{CCN}}{\partial m_{SU}} \right|^2 \sigma_{m_{SU}}^2 \\
 & + 2 \left| \frac{\partial N_{CCN}}{\partial m_{SS}} \right| \left| \frac{\partial N_{CCN}}{\partial m_{OM}} \right| \sigma_{m_{SS,OM}} + 2 \left| \frac{\partial N_{CCN}}{\partial m_{SS}} \right| \left| \frac{\partial N_{CCN}}{\partial m_{BC}} \right| \sigma_{m_{SS,BC}} \\
 & + 2 \left| \frac{\partial N_{CCN}}{\partial m_{SS}} \right| \left| \frac{\partial N_{CCN}}{\partial m_{SU}} \right| \sigma_{m_{SS,SU}} + 2 \left| \frac{\partial N_{CCN}}{\partial m_{OM}} \right| \left| \frac{\partial N_{CCN}}{\partial m_{BC}} \right| \sigma_{m_{OM,BC}} \\
 & + 2 \left| \frac{\partial N_{CCN}}{\partial m_{OM}} \right| \left| \frac{\partial N_{CCN}}{\partial m_{SU}} \right| \sigma_{m_{OM,SU}} + 2 \left| \frac{\partial N_{CCN}}{\partial m_{BC}} \right| \left| \frac{\partial N_{CCN}}{\partial m_{SU}} \right| \sigma_{m_{BC,SU}},
 \end{aligned} \tag{3.13}$$

assuming that aerosol mass is the only source of uncertainty. Since $\log(CCN)$ scales linearly with $\log(m_x)$ for each species x , with a slope of exactly 1.0, this leaves

$$\begin{aligned}
 \sigma_{CCN}^2 = & \sigma_{m_{SS}}^2 + \sigma_{m_{OM}}^2 + \sigma_{m_{BC}}^2 + \sigma_{m_{SU}}^2 \\
 & + 2\sigma_{m_{SS,OM}} + 2\sigma_{m_{SS,BC}} \\
 & + 2\sigma_{m_{SS,SU}} + 2\sigma_{m_{OM,BC}} \\
 & + 2\sigma_{m_{OM,SU}} + 2\sigma_{m_{BC,SU}},
 \end{aligned} \tag{3.14}$$

$$\text{with } \sigma_{m_x} = \sqrt{\frac{1}{n} \sum_{i=1}^n [bias(m_x)_i - \overline{bias(m_x)}]}, \quad (3.15)$$

$$\text{and } \sigma_{m_{x,y}} = \sqrt{\frac{1}{n} \sum_{i=1}^n [bias(m_x)_i - \overline{bias(m_x)}][bias(m_y)_i - \overline{bias(m_y)}]} \quad (3.16)$$

being the uncertainties associated with the log-normal bias distributions of CCN relevant aerosol mass concentrations. The covariance terms are important to include since the uncertainties of the bias distributions of the various aerosol species are not independent (see Figure A.4). Solving Equation 3.14 would give an uncertainty in CCN of $\log(\sigma_{CCN}) = 2.72$. Referring to Table 3.4, with an estimated median CCN concentration of 740 particles/cm³ ($\log(CCN) = 2.87$), the MCONC propagated error alone would add an uncertainty of about 95% to the derived CCN concentration.

This assessment only gives us a hint of how large the MCONC error could be and has to be taken very carefully, since no other uncertainty sources are included and there is no direct link between MCONC and CCN in this case. In order to do a proper error propagation, comprehensive measurements of aerosol masses, size distributions and CCN concentrations for the same locations and time periods would be necessary.

3.5 Conclusions

The MACC-II reanalysis has been used to produce a 10 year long 3-D CCN climatology, which has been analyzed and evaluated in this chapter. Since the reanalysis links modeled aerosols with observed AOD, the resulting total CCN are constrained by the observations. Therefore this climatology offers a unique opportunity to be used for studies of aerosol-cloud interactions in an observationally constrained global framework.

There are several advantages of using reanalysis CCN rather than using AOD as a CCN proxy, as was commonly done in previous observational studies of aerosol-cloud interactions (e.g. Kaufman et al., 2005; Quaas et al., 2008; Gryspeerdt and Stier, 2012; Bellouin et al., 2013). First, the reanalysis CCN have a global coverage while AOD can only be retrieved for cloud free regions. Second, the reanalysis CCN are vertically resolved while AOD is a column integrated quantity. This provides the opportunity to retrieve CCN at cloud base heights, where activation occurs. Third, the reanalysis provides not just total CCN concentrations at several supersaturations but also CCN from four relevant aerosol species, such as black carbon, organic matter, sulfate and sea salt. Therefore the chemical and size determined potential of each aerosol to act as CCN is taken into account, which is not possible from AOD to that accuracy. Furthermore, hygroscopic growth of the aerosols is taken into account in the IFS-LMD when computing optical properties. This reduces uncertainties associated with hygroscopic effects enhancing AOD without actually increasing CCN numbers.

The CCN climatology is available from 2003 to 2012, as daily averages on a Gaussian grid at a resolution of $0.7^\circ \times 0.7^\circ$ and 60 vertical levels. It is derived from the MACC-II reanalysis with 6 hour time steps on the corresponding grid (TL255L60), by applying Köhler Theory. For deriving number concentrations from the given MACC-II mass mixing ratios, the same

aerosol size distribution for external mixtures was applied that was initially used in the IFS-LMD aerosol scheme for obtaining aerosol optical properties and converting between aerosol mass and assimilated AOD. This ensures that the proportionality between CCN and AOD is kept and any improvements of derived reanalysis CCN over observed AOD can therefore only result from the vertical distribution and the modeled CCN relevant aerosol specification.

The resulting CCN distribution shows very clearly the dependence on modeled aerosol processes, such as emission and scavenging. Concentrations are pronounced in the mid-latitudes and are hemispherically decoupled. Since fine-mode/anthropogenic emissions dominate in the NH, there is a clear hemispheric gradient in CCN concentrations. Globally, CCN are dominated by sulfate aerosol, followed by black carbon, then organic matter and finally with minor contributions fine-mode sea salt.

The validation with in-situ surface observations has shown, that the aerosol specification is less reliable, since the species fraction to total aerosol mass is not influenced by the assimilated AOD. Except for organic matter, overestimations can be found in all CCN relevant aerosols masses. Conspicuous are also the very low sea salt CCN contributions, the large amount of black carbon CCN over the Southern Ocean and the overall dominating nature of sulfate CCN.

The bias in total CCN is about +50 %, compared to surface in-situ observations. Reducing the bias in CCN relevant aerosol mass concentrations does not produce a better outcome. This indicates that besides the emission rates several other sources of uncertainty influences the estimate of CCN, such as the vertical distribution and the assumed aerosol size distributions probably being a major contributor. A first step to retrieve better results in this regard would be to change the fixed bin-bulk aerosol scheme to a modal variable one, with observationally constrained aerosol size distribution. This is already under development with the new 2-moment aerosol scheme IFS-GLOMAP, and needs to be evaluated in further processing.

However, even with this rather simplistic 1-moment aerosol scheme, the results show that the simulated total CCN agree well with surface observations, with $R = 0.64$. In comparison to AOD with $R = 0.35$, the correlation coefficient almost doubles. This result shows that refining the observed column AOD by a vertical distribution and an aerosol speciation clearly improves estimations of CCN. The final outcome is mainly a matter of how realistic the aerosol processing in a certain model is. In this case, the CCN climatology derived here from the MACC-II reanalysis is a good and robust start of improving assessments of aerosol-cloud interactions.

Analysis of parameterized cloud droplet number concentrations and their susceptibilities in regimes of liquid water clouds

4.1 Abstract

Despite decades of research aerosol-cloud interactions (ACI) are still regarded as one of the largest uncertainty factors in climate predictions. Even for the simplest of all indirect aerosol effects, the change of cloud droplet number concentration (CDNC) with aerosol concentration (Twomey effect), a wide spread of scientific results exists, be it from insitu observations, satellite retrievals or model simulations.

The uncertainty of ACI arises from a variety of sources, such as the high spatial and temporal variability of clouds and aerosols, a low signal-to-noise ratio in the observations, uncertainties in satellite retrievals and assumptions in model parameterizations as well as from a lack of direct observational evidence on global scale.

To obtain a better understanding and quantification of CDNC to aerosol perturbations it as been suggested to use concurrent measurements and observationally constrained model simulations.

In this chapter, a joint satellite-reanalysis approach is introduced which should accommodate the demand for better approaches to estimate ACI and bridge the gap between observations and models. It combines useful cloud property retrievals from multi-component concurrent satellite measurements with the aerosol products from the observationally constrained MACC-II aerosol reanalysis. An aerosol activation parameterization is used to relate aerosol size distribution and composition to the CCN spectrum and activated number concentration.

The advantages of this new approach in comparison to pure satellite retrievals are that 1) aerosols and clouds can be directly linked horizontally and vertically, that 2) CDNC are computed from bottom-up, that 3) the contribution from different aerosol species can be accounted for, that 4) aerosol effects can be evaluated for different cloud regimes on a global scale and finally that 5) updraft and aerosol limited activation regimes can be identified.

The resulting statistical relationships are then compared to the achievements from satellite-only retrievals with the aim to analyze CDNC distribution and CDNC susceptibility to aerosol changes in a variety of cloud regimes. The results show a clear improvement of ACI when parameterized CDNC are used instead of satellite obtained CDNC.

4.2 Introduction

Aerosols are known to have a significant impact on cloud microphysics, acting as cloud condensation nuclei (CCN) and thereby altering cloud properties, such as cloud droplet number concentration (CDNC) and cloud albedo. As previous studies have demonstrated, it is very difficult to properly assess the effects aerosols have on clouds leading to low consensus between scientist and a low knowledge of the involved processes and impacts in the large-scale. Especially in the context of global warming, the role of indirect effects from anthropogenic aerosols is considered as one of the most uncertain features and might play a crucial role in climate predictions (Boucher et al., 2013; Myhre et al., 2013).

To quantify the effect of aerosols on clouds, a variety of ACI metrics can be used to relate changes of cloud microphysical properties to changes of aerosol supply (Feingold et al., 2003; McComiskey and Feingold, 2012). Following previous studies, the relative change of CDNC to a relative change of AOD or CCN will be analyzed here in a log-log regression analysis, and the associated statistical relationship is considered to represent the sensitivity of CDNC to AOD or CCN, respectively.

An overview of such a relationship from previous studies is given in Schmidt et al. (2015) and presented here in Figure 4.1. The values cover the full possible range from almost 0 up to around 1, depending on the observation capabilities and the match between observed/resolved and actual scales of ACI.

As can be inferred from Figure 4.1, in-situ observations (airborne, ground based, field campaigns) show larger sensitivities. However, these observations have a sparse spatiotemporal coverage over the globe and can only be used for specific case studies. But aerosol-cloud interactions (ACI) need to be evaluated in a large-scale context to assess impacts on climate and predictions of climate sensitivity. Therefore, satellite observations and models are often used to gain a global perspective and to analyze ACI within an interactive dynamical system.

Satellite estimates often suffer from uncertain retrievals (as will be discussed in this Chapter) which are reflected in the significance of ACI. According to Figure 4.1 they give lower sensitivities than in-situ observations, up to 0.5 at most.

Model estimates are also associated with a large degree of uncertainty as they rely on assumptions and parameterization concerning the emissions, transport and nonlinear physical processes involving aerosols such as cloud and rain formation and the interaction with radiation (Stevens and Feingold, 2009; Boucher et al., 2013). This is shown by the range of IPCC RF_{ACI} estimates which is based on a range of model studies. However, in climate models the processes are at least traceable and they provide a full global coverage.

In both ACI estimates, from satellites and models, the coarse resolutions and highly scale-dependent assessments complicate estimates of ACI as different processes come together. Processes that can partly offset ACI could imply e.g. the reduced maximum supersaturation if more droplets compete for the available water vapor Twomey (1959), an increased droplet spectrum dispersion Brenguier et al. (2011), a larger evaporation rate of smaller droplets Small et al. (2009). Additionally, the high variability of clouds and increased overall levels of pollution can buffer the effect of aerosols (Stevens and Feingold, 2009; Stevens, 2013) and

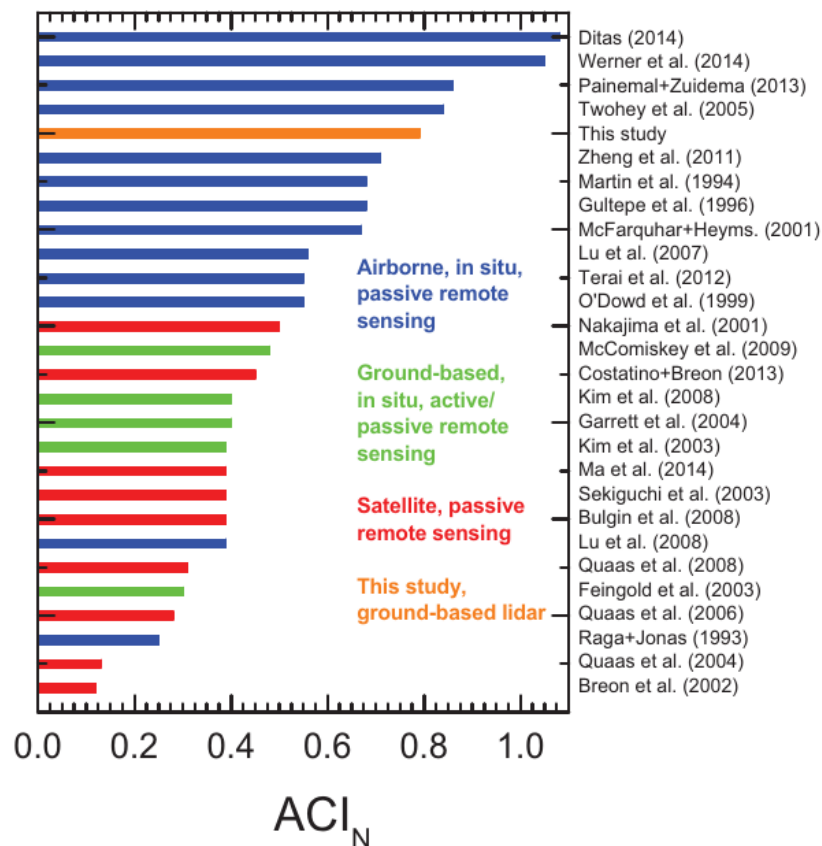


Figure 4.1: Literature review of ACI estimates, as published in Schmidt et al. (2015). “This study” therefore refers to the study of Schmidt et al. (2015), indicated by the orange bar. ACI_N values describe the relative change of the droplet number concentration with a relative change in the aerosol loading. Different methods (in situ measurements, remote sensing) and observational platforms (aircraft, satellite, ground based) are used.

low signal-to-noise ratios are obtained as different regimes of ACI are averaged at the large scale.

This could lead to results that are unsatisfying, that do not agree with the theory (negative aerosol-CDNC relationships) or are simply insignificant. In estimates from Quaas et al. (2008) who analyzed regional ACI effects, in Grandey and Stier (2010) who looked at the impact of resolved spatial scales and in the study of Gryspeerd and Stier (2012) who assessed statistical relationships for different tropical cloud regimes, also negative ACI relationships were found in addition to the generally positive ones hinting to retrieval difficulties, unfitting assumptions, scale problems and/or effects from other unresolved sources that might intervene.

Fan et al. (2016) review recent theoretical studies and ACI mechanisms and discuss their importance for radiative forcing and precipitation associated with different cloud systems. They define the main obstacles as 1) the lack of concurrent profile measurements of cloud dynamics, microphysics, and aerosols over a wide region on the measurement side, and 2) the large variability of cloud microphysics parameterizations resulting in a large spread of modeling results on the modeling side. They recommend concurrent measurements of aerosol properties and cloud microphysical and dynamic properties over a range of temporal and

spatial scales collected over typical climate regimes and closure studies, as well as improving understanding and parameterizations of cloud microphysics.

Also several other studies suggest to use collaborative observations and models - thus increasing the accuracy of the simulated elements while keeping track of the processes and using the full 3D coverage. Lohmann et al. (2007) discusses approaches of advancing ACI estimates by using synergistic approaches involving modeling and observational evidence at different spatial and temporal scales. Seinfeld et al. (2016) suggest a variety of strategies for improving estimates of aerosol-cloud relationships in climate models and for quantifying and reducing model uncertainty – mainly by using observational constraints. Feingold et al. (2016) tries to find new approaches to quantifying aerosol influence on the cloud radiative effect by combining routine process modeling and satellite and surface-based shortwave radiation measurements. They recommend statistical emulator models which when designed with, and driven by, the appropriate regime-based conditions, may be useful for filling in gaps and extending our ability to represent the aerosol-cloud system in different regimes. Bellouin et al. (2013) points to the need of observationally constrained models and makes use of the MACC-II aerosol reanalysis to estimate aerosol effects on climate.

Recently, McCoy et al. (2017) took a step forward and used a combination of remote-sensing estimates of CDNC and a state-of-the-art aerosol reanalysis from Modern-Era Retrospective Analysis for Research and Applications version 2 (MERRA2) to diagnose ACI within stratocumulus regions. They used cloud properties from MODIS and a power law relationship between CDNC and modeled sulfate mass. They obtained a slope of the log-log relationship between CDNC and SO₄ in maritime stratocumulus over the pristine Southern Ocean of about 0.31, which is similar to what has been found in previous studies.

In this study, I like to accommodate the demand for bridging the gap between models and satellite observations. To improve previous estimates I use a joint multi-component approach combining cloud retrievals from various A-Train satellite instruments and aerosol information from the observationally constrained MACC-II reanalysis, which has been discussed in Chapter 3. An aerosol activation parameterization is applied to this synthesized, collocated satellite-reanalysis dataset from which CDNC can be computed. This approach promises a significant improvement over previous work since aerosol properties are linked to cloud properties in an observationally constrained bottom-up approach rather than using metrics (e.g. AOD for CCN) from different satellite retrievals.

4.3 Data and Methods

In order to improve assessments of aerosol-cloud interactions, there is a need for better observational constraints of the relevant parameters (e.g. Bellouin et al., 2013). To accommodate this demand, I use a joint satellite-reanalysis approach, combining the strength of both sites - satellite retrievals and model simulations.

4.3.1 The Joint Satellite-Reanalysis Approach

The reanalysis offers the full spatial and temporal coverage of mostly observationally constrained parameters. The specialty of the MACC-II reanalysis (Morcrette et al., 2009;

Benedetti et al., 2009; Mangold et al., 2011) which was already introduced and described in Chapter 3, is that it also provides aerosol distributions which are constrained by assimilated MODIS observed AOD. Thus, a strong relationship between observation and model is kept, while the vertical distribution, the horizontal and temporal coverage, the aerosol speciation and hygroscopic effects are additionally accounted for by the model. As presented in Chapter 3, the resulting MACC-II reanalysis CCN are an improvement over AOD in estimates of the distribution and variability of aerosol amounts.

However, a weakness in most models is the representation of clouds, and also in the MACC-II reanalysis no aerosol-cloud interaction is represented, and also cloud formation is not based on aerosol activation. Therefore, the cloud properties observed from the satellites are used instead to sample for cloud types, conditions and locations where aerosol activation can occur to the best of the given assumptions.

In the joint satellite-reanalysis approach, the aerosol information from the MACC-II reanalysis is therefore combined with the cloud information from satellite retrievals. This is done in four steps.

In a first step, the MACC-II reanalysis aerosol data is co-located onto the CALIPSO track, using the nearest neighbor approach. Thereby the model's time interval of 6 hours is linearly interpolated to fit the time stepping from the satellite data.

In a second step, the data is filtered for liquid, single-layer and non-precipitating clouds using the CCCM dataset from NASA (Kato et al., 2010, 2011) which merges retrievals from the A-Train satellites (Stephens et al., 2002). By the use of CALIOP lidar retrievals (Winker et al., 2004, 2007, 2009) from the CCCM dataset, it is possible to find approximate cloud base heights for these filtered clouds, for which the MACC-II aerosol mass mixing ratios are selected. More information on the use of CCCM data, data filtering and sampling are given in 4.3.2 and in Unglaub (2017).

In a third step, the co-located aerosol mass mixing ratios at cloud base heights are read into a box model, which diagnostically computes CDNC using the aerosol activation parameterization from Abdul-Razzak and Ghan (2000) (ARG-scheme), and applying assumptions on aerosol size distributions to convert from mass to number concentrations (the same as for the CCN fields described in Section 3.3.5). Why a parameterization is needed and how this is applied in the box model is explained further in 4.3.3. The ARG-scheme is applied on aerosol numbers in a range of experiments, in which cloud-scale updrafts are varied for a set of satellite-retrieved cloud regimes taken from Unglaub (2017). For details please see Section 4.3.4. This is done to account for the dependence of S_{max} on cloud regime and cloud-scale updrafts.

In the last step the total number of activated particles is determined by integrating the fractional number of CDNC over the given updraft PDF and summing over the various species. This is how each of the updraft experiments results into different amounts and distributions of total CDNC, which represent cloud regime-based CDNC estimates.

4.3.2 The CCCM dataset

The CCCM (CALIPSO, CloudSat, Ceres and MODIS, Edition B1) dataset from NASA (Kato et al., 2010, 2011) merges retrievals from selected A-Train satellites (Stephens et al., 2002; L'Ecuyer and Jiang, 2010). The A-Train (or "Afternoon-Train") is a constellation of in total six satellites (Figure 4.2), which orbit the earth sun-synchronously at ~ 705 km above surface

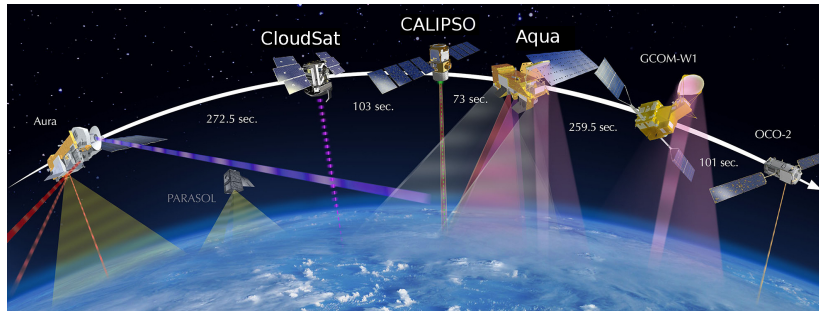


Figure 4.2: The A-Train constellation (following https://atrain.gsfc.nasa.gov/images/A-Train_w-Time2013_Web.jpeg, accessed 12th June, 2017)

at an inclination of 98.2° . They cross the equator at around 1:30 pm local time, and on the night-side at around 1:30 am each day, repeating their tracks every 16 days. Here, only the daytime data is used since passive satellite retrievals are included.

The CCCM dataset includes retrievals from the CloudSat CPR (Revision 4) (Stephens et al., 2002, 2008; Tanelli et al., 2008; Sassen and Wang, 2008; Haynes et al., 2009), CALIPSO lidar (Version 3) (Winker et al., 2004, 2007, 2009), CERES (Wielicki et al., 1996; Minnis et al., 2004; Smith et al., 2004) radiometer and MODIS (Barnes et al., 1998; King et al., 1992, 1998, 2003; Platnick et al., 2003) spectroradiometer on board of the Aqua satellite. The selected satellites Aqua, CloudSat and CALIPSO fly just seconds apart from one another on the same track. However, the orbits of the active satellites are shifted by 215 km (along the equator) east of Aqua’s equator crossing to avoid problems from sun-glint.

CloudSat, launched in April 2006 and operational since June 2006, carries the first space-born CPR (Cloud Profiling Radar) at millimeter wavelength (3.2 mm, 94 GHz). The CPR has a vertical resolution of 485 m (with 125 samples per profile, one every ~ 240 m), a horizontal cross-track coverage of 1.4 km and along-track of 1.8 km (Stephens et al., 2002, 2008). It provides information on the vertical structure and overlap of cloud systems, their liquid and ice-water contents and precipitation by measuring the reflectivity of hydrometeors. This is dependent on the number of cloud particles and their diameters to the power of six. Thus, clouds with small particles such as thin cirrus or shallow cumuli can’t be detected by the CPR. However, the minimum detectable reflectivity of about -30 dBZ ensures that most of the tropospheric warm clouds are detected (Sassen and Wang, 2008; Tanelli et al., 2008).

The primary instrument on board the CALIPSO (Cloud-Aerosol Lidar and Infrared Pathfinder Satellite Observation) satellite, which was launched together with CloudSat, is the Cloud-Aerosol Lidar with Orthogonal Polarization (CALIOP). This lidar is the first near-nadir viewing polarization lidar with two co-aligned wavelengths (1064 nm and 532 nm) that delivers optical properties of vertical cloud structures and aerosol distributions with a global coverage from space. It can also distinguish between ice and water phase by measuring the depolarization of the lidar backscatter signal. The lidar is a solid-state neodymium-doped yttrium aluminum garnet (Nd:YAG), it has a pulse frequency of 20.16 Hz with 20 ns long pulses, which create a beam diameter of 70 m at the surface. In the lower troposphere below 8.2 km the lidar offers a horizontal resolution of 333 m along the ground track and a vertical resolution of 30 m. With increasing altitude the resolution is decreased as the atmosphere becomes more uniform, which means 1 km horizontal and 60 m vertical resolution up to

20.2 km, and 5 km horizontal and 300 m vertical resolution up to a height of 40 km. For measuring cloud layers, the 532 nm backscatter and extinction signal is used. Cloud heights can be measured for layers with $\tau > 0.01$ and cloud thickness for layers with $\tau < 5$ (Winker et al., 2009). Therefore, the instrument is able to detect clouds with smaller droplets or thin clouds, thus complementing the CloudSat CPR.

The Aqua satellite launched in May 2002 is home of two passive instruments being of interest here.

The MODerate resolution Imaging Spectroradiometer (MODIS) is a passive sensor detecting solar and thermal radiation. It has a scanning swath of 2330 km (cross track) and 10 km (along track at nadir) which provides a full global coverage within one to two days. However, here only the near-nadir ground track co-located to CALIPSO is used. It operates on 20 reflective solar bands (0.4 and 2.2 μm) and 16 thermal emissive bands (3.75 and 14.24 μm) with wave-band depending nadir spatial resolution of 250 (bands 1-2), 500 (bands 3-7) and 1000 m (bands 8-36). The optical system consists of a two-mirror off-axis afocal telescope, which directs energy to four refractive objective assemblies, one for each of the spectral regions (VIS, NIR, SWIR/MWIR and LWIR) (Xiong et al., 2009). Due to the large range of capabilities that MODIS possesses, it can be used for a variety of interdisciplinary scientific purposes, e.g. to retrieve information on surface (land & ocean) features, atmospheric water vapor content, surface and cloud temperature, ocean color and phytoplankton, ozone, aerosol and cloud optical and microphysical properties (Platnick et al., 2003).

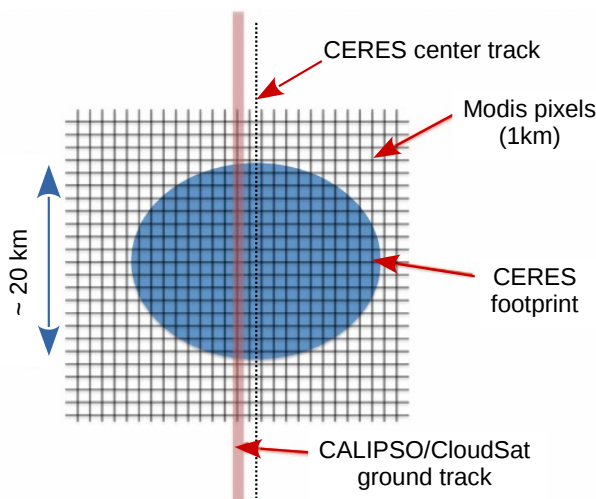


Figure 4.3: The CCCM ground coverage, showing the various resolutions and tracks in a schematic plot following Kato et al. (2011).

The CERES instrument (Clouds and Earth radiant energy system), also on board the Aqua satellite, is a broadband spectroradiometer with only 3 spectral channels and a nadir resolution of 20 km. It consists of three telescopes mounted on a scanning beam with can rotate in azimuth. The three telescopes provide measurements on SW (0.3-5 μm), LW (8-12 μm) and total radiances (Smith et al., 2004). Thus, CERES records continuously data of the Earth's radiation budget. In this study, CERES retrievals are not used, but in the CCCM dataset the CERES footprints are used as a dimension in which MODIS as well as CloudSat and CALIPSO data are merged in.

In the CCCM dataset, the various resolutions and coverages from the different sensors are combined (Figure 4.3), whereby the user can decide which ones to choose. In this study, only ground track data is used, since CloudSat and CALIPSO data mainly determines the cloud location and cloud type, and the high resolution is maintained.

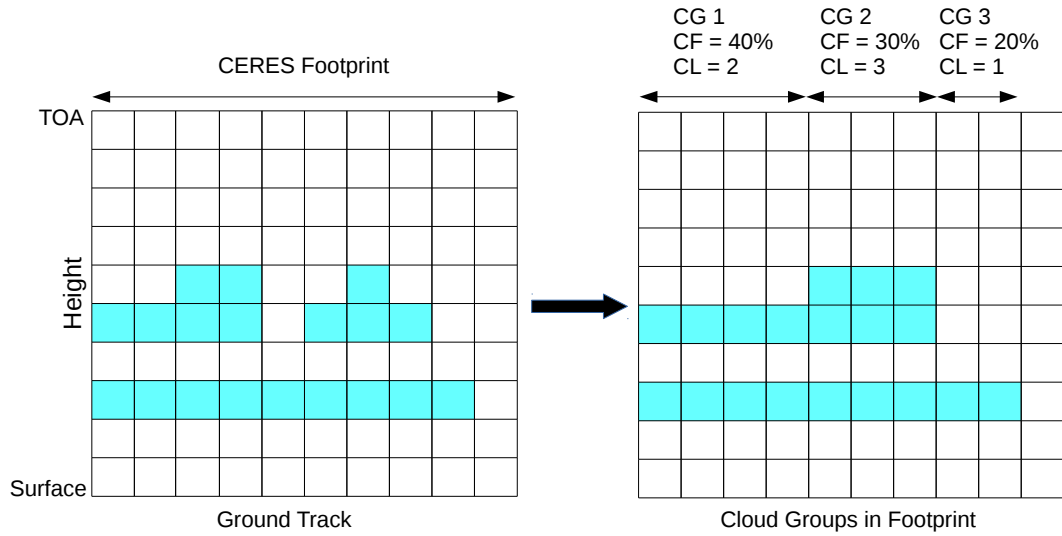


Figure 4.4: The CCCM cloud grouping, illustrated following Kato et al. (2010). Within one CERES footprint there can be up to 16 cloud groups (CG), each with similar cloud profiles. There can be up to 6 cloud layers (CL) within one cloud group. The group number of 1 is assigned to the cloud group having the largest cloud fraction (CF) over a CERES footprint.

The cloud properties are on a varying spatial scale, with a maximum of the CERES footprint ($20 \times 20 \text{ km}$) going down to a scale of $\sim 1 \text{ km}$, depending on the cloud grouping within the CERES footprint (Figure 4.4), which is done by sorting the clouds by layer heights, overlapping layers and cover fraction within the CERES footprint. Apart from the footprint coordinate, this gives an extra dimensions for the cloud properties with up to 16 cloud groups within one footprint and up to 6 cloud layers within one cloud group. The cloud groups are sorted using the PSF-weighted coverage (PSF = Point Spread Function) which associates the cloud group number with its cover fraction within the CERES footprint (Kato et al., 2010, 2011).

Since the vertical resolutions differ as well, the CALIPSO and CloudSat vertical cloud profiles are merged using a vertical feature mask (VFM) from CALIPSO and the 2B-CLDCLASS product from CloudSat. The vertical merging provides cloud top and base heights as well as layered structures, whereby 85 % of cloud top heights and 77 % of cloud base heights are derived from the CALIOP retrievals (Kato et al., 2010, 2011).

The resulting CCCM dataset, available from January 2007 to April 2011 (actual used data here is from January 2007 - December 2010) provides highly resolved daily Level 2 data, applying own algorithms for merging, quality control and processing (Kato et al., 2014). This comprehensive dataset enables filtering for quality-checked ideal-case clouds, which are liquid water only, single-layered and non-precipitating. This ensures clear satellite retrieval signals, and the best selection for assumptions of adiabaticity and droplet activation.

To filter the CCCM data the following criteria are used:

cut-off at 60°

High solar angles and bright surfaces may decrease reliability of satellite retrievals.

daytime data

Since MODIS VIS data are used for retrieving the cloud optical depth, only ascending

(daytime) latitudes are chosen.

good profiles

Only footprints in which the number of quality checked “Good CloudSat/CALIPSO profiles” is larger than zero are used.

cloud occurrence

For each cloud group the cloud fraction in the footprint is determined by combining the `Cloud_group_area_percent_coverage` (F_{CC} , the fraction of the cloud group within a CERES footprint determined from CloudSat/CALIPSO) and the `Cloud_percent_coverage_over_group_area_from_MODIS` (F_{MOD} , the cloud fraction per group area determined from MODIS). Groups with no cloud fraction may also occur, and there is a clearsky fraction outside the cloud groups.

The resulting cloud fraction is then $F = F_{CC} \cdot (F_{MOD}/100)$.

The resulting clearsky fraction is $F_{clr} = F_{CC} \cdot (100 - F_{MOD}/100)$.

cloud top height above surface

This is derived from `Cloud_layer_top_level_height` from CloudSat/CALIPSO merged vertical cloud profiles. This parameter is given above sea level, so that the surface height above sea level needs to be subtracted. For multiple cloud layers, this gives the height of the topmost layer.

cloud base height above surface

This is derived from `Cloud_layer_base_level_height` from CloudSat/CALIPSO merged vertical cloud profiles. This parameter is given above sea level, so that the surface height above sea level needs to be subtracted. For multiple cloud layers, this gives the height of the lowermost layer. The corresponding `Cloud_base_source_flag` is chosen so that the base is either detected from CALIPSO or CloudSat or both, as long as the CALIOP signal is not completely attenuated.

cloud layers

If there is only one base height within a cloud group and the top height is larger than the base height then this group has a single-layer cloud. If there are more than one bases, the cloud group contains a multiple-layered cloud system.

cloud phase

Clouds with cloud top temperatures ≥ 273 K from both MODIS & CALIOP retrievals are assumed to be liquid water only.

precipitation

Here, the `Precipitation_flag_CloudSat` is used and set to be zero (0=no precipitation, 1=liquid precipitation., 2=solid precipitation., 3=possible drizzle). The threshold between drizzle and no precipitation is given by -28 dBZ (minimum sensitivity), whereas heavy precipitation is detected from higher reflectivities, in which also contamination from surface signals is assessed carefully. A threshold of surface temperature of 2°C is used to distinguish between solid and liquid precipitation. The detected precipitation does not necessarily have to reach the surface.

4.3.3 The aerosol activation parameterization

To retrieve the droplet number concentration from a given aerosol number concentration, Köhler theory (Köhler, 1936) can be applied to relate the aerosol composition and size distribution to the number activated as a function of maximum supersaturation S_{max} . The curvature and hygroscopicity parameters (A and B parameter) are described in Section 3.3.5. While CCN are computed for a prescribed S_{max} , CDNC are determined in dependence of a variable S_{max} , which is dependent on the aerosol mode number, their size distributions and chemical properties and of the environmental properties such as temperature, pressure and humidity but most importantly the updraft velocity.

To retrieve S_{max} , one needs to consider the supersaturation balance equation which is determined by the cooling from an upward motion, and by the condensation rate during the activation process and subsequent droplet growth. Assuming an air parcel rising adiabatically at uniform speed, the time rate of change of supersaturation S_{sat} can be expressed as (Leitch et al., 1986; Abdul-Razzak et al., 1998)

$$\frac{dS_{sat}}{dt} = \alpha w - \gamma \frac{dW}{dt}, \quad (4.1)$$

with w being the updraft velocity and dW/dt being the condensation rate. α and γ are size-invariant coefficients.

Technically, the maximum supersaturation S_{max} could be evaluated from Equation 4.1 for $dS/dt = 0$. But the complexity of the governing equations, which are described in full detail in Appendix B, Section B.2, makes a rigorous derivation of an expression for S_{max} impossible without approximations (Abdul-Razzak et al., 1998; Ghan et al., 2011).

Therefore, an approximate solution is used from the aerosol activation parameterization from Abdul-Razzak and Ghan (2000) (ARG-scheme), which is applied here. This is an established and approved parameterization which is applied in many microphysical schemes scaling from global climate models (e.g., CAM, Storelvmo et al., 2006; Morrison and Gettelman, 2008; Ghan et al., 2011), (SPRINTARS, Takemura et al., 2005), (HadGEM3-UKCA, West et al., 2014), to regional models (e.g., COSMO-ART, Bangert et al., 2011) and (WRF Gustafson et al., 2007) down to cloud resolving models (e.g., NASA Langley CRM, Luo et al., 2008).

The parameterization uses the supersaturation balance to determine the maximum supersaturation, accounting for particle growth both before and after the particles are activated. It extends the activation parameterization from log-normally distributed aerosols of a single aerosol type (Abdul-Razzak et al., 1998) to the case of multiple externally mixed log-normal distributions. Therefore it is well suited to be used for the MACC-II aerosols, which are simulated as externally mixed and log-normally distributed. The parameterization accounts for the competition between aerosol particles for available water vapor and for the dependence of this competition on particle sizes, chemical properties and also on the supersaturation forcing rate which is determined by the updraft. Therefore this parameterization can account for a regime-dependent activation as the maximum supersaturation S_{max} can be computed as a function of the regime-dependent updraft.

Like most other parameterizations, the ARG scheme relies on the following assumptions (Ghan et al., 2011):

1. The aerosol population is described with a log-normal size distribution of one or more modes, each with a uniform bulk hygroscopicity (the latter is here the case)
2. The aerosols are internally mixed or externally mixed with one aerosol species within each mode (the latter is here the case)
3. Adiabatic conditions, the air parcel rises at uniform speed
4. Activation starts with no previous droplets to begin with, that is with the dry particle radius r_s
5. At the point of S_{max} , the volume of the wet particle is substantially larger than that of the dry particle
6. The number of activated particles is represented as the number with $S_c < S_{max}$
7. The particles grow in equilibrium with RH until the S_{sat} exceeds the particles' critical value for activation

Additionally, the ARG scheme makes assumptions on the growth rate of droplet radius (Equation B.23) to retrieve an approximate solution for the maximum supersaturation and therefore for CDNC. These simplifications include the neglect of the curvature and solute terms beyond activation as well as gas kinetic effects (that is an infinite radius could be possible within the growth coefficient G). Deviations due to these simplifications are mostly eliminated by employing adjusting coefficients which are tuned using a large number of numerical simulations (Ghan et al., 2011). This leads to two expressions for S_{max} , one for small S_c and one for large S_c , which can then be combined to a single expression for all values of S_c (Abdul-Razzak et al., 1998).

After the tuning the parameterization should fit the behavior of a detailed numerical model which is based on Equation 4.1 and B.23. Finally the approximated S_{max} is being derived as

$$S_{max} = \left\{ \sum_{i=1}^I \frac{1}{S_{0,i}^2} \left[f_i \left(\frac{\zeta}{\eta_i} \right)^{\frac{3}{2}} + g_i \left(\frac{S_{0,i}^2}{\eta_i + 3\zeta} \right)^{\frac{3}{4}} \right] \right\}^{-\frac{1}{2}} \quad (4.2)$$

with

$$\begin{aligned} f_i &= 0.5 \exp(2.5 \ln^2 \sigma_{g,i}) , \quad g_i = 1 + 0.25 \ln \sigma_{g,i} , \\ \zeta &= \frac{2A}{3} \left(\frac{\alpha w}{G} \right)^{\frac{1}{2}} , \quad \eta_i = \frac{(\alpha w / G)^{\frac{3}{2}}}{2\pi\rho_w\gamma N_i} , \\ S_{0,i} &= \frac{2}{\sqrt{K_i}} \left(\frac{A_i}{3r_{0,i}} \right)^{\frac{3}{2}} . \end{aligned}$$

The analysis gives four dimensionless parameters (σ , $S_{0,i}$, ζ and η_i) on which the fraction of activation strongly depend (Abdul-Razzak et al., 1998). $S_{0,i}$ is the mode critical supersaturation for activating particles with $r = r_0$ as described in Section 3.3.5, Equation 3.5. Further

parameters that play a role here are the mode radius r_0 , the geometric standard deviation σ_g , the updraft velocity w , the Köhler parameters A and K and the growth coefficient G which describes the diffusion of heat and moisture to the particle. Temperature, pressure and humidity effects are implemented in G . Note that S_{max} is actually a function of the updraft within the updraft PDF described in Section 4.3.4.

With S_{max} being determined, the next step is to determine the corresponding radius of activation for each mode. If $S_{max} \geq S_{0,i}$, the environment has reached the supersaturation necessary to activate the particle. The particles are expected to grow in equilibrium with relative humidity until the supersaturation exceeds the critical value for activation. Then they can grow spontaneously. Relating Equation 3.6 (Section 3.3.5) with the same equation holding the mode radius $r_{0,i}$ and therefore the mode critical supersaturation $S_{0,i}$, the dry radius of the smallest activated particle for each mode i can then be computed as

$$r_{c,i} = r_{0,i} \left(\frac{S_{0,i}}{S_{max}} \right)^{\frac{2}{3}}. \quad (4.3)$$

The number of particles being activated in each mode is determined by the number with radii larger than mode critical radius. The fractional number of each mode larger than the mode critical radius is calculated by integrating Equation 3.3 and transforming the log-normal distribution to an error function (Ghan et al., 1993; Khvorostyanov and Curry, 2006)

$$N_d = \sum_{i=1}^I N_{a,i} \frac{1}{2} [1 - erf(u_i)] \quad (4.4)$$

where

$$u_i = \frac{\ln(r_{c,i}/r_{0,i})}{\sqrt{2} \ln \sigma_{g,i}} = \frac{2 \ln(S_{0,i}/S_{max})}{3\sqrt{2} \ln \sigma_{g,i}}. \quad (4.5)$$

This computation is performed in the M7 aerosol microphysics scheme (Vignati et al., 2004).

Evaluations with detailed numerical simulations for a wide range of governing parameters (size distributions, number concentrations, compositions, and updraft velocities) reveal an agreement within 10 % for most conditions, and up to 25 % for some extreme conditions or when the mode radius of two competing aerosol populations differ by an order of magnitude (Abdul-Razzak et al., 1998; Abdul-Razzak and Ghan, 2000). Ghan et al. (2011) compares the ARG scheme with other physically-based parameterizations often used in climate models. The ARG scheme is found to perform well under many conditions, even though it is the most sensitive scheme to increases in aerosol concentrations, ranging in the lower bound for S_{max} and activation fractions for low NC and in the higher bound for high NC. Further, it has been shown that the ARG scheme produces estimates of S_{max} and the number of nucleated particles in good agreement (to within 30 %) with detailed numerical integrations of the nucleation process under a wide variety of conditions.

So far, all this has been done for each mode and each updraft bin within the updraft PDF individually. In the last step the total number of activated particles is determined by integrating the mode fractional number over the given updraft PDF and summing over the

various modes. This is how each of the updraft experiments, which are described in the next Section 4.3.4, results into different amounts and distributions of total CDNC.

4.3.4 Cloud regimes and updraft experiments

In Section 2.3, the dependence of cloud type and S_{max} on the meteorological conditions was briefly discussed. Temperature, humidity and vertical coupling can influence the distribution of S_{max} . Here, this relationship should be used to conduct several experiments in which S_{max} is determined as a function of cloud regime.

Cloud regimes can be defined on different ways. They can be identified using parameters describing the large-scale atmospheric dynamical state, e.g. with (SLPA: Tselioudis et al., 2000), (LTS, ω_{500} : Klein and Hartmann, 1993; Bony et al., 2004; Wood and Bretherton, 2006; Medeiros et al., 2008) or (EIS, ω_{700} : Su et al., 2010). They can also be described using specific cloud parameters such as cloud top pressure, cloud optical depth and cloud albedo, (e.g. Rossow and Schiffer, 1999; Williams and Webb, 2008; Gryspeerdt and Stier, 2012), in a specific geographical region/ climate zone (e.g. Webb et al., 2001; Jakob et al., 2005) or globally (e.g. Oreopoulos et al., 2014). The usefulness of geographically defined cloud regimes in comparison to dynamically defined ones for low-level clouds has been discussed by Nam and Quaas (2013). Both have their advantages and disadvantages depending on the conditions they are retrieved for and are therefore not universally applicable. Other satellite-derived cloud climatologies using passive or active retrievals are described in Chepfer et al. (2010).

Some of the cloud regimes are derived using statistics from observations of resolutions of about $2.5^\circ \times 2.5^\circ$, a rather large-scale resolution which does not provide much information on the strong spatial cloud variability. Others depend on parameters which are not suitable to answer certain scientific questions. Thus, for our purpose we need to ensure that the cloud regimes chosen have input parameters that do not interfere with the independence of the wanted result, and do not include more cloud types as necessary for the targeted scientific question. That means, that for analyzing satellite-observed regime-based CDNC the regimes must not be derived from effective radius nor optical depth, as the satellite-derived adiabatic CDNC depend on these parameters. Further, if one wants to analyze warm liquid clouds only, it is not useful to take the ISCCP cloud regimes into account, since these contain also mixed and ice clouds and would only give two major cloud regimes which roughly fit the required conditions.

Table 4.1: Parameters for each cloud regime corresponding to Figure 4.5.

Cloud base/variability	$V_{H_{top}} < 11\%$ (homogeneous/stratiform)	$V_{H_{top}} > 11\%$ (inhomogeneous/cumuliform)
$H_{cb} < 350\text{ m}$	St_{low}	Cu_{low}
$350\text{ m} < H_{cb} < 950\text{ m}$	St_{med}	Cu_{med}
$H_{cb} > 950\text{ m}$	St_{high}	Cu_{high}

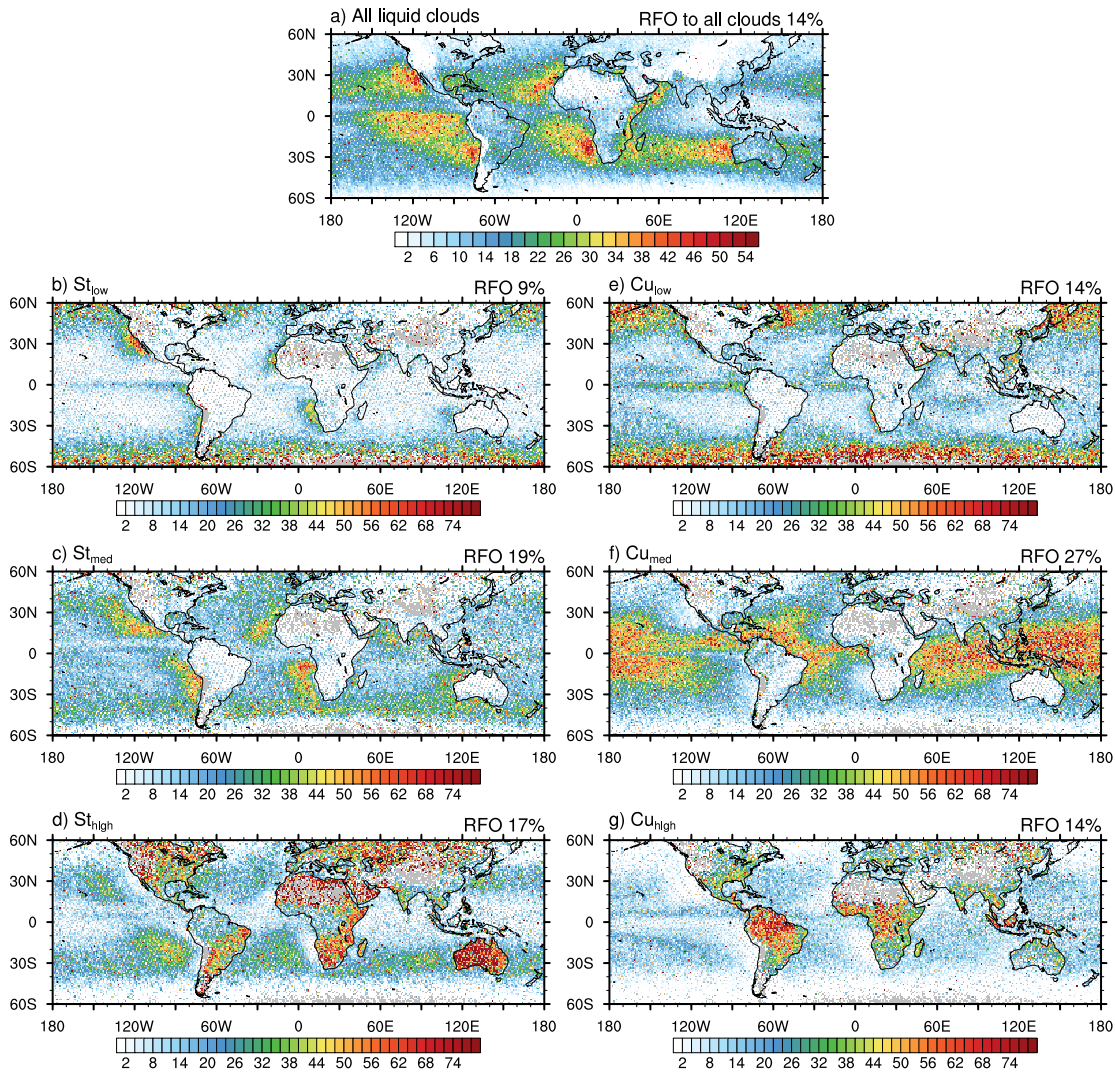


Figure 4.5: Cloud regimes for liquid water clouds only, filtered for single-layered and non-precipitating clouds. Shown is the frequency of occurrence (RFO) for a) all filtered liquid clouds relative to all clouds found, b-d) stratiform cloud regimes relative to all filtered liquid clouds and e-g) cumuliform clouds relative to all filtered liquid clouds. The mean RFO values between 60S and 60N are written at the top of each panel. These cloud regimes are developed by Unglaub (2017) and are based on filtered CCCM retrievals (Kato et al., 2010, 2011) on a daily basis from 2007 to 2010 from a 20 km resolution, plotted here on a $1 \times 1^\circ$ grid.

Having this in mind, and regarding the resolution and capabilities of the satellite instruments used for this study, I decided to make use of the new cloud classification from Unglaub (2017). The cloud regimes are derived from CCCM data at a high spatial resolution of 20 km (one CERES footprint), using cloud geometrical parameters. First, the mean cloud base height H_{cb} for each CERES footprint is computed from the cloud group base heights. Multilayer clouds are also taken into consideration here. A PDF of base height occurrence is then taken as reference for a separation of three cloud classes with thresholds of 350 m and 950 m. The second classification parameter is the cloud top height variability $V_{H_{top}}$ which represents cloud inhomogeneity. Again, multilayer clouds are included when defining the cloud regimes. In three consecutive footprints, a cloud fraction weighted deviation of the cloud group top heights from the footprint’s mean cloud top heights is calculated. Then the mean cloud top variability of these three footprints is calculated using the total cloud fraction

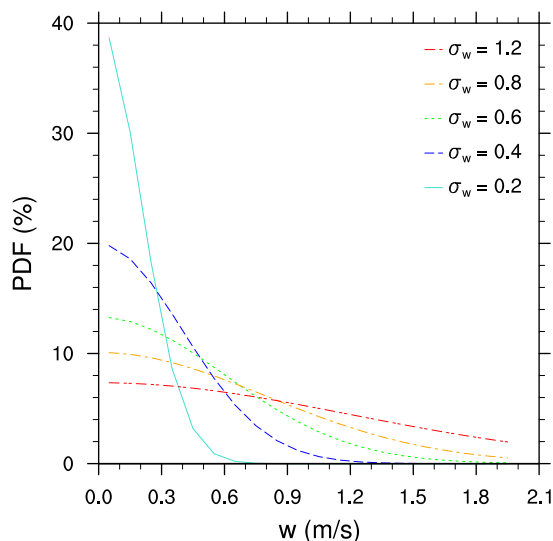


Figure 4.6: Updraft PDFs, with varying standard deviations σ_w shown for the positive part of the PDF.

Experiment	Cloud Regime	σ_w [$m s^{-1}$]
Exp1: fixed updraft	<i>All</i>	0.4
Exp2: St/Cu updraft	<i>All_{St}</i>	0.4
	<i>All_{Cu}</i>	0.8
Exp3: regime updraft	<i>St_{low}</i>	0.2
	<i>St_{med}</i>	0.4
	<i>St_{high}</i>	0.6
	<i>Cu_{low}</i>	0.4
	<i>Cu_{med}</i>	0.8
	<i>Cu_{high}</i>	1.2

Table 4.2: Updraft experiments, in which the various σ_w are applied to the cloud regime updraft PDF.

within each footprint. Again a PDF of the occurrence of cloud top variability (%) is used as a reference to distinguish two classes of cloud regimes. The resulting regimes can then be filtered for the selected ideal-case clouds, which are warm liquid water only, single-layered and non-precipitating clouds. This new classification results in six liquid water cloud classes (Figure 4.5), which distinguish between marine and continental clouds as well as between stratiform and cumuliform clouds for latitudes between $60^\circ S$ and $60^\circ N$. The corresponding values are given in Table 4.1.

As shown in Figure 4.5, the RFO of ideal-case clouds is largest over the subtropical oceans, still as inferred from the lowest panels, there is a considerable fraction (note the scale!) of liquid clouds over the continents which almost entirely consists of clouds with high bases. This is expected as continental updrafts are larger due to a warmer surface, and the clouds form in a less stable troposphere. Please note, that because A-train daytime data are used the cloud day-night cycle is not considered. Still, differences for the high continental clouds can be seen as stratiform clouds form mainly in the mid-latitudes and in the dry desert regions, whereas cumuliform clouds mainly develop in the tropical area. Low and medium high clouds can be found mainly over the oceans. The cumuliform medium high clouds have the largest global mean RFO of about one quarter of overall liquid cloud occurrence. These patterns reveal that these clouds cover the shallow and transition cumulus regions, whereas the stratiform clouds in the same height class, and also part of the lower class cover the subtropical stratocumulus decks. The lowest clouds are usually also the deepest. This reveals the dominant occurrence in the mid-latitude storm tracks and in the thin line of stronger RFO along the tropical rain belt, which probably corresponds to developing cumulus congestus.

For the new liquid water cloud regimes S_{max} is computed using the parameterization from Abdul-Razzak and Ghan (2000) with input parameters from the MACC-II reanalysis co-located to the CALIPSO track. The only parameter that is missing and can not be derived from the MACC-II reanalysis but is very much needed to compute the cooling rate for S_{max} is the updraft velocity at cloud scale. It is described in the following how this is parameterized in the present study.

To account for subgrid-scale variability within the CERES footprint ($20 \times 20 \text{ km}$) the updraft is not simply assumed to be a characteristic fixed value, but rather taken as a PDF in the form

$$f(w) = \frac{1}{\sqrt{2\pi}\sigma_w} \exp\left(-\frac{(w - \bar{w})^2}{2\sigma_w^2}\right) \quad (4.6)$$

with a mean large-scale vertical velocity $\bar{w} = 0 \text{ m s}^{-1}$ and a standard deviation σ_w , which is varied as seen in Figure 4.6. The PDF is composed of 20 updraft bins from 0 to 2 m s^{-1} . Only the positive part of the vertical velocity distribution is taken into account to ensure that only updrafts and not downdrafts are used for the computation of S_{max} .

The use of a PDF-based updraft description is motivated from findings of West et al. (2014) who showed that the choice of updraft and the representation of updraft variability is essential for estimates of ACI effects. Their results show that the use of a characteristic vertical velocity cannot replicate the results derived with a distribution of vertical velocities. The presentation of subgrid-scale variability of updrafts does not only hold for coarse-grid climate models, but also for kilometer-scale models subgrid-scale contributions to vertical velocity need to be parametrized or constrained to properly represent the activation of CCN (Malavelle et al., 2014; Tonntila et al., 2011). Thus, also for the high resolution of the CCCM data used here, it is necessary to account for these effects.

To assess the cloud-regime dependence on S_{max} , all regimes have the same mean updraft velocity $\bar{w} = 0 \text{ m s}^{-1}$ and σ_w is varied in a systematic manner in three updraft experiments (see Table 4.2). The σ_w chosen for each experiment are justified by the range of in-situ observations from aircraft campaigns and ground base measurements (see Table 4.3), which are sorted into the different categories according to measured cloud type, base height and location. The range of observations is large and indicates that even for a single cloud type updraft distributions vary considerably, so that some of the measurements fit better to the chosen σ_w values than others and there is a considerable amount of overlapping σ_w ranges.

In Experiment 1, S_{max} in all cloud regimes is computed with $\sigma_w = 0.4 \text{ m s}^{-1}$, a mid-range value of marine stratocumulus, on which most of the measurement campaigns focus (West et al., 2014). Thus, differences in S_{max} can only result from variations in temperature, pressure and specific humidity of the cloud regimes.

In Experiment 2, the difference in S_{max} between stratiform and cumuliform clouds is assessed by doubling σ_w for cumuliform clouds. That cumuliform clouds have larger updrafts, but also larger updraft variations, is found from a range of in-situ observations (e.g. de Roode and Duynkerke, 1997; Hogan et al., 2009; Kollias and Albrecht, 2010) and LES studies (e.g. LEM-CONSTRAIN, Malavelle et al., 2014). Also in coarse-grid model parameterizations a variation of σ_w is implemented. Hoose et al. (2010) relates it to in-cloud LWC, which increases the more convective the cloud type is, and therefore also supporting a larger σ_w for cumuliform cloud types.

Table 4.3: Regime-based σ_w references, which support the chosen updraft distributions used in this study.

Cloud Regime	σ_w [$m s^{-1}$]	reference: technique, campaign, location	cloud type	observed σ_w [$m s^{-1}$]
St_{low}	0.2	[1] Peng et al. (2005): aircraft, RACE&NARE, North Atlantic	Stratus	~ 0.23
		[2] Lu et al. (2007): aircraft, MASE, eastern Pacific	Stratocumulus ($H_{cb} < 350m$)	0.06 - 0.29
St_{med}	0.4	[3] Lu et al. (2009): aircraft, MASE-II, eastern Pacific	Stratocumulus (mixed H_{cb})	0.25 - 0.41
		[4] Yum et al. (1998): aircraft, ACE-I, Southern Ocean	Stratocumulus	0.33 - 1.06
		[5] Guibert et al. (2003): aircraft, ACE-II, eastern Atlantic Ocean	Stratocumulus (in-cloud)	0.33 - 0.55
		[6] Romakkaniemi et al. (2009): aircraft, CLOPAP, North Sea	Stratocumulus	~ 0.23
		[7] Ditas et al. (2012) helicopter-ACTOS, Baltic Sea	Stratocumulus	~ 0.6
		[8a] Meskhidze et al. (2005): aircraft, CSTRIFE, Monterey, California	Stratocumulus	0.07 - 0.47
St_{high}	0.6	[9] Bretherton et al. (2010): aircraft, VOCALS-REx, Southeast Pacific	Stratocumulus	0.4 - 0.6
		[10] Ghate et al. (2010): Doppler radar, ARM SGP, Lamont, Oklahoma	Stratocumulus	~ 0.5
Cu_{low}	0.4	[11a] Hogan et al. (2009): Doppler lidar, Chilbolton Observatory, England	Stratocumulus	~ 0.6
		[12] de Roode and Duynkerke (1997): aircraft, ASTEX, Central&North Atlantic	Stratocumulus-Cumulus transition	0.22 - 0.45
Cu_{med}	0.8	[13a] Zheng and Rosenfeld (2015): linear relationship to satellite-derived H_{cb} , global	Cumulus with $H_{cb} < 350m$	< 0.7
		[8b] Meskhidze et al. (2005): aircraft, CRYSTAL-FACE, Key West, Florida	Cumulus	0.1 - 1.0
		[14a] Kollias and Albrecht (2010): Millimeter Wavelength Cloud Radar, ARM CRF, Nauru Island, tropical western Pacific	shallow Cumulus (land-forced)	~ 0.75
		[14b] Kollias and Albrecht (2010): Millimeter Wavelength Cloud Radar, ARM CRF, Nauru Island, tropical western Pacific	shallow Cumulus (marine-forced)	0.55 - 0.65
Cu_{high}	1.2	[13b] Zheng and Rosenfeld (2015): linear relationship to satellite-derived H_{cb} , global	Cumulus with $350 m < H_{cb} < 950 m$	0.7 - 1.06
		[11b] Hogan et al. (2009): Doppler lidar, Chilbolton Observatory, South England	Cumulus	~ 1.2
		[13c] Zheng and Rosenfeld (2015): linear relationship to satellite-derived H_{cb} , global	Cumulus with $H_{cb} > 950m$	> 1.06

In Experiment 3, each cloud regime has its own σ_w , varying about $\pm 50\%$ for upper/lower cloud bases from the mid-range values in stratiform and cumuliform regimes. Even though $\bar{w} = 0 \text{ m s}^{-1}$, this still accounts for larger updraft speeds with higher cloud bases, which is supported by findings of Zheng and Rosenfeld (2015). They showed that more than 80% variability in W_{cb} can be explained by H_{cb} , both over land and ocean, and that H_{cb} is a good indicator of thermal strength in sub-cloud layers of convective planetary boundary layers. Using satellite-derived cloud base heights, they proposed a universal linear relationship describing $W_{cb} = 0.59 H_{cb} + 0.5$. Since this relationship is derived for convective boundary layers, it is applied here as a reference check to the base height limits of the cumuliform cloud regimes, and the theoretical results support the chosen σ_w well (Table 4.3).

4.3.5 Comparison with MODIS retrieved CDNC and CDNC sensitivity

In Section 4.4, the parameterized CDNC and CDNC sensitivity from the joint satellite-reanalysis approach are compared to the ones retrieved only using MODIS. CDNC are not directly retrieved from satellites, but are routinely computed as a function of the retrieved effective radius r_{eff} , representing the mean droplet size near the cloud top, and the retrieved cloud optical depth τ_c , assuming adiabaticity and plane-parallel homogeneous clouds above a black surface (Quaas et al., 2006, 2008; Schüller et al., 2005; Brenguier et al., 2000). CDNC can be derived as

$$N_d = \beta \tau_c^{0.5} r_{eff}^{-2.5} \quad (4.7)$$

with the coefficient $\beta = 1.37 \cdot 10^{-5} \text{ m}^{-0.5}$ (Quaas et al., 2006) derived from constants given in Brenguier et al. (2000) describing the shape and lapse-rate of liquid water mixing ratio and thus the adiabatic condensation rate.

The assumption of adiabatic clouds implies that CDNC is constant throughout the vertical extent of the cloud, while liquid water content and droplet size is monotonically increasing. More information about these cloud microphysical properties is given in the Appendix, Section B.1.

The satellite estimated CDNC and CDNC sensitivities are uncertain to an unknown degree depending on retrieval assumptions and uncertainties from:

- **3D radiative effects** in sub-pixel heterogeneous, not plane-parallel clouds (e.g. Grosvenor and Wood, 2014; Zhang et al., 2012; Marshak et al., 2006)
- the assumption of **adiabaticity**, which is not necessarily given for all cloud types and development stages and can be impacted by entrainment or the formation of precipitation which is not detected when only using MODIS (discussions in (e.g. Merk et al., 2016; Rosenfeld et al., 2012; Kim et al., 2008, 2005; Zuidema et al., 2005))
- high **solar zenith angles** and surface reflectivities (e.g. Grosvenor and Wood, 2014)
- choice of r_{eff} **retrieval bands**, which could lead to differing results dependent on the cloud thickness (see e.g. Zhang and Platnick, 2011; Rosenfeld et al., 2004)

- usage of **data product and retrieval algorithms**, e.g. different cloud masks (Yuan et al., 2008) from the CERES Science Team (e.g. Minnis et al., 2004) (which is used here) versus the MODIS Science Team (e.g. Platnick et al., 2003), or the processing level: Level-2 (which is used here) or Level-3 data
- the assumed **droplet distribution** (e.g. Zhang, 2013; Painemal and Zuidema, 2011) and associated to that, the **formation of precipitation** which can significantly reduce CDNC (Wood et al., 2012)
- **cloud type**, development stage, region as well as **sampling** and spatial resolution (e.g. Gryspeerdt and Stier, 2012; Gryspeerdt et al., 2016; McComiskey and Feingold, 2012; Painemal and Zuidema, 2011; Reutter et al., 2009; Schutgens et al., 2016)
- signals from **multi-layered** clouds or upper layer aerosols (e.g. Haywood et al., 2004)
- contributions from **mixed phase clouds** or ice clouds with a top layer of supercooled liquid (e.g. Fridlind et al., 2007)

Some of these uncertainties can be eliminated or at least decreased by filtering for ideal case clouds, and selecting appropriate retrievals. This is achieved by using only near-nadir viewing angles (CDNC are given for the cloud groups within the CERES footprints) and filtering according to the criteria given in Section 4.3.2. Additionally, to ensure reliable retrievals of r_{eff} and τ as suggested in Nakajima and King (1990), the following criteria are sampled from the CCCM dataset:

cloud optical depth

τ_c is the `Mean_group_visible_optical_depth_from_MODIS_radiance` retrieved from MODIS, with an “enhance track” processing algorithm being applied on. This parameter is set to be ≥ 4 to avoid clouds which are too thin and might be confused with thick smoke.

effective radius

r_{eff} is the `Mean_group_water_particle_radius_from_MODIS_rad_3_7` retrieved from MODIS, with an “enhance track” processing algorithm being applied on. This parameter is set to be $\geq 4 \mu m$ to avoid clouds with too small particles which could be confused with a big aerosol plume. Here, $r_{eff} = 10 \mu m$ is eliminated since this is set as a default value within CCCM when no proper retrieval is obtained. MODIS originally retrieves r_{eff} at three different wavelengths (1.6, 2.1 and 3.7 μm), while in the CCCM dataset only 2.1 and 3.7 μm are given, whereby the 2.1 μm retrievals are erroneous. Nevertheless, using r_{eff} at 3.7 μm is assumed to be the best choice as it represents the droplet size closest to the cloud top, and also is less sensitive to 3-D radiative effects (Platnick, 2000; Zhang and Platnick, 2011; Zeng et al., 2014).

The sensitivity of CDNC to aerosol perturbations can be written as (Feingold et al., 2003; Gryspeerdt and Stier, 2012)

$$ACI_{MODIS} = \frac{d \ln N_d}{d \ln \tau} \quad (4.8)$$

with N_d as adiabatically derived CDNC and τ as AOD being used as a proxy for CCN. By using the natural logarithms in the derivatives only relative changes are considered.

The AOD retrievals are obtained from an updated dataset which is retrieved from the ICARE data server (<http://www.icare.univ-lille1.fr/>) in November 2016 containing land and ocean mean AOD (AOD_LOMean) from MODISL2c6 data (CERES Science Team, Hampton, VA, USA: NASA Atmospheric Science Data Center (ASDC), DOI:10.5067/AQUA/CERES/NEWS_CCCM-FM3-MODIS-CAL-CS_L2.RelB1). This AOD is given on the CERES footprints, and is applied everywhere where MODIS CDNC are found for the selected ideal-case clouds.

4.4 Results and Discussions

4.4.1 Assessment of regime-based supersaturations

In order to assess the regime dependence of CDNC sensitivity, the regime dependency of the maximum supersaturation S_{max} as described in Section 4.3.4 should be analyzed first. S_{max} as a function of updraft speed w for each cloud regime is shown in Figure 4.7. As it is not integrated over the updraft PDF, for each updraft-bin S_{max} depends purely on the mean meteorological conditions and the CCN spectrum of the cloud regime (see Appendix B, Section B.3).

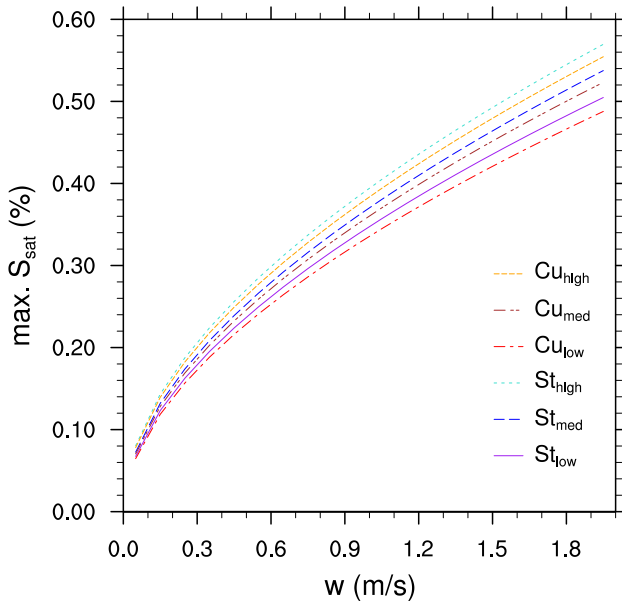


Figure 4.7: Regime-based S_{max} as a function of updraft speed w .

the same height class pressure, temperature and specific humidity are marginally larger for cumulus clouds. Therefore, since cumulus clouds are slightly warmer ($\Delta T \sim 1K$), lower ($\Delta p \sim 2 - 10 hPa$) and thus contain a little more specific humidity ($\Delta q \sim 0.7 g kg^{-1}$) for the same height class, their cooling rate is lower leading to a smaller S_{max} . Also the slightly larger CCN amount (Figure B.6) for cumulus clouds (max. $\Delta CCN \sim 10 cm^{-3}$) could lead to a smaller S_{max} , since more particles take up the available water vapor so that

The result gives a very clear and structured picture. S_{max} increases strongly with updraft speed as the cooling rate becomes stronger. This shows that the updraft velocity is a key parameter controlling the nucleation process. S_{max} also increases with cloud base height for a prescribed updraft speed, with increasing differences the larger the updraft speed becomes. This behavior corresponds to an increasing cooling rate as the adiabatic expansion gets larger the higher the air parcel has to rise. Besides these two features, Figure 4.7 further shows a slightly larger S_{max} for stratiform clouds than for cumulus clouds of the same height class. The cloud base parameters for each regime (Figure B.3, B.4 and B.5) reveals that for

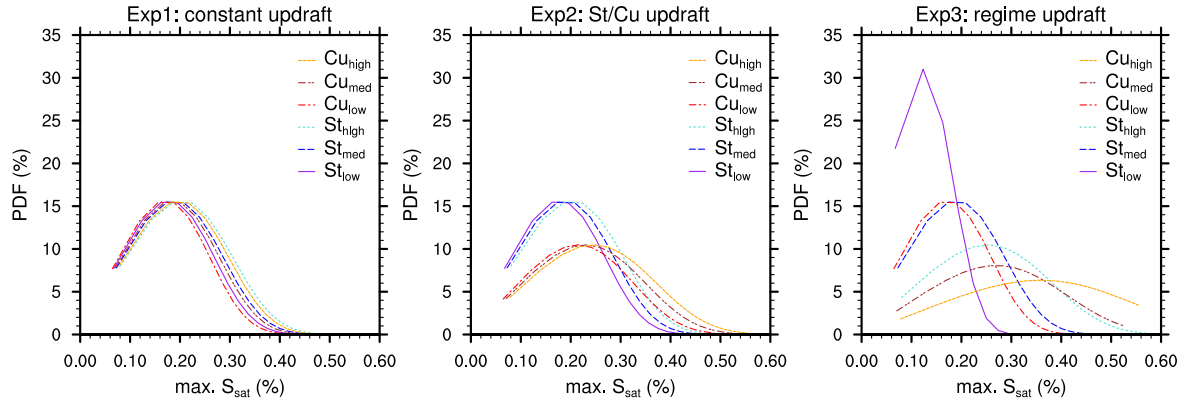


Figure 4.8: Regime-based S_{max} for the various updraft experiments, with S_{max} being integrated over the updraft PDF prescribed in the updraft experiments.

the condensation rate increases. Even though all these differences are marginal, taken together they result in a slightly larger stratiform S_{max} as seen in Figure 4.7, with increasing differences to cumuliiform S_{max} as updrafts increase.

Figure 4.8 shows how S_{max} varies with cloud regime for the various updraft experiments. In Experiment 1, with constant $\sigma_w = 0.4 \text{ m s}^{-1}$ for all cloud regimes, S_{max} shows the same behavior as in Figure 4.7, with the largest occurrence around 0.18%. In Experiment 2, the S_{max} -distribution becomes wider as σ_w increases, with a maximum around 0.17-0.19% for stratiform clouds and 0.22-0.25% for cumuliiform clouds. The doubling in σ_w in this experiment does not result in a doubling in S_{max} , revealing its non-linear relationship and the limitation by the condensational growth rate of the available particles. In Experiment 3, S_{max} varies with cloud regime σ_w from $\sim 0.12\%$ to $\sim 0.36\%$ maximum occurrence.

Figure 4.9 shows the global distribution of S_{max} for each updraft experiment, for all the cloud regimes taken together, each weighted by its respective RFO. The global mean values are given on top of each panel. The distributions of S_{max} for each cloud regime in each experiment are depicted in Appendix B, Section B.4.

Figure B.8 illustrates that the global pattern of S_{max} in each cloud regime is very similar, whereby S_{max} is remarkably determined by the interplay between meteorological conditions and CCN-active aerosols. Assuming globally constant updrafts (Experiment 1), S_{max} is generally higher over the oceans than over the continents. This is due to two reasons. First, the lower CCN amount (as discussed in Section 3) over the oceans considerably reduces the condensation rate, thus leading to a higher S_{max} . Secondly, the larger relative humidity over the oceans provides the basis for stronger S_{max} as a moist oceanic air parcel is closer to saturation than a continental one rising the same distance and experiencing similar gradients in pressure, temperature and moisture. Low CCN amounts (see Figure 3.2) are furthermore responsible for the larger S_{max} along the ITCZ and over West-Australia. In all cloud height classes, S_{max} is relatively large in the mid-latitude oceanic storm tracks, especially over the Southern Ocean. This is independent of CCN availability, but rather an effect from atmospheric dynamics. A warm moist air parcel from lower latitudes being mixed into colder drier

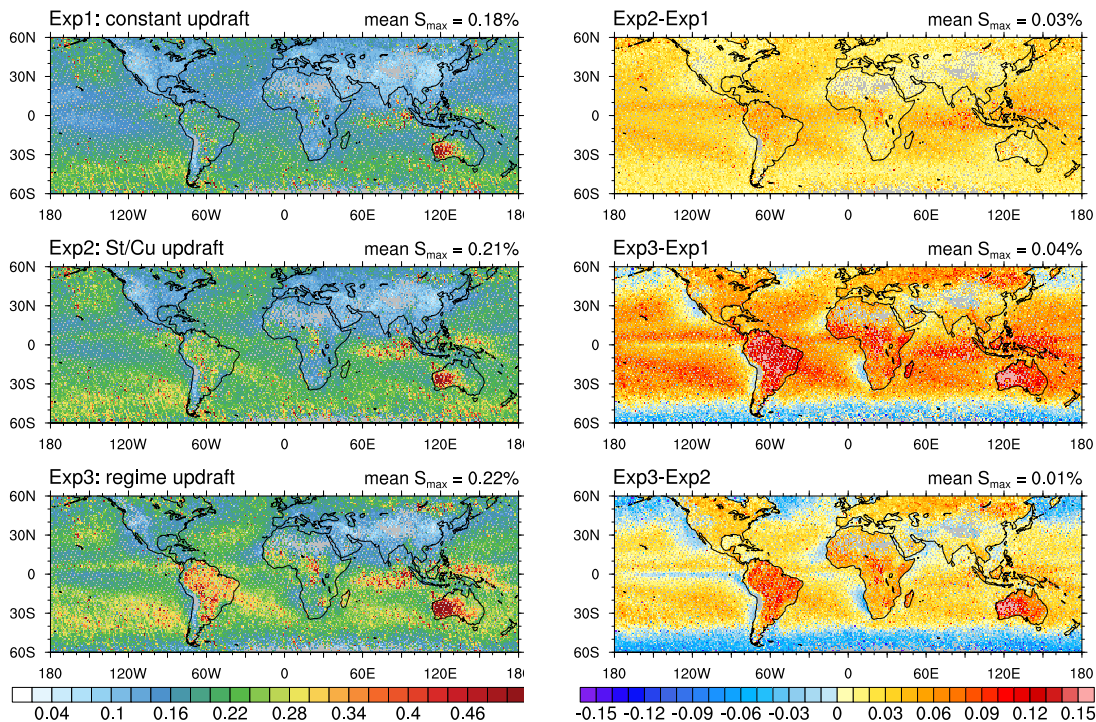


Figure 4.9: Global distribution of regime-based S_{max} , for the three different updraft experiments listed in Table 4.2. 4 years of daily data are used with MACC-II aerosol reanalysis products and CCCM cloud products evaluated along the A-Train track.

Figure 4.10: Experiment differences in global distribution of regime-based S_{max} . 4 years of daily data are used with MACC-II aerosol reanalysis products and CCCM cloud products evaluated along the A-Train track.

air from the poles by large cyclones thus ends up having a higher temperature and moisture difference to its environment - resulting in larger S_{max} .

Changes in the updraft distributions results only in slight changes of the global pattern of S_{max} . Figure 4.9 and 4.10 illustrate these changes. Increasing the cumuliform updrafts in Experiment 2 increases the overall S_{max} by $\sim 17\%$ globally rather homogeneously, whereas the actual increase in the cumuliform clouds alone is about $\sim 27\%$. Experiment 3 increases the overall S_{max} by $\sim 22\%$ in comparison to Experiment 1, where S_{max} is increased everywhere except for the low cloud classes which represent the storm tracks and the coastal stratus decks. The deviations of σ_w from Experiment 3 to Experiment 2 only increase S_{max} by $\sim 5\%$ in the global annual average due to compensating effects of different regimes. On the one side S_{max} increases over land (St_{high} , Cu_{high}), especially over Australia and South America, and over the oceanic shallow cumulus regimes (Cu_{med}). On the other side S_{max} decreases even further in the mid-latitude storm tracks and Pacific trough (St_{low} , Cu_{low}) as well as in the stratocumulus decks (St_{med}).

As different large-scale mean vertical velocities are not included here, the departures in regime-based S_{max} due to differing regime-based σ_w are very small and do not change the global S_{max} distribution markedly. The mean vertical velocities were not included because in the model they are very low (up to 0.5 m s^{-1}) owing to the coarse resolution, and it was not possible to compute them from turbulent kinetic energy fluxes (as was done in West et al.

(2014)) as this was no general output. Therefore, it was best to set them equal here in order to do a systematic analysis of the impact from σ_w .

An inclusion of cloud-scale mean vertical velocities however would increase the regime-based S_{max} and their differences much more effectively as they are expected to be below $1 m s^{-1}$ for stratiform clouds (e.g. Yum et al., 1998; Guibert et al., 2003; Meskhidze et al., 2005; Lu et al., 2009; Seinfeld and Pandis, 2006; Pruppacher and Klett, 1997), or vary up to $\sim 2.5 m s^{-1}$ (e.g. Seinfeld and Pandis, 2006; Pruppacher and Klett, 1997) or $\sim 2.8 m s^{-1}$ (Meskhidze et al., 2005) for maritime cumuliform clouds, and even more for continental cumuliform clouds ($> 5 m s^{-1}$) (Seinfeld and Pandis, 2006; Pruppacher and Klett, 1997).

4.4.2 Assessment of regime-based CDNC

The resulting CDNC depend and therefore follow the distribution of the regime-based S_{max} . This can clearly be seen from Figure 4.11, in which the global mean CDNC (taken as medians of the CDNC distribution for each location) is plotted as a function of cloud regime and updraft experiment.

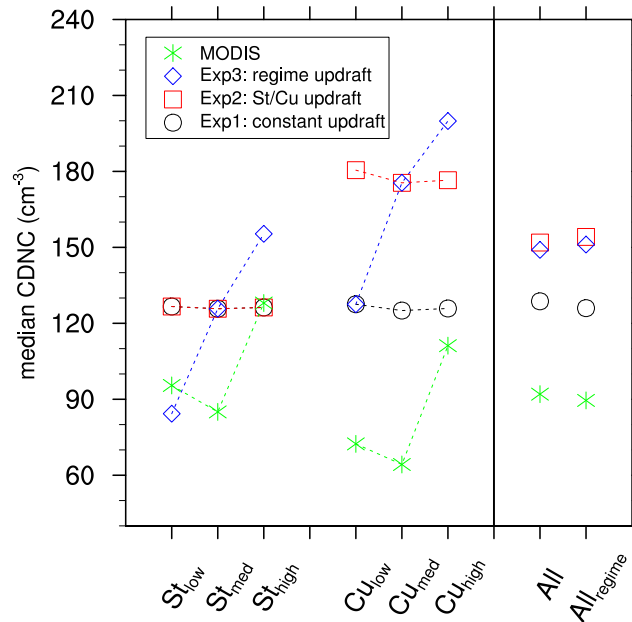


Figure 4.11: Regime-based median CDNC, computed from global averages of median CDNC occurring in a specific cloud regime over the time period 2007-2010. Category “All” shows the average median CDNC with equal regime weighting, and category “*All_{regime}*” shows the average median CDNC weighted by the RFO of the cloud regime. Dashed lines are drawn for orientation and overview for each experiment.

In Experiment 1, CDNC are roughly constant ($\sim 126 cm^{-3}$) over all cloud regimes. The column “All” and “*All_{regime}*” represent different weightings. For the median CDNC in column “All” all liquid filtered clouds are taken into consideration without splitting them into regimes. This is the same principle as computing an arithmetic average. “*All_{regime}*” represents the average CDNC of the regime medians weighted by their respective RFOs. As can be seen here, the effect of the RFO-weighted average on the mean CDNC is very small, as the regimes are well balanced. For a different choice of regimes, those deviations could be much larger.

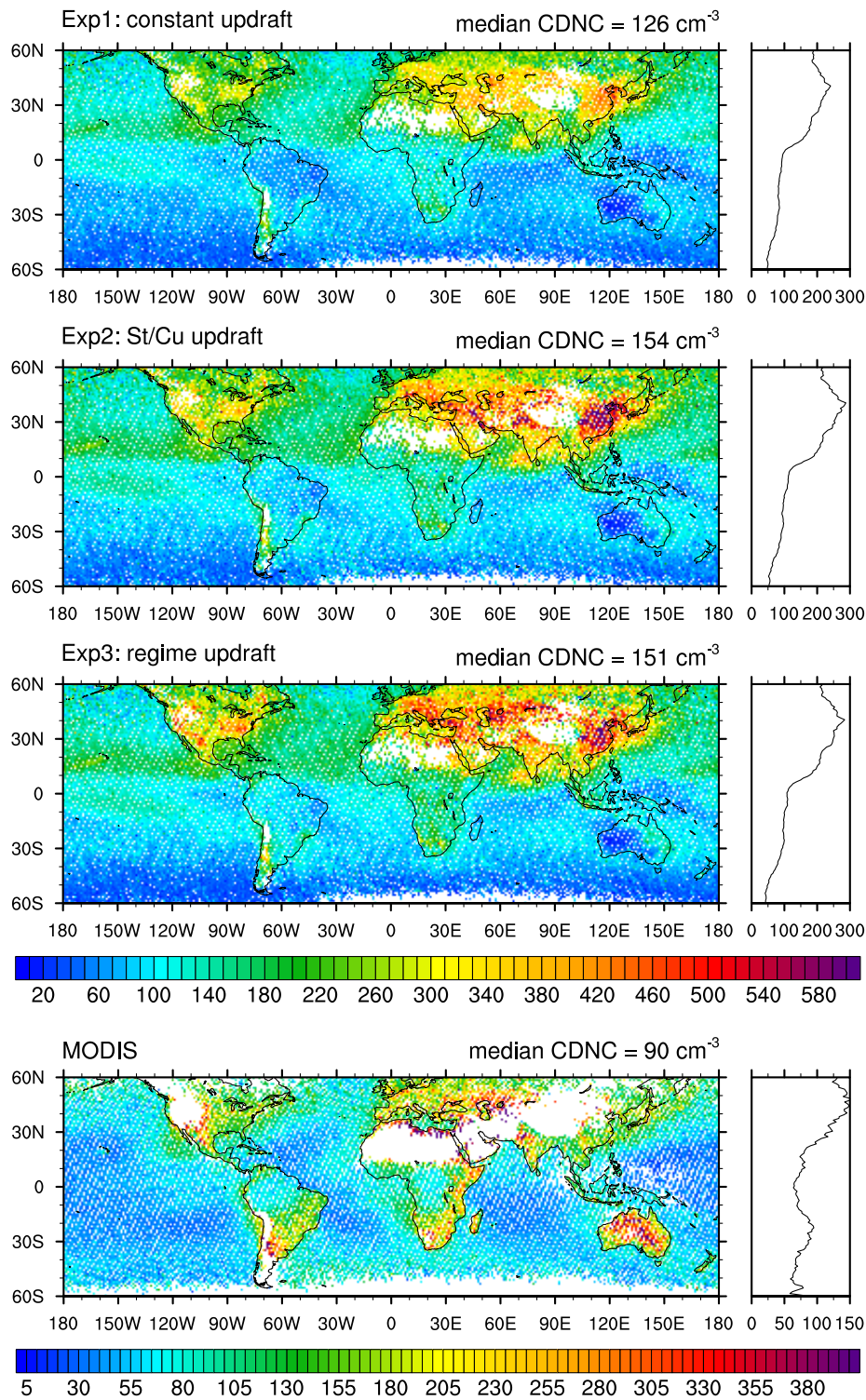


Figure 4.12: Global distribution of median CDNC, from all cloud regimes together (not weighted) for each updraft experiment. The lowest panel shows the adiabatically estimated CDNC distribution computed from MODIS Reff (3.7 microns) and COD, which have been processed from the CCCM dataset. All CDNC estimates are filtered for single-layer, non-precipitating liquid water clouds only along the nadir A-Train track. MACC CDNC are parameterized near cloud bases, while MODIS CDNC are retrieved from cloud tops. The global average of median CDNC is given at the top of each panel.

In Experiment 2, median CDNC are about 125 cm^{-3} for stratiform clouds and about 180 cm^{-3} for cumuliform clouds. The shift of about 55 cm^{-3} (44%) for cumuliform clouds corresponds to an absolute increase in S_{max} about 0.05% ($\sim 28\%$). The total median CDNC is about 154 cm^{-3} . Here, it can also be seen that despite of an increase in S_{max} from low to medium high cloud regimes, CDNC are slightly reduced. This is because low altitude clouds have their highest RFO in the storm track regions where S_{max} is relatively large. Since the differences in S_{max} between height classes are low, the occurrence of clouds in a specific S_{max} domain as plotted e.g. in the Appendix B.4, Figure B.9 plays a larger role. Thus, in combination with the regime-based RFO, mid-level clouds effectively have a lower S_{max} than low-level clouds (not shown).

This is no longer an object in Experiment 3 as differences in S_{max} are large enough to overrule the RFO dependence. Here, CDNC clearly increase with S_{max} and thus with σ_w . The median values vary from $\sim 85 \text{ cm}^{-3}$ in low stratiform clouds to $\sim 155 \text{ cm}^{-3}$ in high stratiform clouds, whereas CDNC increases from $\sim 130 \text{ cm}^{-3}$ to $\sim 200 \text{ cm}^{-3}$ in the cumuliform cases. Such a wide spread is not negligible and shows how important an evaluation of CDNC by cloud regime actually is, and how much the choice of updraft distribution matters in this case. However, the reduction via updraft in the low regimes and the increase in the high regimes roughly balance each other so that the total median CDNC are very similar to the ones in Experiment 2.

For comparison, the regime-based MODIS retrieved CDNC are also shown in Figure 4.11. They are significantly lower than the estimated MACC-II CDNC. The parameterized total median CDNC are $\sim 40\%$ (Experiment 1) to $\sim 70\%$ (Experiment 2 & 3) larger than the retrieved ones. The main reason for this deviation might be the positive bias in CCN of $\sim 50\%$ (see Chapter 3) which is propagated onwards.

Another remarkable difference is that in contrast to the parameterized CDNC (especially in Experiment 2 & 3), MODIS retrieved CDNC are lower in the cumuliform regimes than in the stratiform regimes for the same height class. This agrees with results from Unglaub (2017) who used the same CCCM-MODIS retrievals applying almost the same filtering. She found larger r_{eff} , τ_c and L_p for Cu-regimes than for St-regimes, and also that commonly $r_{eff,med} > r_{eff,low} > r_{eff,high}$ while for τ_c and L_p it is the other way around. This fits to the respective regime-based CDNC distribution found here and can be explained by the larger vertical extent of cumuliform clouds, which tend to growth thicker especially over land when updrafts are higher. Estimates of CDNC increase the larger τ_c (and L_p) are measured, that is the larger the cloud geometrical thickness is, but they are reduced even more for larger r_{eff} which is $\propto H^{1/3}$.

However, there is no evidence or indications in previous peer-reviewed studies that cumuliform clouds actually have smaller CDNC per cm^3 than stratiform clouds, in contrast one would expect them to have higher CDNC since cumuliform clouds are associated with larger updrafts and thus a higher activation efficacy. Instead, retrieval uncertainties may be the reason for the behavior found here. It has been shown, that especially for inhomogeneous (that is broken cumuliform) clouds uncertainties in τ_c and r_{eff} are high due to effects of sub-pixel variability which is not accounted for in the assumptions of horizontally homogeneous

plane-parallel cloud fields used for MODIS retrievals.

For a given footprint with several broken clouds each with a $\tau_{c,i}$, a passive satellite retrieval would give the average visible reflectance of this pixel $R_{vis}(\bar{\tau}_{c,i})$ including the cloud free areas instead of the reflectance of the average optical depths $R_{vis}(\tau_{c,i})$. This leads to an underestimated $\bar{\tau}_c$ of the pixel or footprint which is also associated with the plane-parallel albedo bias (Oreopoulos et al., 2007; Cahalan et al., 1994; Marshak et al., 2006).

Additionally to the reduced τ_c , also an increased r_{eff} may contribute to a low bias of retrieved CDNC for various reasons. Painemal and Zuidema (2011) found a positive bias of MODIS r_{eff} of 15 % to 20 % compared to in-situ aircraft observations during the VOCALS-REx campaign over the Chile-Peru stratocumulus cloud deck. They argued that combined uncertainties on the shape of the cloud mode droplet spectrum, the influence of drizzle, the above-cloud water vapor absorption as well as the viewing geometry could lead to effective radii larger than in-situ values.

Neglecting cloud entrainment and horizontal photon transport (the 3-D radiative bias) particularly within heterogeneous clouds are also found to contribute to r_{eff} larger than the true value (Zeng et al., 2014; Zhang and Platnick, 2011). Cho et al. (2015) analyzed the frequency and potential causes of “failed” MODIS retrievals over marine liquid water clouds for which the observed cloud reflectivities cannot be explained by using a combination of τ_c and r_{eff} . They found an overall failure rate of about 10 % to 16 %, with higher values found for broken cumulus regimes. 60 % to 85 % of these failed retrievals are associated with “too large” r_{eff} . This is especially the case for high sub-pixel inhomogeneities, locations with special sun-satellite viewing geometries (sun glint) or high solar zenith angles, possible precipitation occurrence, or for pixels where clouds are masked, overlapped or cloud phases were difficult to retrieve.

Regarding the strong sensitivity of CDNC on r_{eff} , and considering a low bias of τ_c and a high bias of r_{eff} especially for inhomogeneous cloud fields, the lower cumuliform CDNC may be explained by some of these retrieval uncertainties.

As seen in Figure 4.11, MODIS retrieved CDNC are larger in the high altitude regimes, which dominantly occur over land. This could either be due to a larger CCN supply or due to increased updrafts increasing S_{sat} . Without proper measurements these effects could not be disentangled from the observations used here. The effect however is included in Experiment 3, in which maximum S_{sat} is increased by larger updrafts in the high regime. The CCN is only slightly larger for the high regimes (see Figure B.6), so that CDNC is not strongly influenced by CCN supply. This must not be the case for observed CDNC, since the regime-based distribution of real CCN-active aerosols is not known.

The lowest MODIS retrieved CDNC are found for the medium high cloud regimes probably because they have the largest observed r_{eff} . This contradicts the assumptions made in Experiment 3. But Experiment 1 & 2 show very weak indications to this behavior for the cumuliform clouds which is explained by a combination of RFO and S_{max} distribution. It could be speculated that this is the reason why this behavior is found in the observations, however it could also be possible that retrieval uncertainties impact the CDNC distribution

here as well.

Even though parameterized and observed CDNC do not agree well, it must be taken into account that also the MODIS retrieved CDNC underly measurement uncertainties which are not negligible and on assumptions which have been shown to not represent real clouds but rather give idealized states (see Sections B.1 in Appendix B). Therefore, MODIS retrieved CDNC should not be seen as the true reference case to any CDNC parameterization. Their distribution and variance is not fully understood as several mechanisms play together and the measurements are too poor or too few to accurately account for their impacts.

The global distribution of CDNC and the variation by updraft experiment is illustrated in Figure 4.12. Regarding the nature of log-normally distributed CDNC (as for CCN), each grid cell represents the median of the CDNC distributions over time (2007-2010). The global CDNC distribution is very similar between the different experiments and compares well with near-surface CCN distribution (Figure 3.4). CDNC are highest in the Northern Hemisphere with particular large values over China, and the industrial regions. The tropical rain belt seems to be a natural barrier of atmospheric CDNC distribution, as in the Southern Hemisphere CDNC are decreasing very rapidly. Especially low amounts are found over western Australia, the Indonesian warm pool and the Southern Ocean. CDNC over South America and Africa are increasing slightly with increasing updraft. The global average CDNC increases by $\sim 22\%$ just due to the distinction of stratiform and cumuliform updrafts. Due to compensating effects of different regimes, and the combination of regime-based RFO and S_{max} , the average CDNC in Experiment 3 is about 2% lower than in Experiment 2.

MODIS retrieved CDNC (Figure 4.12, lowest panel) shows distinct differences. First of all, the data coverage is limited leaving larger gaps over terrain of high altitude and deserts. Even though the data is filtered for the same clouds as for the parameterized CDNC - referring to non-precipitating, single-layered liquid clouds - the measurement of τ_c and r_{eff} is not good enough in these regions to retrieve CDNC. Additionally, the use of only nadir imaging data further reduces the possibility of data coverage over the MODIS swath. The presence of more missing values over the continents reduces the average CDNC, as more oceanic data with lower concentrations go into the average. Still, a clear contrast can be detected between land and ocean and also the inter-hemispheric gradient can clearly be seen, which is similar to the parameterized CDNC distributions.

MODIS retrieved and parameterized CDNC show various differences. Over oceans, the extra-tropical storm tracks especially in the Atlantic show similar concentrations for the MODIS retrievals in both hemispheres, while in the parameterizations CDNC in the southern storm track is much lower than in the northern one. The same is valid for the trade wind regions, for which MODIS does not detect higher CDNC at all except close to the coastlines. Over land, MODIS retrieved CDNC are much higher over Australia than they are over China, which seems spurious regarding the nature of aerosols emitted in these regions. For parameterized CDNC this is exactly the opposite. Furthermore, MODIS CDNC seem to be especially high just at the border to areas which contain missing values which hints to retrieval artifacts. Increased concentrations along the east coasts of South America and South Africa also contradict with parameterized CDNC.

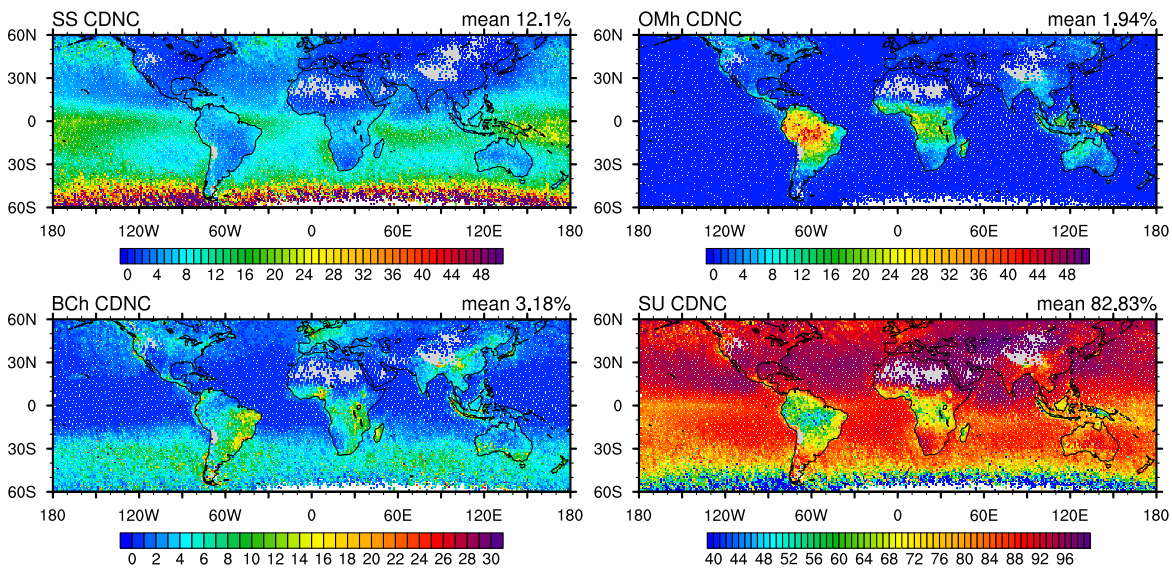


Figure 4.13: Aerosol species contribution to total CDNC from CCN relevant aerosols, in Experiment 3 (regime-based updraft PDF) for all cloud regimes taken together (not weighted). The global mean values are given at the top of each panel.

As discussed in Section 4.3.5 as well as in Appendix B, Section B.1, MODIS derived CDNC depends on a variety of assumptions and is uncertain to an unknown degree. This can lead to differing CDNC distributions even on the basis of the same retrieval sources as is shown in Figure B.2. Therefore, the MODIS retrieved CDNC in Figure 4.12 is just an indication of possible differences to parameterized CDNC and should not be taken as the absolute truth.

Figure 4.13 indicates the activated fraction of each CCN-relevant aerosol species. More than 80% of total CDNC is produced of SU particles, with at least 40% in the Southern Ocean and more than 90% in the Northern Hemisphere. Roughly 12% is taken up from sea salt particles which balance the contribution of SU in the Southern Ocean between 50 and 60°S. SS also takes up to 25% over the Indonesian warm pool. Organic matter only comprises ~ 2% of total CDNC, but can vary up to almost 40% in the South American Rainforest and 25% in the African Rainforest. BC aerosols have an average contribution of ~ 3%. The BC fraction is heterogeneously distributed, with the largest fractions up to ~ 15% especially over South America, South Africa and the oceans between 30 and 60°S. Central Europe, North-West America, India and China also show larger contributions to CDNC from BC.

For various reasons which already have been discussed in the validation of Section 3, it is debatable how much these contributions resemble the truth, especially when it comes to the overall dominating contribution from SU. Besides the actual numbers of contribution, the global distribution of each individual aerosol species seems to be at least reasonable, except for the large amount of BC over the Southern Ocean.

4.4.3 Assessment of regime-based CDNC sensitivity to aerosol changes

Many previous studies used to estimate the sensitivity of CDNC to aerosol changes by computing the relative change of adiabatically retrieved MODIS CDNC to AOD. Global distributions of this sensitivity between 60°S to 60°N are shown in Grandey and Stier (2010) for different spatial scales. Gryspeerdt and Stier (2012) shows the distribution between 30°S to 30°N for different tropical cloud regimes. Both studies find generally positive but small sensitivities (< 0.5). The largest sensitivities have been found over ocean regions (in agreement with Quaas et al. (2008)) while over land sensitivities are very low and can even be negative. Depending on the scale, dataset and methodology the sensitivity estimates vary.

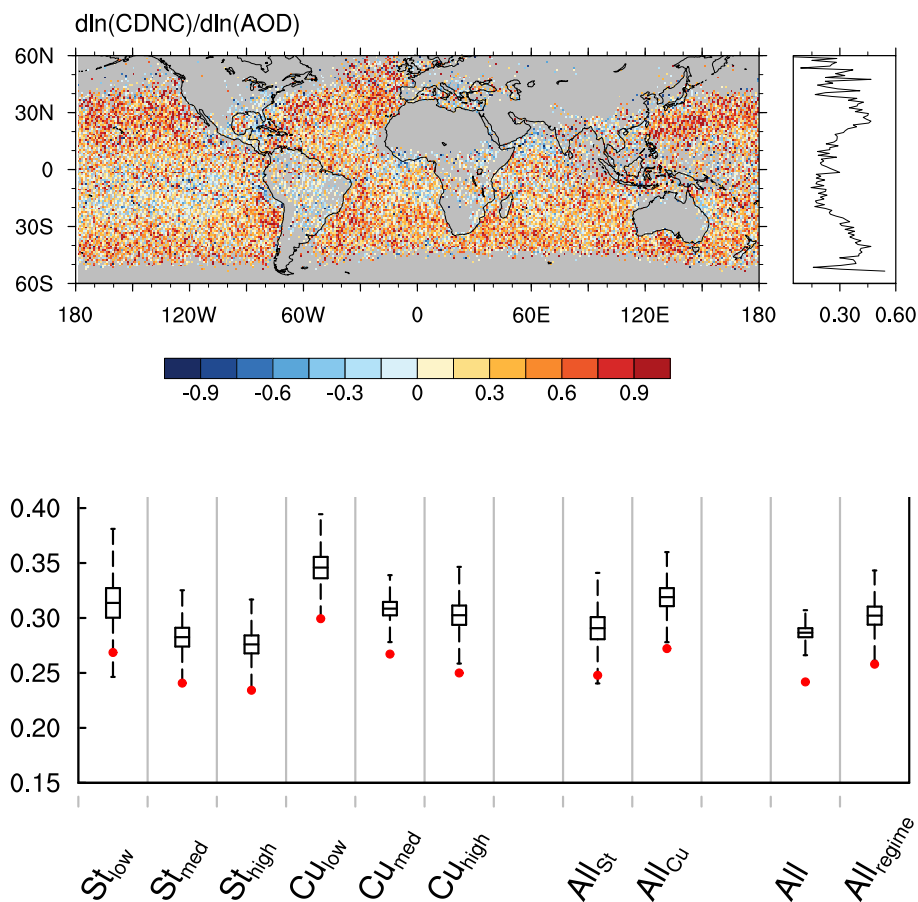


Figure 4.14: MODIS CDNC-AOD sensitivity, for relative changes over time (daily data, 2007-2010) within a $1 \times 1^{\text{deg}}$ grid cell (top panel) and relative changes in time within liquid cloud regimes (bottom panel). For each cloud regime the mean sensitivity, 2σ & 10σ are plotted. Category “All” describes the average of cloud regimes, while “ All_{regime} ” is the average weighted by the RFO of each regime. The red dots represent the correlation coefficients.

Here, the relative sensitivity of MODIS retrieved CDNC to changes in AOD over time within a $1^{\circ} \times 1^{\circ}$ grid cell is shown in Figure 4.14. CDNC are retrieved adiabatically from τ_c and r_{eff} from the CCCM data along the CALIPSO ground track for the filtered ideal-case clouds, and the land-ocean mean AOD is retrieved from Aqua MODIS Level-2, collection 6. Most of the land and high latitude values are missing because of the data handling. The

global distribution compares well with Grandey and Stier (2010) and Gryspeerdt and Stier (2012), and in terms of regional distribution it compares also well with Quaas et al. (2008). Larger sensitivities are found over oceans, the largest in the stratocumulus regions off the west coast of North & South America, in the extra-tropical storm track regions and over the Northwest Pacific Ocean. Also very low and even negative sensitivities can be found in an irregular pattern, but more commonly over or near land. This is comparable with findings of Gryspeerdt and Stier (2012) and according to them this could be attributed to uncertainties in the cloud retrievals at low cloud fractions or to larger deviations from adiabatic assumptions rather than to physical mechanisms such as semi-direct aerosol effects. However, these cannot be ruled out completely here.

The sensitivities computed from regressions over time within the liquid cloud regimes are shown in the lower panel of Figure 4.14. Here, the same methodology as in Quaas et al. (2008) is applied, but instead of using geographical regions, the cloud regimes originating from all over the world are employed. The mean sensitivity of all liquid filtered clouds is ~ 0.29 ($R = 0.24$). This is only slightly increased to ~ 0.3 ($R = 0.26$) for the RFO-weighted average of regime means.

The analysis by cloud regime reveals a decrease of sensitivity with cloud base height, which also implies that regimes dominantly occurring over continents (CU_{high} and ST_{high}) have the lowest sensitivities. These two features can be explained by the overall amount of CCN relevant aerosols which determine CDNC sensitivities. Higher sensitivities over ocean are found because the clouds are in general cleaner. In a remote marine site, a given aerosol perturbation is used to the full potential to activate droplets, while the same perturbation over land does not give as much more CDNC as in a clean environment because there already are a lot of aerosols which need to fight for the available water vapor. The decrease of sensitivity by cloud base height can also be explained by a higher aerosol availability closer to the ground.

Hence, one could argue that in clean marine sites the activation is more CCN-limited, while in a more polluted continental case the activation is more limited by the environmental conditions described by S_{max} . This is of course a very simplified and crude approach, however this concept is not new. Reutter et al. (2009) has already shown that such limitations can significantly impact droplet formation of convective clouds. They distinguished aerosol-limited regimes with low activated aerosol fractions from updraft-limited regimes with high activated aerosol fractions under pyro-convective conditions using a parcel model.

This approach of thinking about the impact of S_{max} on CDNC sensitivity could also explain why cumuliform clouds (with potentially larger S_{max}) are found here to have larger CDNC sensitivities than stratiform clouds (with smaller S_{max}) in the same height class. This is just speculation so far and unfortunately one cannot tell from just the observations how much impact S_{max} has on the overall sensitivity. But when analyzing the modeled sensitivities, this will be discussed below in more detail (see discussion on Figure 4.16).

To some extent the results contradict the findings from Gryspeerdt and Stier (2012) who argued that stratocumulus clouds occurring near the coasts contribute most to the overall sensitivity with 58%, followed by a shallow cumulus regime occurring more in remote ocean

regions with only 11 %. However, Gryspeerdt and Stier (2012) makes use of different regimes only between 30° N and 30° S, different data and applies different sampling and filtering. Therefore, the results cannot be compared well and it cannot be determined whether one or the other result is more correct.

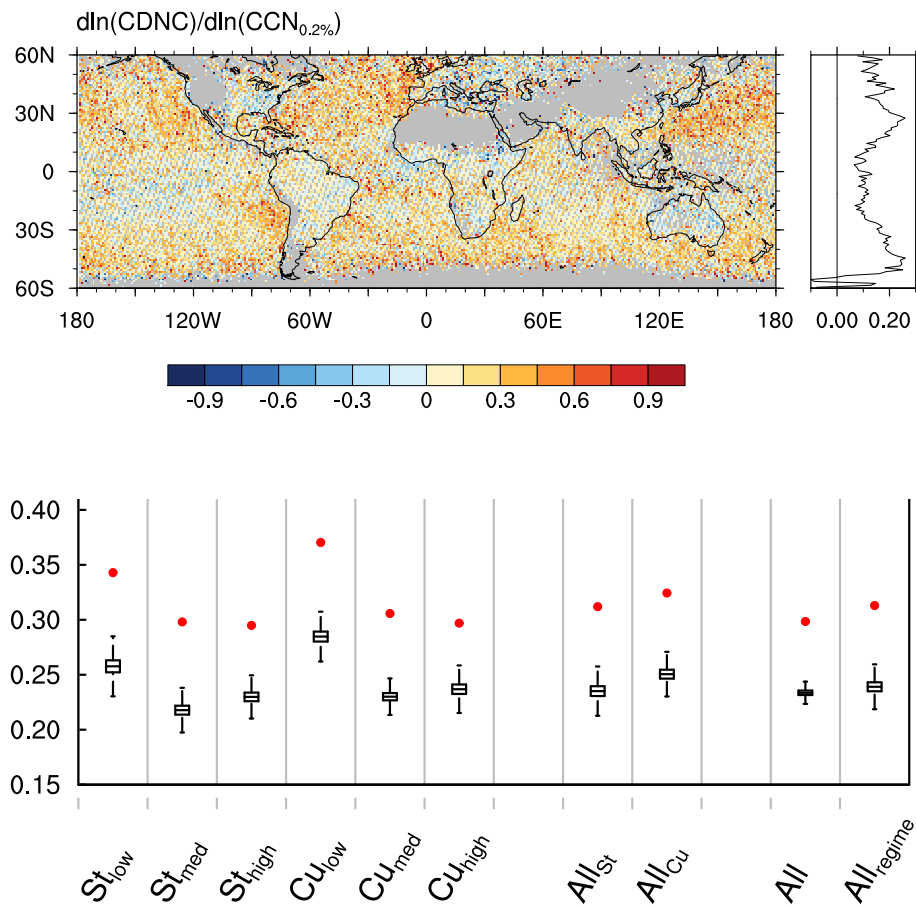


Figure 4.15: MODIS CDNC-CCN sensitivity, for relative changes of MODIS derived CDNC and MACC-II CCN over time (daily data, 2007-2010) within a $1 \times 1^\circ$ grid cell (top panel) and relative changes in time within liquid cloud regimes (bottom panel). For each cloud regime the mean sensitivity, 2σ & 10σ are plotted. Category “All” describes the average of cloud regimes, while “ All_{regime} ” is the average weighted by the RFO of each regime. The red dots represent the correlation coefficients.

Figure 4.15 shows the sensitivities of changes in MODIS retrieved CDNC relative to changes in MACC-II computed CCN, instead of AOD. The overall distribution pattern does not change much from that in Figure 4.14. The estimated mean sensitivities are slightly lower (~ 0.24 for “ All_{regime} ”). However, lower standard deviations and higher correlations coefficients ($R = 0.3$ for “ All_{regime} ”) show a better temporal fit and therefore a slight improvement of CCN over AOD in this estimate, just as was shown in Chapter 3. Still, low clouds and cumuliform clouds show larger sensitivities in agreement with Figure 4.14. However, the decrease of sensitivity with increasing cloud base height is not as evident as in Figure 4.14.

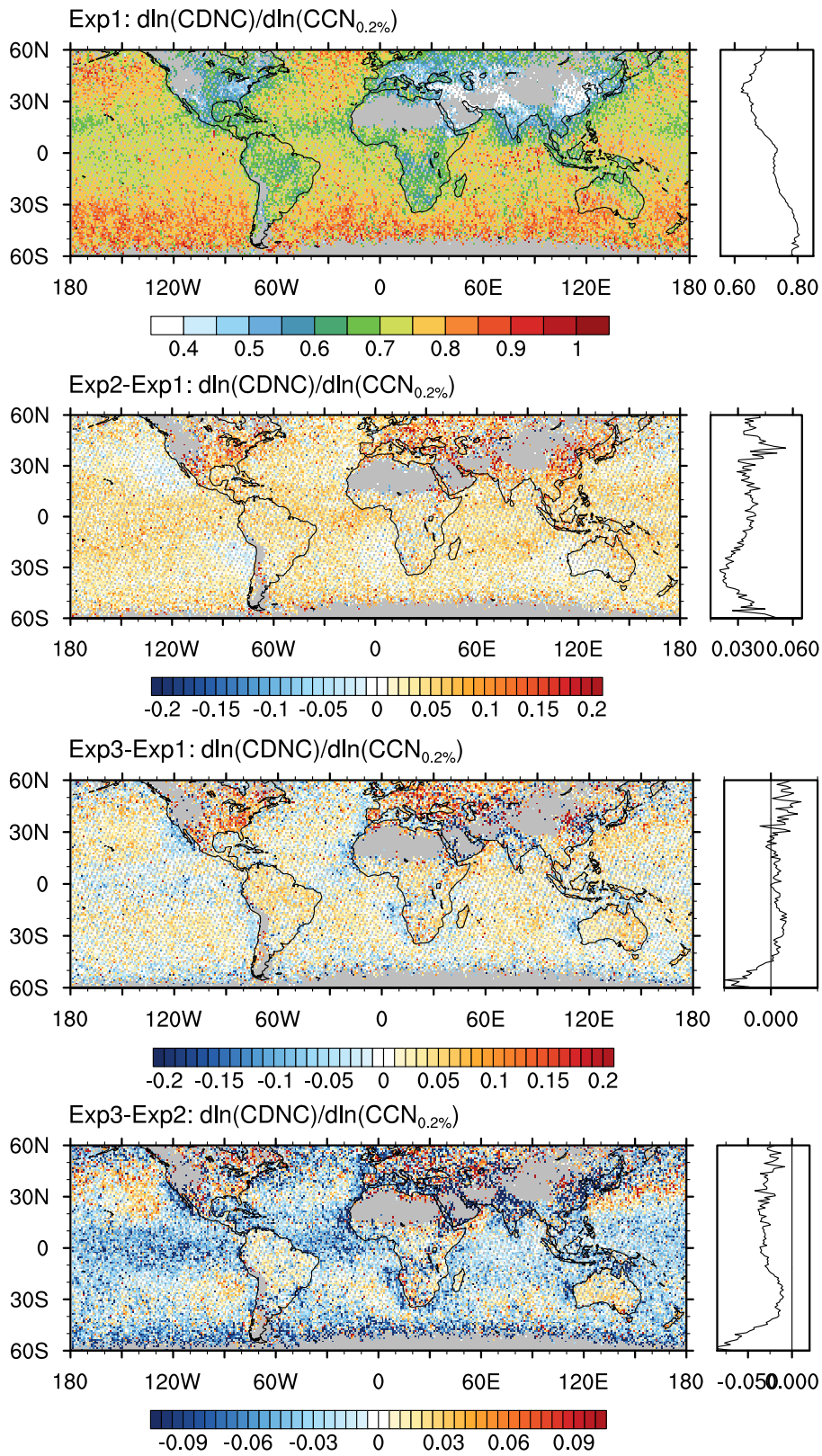


Figure 4.16: MACC derived CDNC sensitivity relative to changes in CCN ($0.2\% S_{sat}$) for Experiment 1 (top panel). The lower three panels show absolute differences between the updraft experiments.

Figure 4.16 shows the distribution of sensitivities in MACC-II CDNC relative to changes in CCN. Because CDNC are parameterized on the basis of CCN, the sensitivities are all positive and very high. For Experiment 1 (Figure 4.16, top panel) the mean sensitivity is ~ 0.74 ($R = 0.97$). In agreement with previous studies and Figures 4.15 and 4.14, sensitivities are smaller over land and also along the ITCZ. Especially low values are found in areas which are commonly known to be very polluted such as India, China, North America and Central Europe. The largest sensitivities are found in the extra-tropical storm tracks over the Southern Ocean as well as over the North Pacific and Atlantic. The inter-hemispheric gradient of CDNC sensitivity is opposite of the one for CDNC itself, with larger sensitivities in the Southern Hemisphere.

Since the sensitivities of the updraft experiments are very similar, the other panels in Figure 4.16 show only the differences between the various experiments. Due to the differentiation of stratiform and cumuliform activation, CDNC sensitivities are generally increased in Experiment 2 owing to larger supersaturations in cumuliform clouds. The global mean increase is about 0.03, but sensitivities can even grow by ~ 0.2 in some regions over land. Only in regions of frequently occurring stratiform clouds the sensitivities are not increased, as the updraft widths stay the same.

The regime-dependent activation parameterization in Experiment 3 gives a more heterogeneous structure compared to Experiment 1. Because most regimes are parametrized with larger updrafts, overall sensitivities are increased by 0.02. Only for low stratus clouds the activation efficiency is decreased. Still, this is enough to make the sensitivity distribution more heterogeneous as this decrease in regions with frequently occurring low-level stratus is more pronounced than the increase by the other regimes.

This feature is well illustrated in the difference of Experiment 3 to Experiment 2 in the lowest panel of Figure 4.16. The decrease of CDNC sensitivity by the low regimes is much stronger than the increase by high regimes. Therefore mean CDNC sensitivities are reduced even though high regimes occur 8% more frequently than low regimes. This behavior is independent from CCN concentrations and only due to the non-linearity of S_{max} with σ_w as seen in Figure 4.7. This feature demonstrates how important a correct description of S_{max} is for estimates of CDNC sensitivities.

The differentiation between cloud heights in addition to the distinction of cloud top heterogeneity puts an extra variability onto CDNC sensitivities. Outstanding in Figure 4.16, lowest panel, are now regions of higher sensitivities caused by high-level liquid clouds which can in parts also be detected in sensitivities estimated from satellite retrievals (see Figure 4.14 and 4.15). This includes for example the region over the Northwest Pacific Ocean (Philippine Sea). Higher sensitivities found in this region from passive satellite retrievals are usually associated with higher CCN supply coming from China. However, as can be speculated from Figure 4.16, probably most of the increased sensitivities can be attributed to larger S_{max} of the occurring cloud regimes (mostly St_{high} and Cu_{med}) which primarily depend on the prevailing meteorological conditions. The same is valid for stratocumulus regions off the west coast of North & South America.

The regime-based CDNC sensitivity to CCN changes from the parameterization is presented for each of the updraft experiments in Figure 4.17, bottom panel. For comparison, also the sensitivity from MACC CDNC to MODIS AOD instead of CCN is shown (top panel). The colored symbols along the abscissa represent the updraft experiments. They are shown next to each other for each cloud regime. The colors of the boxes representing the sensitivity and the associated uncertainty for each regime indicate the updraft width which is used in the activation parameterization within an experiment. For the categories "All_{st}" and "All_{Cu}" as well as for "All" and "All_{regime}" the colors are different from that in the color bar because they represent mixtures of regimes using different updraft distributions. Because uncertainties are very small ($0.96 < R < 0.98$) for the parameterized CDNC-CCN sensitivity (bottom panel), the uncertainty ranges are plotted with 10σ and 30σ , while for the CDNC-AOD sensitivity (top panel, with $0.4 < R < 0.48$) 2σ and 10σ are enough for illustration.

No matter if AOD or CCN is used, the general variations of the MACC-II CDNC sensitivity by regime and experiment in Figure 4.17 are very similar although the absolute values and uncertainties differ. The same could be seen from the comparison of Figure 4.14 and Figure 4.15, both using MODIS retrieved CDNC. This shows that the difference in MODIS CDNC and parameterized CDNC primarily determines the difference in the regime-based sensitivity distribution.

A feature that is found in most experiments is the higher CDNC sensitivity of cumuliform cloud regimes compared to stratiform regimes which confirms the results from observations for MODIS CDNC sensitivities found in Figure 4.14 and Figure 4.15. In this regard, observed sensitivities are best simulated using the assumption of increased updrafts in cumuliform cloud regimes as expressed in Experiment 2 and 3. Natural activation differences between stratiform and cumuliform regimes, using CCN, are apparently not enough to generate this difference as seen from Experiment 1 in the lower panel.

In agreement with previous studies in which higher sensitivities are found in clean marine regions, larger sensitivities are found for the low and medium-high cloud regimes which predominantly occur over oceans and show slightly lower CCN concentrations (see Figure B.6). This holds for the satellite retrievals as well as for parameterization Experiments 1 & 2. In Experiment 3, the sensitivities of high regimes are in between those of low and medium high ones, indicating that the updraft assumptions used here may be a little overestimated.

The consistent variation by cloud base height from Figure 4.14, which was already diminished in Figure 4.15 by introducing CCN instead of AOD, is now completely eliminated in the parameterization under the use of MACC-II CDNC.

As can be seen from Figure 4.17, not the low but the medium high cloud regimes now show the largest sensitivities throughout all experiments. It may be speculated here that this behavior found for MODIS CDNC sensitivities is not a real feature, but might be due to retrieval uncertainties of CDNC instead.

Furthermore, it is notable in Figure 4.17, that even in Experiment 3 the sensitivity of medium-level clouds is higher or levels with that of high clouds although the mean S_{max} of high clouds is larger. This might be due to the smaller CCN supply for medium high regimes as seen from Figure B.6. In this case, the cleaner environment seems to contribute more than

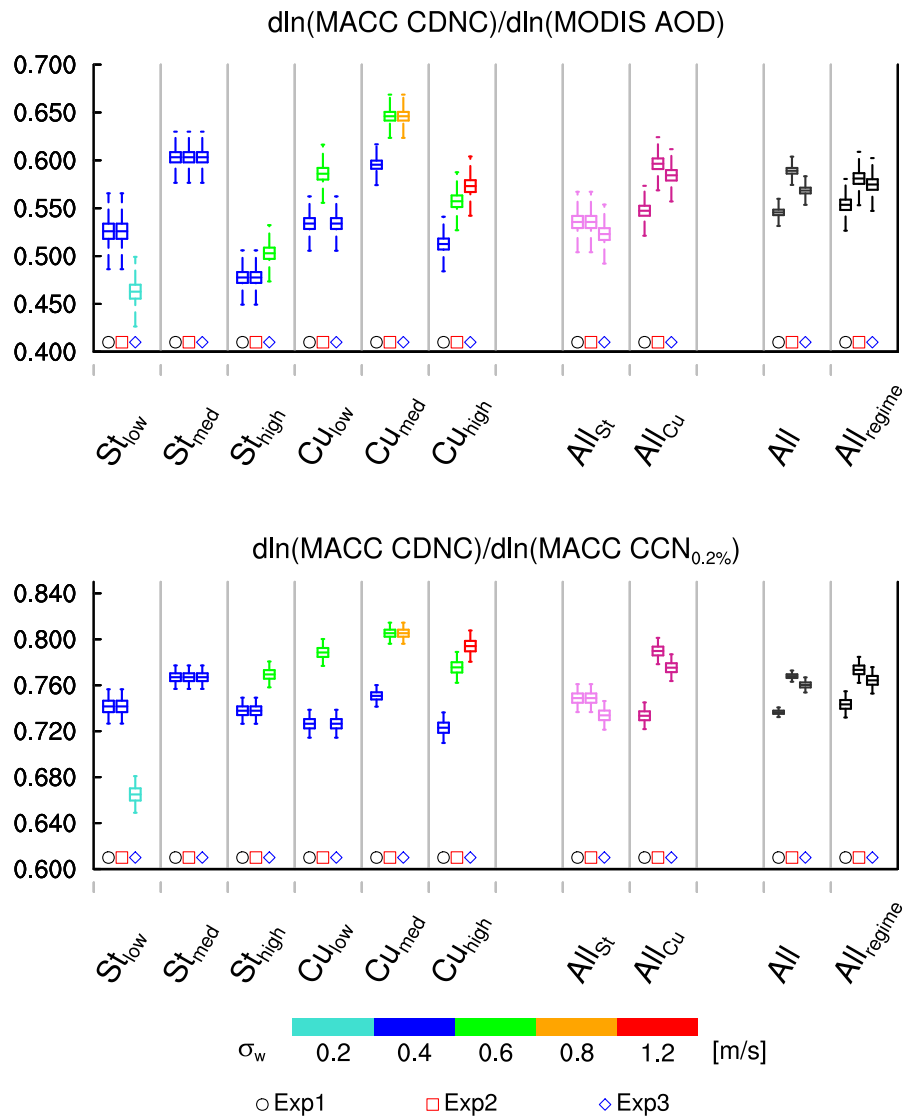


Figure 4.17: MACC CDNC sensitivity relative to changes in MODIS retrieved AOD (top), and changes in MACC CCN ($0.2\%S_{sat}$) (bottom). In the top panel the mean sensitivity, 2σ & 10σ are plotted. Correlation coefficients vary between 0.4 and 0.48. In the bottom panel the mean sensitivity, 10σ & 30σ are plotted. Here, correlation coefficients are all between 0.96 and 0.98. For a better overview the correlation coefficients are not shown here. Category “All” describes the average of all liquid filtered clouds found, while “ All_{regime} ” is the average of regime means weighted by the RFO of each regime. The red dots represent the correlation coefficients.

the contribution from S_{max} , and to use the concept from Reutter et al. (2009), they can be described as aerosol-limited regimes in an extended meaning.

As has been discussed before, changes of the updraft distributions changes not only the overall CDNC sensitivity compared to an estimate with homogeneous assumptions but also the variability. Therefore, to link back to the analysis on Figure 4.16, the overall variability between minimum and maximum averages of regime mean sensitivities can be quantified here. In Experiment 1 this is about 7% between regimes. In Experiment 2 the variability increases only slightly to 8% due to the distinction of stratiform and cumuliform clouds and can therefore be regarded as almost negligible. However, in Experiment 3 in which each regime is treated differently this variability increases to 19%. The differentiation by cloud base height therefore has the largest contribution to the CDNC-CCN sensitivity spread.

When averaging over cloud regimes, it can be seen that for all analyses shown here, the regime-weighted mean is slightly larger than the common arithmetic mean over all liquid filtered clouds regardless their regime. In this regard, the result agrees with the findings of Gryspeerd and Stier (2012) even though differences occur due to the choice of regimes. This shows that accounting for regimes gives an overall better estimate of global mean CDNC sensitivities.

4.5 Conclusions

In this chapter, a joint satellite-reanalysis approach is applied in order to improve assessments of CDNC sensitivities to aerosol perturbations.

The new approach combines the strength of multi-sensor satellite cloud retrievals from NASA's CCCM dataset (Kato et al., 2010) with advantages of the ECMWF MACC-II aerosol reanalysis providing a full coverage of meteorological and MODIS constrained aerosol products. The model data is co-localized to the CALIPSO track for each day (no nighttime data used) from January 2007 to December 2010 and all the data is filtered for selected ideal-case clouds, which are warm liquid water, single-layer and non-precipitating clouds in order to reduce retrieval uncertainties. These clouds are classified into six cloud regimes depending on height and heterogeneity using the new regime classification from Unglaub (2017) to account for cloud regime-based differences in CDNC sensitivities as suggested from Gryspeerd and Stier (2012). An aerosol activation parameterization (Abdul-Razzak and Ghan, 2000) is then applied to compute CDNC directly near the cloud base from these selected clouds in a set of experiments using systematically varied assumptions of the updraft distribution to account for a variety of S_{max} and activation efficiencies. The outcome is a regime-based distribution of CDNC which can primarily be described as functions of CCN supply and supersaturation. The CDNC sensitivity is determined from regressions over time and cloud regime to relative aerosol changes, may it be MODIS retrieved AOD or MACC-II computed CCN.

Extensive comparisons between results using the parameterized CDNC and results with the MODIS derived CDNC are done. Both of which underly uncertainties originating from various sources which are discussed - MODIS derived CDNC are therefore not taken as a reference for correctness of parameterized MACC-II CDNC. Instead, the results are discussed for their similarities and differences.

The results present an overall low relationship between MODIS AOD and MODIS CDNC ($R \approx 0.25$) with a sensitivity of about 0.3. This is in the range of previous assessments, the complicated data handling and filtering does not seem to give a significant improvement here. When using MACC CCN instead of MODIS AOD, the sensitivity is decreased to ~ 0.3 , however the uncertainty is reduced (increased $R \approx 0.3$) hinting to an improvement of using CCN over AOD. Using parameterized CDNC, on the basis of MACC CCN, and relate relative changes to changes in MODIS AOD however gives a significant improvement in sensitivity (~ 0.58) and uncertainty range ($R \approx 0.45$) showing that the bottom-up approach in the joint satellite-reanalysis framework is useful in improving ACI estimates. Finally, when using the full parameterized relation between MACC CCN and MACC CDNC, the overall (all regimes together) sensitivity is about 0.76 (with $R \approx 0.97$) which falls into the higher range of previous estimates and was so far not yet achieved by large-scale observations, not observationally constrained models.

The results show that in agreement with previous studies, larger sensitivities are found in regimes predominantly occurring over oceans - here, they correspond to low and medium high cloud regimes. This is found in both the observations as well as in the parameterizations. This feature is associated with a lower CCN supply and a good availability of water vapor necessary for activation. The sensitivities of these regimes can be regarded as CCN-limited, while the more polluted high regimes occurring mostly over land are more S_{max} -limited as they are characterized with many CCN fighting for available water vapor.

In contrast to findings of Gryspeerd and Stier (2012), stratiform clouds do not contribute most to the overall CDNC sensitivities. In this analysis, cumuliform clouds are found to have larger sensitivities in addition to larger RFOs, making them the dominant contributor over stratiform clouds in both the parameterization as well as in the observations. From the parameterization this can be explained by larger updrafts enhancing S_{max} and thus the activation efficiency. However, S_{max} cannot be detected from the observations. Here, lower CDNC for cumuliform clouds, which may result from retrieval uncertainties making these clouds artificially cleaner, cannot be ruled out as a possible reason for this behavior in the observed CDNC-AOD relationship. The robust feature of higher sensitivities for cumuliform regimes defends assumptions on increased updraft speeds or distribution widths made in the activation parameterization. Overall, this difference to the result from Gryspeerd and Stier (2012) does not infer that their result is incorrect. It may simply be due to the different choice of cloud regimes and the data handling.

A feature that is not robust and might be due to erroneous retrievals is the height-dependent sensitivity in the observations with the largest values in the low regimes. This changes when CCN is used instead of AOD and even more when parameterized CDNC are used for which medium high cloud regimes show the largest CDNC sensitivities. This indicates that this feature might not be a physical one, but rather occurs from retrieval uncertainties in CDNC. But since a validation of MACC CCN's vertical distribution is missing, it cannot be ruled out that this somehow contributes to the shifted height dependency. However, the larger sensitivities of the medium high clouds in the parameterization can be associated with the lowest CCN supply which seems more realistic. This seems to contribute more to the

overall sensitivity than variations in S_{max} do.

Comparing the impact of regime-based updraft distributions, it can be seen that a distinction by cloud base height contributes more to the regime-based variability than the distinction between stratiform and cumuliform cloud regimes characterized by cloud top heterogeneity. Independent from CCN concentrations and only due to the non-linearity of S_{max} with σ_w , regions of increased sensitivities may appear due to a regime-based differentiation which can also be seen in some observations. This includes for example the Northwest Pacific Ocean for which usually a higher CCN supply coming from China is made responsible for the enhanced sensitivity. However, as seen from the parameterization experiments, at least part of this sensitivity can be attributed to larger S_{max} of the occurring cloud regimes in this region. The same is valid for stratocumulus regions off the west coast of North & South America. This shows how important a correct description of S_{max} is for estimates of CDNC sensitivities.

The overall goal to improve assessments of CDNC sensitivities has been reached, because

1. the joint satellite-reanalysis approach has enabled us to overcome uncertainties from observations which has limited the accuracy of many previous studies,
2. the satellite retrievals themselves have been refined for the use in CDNC-AOD relationship studies by making use of several sensors which enhance possible uses of filtering criteria in order to increase the signal-to-noise ratio,
3. the MACC-II CCN could be used instead of AOD, which has been shown to not only give better agreements with in-situ observations (see Chapter 3), but also improve uncertainties in the CDNC sensitivity estimates,
4. the experimental activation parameterization has helped us to better understand the variability and dependency of CDNC sensitivities,
5. the CDNC sensitivity has been quantified for a set of liquid water cloud regimes which now gives us the opportunity to validate this with in-situ aircraft measurements.

A cloud regime based assesment of the cloud albedo effect

5.1 Abstract

Despite large efforts and decades of research, the level of scientific understanding of the impact of aerosols on climate is still low, and the huge spread on anthropogenic forcing estimates from aerosol-cloud-interactions has hampered the improvement of climate predictions.

In this study, the present-day radiative forcing due to anthropogenic aerosol-cloud-interactions (or simply the cloud albedo effect, RF_{aci}) is quantified on the basis of the parameterized MACC-II reanalysis cloud droplet number concentrations (CDNC) for regimes of liquid water clouds. The results are tested for its contributions from CDNC and anthropogenic fractions to better understand the variability of forcing estimates.

The resulting global-mean values of RF_{aci} vary around -0.32 Wm^{-2} and are situated in the lower range of previous RF_{aci} estimates. Stratiform clouds contribute most to this estimate with $\sim 61\%$, which is mostly due to its high cloud cover and liquid water path. In agreement with previous studies it has been found that macrophysical cloud properties contribute more to top-of-atmosphere short-wave fluxes and RF_{aci} than anthropogenic aerosol changes do.

Even though SW fluxes and radiative forcings are more sensitive to CDNC changes in regions of lower concentrations than in regions with higher CDNC, the variability of CDNC does not change the forcing estimates significantly. However, the variability of anthropogenic fraction increases the total RF_{aci} by 24% with differing contributions from cloud regimes, in comparison of global-mean fixed assumptions.

This analysis of the regime-based RF_{aci} represents the final conclusion of the bottom-up methodology applied throughout this thesis, improving our understanding of impacts from anthropogenic contributions on aerosol-cloud-radiation interactions.

5.2 Introduction

As already discussed in Chapter 1, the range of forcing estimates from indirect aerosol effects RF_{aci} , especially that from the cloud albedo forcing (Twomey, 1977), is very large but might play a crucial role for climate predictions Andreae et al. (2005).

The cloud albedo forcing (RF_{aci}) in Solomon et al. (2007) ranges between -0.3 and -1.8 Wm^{-2} with a best estimate of -0.7 Wm^{-2} . In Myhre et al. (2013) the RF_{aci} is not sep-

arately determined as adjustment effects are also considered. They give an estimate of the ERF_{aci} with a range between 0 and -1.2 Wm^{-2} with a best estimate of -0.45 Wm^{-2} which is smaller in total than the previous estimate from the cloud albedo forcing alone.

Some studies suggest higher estimates from observational constraints (Quaas et al., 2009b; Cherian et al., 2014), however Stevens (2015) argues that the upper end of the uncertainty range given by the IPCC is not consistent with historical temperature trends which may make a lower estimate more reasonable (Gryspeerd et al., 2016).

Studies using satellite observations give estimates of RF_{aci} as $-0.2 \pm 0.1 \text{ Wm}^{-2}$ (Quaas et al., 2008) or -0.42 Wm^{-2} (Lebsock et al., 2008). These studies depend on the strength of the AOD-CDNC relationship. However, Gryspeerd et al. (2016) shows that cloud fraction, which mostly determines the shortwave radiative effect (Goren and Rosenfeld, 2014), is also related to AOD via a mediation through CDNC. Thus, considering a linear regression of the AOD-CDNC-CF relationship an implied forcing of $-0.48 \pm 0.1 \text{ Wm}^{-2}$ with an uncertainty range from -0.1 to -0.64 Wm^{-2} is obtained.

Still, the uncertainty range remains large, and even qualitatively, no clear evidence for a change in cloud albedo due to anthropogenic aerosol changes is found from other studies which rely on cloud property and radiation observations as well as on model simulations. Ruckstuhl et al. (2008) for example did not find significant global dimming/brightening for cloudy skies in response to aerosols despite significant trends in clear skies. Quaas et al. (2009a) did not find evidence for a weekly cycle in cloud albedo over Europe despite significant cycle in aerosols. And Feng and Ramanathan (2010) found no evidence for a hemispherical gradient in cloud optical depth, although one was expected.

Generally models, and even better observationally constrained models, may give a more comprehensive picture on the cloud albedo forcing because A) the Twomey effect can be singled out from other effects contributing to increased cloud albedo and B) the impact of anthropogenic aerosols (PI to PD, or PD natural to anthropogenic) can be tested for their assumed change in distribution, species and amount.

Recent examples of constrained model approaches are the study of Bellouin et al. (2013) who estimated an global mean RF_{aci} of $-0.6 \pm 0.4 \text{ Wm}^{-2}$ by using the MACC-II reanalysis together with an estimate of PD anthropogenic AOD fraction. They state that the largest uncertainty in this estimate arises from the CDNC susceptibility to aerosol changes closely followed by uncertainties in the PD anthropogenic fraction estimates.

McCoy et al. (2017), who used a combination of MODIS cloud property retrievals and MERRA2 aerosols together with a preindustrial emissions model to obtain the anthropogenic change, retrieved an RF_{aci} by the isolated Twomey effect of about $-0.97 \pm 0.23 \text{ Wm}^{-2}$ relative to preindustrial times. Here, poor knowledge of the preindustrial aerosol concentration is regarded as the main uncertainty.

In fact, retrieving anthropogenic aerosol contributions is a huge effort. Ghan et al. (2016) use AeroCom model simulations to analyze the applicability of PD spatiotemporal variability of aerosol effects for estimating the radiative forcing from preindustrial to present-day.

They find that relationships from recent variability are poor constraints on relationships from anthropogenic change, and they point to the need of proxies connecting recent spatial and temporal variability to anthropogenic change. This agrees with the study of Penner et al. (2011) who pointed out that statistics sampled from present-day variability in AOD and CDNC may not be sufficient to sample the full difference between PI and PD conditions.

Quaas (2015) discussed approaches to isolate the impact of anthropogenic aerosol on clouds from natural cloud variability to estimate or constrain the effective forcing. They recommend ship track analyses or (modeled) intentional cloud modification for detailed process understanding while the analysis of weekly cycles and long-term trends is most promising to derive estimates or constraints on the effective radiative forcing. Analyses on the differences between the hemispheres or the use of trace gases appear to be of little use for studying the anthropogenic impact on RF_{aci} .

Here, the RF_{aci} should be quantified on the basis of the previous results written in Chapters 3 and 4, which provides a whole new perspective on disentangling various forcing contributions. The previously computed CDNC which were retrieved on the basis of the observationally constrained MACC-II reanalysis and satellite obtained cloud properties are now used in a radiation transfer code to compute RF_{aci} from CDNC changes to anthropogenic aerosol fractions alone keeping macrophysical cloud properties fixed. The anthropogenic aerosol fraction f_{anth} is obtained from Nicolas Bellouin on the basis of his study Bellouin et al. (2013), fitting to the MACC-II reanalysis. Thus, the forcing calculated here is only due to non-natural changes in the present-day era, and do not refer to pre-industrial pristine times. The resulting RF_{aci} will be discussed for its contribution by cloud regimes as well as for the variability of anthropogenic fractions and CDNC.

5.3 Data and Methods

For estimating the first indirect aerosol effect, or cloud albedo forcing RF_{aci} , the method of Bellouin et al. (2013) is used, writing

$$RF_{aci} = f_{cd,liq} \cdot F^\downarrow \cdot \frac{\partial \alpha}{\partial N_d} \cdot \frac{\partial N_d}{\partial \tau} \cdot (\ln \tau - \ln \tau_{nat}) \quad (5.1)$$

with

- $f_{cd,liq}$ being the liquid cloud cover fraction, which is regime dependent
- F^\downarrow being the incoming TOA irradiance (Wm^{-2}) for each measured CERES footprint, which is calculated from the latitude and day-of-year dependent mean irradiance, using the solar zenith angle for the Julian day of the year
- α being the broadband SW planetary albedo
- N_d being the MACC-II parameterized CDNC near cloud base estimated from the joint satellite-reanalysis approach, which are regime dependent
- τ and τ_{nat} being the total present-day AOD, and the natural estimated AOD respectively, the latter is derived from the total and anthropogenic AOD as in Bellouin et al. (2013).

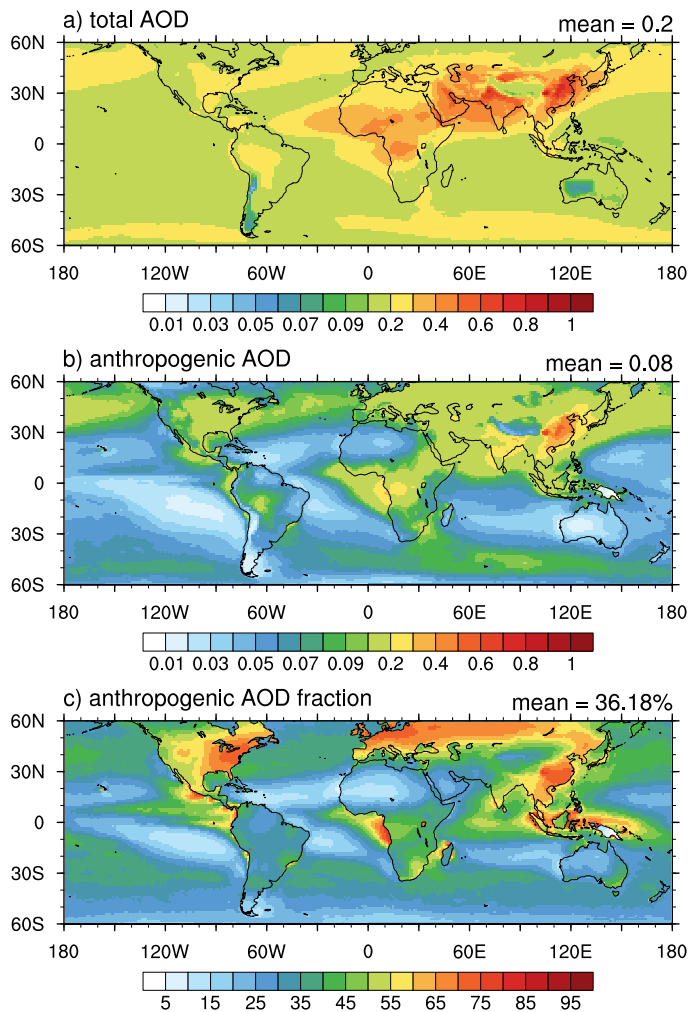


Figure 5.1: Anthropogenic AOD fraction (c), from the CAMS anthropogenic AOD product (Bellouin et al., 2013) derived from MACC-II total AOD (a) and estimated anthropogenic AOD (b), plotted on a $1.125^\circ \times 1.125^\circ$ grid using daily means from 2003 to 2012.

Modeled sources of extinction are water vapor, aerosols, carbon dioxide, oxygen, methane, ozone, nitrogen, and Rayleigh scattering. For further specifications, please see http://rtweb.aer.com/rrtm_frame.html.

Beside the regime-dependent MACC-II parameterized CDNC, other input parameters for the radiation scheme are the MACC-II reanalysis surface temperature, surface emissivity, surface albedo, atmospheric temperature and pressure profiles, cloud cover, cloud liquid and ice water mixing ratios q_l and q_i , specific humidity q , ozone mixing ratio q_{O_3} , and climatological global means of CO_2 , CH_4 , and N_2O mixing ratios. To compute partial derivatives, the radiation scheme is run with various regime-dependent MACC-II parameterized CDNC while all other parameters are kept fixed.

To calculate the radiative fluxes, a standalone radiative transfer code is used which is a version of the RRTM-G (Iacono et al., 2008; Mlawer et al., 1997) (GCM application of the Rapid Radiative Transfer Model) implementation in ECHAM6 (Stevens et al., 2013). The RRTM-G uses a two-stream algorithm for multiple scattering (Oreopoulos and Barker, 1999). Fluxes and heating rates can be calculated over fourteen contiguous bands in the shortwave and over sixteen bands in the longwave. Absorption coefficient data required for the k-distribution method used in the RRTM are obtained directly from the LBLRTM (Line-By-Line Radiative Transfer Model) which has been extensively validated with observations, principally at the ARM SGP site.

The last two terms in Equation 5.1 describing the change of CDNC to anthropogenic aerosol perturbations, could be replaced with the anthropogenic perturbation in CDNC itself which is calculated using the anthropogenic AOD fraction f_{anth} from the CAMS anthropogenic AOD product (Bellouin et al., 2013)

$$N_{d,\text{anth}} = f_{\text{anth}} N_d . \quad (5.2)$$

The anthropogenic fraction f_{anth} is derived from an algorithm (a modified version of Bellouin et al. (2008)) which uses aerosol size as a proxy for aerosol origin. It is applied by Bellouin et al. (2013) to identify mineral dust, anthropogenic and marine aerosols from the AOD and modeled FMF (fine-mode fraction, that is particles smaller than $0.5 \mu\text{m}$), using different approaches over ocean and over land. The result is a size-based proxy for the actual anthropogenic AOD in comparison to the AOD from natural occurring aerosols, both of which can hardly be actually measured. Bellouin et al. (2013) give a global mean anthropogenic AOD of 0.073 ± 0.013 over the period from 2003 to 2010, with relative standard deviation of 18% on a global average (16% over ocean, 23% over land) obtained from a Monte-Carlo uncertainty analysis.

Figure 5.1 shows the total AOD, anthropogenic AOD and the resulting anthropogenic fraction f_{anth} used in this study (and converted into CDNC anthropogenic fractions), for a time period from 2003 to 2012. As in (Bellouin et al., 2008), the distributions of f_{anth} (Figure 5.1, Panel c) reveal dominant anthropogenic industrial aerosols over North America, Europe and Asia. Larger anthropogenic fractions can also be seen near Central Africa, Central America and Indonesia which can be attributed to biomass-burning aerosols. Even the pollution outflow from North-West America and China, as well as the biomass-burning plume transported from Southern Africa can be detected by the algorithm. Uncertainties of the f_{anth} scale and distribution resulting from uncertainties in total AOD, assumed FMF and assumptions in the algorithm propagate onto estimates of anthropogenic CDNC.

Using the anthropogenic CDNC, the RF_{aci} can then be expressed in a more general form as

$$RF_{\text{aci}} = [F_{\text{SW}}(N_d, x) - F_{\text{SW}}(N_d - N_{d,\text{anth}}, x)] \cdot f_{\text{cld},\text{liq}} \quad (5.3)$$

with $F_{\text{SW}}(N_d, x)$ being the net TOA all-sky shortwave radiative flux calculated by the radiative transfer code based on CDNC and the remaining controlling variables x listed above. The difference between total and natural all-sky shortwave radiative flux is multiplied with the liquid cloud cover fraction $f_{\text{cld},\text{liq}}$ of the individual regimes. The total RF_{aci} is then the sum of the cloud regime dependent individual $RF_{\text{aci},\text{regime}}$.

The radiative transfer calculation is performed for each CERES footprint using the CDNC calculated for that footprint and the CAMS f_{anth} in the CAMS anthropogenic AOD product from a grid box at the time and location corresponding to the CERES footprint.

Prior to the flux calculation or thereafter, several further processing steps are applied to filter and scale the fluxes, such as the following:

- Even though within the radiation calculation the MACC-II cloud cover is used, in the post-processing the results are again filtered and scaled by the satellite retrieved liquid cloud cover $f_{cld,liq}$ of each regime (see Figure 5.2) in order to fulfill Equation 5.3. The mismatch between MACC-II cloud cover and satellite retrieved cloud cover could lead to a reduced sample size of radiative fluxes. However if this mismatch is evenly distributed between liquid and non-liquid clouds, that is there is a 50 % chance for MACC getting the observed cloud cover correctly in both cases, then the resulting error in RF_{aci} is almost negligible.
- No changes in CDNC are considered for ice, mixed-phase or multi-layer clouds as well as in clearsky regions found from the satellite retrievals. The radiative fluxes are set to zero in these cases.
- If no valid CDNC can be retrieved (e.g. because of lacking filtering criteria), the radiative flux perturbation is also defined as zero.
- In order to produce monthly-mean gridded results, the radiative flux in each CERES footprint must be corrected for the diurnal cycle in insolation. This is done by scaling the flux by the ratio $\cos Z/\overline{\cos Z}$, that is the cosine of the instantaneous zenith angle at CERES overpass and the diurnal mean of the cosine of the zenith angle at the location of the CERES footprint, respectively.

Applying these filtering criteria (please also see the filtering criteria given in Section 4.3.2), the resulting RF_{aci} is that due to liquid, single-layered, non-precipitating clouds only, given for the individual cloud regimes and for all regimes together.

To test the resulting RF_{aci} for its variability and contributions from different effects, 3 experimental setups are applied:

1. RF_{aci} is computed using globally constant values of CDNC and a fixed anthropogenic fraction
2. RF_{aci} is computed using a regime-based variable distribution of CDNC and a fixed anthropogenic fraction
3. RF_{aci} is computed using a regime-based variable distribution of CDNC and the full distribution of variable anthropogenic fractions

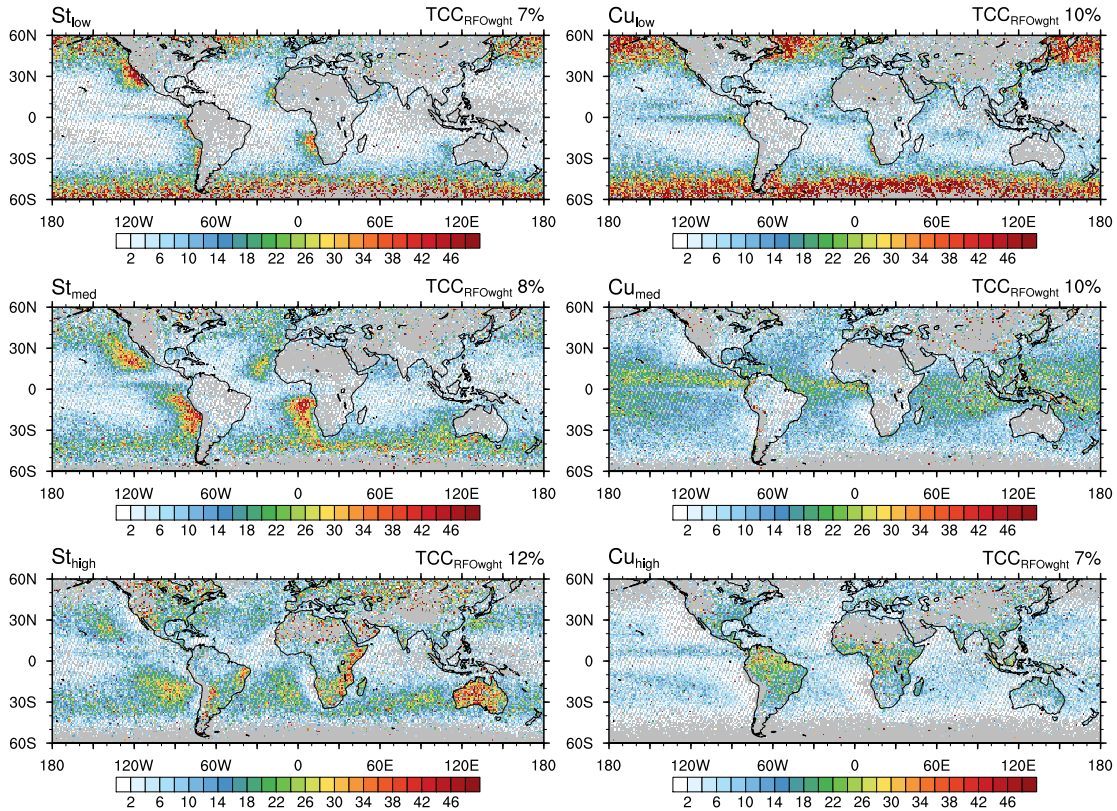


Figure 5.2: Regime-based total cloud cover, weighted by the regime RFO as shown in Figure 4.5. The mean value between 60S and 60N is written at the top of each panel. Their sum equals the total cloud cover of all filtered liquid clouds found (see Figure B.7, b).

5.4 Results and Discussions

5.4.1 Experimental setup 1: Constant CDNC and fixed anthropogenic fractions

To understand the variability of the anthropogenic cloud albedo effect, I first computed the RF_{aci} for globally constant values of CDNC and a fixed anthropogenic fraction of 36% corresponding to its global-mean value. Figure 5.3 shows the change of RF_{aci} and allsky net SW flux at TOA for four droplet concentrations representing global mean values. In both cases, the values decrease non-linearly with increasing CDNC - resulting in stronger SW fluxes and RF_{aci} for higher CDNC. Even though RF_{aci} is stronger with larger CDNC, its rate of change decreases clearly showing the buffering effect of clouds in polluted environments.

This implies that SW fluxes and radiative forcings are more sensitive to CDNC changes in regions of lower concentrations than in regions with higher CDNC. The change in total average RF_{aci} is very small ranging from -0.24 to $-0.28 Wm^{-2}$ for a respective range of CDNC between 50 and 200 droplets per cm^{-3} . The small difference of $-0.04 Wm^{-2}$ for a large change in CDNC of $150 cm^{-3}$ already hints to very small changes in regime-based RF_{aci} as the differences in CDNC are not as big.

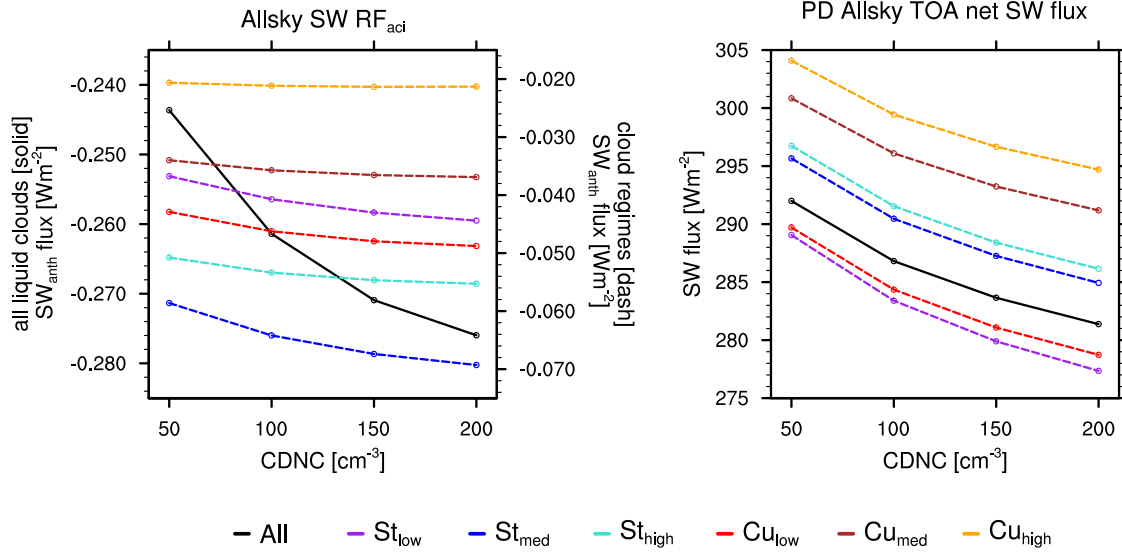


Figure 5.3: SW fluxes for globally fixed CDNC (CDNC = [50,100,150,200 cm^{-3}]) and anthropogenic fraction ($f_{anth} = 36\%$). The left panel shows the change in RF_{aci} for each regime (dashed, right scale) and for all liquid filtered clouds together (solid, left scale) which is the sum of the regime values. The right panel shows the change in PD allsky net SW flux at TOA, in which the flux for all liquid filtered clouds is the RFO weighted average of the regimes.

Since CDNC and f_{anth} are fixed, any variability in RF_{aci} can only result from the variability of macrophysical cloud properties used in the radiation scheme. When analyzing Figure 5.4, for which CDNC are set to 150 cm^{-3} in all cloud regimes (relating to the median value of parameterized CDNC in updraft Experiment 3), the occurring global distribution and regime-based variability is mainly dependent on the liquid cloud cover fractions $f_{cl,liq}$ and liquid water mixing ratios W . Comparing with Figure 5.2, it can be seen that the global distribution in each regime is following the pattern of the RFO-weighted cloud fractions, and areas with higher cloud fractions represent areas of larger RF_{aci} . This is reasonable, since anthropogenic CDNC are calculated based on existing CDNC, prohibiting new cloud formation by enhancing anthropogenic fractions.

In low and medium high stratiform cloud regimes, the RF_{aci} can locally go down to around -1 Wm^{-2} , and for all liquid filtered clouds the local RF_{aci} can decrease from around 0 to around -2.5 Wm^{-2} . The distribution gives the largest contribution from the St_{med} regime with $\sim 25\%$, followed by St_{high} with $\sim 20\%$, Cu_{low} with $\sim 18\%$, St_{low} with $\sim 16\%$, Cu_{med} with $\sim 13\%$ and finally Cu_{high} with $\sim 8\%$. The regimes with high RFO over oceans (low and medium high regimes) are contributing with $\sim 72\%$. But especially the Stratus decks on the west coast of North and South America as well as South Africa are peaking out - stratiform clouds contribute to RF_{aci} with $\sim 61\%$. This partitioning should remain throughout all conducted experiments which follow.

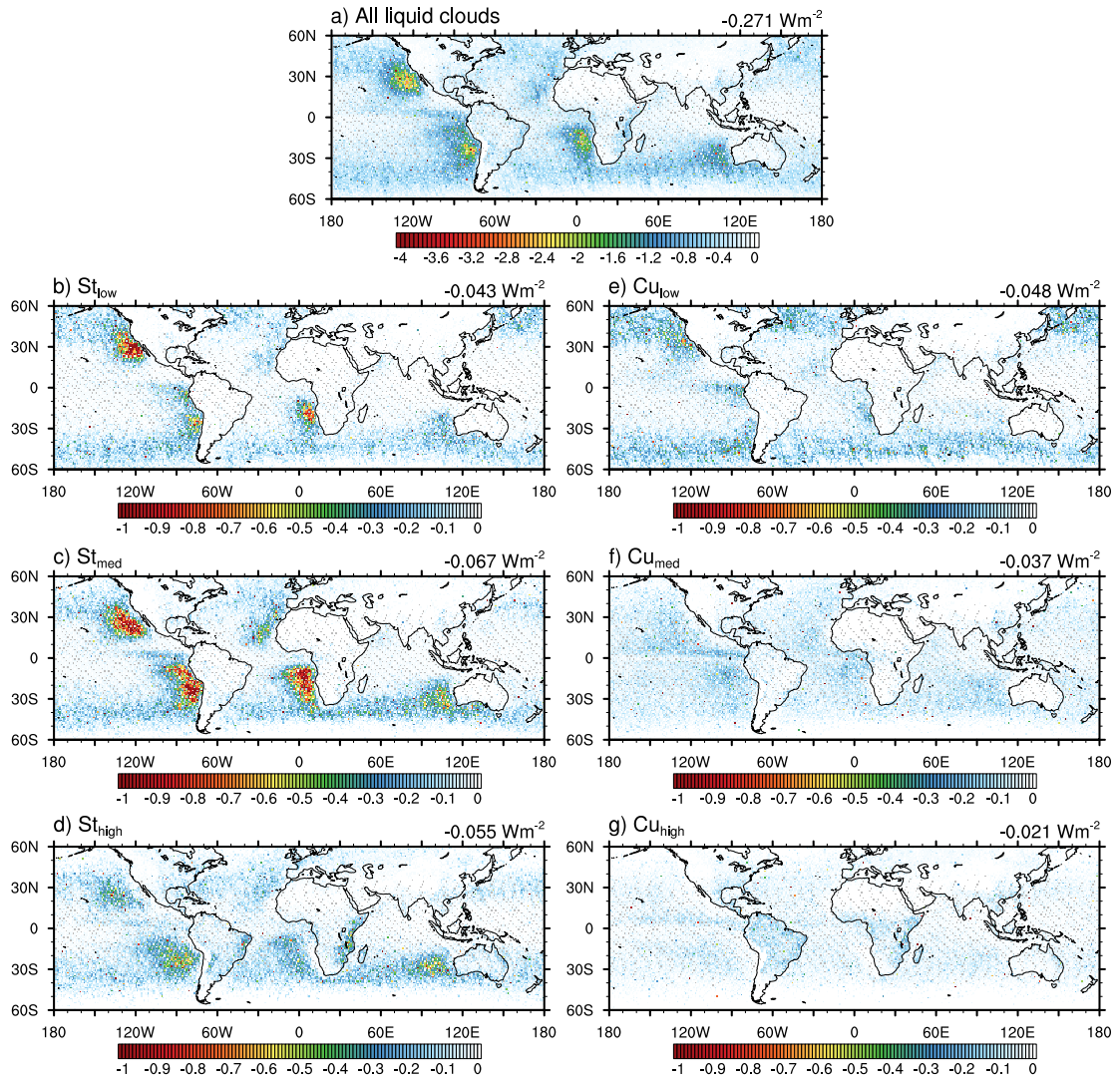


Figure 5.4: RF_{aci} for globally fixed CDNC and anthropogenic fraction ($CDNC = 150 \text{ cm}^{-3}$, $f_{anth} = 36\%$).

5.4.2 Experimental setup 2: Variable CDNC and fixed anthropogenic fractions

In a next step, the PD regime-based CDNC distribution as laid out in Chapter 4 (see Figure 4.12) is substituted for the globally fixed CDNC, while the anthropogenic fraction is kept at the mean value of 36%. As shown in Figure 5.5, the distribution pattern and contribution fractions of the individual regimes to the total liquid RF_{aci} do not change much relative to Figure 5.4. The variation in CDNC around its median value of $\sim 150 \text{ cm}^{-3}$ does not affect anthropogenic SW RF_{aci} , as could have been expected from Figure 5.3. This analysis shows once again, that not CDNC but cloud cover and liquid water path determine radiative fluxes.

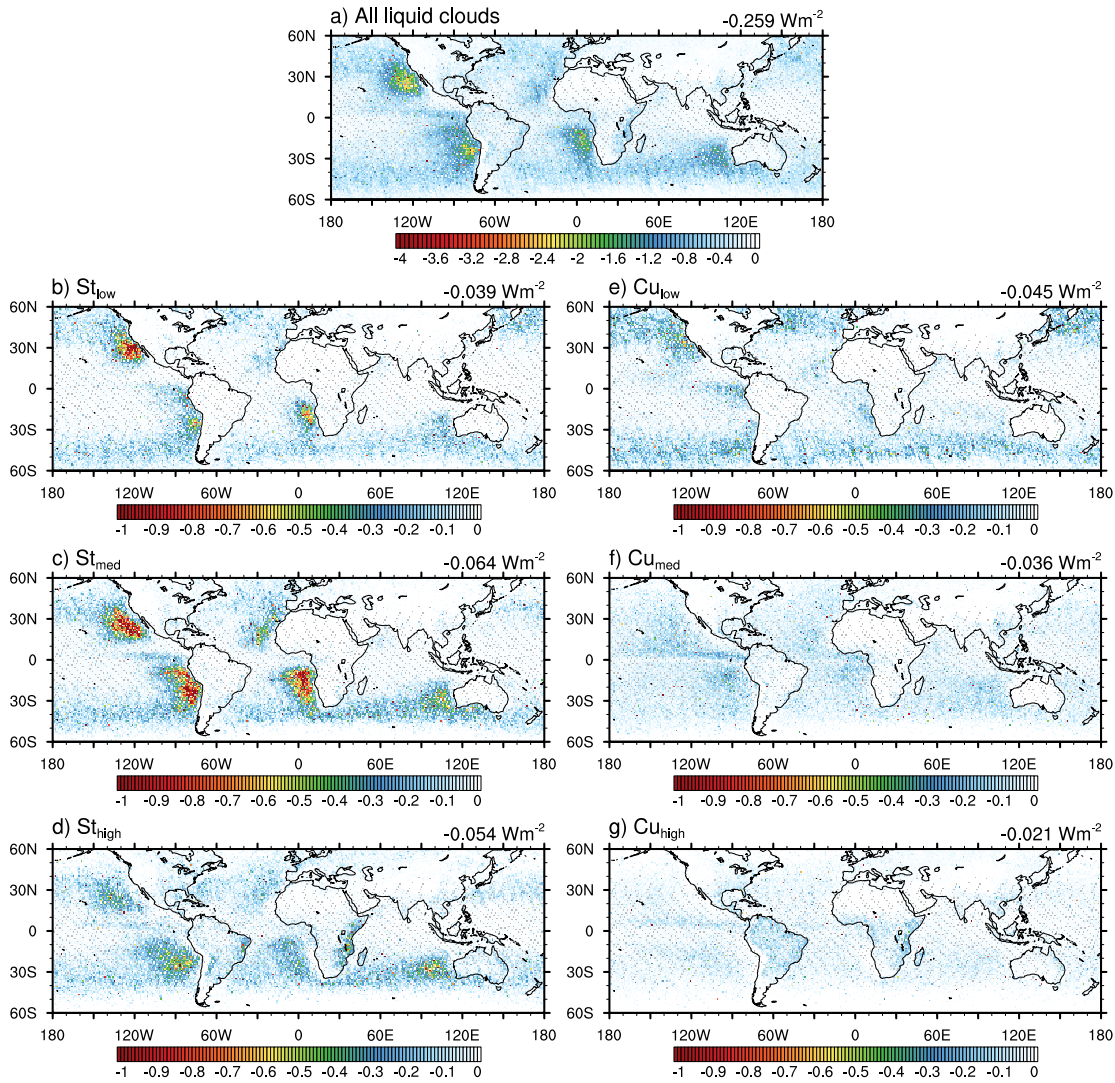


Figure 5.5: RF_{aci} for regime-based CDNC from Exp3 and fixed anthropogenic fraction ($f_{anth} = 36\%$). The Figures for Experiment 1 & 2 can be found in the Appendix, C, Section C.1.

5.4.3 Experimental setup 3: Variable CDNC and variable anthropogenic fractions

In the last step, together with the full PD CDNC distribution also the full distribution of anthropogenic fraction f_{anth} , as shown in Figure 5.1, is used to compute RF_{aci} . The result is presented in Figure 5.6. Here, it can be seen that the global pattern of RF_{aci} has changed in comparison to Figure 5.5, due to the influence of the f_{anth} distribution. The difference is more clearly presented in Figure 5.7 with negative values showing an increase in strength of the negative RF_{aci} .

The average values (Table 5.1) reveal that the total RF_{aci} strengthens by 24% independent of the updraft experiment. Generally the contribution from cumuliform regimes increase more (in absolute terms) than the contribution from stratiform regimes hinting to larger anthropogenic aerosol differences (compared to the mean value) in these regimes. The Cu_{low} regime strengthens the most by $\sim 30\%$, and the St_{med} strengthens the least with $\sim 17\%$.

As can be seen from Figure 5.7, there are regions with especially high RFO of stratiform clouds which oppose the overall RF_{aci} strengthening (shown by the positive values). Here, the variation of f_{anth} in comparison to the fixed mean value seems to weaken the RF_{aci} by reducing cloud albedo. This can only mean that anthropogenic perturbations are considered to be especially low (lower than 36 %) in these areas, making them the most pristine in this analysis.

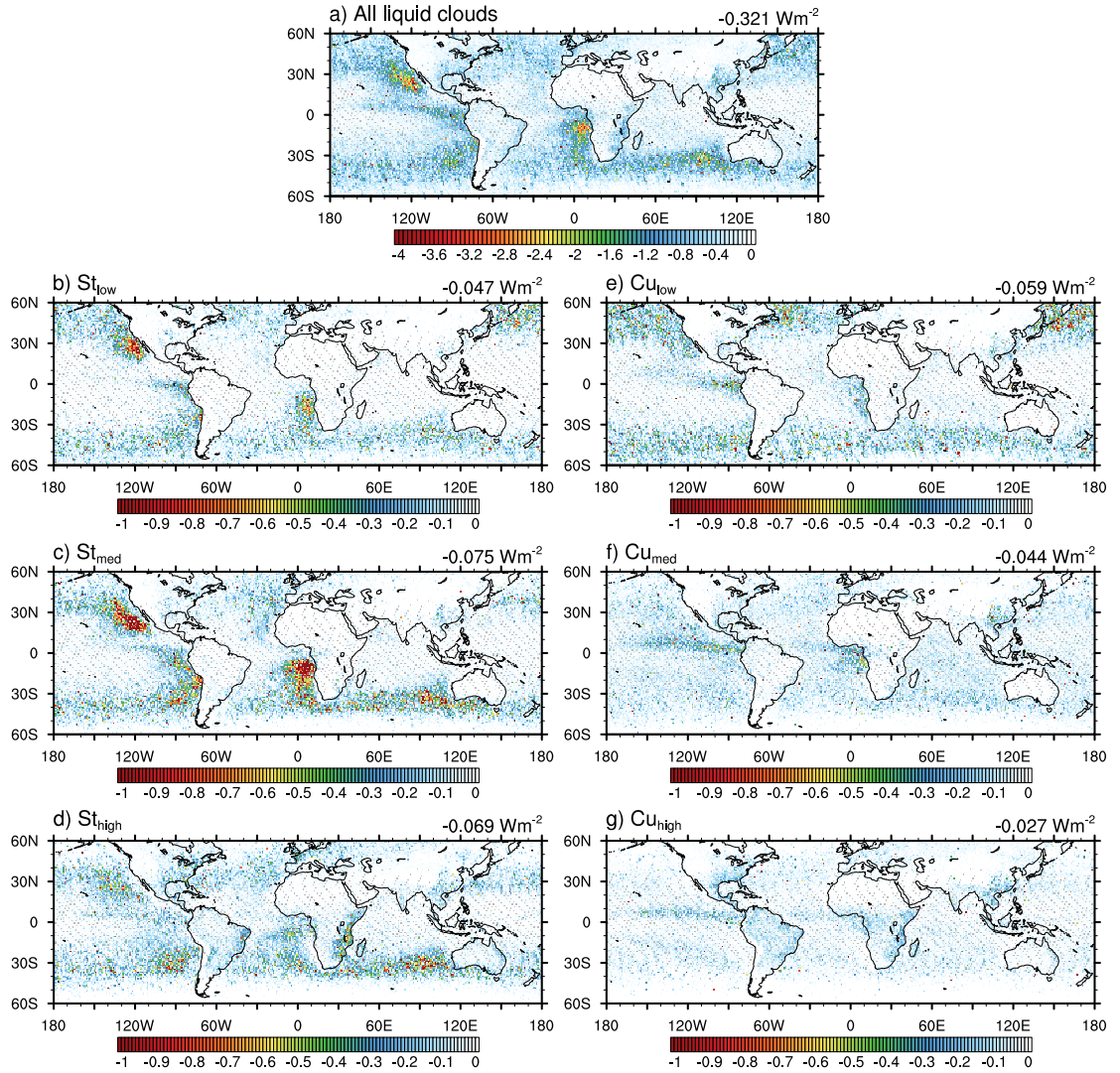


Figure 5.6: RF_{aci} for regime-based CDNC from Exp3 and full distribution of f_{anth} . The Figures for Exp1 and Exp2 can be found in the Appendix, C, Section C.2.

Now, with the full CDNC and f_{anth} distribution the cloud regimes contribute to the total liquid RF_{aci} of $-0.32 W m^{-2}$ in the following order: St_{med} with 23 %, St_{high} with 21 %, Cu_{low} with 18 %, St_{low} with 15 %, Cu_{med} with 13 % finally followed by Cu_{high} with 8 %. It is the same order as in Experiment 1 with constant CDNC of $150 cm^{-3}$ and fixed f_{anth} of 36 % - therefore most of the estimated RF_{aci} contributions can be attributed to contributions from the liquid cloud cover fractions and cloud water paths of each cloud regime. This agrees with results from Goren and Rosenfeld (2014).

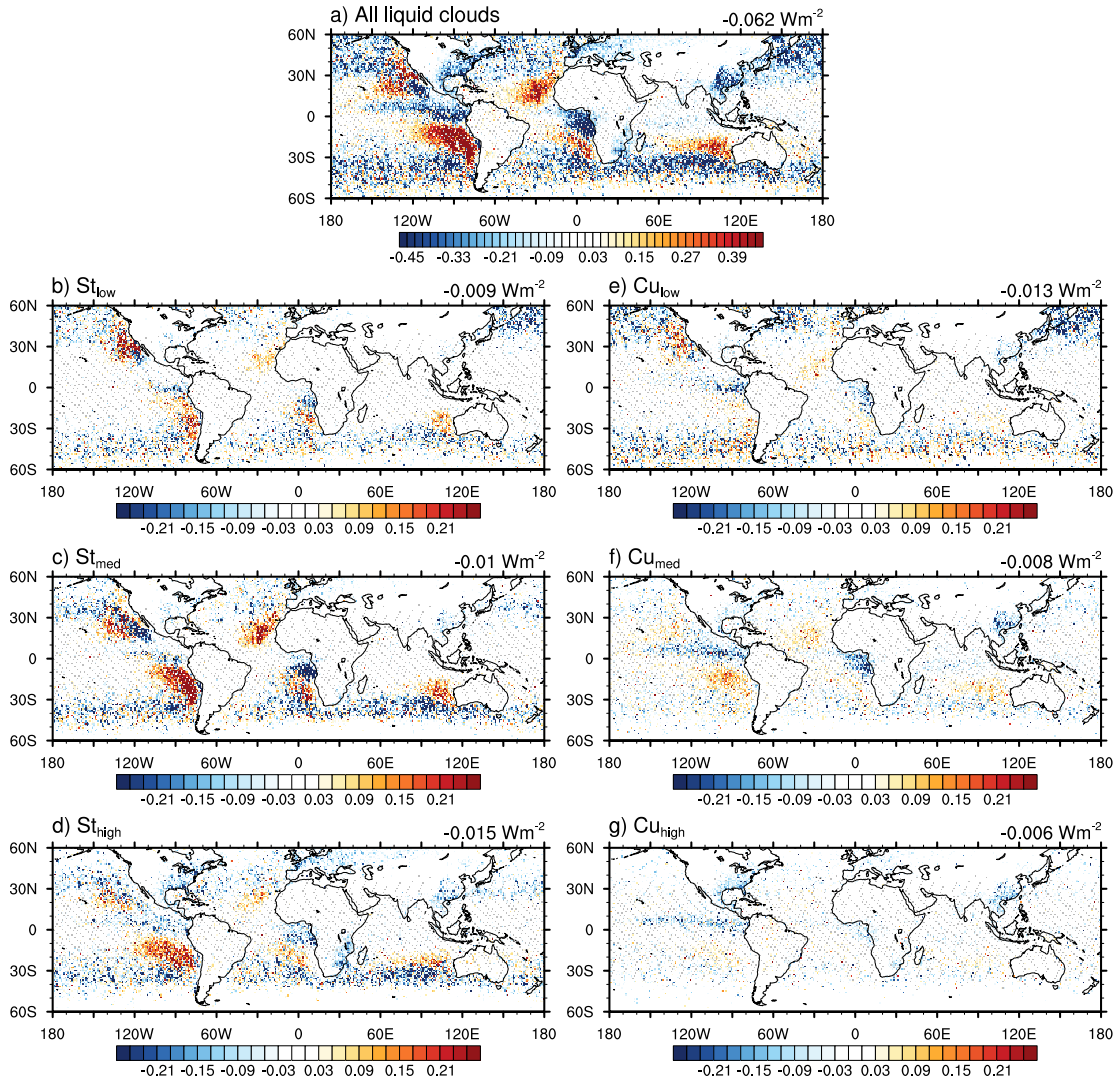


Figure 5.7: Difference of RF_{aci} from full to fixed anthropogenic fraction. Negative values show an increase in strength of the negative RF_{aci} . Positive values depict an weakening of the RF_{aci} .

Table 5.1: RF_{aci} in $W m^{-2}$ for each experiment and cloud regime, once for constant f_{anth} of 36% and once with the full f_{anth} distribution. The sum of the regimes is expressed in category “All”.

Regime	Exp1	Exp2	Exp3	Exp1	Exp2	Exp3
	RF _{aci} for constant f_{anth}			RF _{aci} for f_{anth} distribution		
St_{low}	-0.040	-0.040	-0.039	-0.050	-0.050	-0.047
St_{med}	-0.064	-0.064	-0.064	-0.075	-0.075	-0.075
St_{high}	-0.053	-0.053	-0.054	-0.068	-0.068	-0.069
Cu_{low}	-0.045	-0.046	-0.045	-0.059	-0.060	-0.059
Cu_{med}	-0.035	-0.036	-0.036	-0.043	-0.044	-0.044
Cu_{high}	-0.021	-0.021	-0.021	-0.027	-0.027	-0.027
<i>All_{regime}</i>	-0.260	-0.261	-0.259	-0.322	-0.324	-0.321

5.5 Conclusions

In this chapter the present-day cloud albedo forcing for regimes of liquid water clouds on the basis of the parameterized MACC-II reanalysis CDNC, which is derived and discussed in the previous chapter, is quantified and tested for its contributions from CDNC and anthropogenic fraction variability.

A radiative transfer calculation is performed to determine the anthropogenic perturbation to TOA SW radiative fluxes, under the use of different updraft experiments, cloud regimes and distributions of anthropogenic fractions f_{anth} . The anthropogenic CDNC fraction use here is assumed to equal the anthropogenic AOD fraction derived by Bellouin et al. (2013). Starting off by evaluating CCN from the MACC-II aerosol reanalysis, and calculating regime-based CDNC within a joint satellite-reanalysis approach, the analysis of the resulting regime-based RF_{aci} represents the final conclusion of this bottom-up methodology.

Global-mean values of RF_{aci} vary around -0.32 Wm^{-2} considering the full distribution of f_{anth} and CDNC. This results is situated in the lower range of previous RF_{aci} estimates. However, since only liquid water, single-layered and non-precipitating clouds are considered in the computation, indirect aerosol effects from other clouds can attribute to this number, increasing the overall forcing estimate.

Cloud regimes contribute differently to this estimate, again showing that a regime-based analysis is of great value for ACI studies. Stratiform clouds contribute most to RF_{aci} with $\sim 61\%$, which is mostly due to its high cloud cover and liquid water path. In agreement with findings of Goren and Rosenfeld (2014), this analysis clearly shows, that natural meteorological conditions and thus macrophysical cloud properties, such as cloud cover and liquid water path, contribute much more to TOA SW fluxes and RF_{aci} than anthropogenic aerosol changes would do.

This is underlined by testing the change in RF_{aci} when a variability of CDNC is applied in comparison to using fixed global-mean values in each regime. Even though SW fluxes and radiative forcings are more sensitive to CDNC changes in regions of lower concentrations than in regions with higher CDNC, the different CDNC concentrations in the 3 updraft experiments as well as the variability of CDNC around its median value are of little consequence for the forcing estimates.

However, the variability of anthropogenic fractions contributes more to the variability in RF_{aci} than regime-based differences of CDNC do. The assumed distribution of anthropogenic fraction enhances the CDNC distribution and therefore increases cloud albedo. The total RF_{aci} is increased by 24% by this effect. Cumuliform regimes are found to mostly contribute to this strengthening of the forcing hinting to larger anthropogenic aerosol differences (in comparison to using fixed mean values) in these regimes.

Concluding from this analysis, the goal of a better understanding of the variability of anthropogenic PD cloud albedo effects is achieved and the RF_{aci} could be quantified globally and from different liquid water cloud regimes.

Bibliography

- Abdul-Razzak, H. and Ghan, S. J.: A parameterization of aerosol activation: 2. Multiple aerosol types, *J. Geophys. Res.*, 105, 6837–6844, doi:10.1029/1999JD901161, 2000. (Cited on pages 57, 62, 64, 68, 88, and 138.)
- Abdul-Razzak, H., Ghan, S. J., and Rivera-Carpio, C.: A parameterization of aerosol activation: 1. Single aerosol type, *J. Geophys. Res.*, 103, 6123–6131, doi:10.1029/97JD03735, 1998. (Cited on pages 20, 34, 62, 63, 64, 138, and 139.)
- Ackerman, A. S., Toon, O. B., Taylor, J. P., Johnson, D. W., Hobbs, P. V., and Ferek, R. J.: Effects of Aerosols on Cloud Albedo: Evaluation of Twomey's Parameterization of Cloud Susceptibility Using Measurements of Ship Tracks, *J. Atmos. Sci.*, 57, 2684–2695, doi:10.1175/1520-0469(2000)057<2684:EOAOCA>2.0.CO;2, 2000. (Cited on page 5.)
- Ackerman, T. P. and Toon, O. B.: Absorption of visible radiation in atmosphere containing mixtures of absorbing and non-absorbing particles, *Appl. Opt.*, 20, 3661–3667, doi:10.1364/AO.20.003661, 1981. (Cited on page 28.)
- Albrecht, B. A.: Aerosols, Cloud Microphysics, and Fractional Cloudiness, *Science*, 245, 1227–1230, doi:10.1126/science.245.4923.1227, 1989. (Cited on page 4.)
- Anderson, T. L., Charlson, R. J., Schwartz, S. E., Knutti, R., Boucher, O., Rodhe, H., and Heintzenberg, J.: Climate Forcing by Aerosols - a Hazy Picture, *Science*, 300, 1103–1104, doi:10.1126/science.1084777, 2003. (Cited on page 6.)
- Andreae, M. and Rosenfeld, D.: Aerosol-cloud-precipitation interactions. Part 1. The nature and sources of cloud-active aerosols, *Earth-Sc. Rev.*, 89, 13–41, doi:10.1016/j.earscirev.2008.03.001, 2008. (Cited on page 11.)
- Andreae, M. O.: Correlation between cloud condensation nuclei concentration and aerosol optical thickness in remote and polluted regions, *Atmos. Chem. Phys.*, 9, 543–556, doi:10.5194/acp-9-543-2009, 2009. (Cited on pages 24 and 36.)
- Andreae, M. O., Jones, C. D., and Cox, P. M.: Strong present-day aerosol cooling implies a hot future, *Nature*, 435, 1187–1190, doi:http://dx.doi.org/10.1038/nature03671, 10.1038/nature03671, 2005. (Cited on pages 3 and 91.)
- Asmi, A., Wiedensohler, A., Laj, P., Fjaeraa, A.-M., Sellegri, K., Birmili, W., Weingartner, E., Baltensperger, U., Zdimal, V., Zikova, N., Putaud, J.-P., Marinoni, A., Tunved, P., Hansson, H.-C., Fiebig, M., Kivekäs, N., Lihavainen, H., Asmi, E., Ulevicius, V., Aalto, P. P., Swietlicki, E., Kristensson, A., Mihalopoulos, N., Kalivitis, N., Kalapov, I., Kiss, G., de Leeuw, G., Henzing, B., Harrison, R. M., Beddows, D., O'Dowd, C., Jennings, S. G., Flentje, H., Weinhold, K., Meinhardt, F., Ries, L., and Kulmala, M.: Number size distributions and seasonality of submicron particles in Europe 2008-2009, *Atmos. Chem. Phys.*, 11, 5505–5538, doi:10.5194/acp-11-5505-2011, 2011. (Cited on pages 9 and 24.)
- Bangert, M., Kottmeier, C., Vogel, B., and Vogel, H.: Regional scale effects of the aerosol cloud interaction simulated with an online coupled comprehensive chemistry model, *Atmos. Chem. Phys.*, 11, 4411–4423, doi:10.5194/acp-11-4411-2011, 2011. (Cited on page 62.)

- Barnes, W. L., Pagano, T. S., and Salomonson, V. V.: Prelaunch characteristics of the Moderate Resolution Imaging Spectroradiometer (MODIS) on EOS-AM1, *IEEE Transact. Geosci. Remote Sens.*, 36, 1088–1100, doi:10.1109/36.700993, 1998. (Cited on page 58.)
- Bellouin, N., Jones, A., Haywood, J., and Christopher, S. A.: Updated estimate of aerosol direct radiative forcing from satellite observations and comparison against the Hadley Centre climate model, *J. Geophys. Res.*, 113, doi:10.1029/2007JD009385, URL <http://dx.doi.org/10.1029/2007JD009385>, D10205, 2008. (Cited on page 95.)
- Bellouin, N., Rae, J., Jones, A., Johnson, C., Haywood, J., and Boucher, O.: Aerosol forcing in the Climate Model Intercomparison Project (CMIP5) simulations by HadGEM2-ES and the role of ammonium nitrate, *J. Geophys. Res.*, 116, doi:10.1029/2011JD016074, URL <http://dx.doi.org/10.1029/2011JD016074>, D20206, 2011. (Cited on page 5.)
- Bellouin, N., Quaas, J., Morcrette, J.-J., and Boucher, O.: Estimates of aerosol radiative forcing from the MACC re-analysis, *Atmos. Chem. Phys.*, 13, 2045–2062, doi:10.5194/acp-13-2045-2013, 2013. (Cited on pages 7, 24, 51, 56, 92, 93, 94, 95, and 103.)
- Benedetti, A., Morcrette, J.-J., Boucher, O., Dethof, A., Engelen, R. J., Fisher, M., Flen-tje, H., Huneeus, N., Jones, L., Kaiser, J. W., Kinne, S., Mangold, A., Razinger, M., Simmons, A. J., and Suttie, M.: Aerosol analysis and forecast in the European Centre for Medium-Range Weather Forecasts Integrated Forecast System: 2. Data assimilation, *J. Geophys. Res.*, 114, doi:10.1029/2008JD011115, D13205, 2009. (Cited on pages 25, 27, 28, 33, 43, and 57.)
- Bennartz, R.: Global assessment of marine boundary layer cloud droplet number concentration from satellite, *J. Geophys. Res.*, 112, doi:10.1029/2006JD007547, URL <http://dx.doi.org/10.1029/2006JD007547>, D02201, 2007. (Cited on pages 132 and 133.)
- Boers, R., Acarreta, J. R., and Gras, J. L.: Satellite monitoring of the first indirect aerosol effect: Retrieval of the droplet concentration of water clouds, *J. Geophys. Res.*, 111, doi:10.1029/2005JD006838, D22208, 2006. (Cited on pages 5 and 134.)
- Bony, S., Dufresne, J.-L., Treut, H. L., Morcrette, J.-J., and Senior, C.: On dynamic and thermodynamic components of cloud changes, *Clim. Dyn.*, 22, 71–86, doi:10.1007/s00382-003-0369-6, 2004. (Cited on page 65.)
- Boucher, O., Pham, M., and Venkataraman, C.: Simulation of the atmospheric sulfur cycle in the LMD GCM: Model description, model evaluation, and global and European budgets, *Inst. Pierre-Simon Laplace, Paris, France.*, Note 23, 26 pp., URL http://icmc.ipsl.fr/images/publications/scientific_notes/note23.pdf, 2002. (Cited on page 26.)
- Boucher, O., Randall, D., Artaxo, P., Bretherton, C., Feingold, G., Forster, P., Kermi-nen, V.-M., Kondo, Y., Liao, H., Lohmann, U., Rasch, P., Satheesh, S., Sherwood, S., Stevens, B., and Zhang, X.: Clouds and Aerosols, in: *Climate Change 2013: The Physical Science Basis. Contribution of Working Group I to the Fifth Assessment Report of the Intergovernmental Panel on Climate Change*, edited by Stocker, T., Qin, D., Plattner, G.-K., Tignor, M., Allen, S., Boschung, J., Nauels, A., Xia, Y., Bex, V., and Midgley, P., Cambridge University Press, Cambridge, United Kingdom and New York, NY, USA, doi:10.1017/CBO9781107415324.016, 2013. (Cited on pages 2, 3, 4, 11, 16, 17, 18, and 54.)

- Brenguier, J., Pawlowska, H., Schüller, L., Preusker, R., Fischer, J., and Y., F.: Radiative Properties of Boundary Layer Clouds: Droplet Effective Radius versus Number Concentration, *J. Atmos. Sci.*, 57, 803–821, doi:10.1175/1520-0469(2000)057<0803:RPOBLC>2.0.CO;2, 2000. (Cited on pages 70, 133, 134, and 135.)
- Brenguier, J.-L., Burnet, F., and Geoffroy, O.: Cloud optical thickness and liquid water path â does the k coefficient vary with droplet concentration?, *Atmos. Chem. Phys.*, 11, 9771–9786, doi:10.5194/acp-11-9771-2011, URL <https://www.atmos-chem-phys.net/11/9771/2011/>, 2011. (Cited on page 54.)
- Bretherton, C. S., Wood, R., George, R. C., Leon, D., Allen, G., and Zheng, X.: South-east Pacific stratocumulus clouds, precipitation and boundary layer structure sampled along 20° S during VOCALS-REx, *Atmos. Chem. Phys.*, 10, 639–10 654, doi:10.5194/acp-10-10639-2010, 2010. (Cited on page 69.)
- Cahalan, R. F., Ridgway, W., Wiscombe, W. J., Bell, T. L., and Snider, J. B.: The Albedo of Fractal Stratocumulus Clouds, *J. Atmos. Sci.*, 51, 2434–2455, doi:10.1175/1520-0469(1994)051<2434:TAOFSC>2.0.CO;2, URL [https://doi.org/10.1175/1520-0469\(1994\)051<2434:TAOFSC>2.0.CO;2](https://doi.org/10.1175/1520-0469(1994)051<2434:TAOFSC>2.0.CO;2), 1994. (Cited on page 78.)
- Carslaw, K. S., Lee, L. A., Reddington, C. L., Pringle, K. J., Rap, A., Forster, P. M., Mann, G. W., Spracklen, D. V., Woodhouse, M. T., Regayre, L. A., and Pierce, J. R.: Large contribution of natural aerosols to uncertainty in indirect forcing, *Nature*, 503, 67–71, doi:http://dx.doi.org/10.1038/nature12674, 2013. (Cited on page 6.)
- Chepfer, H., Bony, S., Winker, D., Cesana, G., Dufresne, J. L., Minnis, P., Stubenrauch, C. J., and Zeng, S.: The GCM-Oriented CALIPSO Cloud Product (CALIPSO-GOCCP), *J. Geophys. Res.*, 115, doi:10.1029/2009JD012251, D00H16, 2010. (Cited on page 65.)
- Cherian, R., Quaas, J., Salzmann, M., and Wild, M.: Pollution trends over Europe constrain global aerosol forcing as simulated by climate models, *Geophys. Res. Lett.*, 41, doi:10.1002/2013GL058715, URL <http://dx.doi.org/10.1002/2013GL058715>, 2014. (Cited on page 92.)
- Cho, H.-M., Zhang, Z., Meyer, K., Lebsock, M., Platnick, S., Ackerman, A. S., Di Girolamo, L., C-Labonnote, L., Cornet, C., Riedi, J., and Holz, R. E.: Frequency and causes of failed MODIS cloud property retrievals for liquid phase clouds over global oceans, *J. Geophys. Res.*, 120, 4132–4154, doi:10.1002/2015JD023161, URL <http://dx.doi.org/10.1002/2015JD023161>, 2015JD023161, 2015. (Cited on page 78.)
- Cohard, J., Pinty, J., and Bedos, C.: Extending Twomey’s Analytical Estimate of Nucleated Cloud Droplet Concentrations from CCN Spectra, *J. Atmos. Sci.*, pp. 3348–3357, doi:http://dx.doi.org/10.1175/1520-0469(1998)055<3348:ETS AEO>2.0.CO;2, 1998. (Cited on page 37.)
- Davies, T., Cullen, M. J. P., Malcolm, A. J., Mawson, M. H., Staniforth, A., White, A. A., and Wood, N.: A new dynamical core for the Met Office’s global and regional modelling of the atmosphere, *Quart. J. Royal Meteor. Soc.*, 131, 1759–1782, doi:10.1256/qj.04.101, 2005. (Cited on page 33.)

- de Roode, S. R. and Duynkerke, P. G.: Observed Lagrangian Transition of Stratocumulus into Cumulus during ASTEX: Mean State and Turbulence Structure, *J. Atmos. Sci.*, 54, 2157–2173, doi:10.1175/1520-0469(1997)054<2157:OLTOSI>2.0.CO;2, 1997. (Cited on pages 68 and 69.)
- Deng, M., Mace, G. G., Wang, Z., and Okamoto, H.: Tropical Composition, Cloud and Climate Coupling Experiment validation for cirrus cloud profiling retrieval using CloudSat radar and CALIPSO lidar, *J. Geophys. Res.*, 115, doi:10.1029/2009JD013104, D00J15, 2010. (Cited on page 17.)
- Dentener, F., Kinne, S., Bond, T., Boucher, O., Cofala, J., Generoso, S., Ginoux, P., Gong, S., Hoelzemann, J. J., Ito, A., Marelli, L., Penner, J. E., Putaud, J.-P., Textor, C., Schulz, M., van der Werf, G. R., and Wilson, J.: Emissions of primary aerosol and precursor gases in the years 2000 and 1750 prescribed data-sets for AeroCom, *Atmos. Chem. Phys.*, pp. 4321–4344, doi:10.5194/acp-6-4321-2006, 2006. (Cited on page 26.)
- Deuzé, J. L., Bréon, F. M., Devaux, C., Goloub, P., Herman, M., Lafrance, B., Maignan, F., Marchand, A., Nadal, F., Perry, G., and Tanré, D.: Remote sensing of aerosols over land surfaces from POLDER-ADEOS-1 polarized measurements, *J. Geophys. Res.*, 106, 4913–4926, doi:10.1029/2000JD900364, URL <http://dx.doi.org/10.1029/2000JD900364>, 2001. (Cited on page 137.)
- Ditas, F., Shaw, R. A., Siebert, H., Simmel, M., Wehner, B., and Wiedensohler, A.: Aerosols-cloud microphysics-thermodynamics-turbulence: evaluating supersaturation in a marine stratocumulus cloud, *Atmos. Chem. Phys.*, 12, 2459–2468, doi:10.5194/acp-12-2459-2012, 2012. (Cited on page 69.)
- Eck, T. F., Holben, B. N., Reid, J. S., Dubovik, O., Smirnov, A., O'Neill, N. T., Slutsker, I., and Kinne, S.: Wavelength dependence of the optical depth of biomass burning, urban, and desert dust aerosols, *J. Geophys. Res.*, 104, 31 333–31 349, doi:10.1029/1999JD900923, URL <http://dx.doi.org/10.1029/1999JD900923>, 1999. (Cited on page 137.)
- Eiseley, L. C.: The Flow of the River, *The American Scholar*, 22, 451–458, URL <http://www.jstor.org/stable/41207692>, 1953. (Cited on page 16.)
- Fan, J., Wang, Y., Rosenfeld, D., and Liu, X.: Review of Aerosol-Cloud Interactions: Mechanisms, Significance, and Challenges, *J. Atmos. Sci.*, 73, 4221–4252, doi:10.1175/JAS-D-16-0037.1, URL <https://doi.org/10.1175/JAS-D-16-0037.1>, 2016. (Cited on page 55.)
- Feingold, G., Eberhard, W. L., Veron, D. E., and Previdi, M.: First measurements of the Twomey indirect effect using ground-based remote sensors, *Geophys. Res. Lett.*, 30, doi:10.1029/2002GL016633, 1287, 2003. (Cited on pages 5, 54, and 71.)
- Feingold, G., McComiskey, A., Yamaguchi, ., Johnson, J., Carslaw, K., and Schmidt, K. S.: New approaches to quantifying aerosol influence on the cloud radiative effect, *Proc. Nat. Acad. Sci.*, 113, doi:10.1073/pnas.1514035112, 2016. (Cited on page 56.)
- Feng, Y. and Ramanathan, V.: Investigation of aerosol-cloud interactions using a chemical transport model constrained by satellite observations, *Tellus B*, 62, 69–86, doi:10.1111/j.1600-0889.2009.00444.x, 2010. (Cited on page 92.)

- Freud, E., Rosenfeld, D., and Kulkarni, J. R.: Resolving both entrainment-mixing and number of activated CCN in deep convective clouds, *Atmos. Chem. Phys.*, 11, 12 887–12 900, doi:10.5194/acp-11-12887-2011, 2011. (Cited on page 20.)
- Fridlind, A. M., Ackerman, A. S., McFarquhar, G., Zhang, G., Poellot, M. R., DeMott, P. J., Prenni, A. J., and Heymsfield, A. J.: Ice properties of single-layer stratocumulus during the Mixed-Phase Arctic Cloud Experiment: 2. Model results, *J. Geophys. Res.*, 112, doi:10.1029/2007JD008646, URL <http://dx.doi.org/10.1029/2007JD008646>, D24202, 2007. (Cited on page 71.)
- Ghan, S. J. and Schwartz, S. E.: Aerosol Properties and Processes: A Path from Field and Laboratory Measurements to Global Climate Models, *Bull. Amer. Meteor. Soc.*, pp. 1059–1083, doi:10.1175/BAMS-88-7-1059, 2007. (Cited on pages 9 and 10.)
- Ghan, S. J., Chuang, C. C., and Penner, J. E.: A parameterization of cloud droplet nucleation, I, single aerosol type, *Atmos. Res.*, pp. 197–221, doi:10.1016/0169-8095(93)90024-I, 1993. (Cited on pages 21, 35, and 64.)
- Ghan, S. J., Abdul-Razzak, H., Nenes, A., Ming, Y., Liu, X., Ovchinnikov, M., Shipway, B., Meskhidze, N., Xu, J., and Shi, X.: Droplet nucleation: Physically-based parameterizations and comparative evaluation, *J. Adv. Model. Earth Systems*, 3, doi:10.1029/2011MS000074, M10001, 2011. (Cited on pages 62, 63, 64, and 138.)
- Ghan, S. J., Wang, M., Zhang, S., Ferrachate, S., Gettelman, A., Griesfeller, J., Kipling, Z., Lohmann, U., Morrison, H., Neubauer, D., Partridge, D. G., Stier, P., Takemura, T., Wang, H., and Zhang, K.: Challenges in constraining anthropogenic aerosol effects on cloud radiative forcing using present-day spatiotemporal variability, *Proc. Nat. Acad. Sci.*, 113, doi:10.1073/pnas.1514036113, 2016. (Cited on page 92.)
- Ghate, V. P., Albrecht, B. A., and Kollias, P.: Vertical velocity structure of nonprecipitating continental boundary layer stratocumulus clouds, *J. Geophys. Res.*, 115, doi:10.1029/2009JD013091, D13204, 2010. (Cited on page 69.)
- Goren, T. and Rosenfeld, D.: Decomposing aerosol cloud radiative effects into cloud cover, liquid water path and Twomey components in marine stratocumulus, *Atmos. Res.*, 138, 378–393, doi:10.1016/j.atmosres.2013.12.008, URL <http://www.sciencedirect.com/science/article/pii/S0169809513003578>, 2014. (Cited on pages 92, 101, and 103.)
- Grandey, B. S. and Stier, P.: A critical look at spatial scale choices in satellite-based aerosol indirect effect studies, *Atmos. Chem. Phys.*, 10, 11 459–11 470, doi:10.5194/acp-10-11459-2010, 2010. (Cited on pages 5, 24, 55, 81, and 82.)
- Grosvenor, D. P. and Wood, R.: The effect of solar zenith angle on MODIS cloud optical and microphysical retrievals within marine liquid water clouds, *Atmos. Chem. Phys.*, 14, 7291–7321, doi:10.5194/acp-14-7291-2014, URL <http://www.atmos-chem-phys.net/14/7291/2014/>, 2014. (Cited on pages 70 and 134.)
- Gryspeerdt, E. and Stier, P.: Regime-based analysis of aerosol-cloud interactions, *Geophys. Res. Lett.*, 39, doi:10.1029/2012GL053221, L21802, 2012. (Cited on pages 24, 51, 55, 65, 71, 81, 82, 83, 88, and 89.)

- Gryspeerdt, E., Quaas, J., and Bellouin, N.: Constraining the aerosol influence on cloud fraction, *J. Geophys. Res.*, 121, 3566–3583, doi:10.1002/2015JD023744, URL <http://dx.doi.org/10.1002/2015JD023744>, 2015JD023744, 2016. (Cited on pages 5, 71, and 92.)
- Guibert, S., Snider, J. R., and Brenguier, J.-L.: Aerosol activation in marine stratocumulus clouds: 1. Measurement validation for a closure study, *J. Geophys. Res.*, 108, doi:10.1029/2002JD002678, 8628, 2003. (Cited on pages 69 and 75.)
- Gustafson, W. I., Chapman, E. G., Ghan, S. J., Easter, R. C., and Fast, J. D.: Impact on modeled cloud characteristics due to simplified treatment of uniform cloud condensation nuclei during NEAQS 2004, *Geophys. Res. Lett.*, 34, doi:10.1029/2007GL030021, L19809, 2007. (Cited on page 62.)
- Hand, J. L., Copeland, S. A., McDade, C. E., Day, D. E., Moore, C. T., Dillner, A. M., Pitchford, M. L., Indresand, H., Schichtel, B. A., Malm, W. C., and Watson, J. G.: IMPROVE (Interagency Monitoring of Protected Visual Environments): Spatial and seasonal patterns and temporal variability of haze and its constituents in the United States, Tech. rep., CIRA, 2011. (Cited on pages 31 and 32.)
- Hansen, J. and Travis, L.: Light scattering in planetary atmospheres, *Space Sci. Rev.*, 16, 527–610, doi:10.1007/BF00168069, 1974. (Cited on page 132.)
- Haynes, J. M., L’Ecuyer, T. S., Stephens, G. L., Miller, S. D., Mitrescu, C., Wood, N. B., and Tanelli, S.: Rainfall retrieval over the ocean with spaceborne W-band radar, *J. Geophys. Res.*, 114, doi:10.1029/2008JD009973, D00A22, 2009. (Cited on page 58.)
- Haywood, J. M., Osborne, S. R., and Abel, S. J.: The effect of overlying absorbing aerosol layers on remote sensing retrievals of cloud effective radius and cloud optical depth, 130, 779–800, doi:10.1256/qj.03.100, URL <http://dx.doi.org/10.1256/qj.03.100>, 2004. (Cited on page 71.)
- Heintzenberg, J.: Properties of the Log-Normal Particle Size Distribution, *Aerosol Sci. Tech.*, 21, 46–48, doi:10.1080/02786829408959695, 1994. (Cited on page 9.)
- Heintzenberg, J., Covert, D., and Dingenen, R.: Size distribution and chemical composition of marine aerosols: a compilation and review, *Tellus B*, 52, doi:10.1034/j.1600-0889.2000.00136.x, 2011. (Cited on page 9.)
- Hewitt, H. T., Copsey, D., Culverwell, I. D., Harris, C. M., Hill, R. S. R., Keen, A. B., McLaren, A. J., and Hunke, E. C.: Design and implementation of the infrastructure of HadGEM3: the next-generation Met Office climate modelling system, *Geosci. Model Develop.*, 4, 223–253, doi:10.5194/gmd-4-223-2011, 2011. (Cited on page 33.)
- Hinds, W. C.: *Aerosol Technology*, A Wiley-Interscience publication, second edn., ISBN:0-471-19410-7, 1998. (Cited on page 33.)
- Hogan, R. J., Grant, A. L. M., Illingworth, A. J., Pearson, G. N., and O’Connor, E. J.: Vertical velocity variance and skewness in clear and cloud-topped boundary layers as revealed by Doppler lidar, *Quart. J. Royal Meteor. Soc.*, 135, 635–643, doi:10.1002/qj.413, 2009. (Cited on pages 68 and 69.)

- Holben, B. N., Eck, T. F., and Fraser, R. S.: Temporal and spatial variability of aerosol optical depth in the Sahel region in relation to vegetation remote sensing, *Internat. J. Remote Sens.*, 12, 1147–1163, doi:10.1080/01431169108929719, URL <http://dx.doi.org/10.1080/01431169108929719>, 1991. (Cited on page 137.)
- Hoose, C., Kristjansson, J. E., Arabas, S., Boers, R., Pawlowska, H., Puygrenier, V., Siebert, H., and Thouron, O.: Parameterization of in-cloud vertical velocities for cloud droplet activation in coarse-grid models: Analysis of observations and cloud resolving model results, *Am. Meteorol. Soc.*, p. 5 pp, URL <http://ams.confex.com/ams/pdfpapers/170866.pdf>, 2010. (Cited on page 68.)
- Iacono, M. J., Delamere, J. S., Mlawer, E. J., Shephard, M. W., Clough, S. A., and Collins, W. D.: Radiative forcing by long-lived greenhouse gases: Calculations with the AER radiative transfer models, *J. Geophys. Res.*, 113, doi:10.1029/2008JD009944, D13103, 2008. (Cited on page 94.)
- Jakob, C., Tselioudis, G., and Hume, T.: The Radiative, Cloud, and Thermodynamic Properties of the Major Tropical Western Pacific Cloud Regimes, *J. Clim.*, 18, 1203–1215, doi:10.1175/JCLI3326.1, 2005. (Cited on page 65.)
- Kapustin, V. N., Clarke, A. D., Shinozuka, Y., Howell, S., Brekhovskikh, V., Nakajima, T., and Higurashi, A.: On the determination of a cloud condensation nuclei from satellite: Challenges and possibilities, *J. Geophys. Res.*, 111, doi:10.1029/2004JD005527, 2006. (Cited on pages 24 and 137.)
- Karydis, V. A., Kumar, P., Barahona, D., Sokolik, I. N., and Nenes, A.: On the effect of dust particles on global cloud condensation nuclei and cloud droplet number, *J. Geophys. Res.*, 116, doi:10.1029/2011JD016283, D23204, 2011. (Cited on page 46.)
- Kato, S., Sun-Mack, S., Miller, W. F., Rose, F. G., Chen, Y., Minnis, P., and Wielicki, B. A.: Relationships among cloud occurrence frequency, overlap, and effective thickness derived from CALIPSO and CloudSat merged cloud vertical profiles, *J. Geophys. Res.*, 115, doi:10.1029/2009JD012277, D00H28, 2010. (Cited on pages 57, 60, 66, and 88.)
- Kato, S., Rose, F. G., Sun-Mack, S., Miller, W. F., Chen, Y., Rutan, D. A., Stephens, G. L., Loeb, N. G., Minnis, P., Wielicki, B. A., Winker, D. M., Charlock, T. P., Stackhouse, P. W., Xu, K.-M., and Collins, W. D.: Improvements of top-of-atmosphere and surface irradiance computations with CALIPSO-, CloudSat-, and MODIS-derived cloud and aerosol properties, *J. Geophys. Res.*, 116, doi:10.1029/2011JD016050, D19209, 2011. (Cited on pages 57, 59, 60, and 66.)
- Kato, S., Miller, W. F., Sun-Mack, S., Rose, F. G., Chen, Y., and Mlynczak, P. E.: Variable Descriptions of the A-Train Integrated CALIPSO, CloudSat, CERES, and MODIS Merged Product (CCCM or C3M), Tech. rep., Atmospheric Science Data Center (ASDC) at NASA Langley Research Center, 2014. (Cited on page 60.)
- Kaufman, Y. J., Setzer, A., Ward, D., Tanre, D., Holben, B. N., Menzel, P., Pereira, M. C., and Rasmussen, R.: Biomass Burning Airborne and Spaceborne Experiment in the Amazonas (BASE-A), *J. Geophys. Res.*, 97, 14 581–14 599, doi:10.1029/92JD00275, URL <http://dx.doi.org/10.1029/92JD00275>, 1992. (Cited on page 137.)

- Kaufman, Y. J., Tanré, D., and Boucher, O.: A satellite view of aerosols in the climate system, *Nature*, 419, 215–223, doi:10.1038/nature01091, 2002. (Cited on pages 9 and 10.)
- Kaufman, Y. J., Koren, I., Remer, L. A., Tanré, D., Ginoux, P., and Fan, S.: Dust transport and deposition observed from the Terra-Moderate Resolution Imaging Spectroradiometer (MODIS) spacecraft over the Atlantic Ocean, *J. Geophys. Res.*, 110, doi:10.1029/2003JD004436, D10S12, 2005. (Cited on pages 24 and 51.)
- Khvorostyanov, V. I. and Curry, J. A.: Aerosol size spectra and CCN activity spectra: Reconciling the lognormal, algebraic, and power laws, *J. Geophys. Res.*, 111, doi:10.1029/2005JD006532, 2006. (Cited on pages 35 and 64.)
- Kim, B.-G., Klein, S. A., and Norris, J. R.: Continental liquid water cloud variability and its parameterization using Atmospheric Radiation Measurement data, *J. Geophys. Res.*, 110, doi:10.1029/2004JD005122, URL <http://dx.doi.org/10.1029/2004JD005122>, D15S08, 2005. (Cited on pages 70 and 134.)
- Kim, B.-G., Miller, M. A., Schwartz, S. E., Liu, Y., and Min, Q.: The role of adiabaticity in the aerosol first indirect effect, *J. Geophys. Res.*, 113, doi:10.1029/2007JD008961, D05210, 2008. (Cited on pages 70 and 134.)
- King, M. D., Kaufman, Y. J., Menzel, W. P., and Tanré, D.: Remote sensing of cloud, aerosol and water vapor properties from the Moderate Resolution Imaging Spectrometer (MODIS), *IEEE Transact. Geosci. Remote Sens.*, 30, 2–27, doi:10.1109/36.124212, 1992. (Cited on pages 18 and 58.)
- King, M. D., Tsay, S., Platnick, S. E., Wang, M., and Liou, K.: Cloud Retrieval Algorithms for MODIS: Optical Thickness, Effective Particle Radius, and Thermodynamic Phase, Algorithm Theor. Basis Doc., URL http://modis.gsfc.nasa.gov/data/atbd/atbd_mod05.pdf, MOD06 - Cloud product, 1998. (Cited on pages 18 and 58.)
- King, M. D., Menzel, W. P., Kaufman, Y. J., Tanre, D., Gao, B.-C., Platnick, S., Ackerman, S. A., Remer, L. A., Pincus, R., and Hubanks, P. A.: Cloud and aerosol properties, precipitable water, and profiles of temperature and water vapor from MODIS, *IEEE Transact. Geosci. Remote Sens.*, 41, 442–458, doi:10.1109/TGRS.2002.808226, 2003. (Cited on page 58.)
- Kinne, S., O'Donnel, D., Stier, P., Kloster, S., Zhang, K., Schmidt, H., Rast, S., Giorgetta, M., Eck, T. F., and Stevens, B.: MAC-v1: A new global aerosol climatology for climate studies, *J. Adv. Model. Earth Systems*, 5, 704–740, doi:10.1002/jame.20035, 2013. (Cited on page 24.)
- Klein, S. A. and Hartmann, D. L.: The Seasonal Cycle of Low Stratiform Clouds, *J. Clim.*, 6, 1587–1606, doi:10.1175/1520-0442(1993)006<1587:TSCOLS>2.0.COand2, 1993. (Cited on page 65.)
- Köhler, H.: The nucleus in and the growth of hygroscopic droplets, doi:10.1039/TF9363201152, 1936. (Cited on pages 12, 33, and 62.)

- Kollias, P. and Albrecht, B.: Vertical Velocity Statistics in Fair-Weather Cumuli at the ARM TWP Nauru Climate Research Facility, *J. Clim.*, 23, 6590–6604, doi:10.1175/2010JCLI3449.1, 2010. (Cited on pages 68 and 69.)
- Koren, I., Kaufman, Y. J., Rosenfeld, D., Remer, L. A., and Rudich, Y.: Aerosol invigoration and restructuring of Atlantic convective clouds, *Geophys. Res. Lett.*, 32, doi:10.1029/2005GL023187, L14828, 2005. (Cited on page 4.)
- Koren, I., Dagan, G., and Altaratz, O.: From aerosol-limited to invigoration of warm convective clouds, *Science*, 344, 1143–1146, doi:10.1126/science.1252595, 2014. (Cited on page 24.)
- Lance, S., Medina, J., Smith, J., and Nenes, A.: Mapping the operation of the DMT continuous flow CCN counter, *Aerosol Sci. Tech.*, 40, 242–254, doi:10.1080/02786820500543290, 2006. (Cited on page 35.)
- Leitch, W., Strapp, J., Isaac, G., and Hudson, J.: Cloud droplet nucleation and cloud scavenging of aerosol sulphate in polluted atmospheres, *Tellus B*, 38, 328–344, doi:10.1111/j.1600-0889.1986.tb00258.x, 1986. (Cited on pages 20, 62, and 138.)
- Lebsock, M. D., Stephens, G. L., and Kummerow, C.: Multisensor satellite observations of aerosol effects on warm clouds, *J. Geophys. Res.*, 113, doi:10.1029/2008JD009876, URL <http://dx.doi.org/10.1029/2008JD009876>, D15205, 2008. (Cited on page 92.)
- L'Ecuyer, T. S. and Jiang, J. H.: Touring the atmosphere aboard the A-Train, *Physics Today*, 63, 36–41, doi:10.1063/1.3463626, 2010. (Cited on page 57.)
- Liu, J. and Li, Z.: Estimation of cloud condensation nuclei concentration from aerosol optical quantities: influential factors and uncertainties, *Atmos. Chem. Phys.*, 14, 471–483, doi:10.5194/acp-14-471-2014, 2014. (Cited on pages 24 and 137.)
- Loeb, N. G., Wielicki, B. A., Doelling, D. R., Smith, G. L., Keyes, D. F., Kato, S., Manalo-Smith, N., and Wong, T.: Toward Optimal Closure of the Earth's Top-of-Atmosphere Radiation Budget, *J. Clim.*, 22, 748–766, doi:10.1175/2008JCLI2637.1, 2009. (Cited on page 16.)
- Logan, T., Xi, B., and Dong, X.: Aerosol properties and their influences on marine boundary layer cloud condensation nuclei at the ARM mobile facility over the Azores, *J. Geophys. Res.*, 119, 4859–4872, doi:10.1002/2013JD021288, 2013JD021288, 2014. (Cited on page 46.)
- Lohmann, U.: A glaciation indirect aerosol effect caused by soot aerosols, *Geophys. Res. Lett.*, 29, doi:10.1029/2001GL014357, URL <http://dx.doi.org/10.1029/2001GL014357>, 2002. (Cited on page 4.)
- Lohmann, U., Quaas, J., Kinne, S., and Feichter, J.: Different Approaches for Constraining Global Climate Models of the Anthropogenic Indirect Aerosol Effect, *Bull. Amer. Meteor. Soc.*, 88, 243–249, doi:10.1175/BAMS-88-2-243, 2007. (Cited on page 56.)
- Lu, C., Liu, Y., Niu, S., Krueger, S., and Wagner, T.: Exploring parameterization for turbulent entrainment-mixing processes in clouds, *J. Geophys. Res.*, 118, doi:10.1029/2012JD018464, 2013. (Cited on page 20.)

- Lu, M.-L., Conant, W. C., Jonsson, H. H., Varutbangkul, V., Flagan, R. C., and Seinfeld, J. H.: The Marine Stratus/Stratocumulus Experiment (MASE): Aerosol-cloud relationships in marine stratocumulus, *J. Geophys. Res.*, 112, doi:10.1029/2006JD007985, D10209, 2007. (Cited on page 69.)
- Lu, M.-L., Sorooshian, A., Jonsson, H. H., Feingold, G., Flagan, R. C., and Seinfeld, J. H.: Marine stratocumulus aerosol-cloud relationships in the MASE-II experiment: Precipitation susceptibility in eastern Pacific marine stratocumulus, *J. Geophys. Res.*, 114, doi:10.1029/2009JD012774, D24203, 2009. (Cited on pages 69 and 75.)
- Luo, Y., Xu, K., Morrison, H., and McFarquhar, G.: Arctic Mixed-Phase Clouds Simulated by a Cloud-Resolving Model: Comparison with ARM Observations and Sensitivity to Microphysics Parameterizations, *J. Atmos. Sci.*, 65, 1285–1303, doi:10.1175/2007JAS2467.1, 2008. (Cited on page 62.)
- Mace, G. G., Zhang, Q., Vaughan, M., Marchand, R., Stephens, G., Trepte, C., and Winker, D.: A description of hydrometeor layer occurrence statistics derived from the first year of merged Cloudsat and CALIPSO data, *J. Geophys. Res.*, 114, doi:10.1029/2007JD009755, D00A26, 2009. (Cited on page 17.)
- Malavelle, F. F., Haywood, J. M., Field, P. R., Hill, A. A., Abel, S. J., Lock, A. P., Shipway, B. J., and McBeath, K.: A method to represent subgrid-scale updraft velocity in kilometer-scale models: Implication for aerosol activation, *J. Geophys. Res.*, 119, 4149–4173, doi:10.1002/2013JD021218, 2014. (Cited on page 68.)
- Malm, W. C., Sisler, J. F., Huffman, D., Eldred, R. A., and Cahill, T. A.: Spatial and seasonal trends in particle concentration and optical extinction in the United States, *J. Geophys. Res.*, 99, 1347–1370, doi:10.1029/93JD02916, 1994. (Cited on page 31.)
- Mangold, A., De Backer, H., De Paepe, B., Dewitte, S., Chiapello, I., Derimian, Y., Kacenenbogen, M., Léon, J.-F., Huneeus, N., Schulz, M., Ceburnis, D., O’Dowd, C., Flentje, H., Kinne, S., Benedetti, A., Morcrette, J.-J., and Boucher, O.: Aerosol analysis and forecast in the European Centre for Medium-Range Weather Forecasts Integrated Forecast System: 3. Evaluation by means of case studies, *J. Geophys. Res.*, 116, doi:10.1029/2010JD014864, D03302, 2011. (Cited on pages 28, 29, 30, 31, 43, 44, and 57.)
- Mann, G. W., Carslaw, K. S., Spracklen, D. V., Ridley, D. A., Manktelow, P. T., Chipperfield, M. P., Pickering, S. J., and Johnson, C. E.: Description and evaluation of GLOMAP-mode: a modal global aerosol microphysics model for the UKCA composition-climate model, 3, doi:10.5194/gmd-3-519-2010, 2010. (Cited on pages 31 and 33.)
- Mann, G. W., Carslaw, K. S., Ridley, D. A., Spracklen, D. V., Pringle, K. J., Merikanto, J., Korhonen, H., Schwarz, J. P., Lee, L. A., Manktelow, P. T., Woodhouse, M. T., Schmidt, A., Breider, T. J., Emmerson, K. M., Reddington, C. L., Chipperfield, M. P., and Pickering, S. J.: Intercomparison of modal and sectional aerosol microphysics representations within the same 3-D global chemical transport model, *Atmos. Chem. Phys.*, 12, doi:10.5194/acp-12-4449-2012, 2012. (Cited on page 31.)
- Marshak, A., Platnick, S., Varnai, T., Wen, G., and Cahalan, R. F.: Impact of three-dimensional radiative effects on satellite retrievals of cloud droplet sizes,

- J. Geophys. Res., 111, doi:10.1029/2005JD006686, URL <http://dx.doi.org/10.1029/2005JD006686>, D09207, 2006. (Cited on pages 70 and 78.)
- McComiskey, A. and Feingold, G.: The scale problem in quantifying aerosol indirect effects, *Atmos. Chem. Phys.*, 12, 1031–1049, doi:10.5194/acp-12-1031-2012, 2012. (Cited on pages 5, 54, and 71.)
- McCoy, D. T., Bender, F. A.-M., Mohrmann, J. K. C., Hartmann, D. L., Wood, R., and Grosvenor, D. P.: The global aerosol-cloud first indirect effect estimated using MODIS, MERRA, and AeroCom, *J. Geophys. Res.*, 122, doi:10.1002/2016JD026141, 2017. (Cited on pages 56 and 92.)
- Medeiros, B., Stevens, B., Held, I. M., Zhao, M., Williamson, D. L., Olson, J. G., and Bretherton, C. S.: Aquaplanets, Climate Sensitivity, and Low Clouds, *J. Clim.*, 21, 4974–4991, doi:10.1175/2008JCLI1995.1, 2008. (Cited on page 65.)
- Merk, D., Deneke, H., Pospichal, B., and Seifert, P.: Investigation of the adiabatic assumption for estimating cloud micro- and macrophysical properties from satellite and ground observations, *Atmos. Chem. Phys.*, 16, 933–952, doi:10.5194/acp-16-933-2016, 2016. (Cited on pages 70 and 134.)
- Meskhidze, N., Nenes, A., Conant, W. C., and Seinfeld, J. H.: Evaluation of a new cloud droplet activation parameterization with in situ data from CRYSTAL-FACE and CSTRIFE, *J. Geophys. Res.*, 110, doi:10.1029/2004JD005703, D16202, 2005. (Cited on pages 69 and 75.)
- Min, Q., Joseph, E., Lin, Y., Min, L., Yin, B., Daum, P. H., Kleinman, L. I., Wang, J., and Lee, Y. N.: Comparison of MODIS cloud microphysical properties with in-situ measurements over the Southeast Pacific, *Atmos. Chem. Phys.*, 12, doi:10.5194/acp-12-11261-2012, 2012. (Cited on page 134.)
- Minnis, P., Young, D. F., Sun-Mack, S., Heck, P. W., Doelling, D. R., and Trepte, Q. Z.: CERES cloud property retrievals from imagers on TRMM, Terra, and Aqua, *Proc. SPIE*, 5235, doi:10.1117/12.511210, 2004. (Cited on pages 58 and 71.)
- Mlawer, E. J., Taubman, S. J., Brown, P. D., Iacono, M. J., and Clough, S. A.: RRTM, a validated correlated-k model for the longwave, *J. Geophys. Res.*, 102, 16 663–16 682, doi:10.1029/97JD00237, 1997. (Cited on page 94.)
- Morcrette, J.-J., Boucher, O., Jones, L., Salmond, D., Bechtold, P., Beljaars, A., Benedetti, A., Bonet, A., Kaiser, J. W., Razinger, M., Schulz, M., Serrar, S., Simmons, A. J., Sofiev, M., Suttie, M., Tompkins, A. M., and Untch, A.: Aerosol analysis and forecast in the European Centre for Medium-Range Weather Forecasts Integrated Forecast System: Forward modeling, *J. Geophys. Res.*, 114, doi:10.1029/2008JD011235, D06206, 2009. (Cited on pages 25, 26, 27, 28, and 56.)
- Morrison, H. and Gettelman, A.: A New Two-Moment Bulk Stratiform Cloud Microphysics Scheme in the Community Atmosphere Model, Version 3 (CAM3). Part I: Description and Numerical Tests, *J. Clim.*, 21, 3642–3659, doi:10.1175/2008JCLI2105.1, 2008. (Cited on page 62.)

- Mülmenstädt, J., Sourdeval, O., Delanoë, J., and Quaas, J.: Frequency of occurrence of rain from liquid-, mixed-, and ice-phase clouds derived from A-Train satellite retrievals, *Geophys. Res. Lett.*, 42, doi:10.1002/2015GL064604, 2015GL064604, 2015. (Cited on page 18.)
- Myhre, G., Shindell, D., Bréon, F.-M., Collins, W., Fuglestvedt, J., Huang, J., Koch, D., Lamarque, J.-F., Lee, D., Mendoza, B., Nakajima, T., Robock, A., Stephens, G., Takemura, T., and Zhang, H.: Anthropogenic and Natural Radiative Forcing, in: *Climate Change 2013: The Physical Science Basis. Contribution of Working Group I to the Fifth Assessment Report of the Intergovernmental Panel on Climate Change*, edited by Stocker, T., Qin, D., Plattner, G.-K., Tignor, M., Allen, S., Boschung, J., Nauels, A., Xia, Y., Bex, V., and Midgley, P., Cambridge University Press, Cambridge, United Kingdom and New York, NY, USA, 2013. (Cited on pages 1, 3, 23, 54, and 91.)
- Nakajima, T. and King, M. D.: Determination of the Optical Thickness and Effective Particle Radius of Clouds from Reflected Solar Radiation Measurements. Part I: Theory, *J. Atmos. Sci.*, 47, 1878–1893, doi:10.1175/1520-0469(1990)047<1878:DOTOTA>2.0.CO;2, URL [https://doi.org/10.1175/1520-0469\(1990\)047<1878:DOTOTA>2.0.CO;2](https://doi.org/10.1175/1520-0469(1990)047<1878:DOTOTA>2.0.CO;2), 1990. (Cited on pages 71, 131, and 132.)
- Nakajima, T., Higurashi, A., Kawamoto, K., and Penner, J. E.: A possible correlation between satellite-derived cloud and aerosol microphysical parameters, *Geophys. Res. Lett.*, 28, 1171–1174, doi:10.1029/2000GL012186, 2001. (Cited on pages 24 and 137.)
- Nam, C. and Quaas, J.: Geographically versus dynamically defined boundary layer cloud regimes and their use to evaluate general circulation model cloud parameterizations, *Geophys. Res. Lett.*, 40, 4951–4956, doi:10.1002/grl.50945, 2013. (Cited on page 65.)
- O'Connor, F. M., Johnson, C. E., Morgenstern, O., Abraham, N. L., Braesicke, P., Dalvi, M., Folberth, G. A., Sanderson, M. G., Telford, P. J., Voulgarakis, A., Young, P. J., Zeng, G., Collins, W. J., and Pyle, J. A.: Evaluation of the new UKCA climate-composition model - Part 2: The Troposphere, *Geosci. Model Develop.*, 7, 41–91, doi:10.5194/gmd-7-41-2014, 2014. (Cited on page 33.)
- O'Dell, C. W., Wentz, F. J., and Bennartz, R.: Cloud Liquid Water Path from Satellite-Based Passive Microwave Observations: A New Climatology over the Global Oceans, *J. Clim.*, 21, 172–1739, doi:10.1175/2007JCLI1958.1, 2008. (Cited on page 17.)
- Oreopoulos, L. and Barker, H. W.: Accounting for subgrid-scale cloud variability in a multi-layer 1d solar radiative transfer algorithm, *Quart. J. Royal Meteor. Soc.*, 125, 301–330, doi:10.1002/qj.49712555316, URL <http://dx.doi.org/10.1002/qj.49712555316>, 1999. (Cited on page 94.)
- Oreopoulos, L., Cahalan, R. F., and Platnick, S.: The Plane-Parallel Albedo Bias of Liquid Clouds from MODIS Observations, *J. Clim.*, 20, 5114–5125, doi:10.1175/JCLI4305.1, URL <https://doi.org/10.1175/JCLI4305.1>, 2007. (Cited on page 78.)
- Oreopoulos, L., Cho, N., Lee, D., Kato, S., and Huffman, G. J.: An examination of the nature of global MODIS cloud regimes, *J. Geophys. Res.*, 119, doi:10.1002/2013JD021409, 2013JD021409, 2014. (Cited on page 65.)

- Painemal, D. and Zuidema, P.: Assessment of MODIS cloud effective radius and optical thickness retrievals over the Southeast Pacific with VOCALS-REx in situ measurements, *J. Geophys. Res.*, 116, doi:10.1029/2011JD016155, URL <http://dx.doi.org/10.1029/2011JD016155>, D24206, 2011. (Cited on pages 71, 78, 133, and 134.)
- Paramonov, M., Kerminen, V.-M., Gysel, M., Aalto, P. P., Andreae, M. O., Asmi, E., Baltensperger, U., Bougiatioti, A., Brus, D., Frank, G. P., Good, N., Gunthe, S. S., Hao, L., Irwin, M., Jaatinen, A., Jurányi, Z., King, S. M., Kortelainen, A., Kristensson, A., Lihavainen, H., Kulmala, M., Lohmann, U., Martin, S. T., McFiggans, G., Mihalopoulos, N., Nenes, A., O'Dowd, C. D., Ovadnevaite, J., Petäjä, T., Pöschl, U., Roberts, G. C., Rose, D., Svenningsson, B., Swietlicki, E., Weingartner, E., Whitehead, J., Wiedensohler, A., Wittbom, C., and Sierau, B.: A synthesis of cloud condensation nuclei counter (CCNC) measurements within the EUCAARI network, *Atmos. Chem. Phys.*, 15, 12211–12229, doi:10.5194/acp-15-12211-2015, 2015. (Cited on page 25.)
- Peng, Y., Lohmann, U., and Leitch, R.: Importance of vertical velocity variations in the cloud droplet nucleation process of marine stratus clouds, *J. Geophys. Res.*, 110, doi:10.1029/2004JD004922, D21213, 2005. (Cited on page 69.)
- Penner, J., Xu, L., and Wang, M.: Satellite methods underestimate indirect climate forcing by aerosols, *Proc. Nat. Acad. Sci.*, 108, doi:10.1073/pnas.1018526108, 2011. (Cited on page 93.)
- Pincus, R. and Baker, M. B.: Effect of precipitation on the albedo susceptibility of clouds in the marine boundary layer, *Nature*, 372, 250–252, doi:10.1038/372250a0, 1994. (Cited on page 4.)
- Platnick, S.: Vertical photon transport in cloud remote sensing problems, *J. Geophys. Res.*, 105, 22919–22935, doi:10.1029/2000JD900333, 2000. (Cited on page 71.)
- Platnick, S. and Twomey, S.: Determining the Susceptibility of Cloud Albedo to Changes in Droplet Concentration with the Advanced Very High Resolution Radiometer, *J. Appl. Meteor.*, 33, 334–347, doi:10.1175/1520-0450(1994)033<0334:DTSOCA>2.0.CO;2, 1994. (Cited on page 5.)
- Platnick, S., King, M. D., Ackerman, S. A., Menzel, W. P., Baum, B. A., Riedi, J. C., and Frey, R. A.: The MODIS cloud products: algorithms and examples from Terra, *IEEE Transact. Geosci. Remote Sens.*, 41, 459–473, doi:10.1109/TGRS.2002.808301, 2003. (Cited on pages 58, 59, and 71.)
- Pruppacher, H. R. and Klett, J. D.: *Microphysics of Clouds and Precipitation*, Kluwer Academic Publishers, second edn., ISBN:0-7923-4409-X, 1997. (Cited on pages 10, 14, 19, 20, 33, 75, 138, and 139.)
- Putaud, J.-P., Raes, F., Van Dingenen, R., Brüggemann, E., Facchini, M.-C., Decesari, S., Fuzzi, S., Gehrig, R., Hüglin, C., Laj, P., Lorbeer, G., Maenhaut, W., Mihalopoulos, N., Müller, K., Querol, X., Rodriguez, S., Schneider, J., Spindler, G., Brink, H., Tørseth, K., and Wiedensohler, A.: A European aerosol phenomenology - 2: chemical characteristics of particulate matter at kerbside, urban, rural and background sites in Europe, *Atmos. Env.*, 38, 2579–2595, doi:10.1016/j.atmosenv.2004.01.041, 2004. (Cited on page 24.)

- Putaud, J.-P., Dingenen, R. V., Alastuey, A., Bauer, H., Birmili, W., Cyrys, J., Flentje, H., Fuzzi, S., Gehrig, R., Hansson, H., Harrison, R., Herrmann, H., Hitzenberger, R., Hüglin, C., Jones, A., Kasper-Giebl, A., Kiss, G., Koussa, A., Kuhlbusch, T., Löschau, G., Maenhaut, W., Molnar, A., Moreno, T., Pekkanen, J., Perrino, C., Pitz, M., Puxbaum, H., Querol, X., Rodriguez, S., Salma, I., Schwarz, J., Smolik, J., Schneider, J., Spindler, G., Brink, H., Tursic, J., Viana, M., Wiedensohler, A., and Raes, F.: A European aerosol phenomenology - 3: Physical and chemical characteristics of particulate matter from 60 rural, urban, and kerbside sites across Europe, *Atmos. Env.*, 44, 1308–1320, doi:10.1016/j.atmosenv.2009.12.011, 2010. (Cited on page 24.)
- Quaas, J.: Approaches to Observe Anthropogenic Aerosol-Cloud Interactions, *Curr. Clim. Change Rep.*, 1, 297–304, doi:10.1007/s40641-015-0028-0, 2015. (Cited on page 93.)
- Quaas, J., Boucher, O., and Lohmann, U.: Constraining the total aerosol indirect effect in the LMDZ and ECHAM4 GCMs using MODIS satellite data, *Atmos. Chem. Phys.*, 6, 947–955, doi:10.5194/acp-6-947-2006, 2006. (Cited on pages 70, 135, and 136.)
- Quaas, J., Boucher, O., Bellouin, N., and Kinne, S.: Satellite-based estimate of the direct and indirect aerosol climate forcing, *J. Geophys. Res.*, 113, doi:10.1029/2007JD008962, 2008. (Cited on pages 24, 51, 55, 70, 81, 82, and 92.)
- Quaas, J., Boucher, O., Jones, A., Weedon, G. P., Kieser, J., and Joos, H.: Exploiting the weekly cycle as observed over Europe to analyse aerosol indirect effects in two climate models, *Atmos. Chem. Phys.*, 9, 8493–8501, doi:10.5194/acp-9-8493-2009, 2009a. (Cited on page 92.)
- Quaas, J., Ming, Y., Menon, S., Takemura, T., Wang, M., Penner, J. E., Gettelman, A., Lohmann, U., Bellouin, N., Boucher, O., Sayer, A. M., Thomas, G. E., McComiskey, A., Feingold, G., Hoose, C., Kristjánsson, J. E., Liu, X., Balkanski, Y., Donner, L. J., Ginoux, P. A., Stier, P., Grandey, B., Feichter, J., Sednev, I., Bauer, S. E., Koch, D., Grainger, R. G., Kirkevåg, A., Iversen, T., Seland, Ø., Easter, R., Ghan, S. J., Rasch, P. J., Morrison, H., Lamarque, J.-F., Iacono, M. J., Kinne, S., and Schulz, M.: Aerosol indirect effects - general circulation model intercomparison and evaluation with satellite data, *Atmos. Chem. Phys.*, 9, 8697–8717, doi:10.5194/acp-9-8697-2009, 2009b. (Cited on pages 5, 24, and 92.)
- Ångström, A.: On the Atmospheric Transmission of Sun Radiation and on Dust in the Air, *Geogr. Ann.*, 11, 156–166, URL <http://www.jstor.org/stable/519399>, 1929. (Cited on page 137.)
- Reddy, M. S., Boucher, O., Bellouin, N., Schulz, M., Balkanski, Y., Dufresne, J.-L., and Pham, M.: Estimates of global multicomponent aerosol optical depth and direct radiative perturbation in the Laboratoire de Meteorologie Dynamique general circulation model, *J. Geophys. Res.*, 110, doi:10.1029/2004JD004757, 2005. (Cited on pages 26 and 33.)
- Remer, L., Kaufman, Y. J., Tanre, D., Mattoo, S., Chu, D. A., Martins, J. V., Li, R.-R., Ichoku, C., Levy, R. C., Kleidman, R. G., Eck, T. F., Vermote, E., and Holben, B. N.: The MODIS Aerosol Algorithm, Products, and Validation, *J. Atmos. Sci.*, 62, 947–973, doi:10.1175/JAS3385.1, 2005. (Cited on pages 27, 49, and 137.)

- Reutter, P., Su, H., Trentmann, J., Simmel, M., Rose, D., Gunthe, S. S., Wernli, H., Andreae, M. O., and Pöschl, U.: Aerosol- and updraft-limited regimes of cloud droplet formation: influence of particle number, size and hygroscopicity on the activation of cloud condensation nuclei (CCN), *Atmos. Chem. Phys.*, 9, 7067–7080, doi:10.5194/acp-9-7067-2009, URL <http://www.atmos-chem-phys.net/9/7067/2009/>, 2009. (Cited on pages 71, 82, and 88.)
- Roberts, G. and Nenes, A.: A continuous-flow streamwise thermal-gradient CCN chamber for atmospheric measurements, *Aerosol Sci. Tech.*, 39, 206–221, doi:10.1080/027868290913988, 2005. (Cited on page 35.)
- Romakkaniemi, S., McFiggans, G., Bower, K. N., Brown, P., Coe, H., and Choulaton, T. W.: A comparison between trajectory ensemble and adiabatic parcel modeled cloud properties and evaluation against airborne measurements, *J. Geophys. Res.*, 114, doi:10.1029/2008JD011286, D06214, 2009. (Cited on page 69.)
- Rose, D., Gunthe, S., Mikhailov, E., Frank, G., Dusek, U., Andreae, M., and Pöschl, U.: Calibration and measurement uncertainties of a continuous-flow cloud condensation nuclei counter (DMT-CCNC): CCN activation of ammonium sulfate and sodium chloride aerosol particles in theory and experiment, *Atmos. Chem. Phys.*, 8, 1153–1179, doi:doi:10.5194/acp-8-1153-2008, 2008. (Cited on page 35.)
- Rosenfeld, D., Cattani, E., Melani, S., and Levizzani, V.: CONSIDERATIONS ON DAY-LIGHT OPERATION OF 1.6-VERSUS 3.7- μm CHANNEL ON NOAA AND METOP SATELLITES, *Bull. Amer. Meteor. Soc.*, 85, 873–881, doi:10.1175/BAMS-85-6-873, URL <http://dx.doi.org/10.1175/BAMS-85-6-873>, 2004. (Cited on page 70.)
- Rosenfeld, D., Lohmann, U., Raga, G. B., O’Dowd, C. D., Kulmala, M., Fuzzi, S., Reissell, A., and Andreae, M. O.: Flood or Drought: How Do Aerosols Affect Precipitation?, *Science*, 321, 1309–1313, doi:10.1126/science.1160606, 2008. (Cited on page 4.)
- Rosenfeld, D., Williams, E., Andreae, M. O., Freud, E., Pöschl, U., and Rennó, N. O.: The scientific basis for a satellite mission to retrieve CCN concentrations and their impacts on convective clouds, *Atm. Measur. Tech.*, 5, 2039–2055, doi:10.5194/amt-5-2039-2012, URL <http://www.atmos-meas-tech.net/5/2039/2012/>, 2012. (Cited on page 70.)
- Rossow, W. B. and Schiffer, R. A.: Advances in Understanding Clouds from ISCCP, *Bull. Amer. Meteor. Soc.*, 80, 2261–2288, doi:10.1175/1520-0477(1999)080<2261:AIUCFI>2.0.COand2., 1999. (Cited on pages 18, 19, and 65.)
- Ruckstuhl, C., Philipona, R., Behrens, K., Collaud Coen, M., Dürr, B., Heimo, A., Mätzler, C., Nyeki, S., Ohmura, A., Vuilleumier, L., Weller, M., Wehrli, C., and Zelenka, A.: Aerosol and cloud effects on solar brightening and the recent rapid warming, *Geophys. Res. Lett.*, 35, doi:10.1029/2008GL034228, L12708, 2008. (Cited on page 92.)
- Sassen, K. and Wang, Z.: Classifying clouds around the globe with the CloudSat radar: 1-year of results, *Geophys. Res. Lett.*, 35, doi:10.1029/2007GL032591, URL <http://dx.doi.org/10.1029/2007GL032591>, L04805, 2008. (Cited on page 58.)

- Schmidt, J., Ansmann, A., Böhmler, J., and Wandinger, U.: Strong aerosol-cloud interaction in altocumulus during updraft periods: lidar observations over central Europe, *Atmos. Chem. Phys.*, 15, 10 687–10 700, doi:10.5194/acp-15-10687-2015, 2015. (Cited on pages 54 and 55.)
- Schüller, L., Bennartz, R., Fischer, J., and Brenguier, J.-L.: An Algorithm for the Retrieval of Droplet Number Concentration and Geometrical Thickness of Stratiform Marine Boundary Layer Clouds Applied to MODIS Radiometric Observations, *J. Appl. Meteo*, 44, 28–38, doi:10.1175/JAM-2185.1, URL <https://doi.org/10.1175/JAM-2185.1>, 2005. (Cited on page 70.)
- Schutgens, N. A. J., Gryspeerdt, E., Weigum, N., Tsyro, S., Goto, D., Schulz, M., and Stier, P.: Will a perfect model agree with perfect observations? The impact of spatial sampling, *Atmos. Chem. Phys.*, 16, 6335–6353, doi:10.5194/acp-16-6335-2016, URL <http://www.atmos-chem-phys.net/16/6335/2016/>, 2016. (Cited on page 71.)
- Seinfeld, J. H. and Pandis, S. N.: *Atmospheric Chemistry and Physics - From Air Pollution to Climate Change*, A Wiley-Interscience publication, second edn., ISBN:978-0-471-72018-8, 2006. (Cited on pages 9, 10, 12, 13, 14, 15, 16, 18, 20, 21, 33, 36, and 75.)
- Seinfeld, J. H., Bretherton, C., Carslaw, K. S., Coe, H., DeMott, P. J., Dunlea, E. J., Feingold, G., Ghan, S., Guenther, A. B., Kahn, R., Kraucunas, I., Kreidenweis, S. M., Molina, M. J., Nenes, A., Penner, J. E., Prather, K. A., Ramanathan, V., Ramaswamy, V., Rasch, P. J., Ravishankara, A. R., Rosenfeld, D., Stephens, G., and Wood, R.: Improving our fundamental understanding of the role of aerosol-cloud interactions in the climate system, *Proc. Nat. Acad. Sci.*, 113, doi:10.1073/pnas.1514043113, 2016. (Cited on page 56.)
- Shi, Y., Flynn, C., and Jefferson, A.: *Aerosol Observing System Cloud Condensation Nuclei Average (AOSCCNAV) Value-Added Product*, Tech. rep., U.S. Department of Energy, 2013. (Cited on page 35.)
- Shinozuka, Y., Clarke, A. D., Nenes, A., Jefferson, A., Wood, R., McNaughton, C. S., Ström, J., Tunved, P., Redemann, J., Thornhill, K. L., Moore, R. H., Latham, T. L., Lin, J. J., and Yoon, Y. J.: The relationship between cloud condensation nuclei (CCN) concentration and light extinction of dried particles: indications of underlying aerosol processes and implications for satellite-based CCN estimates, *Atmos. Chem. Phys.*, 15, 7585–7604, doi:10.5194/acp-15-7585-2015, 2015. (Cited on page 24.)
- Small, J. D., Chuang, P. Y., Feingold, G., and Jiang, H.: Can aerosol decrease cloud lifetime?, *Geophys. Res. Lett.*, 36, doi:10.1029/2009GL038888, URL <http://dx.doi.org/10.1029/2009GL038888>, L16806, 2009. (Cited on page 54.)
- Smith, G. L., Wielicki, B. A., Barkstrom, B. R., Lee, R. B., Priestley, K. J., Charlock, T. P., Minnis, P., Kratz, D. P., Loeb, N., and Young, D. F.: Clouds and Earth radiant energy system: an overview, *Adv. Space. Res.*, 33, 1125–1131, doi:[http://dx.doi.org/10.1016/S0273-1177\(03\)00739-7](http://dx.doi.org/10.1016/S0273-1177(03)00739-7), 2004. (Cited on pages 58 and 59.)
- Solomon, S., Qin, D., Manning, M., Chen, Z., Marquis, M., Averyt, K., Tignor, M., and (eds.), H. M.: *Climate Change 2007: The Physical Science Basis*. Contribution of Working Group I to the Fourth Assessment Report of the Intergovernmental Panel on Climate

- Change, Cambridge University Press, Cambridge, United Kingdom and New York, NY, USA, 2007. (Cited on pages 1, 3, and 91.)
- Spracklen, D. V., Carslaw, K. S., Pöschl, U., Rap, A., and Forster, P. M.: Global cloud condensation nuclei influenced by carbonaceous combustion aerosol, *Atmos. Chem. Phys.*, 11, 9067–9087, doi:10.5194/acp-11-9067-2011, 2011. (Cited on pages 25, 33, and 35.)
- Stemmler, J. D., Wood, R., Bretherton, C. S., and Rémillard, J.: Low CCN concentration events over the eastern North Atlantic: seasonality, meteorology and drivers, *J. Geophys. Res.*, submitted. (Cited on pages 35 and 36.)
- Stephens, G. L., Vane, D. G., Boain, R. J., Mace, G. G., Sassen, K., Wang, Z., Illingworth, A. J., O'Connor, E. J., Rossow, W. B., Durden, S. L., Miller, S. D., Austin, R. T., Benedetti, A., Mitrescu, C., and Team, T. C. S.: The CloudSat mission and the A-Train, *Bull. Amer. Meteor. Soc.*, 83, 1771–1790, doi:10.1175/BAMS-83-12-1771, 2002. (Cited on pages 17, 57, and 58.)
- Stephens, G. L., Vane, D. G., Tanelli, S., Im, E., Durden, S., Rokey, M., Reinke, D., Partain, P., Mace, G. G., Austin, R., L'Ecuyer, T., Haynes, J., Lebsock, M., Suzuki, K., Waliser, D., Wu, D., Kay, J., Gettelman, A., Wang, Z., and Marchand, R.: CloudSat mission: Performance and early science after the first year of operation, *J. Geophys. Res.*, 113, doi:10.1029/2008JD009982, D00A18, 2008. (Cited on pages 17, 18, and 58.)
- Stevens, B.: Climate science: Uncertain then, irrelevant now, *Nature*, 503, 47–48, doi:10.1038/503047a10.1038/503047a, 2013. (Cited on pages 6 and 54.)
- Stevens, B.: Rethinking the Lower Bound on Aerosol Radiative Forcing, *J. Clim.*, 28, 4794–4819, doi:10.1175/JCLI-D-14-00656.1, 2015. (Cited on page 92.)
- Stevens, B. and Feingold, G.: Untangling aerosol effects on clouds and precipitation in a buffered system, *Nature*, 461, 607–613, doi:10.1038/nature08281, 2009. (Cited on page 54.)
- Stevens, B., Giorgetta, M., Esch, M., Mauritsen, T., Crueger, T., Rast, S., Salzmann, M., Schmidt, H., Bader, J., Block, K., Brokopf, R., Fast, I., Kinne, S., Kornblüeh, L., Lohmann, U., Pincus, R., Reichler, T., and Roeckner, E.: Atmospheric component of the MPI-M Earth System Model: ECHAM6, *J. Adv. Model. Earth Systems*, 5, 146–172, doi:10.1002/jame.20015, 2013. (Cited on pages 33 and 94.)
- Stier, P.: Limitations of passive satellite remote sensing to constrain global cloud condensation nuclei, *Atmos. Chem. Phys. Discuss.*, 15, 32 607–32 637, doi:10.5194/acpd-15-32607-2015, 2015. (Cited on pages 6, 24, 137, and 138.)
- Stier, P., Feichter, J., Kinne, S., Kloster, S., Vignati, E., Wilson, J., Ganzeveld, L., Tegen, I., Werner, M., Balkanski, Y., Schulz, M., Boucher, O., Minikin, A., and Petzold, A.: The aerosol-climate model ECHAM5-HAM, *Atmos. Chem. Phys.*, 5, 1125–1156, doi:10.5194/acp-5-1125-2005, 2005. (Cited on page 33.)
- Stocker, T., Qin, D., Plattner, G.-K., Tignor, M., Allen, S., Boschung, J., Nauels, A., Xia, Y., Bex, V., and (eds), P. M.: Summary for Policymakers, in: *Climate Change 2013: The Physical Science Basis. Contribution of Working Group I to the Fifth Assessment Report of*

- the Intergovernmental Panel on Climate Change, Cambridge University Press, Cambridge, United Kingdom and New York, NY, USA, doi:10.1017/CBO9781107415324.004, 2013. (Cited on pages 1 and 2.)
- Storelvmo, T., Kristjánsson, J. E., Ghan, S. J., Kirkevåg, A., Seland, O., and Iversen, T.: Predicting cloud droplet number concentration in Community Atmosphere Model (CAM)-Oslo, *J. Geophys. Res.*, 111, doi:10.1029/2005JD006300, D24208, 2006. (Cited on page 62.)
- Stubenrauch, C. J., Rossow, W. B., Kinne, S., Ackerman, S., Cesana, G., Chepfer, H., Girolamo, L. D., Getzewich, B., Guignard, A., Heidinger, A., Maddux, B. C., Menzel, W. P., Minnis, P., Pearl, C., Platnick, S., Poulsen, C., Riedi, J., Sun-Mack, S., Walther, A., Winker, D., Zeng, S., and Zhao, G.: Assessment of global cloud datasets from satellites: Project and database initiated by the GEWEX Radiation Panel, *Bull. Amer. Meteor. Soc.*, 94, doi:10.1175/BAMS-D-12-00117, 2013. (Cited on page 18.)
- Su, W., Loeb, N. G., Xu, K., Schuster, G. L., and Eitzen, Z. A.: An estimate of aerosol indirect effect from satellite measurements with concurrent meteorological analysis, *J. Geophys. Res.*, 115, doi:10.1029/2010JD013948, D18219, 2010. (Cited on page 65.)
- Takemura, T., Nozawa, T., Emori, S., Nakajima, T. Y., and Nakajima, T.: Simulation of climate response to aerosol direct and indirect effects with aerosol transport-radiation model, *J. Geophys. Res.*, 110, doi:10.1029/2004JD005029, D02202, 2005. (Cited on page 62.)
- Tanelli, S., Durden, S., Im, E., Pak, K., Reinke, D., Partain, P., Haynes, J., and Marchand, R.: CloudSat's Cloud Profiling Radar After Two Years in Orbit: Performance, Calibration, and Processing, *Geosci. Remote Sens.*, 46, 3560–3573, doi:10.1109/TGRS.2008.2002030, 2008. (Cited on page 58.)
- Tang, M., Cziczo, D. J., and Grassian, V. H.: Interactions of Water with Mineral Dust Aerosol: Water Adsorption, Hygroscopicity, Cloud Condensation, and Ice Nucleation, *Chem. Rev.*, 116, 4205–4259, doi:10.1021/acs.chemrev.5b00529, PMID: 27015126, 2016. (Cited on page 11.)
- Taylor, J. P. and McHaffie, A.: Measurements of Cloud Susceptibility, *J. Atmos. Sci.*, 51, 1298–1306, doi:10.1175/1520-0469(1994)051<1298:MOCS>2.0.COand2, 1994. (Cited on page 5.)
- Tölle, M. H. and Krueger, S. K.: Effects of entrainment and mixing on droplet size distributions in warm cumulus clouds, *J. Adv. Model. Earth Systems*, 6, doi:10.1002/2012MS000209, 2014. (Cited on page 20.)
- Tonttila, J., O'Connor, E. J., Niemelä, S., Räisänen, P., and Järvinen, H.: Cloud base vertical velocity statistics: a comparison between an atmospheric mesoscale model and remote sensing observations, *Atmos. Chem. Phys.*, 11, 9207–9218, doi:10.5194/acp-11-9207-2011, 2011. (Cited on page 68.)
- Tselioudis, G., Zhang, Y., and Rossow, W. B.: Cloud and Radiation Variations Associated with Northern Midlatitude Low and High Sea Level Pressure Regimes, *J. Clim.*, 13, 312–327, doi:10.1175/1520-0442(2000)013<0312:CARVAW>2.0.COand2, 2000. (Cited on page 65.)

- Twomey, S.: The nuclei of natural cloud formation part II: The supersaturation in natural clouds and the variation of cloud droplet concentration, *Pure and Appl. Geophys.*, 43, 243–249, doi:10.1007/BF01993560, 1959. (Cited on pages 36 and 54.)
- Twomey, S.: Pollution and planetary albedo, *Atmos. Env.*, 8, 1251–1256, doi:10.1016/0004-6981(74)90004-3, 1974. (Cited on page 4.)
- Twomey, S.: The Influence of Pollution on the Shortwave Albedo of Clouds, *J. Atmos. Sci.*, 34, 1149–1152, doi:10.1175/1520-0469(1977)034<1149:TIOPOT>2.0.COand2, 1977. (Cited on page 91.)
- Unglaub, C.: Cloud regime based analysis of adjustments to aerosol-cloud interactions using spaceborne measurements, Ph.D. thesis, submitted to Universität Leipzig, Fakultät für Physik und Geowissenschaften, July, 2017. (Cited on pages 57, 66, 77, and 88.)
- van de Hulst, H. C.: *Light Scattering by Small Particles*, John Wiley and Sons; Reprint by Dover Publications 1981, New York, ISBN:0486642283, 1957. (Cited on page 132.)
- Van Dingenen, R., Raes, F., Putaud, J.-P., Baltensperger, U., Charron, A., Facchini, M.-C., Decesari, S., Fuzzi, S., Gehrig, R., Hansson, H.-C., Harrison, R. M., Hüglin, C., Jones, A. M., Laj, P., Lorbeer, G., Maenhaut, W., Palmgren, F., Querol, X., Rodriguez, S., Schneider, J., Brink, H., Tunved, P., Tørseth, K., Wehner, B., Weingartner, E., Wiedensohler, A., and Wählin, P.: A European aerosol phenomenology - 1: physical characteristics of particulate matter at kerbside, urban, rural and background sites in Europe, *Atmos. Env.*, 38, 2561–2577, doi:10.1016/j.atmosenv.2004.01.040, 2004. (Cited on page 24.)
- Vignati, E., Wilson, J., and Stier, P.: M7: An efficient size-resolved aerosol microphysics module for large-scale aerosol transport models, *J. Geophys. Res.*, 109, doi:10.1029/2003JD004485, 2004. (Cited on pages 35 and 64.)
- Webb, M., Senior, C., Bony, S., and Morcrette, J.-J.: Combining ERBE and ISCCP data to assess clouds in the Hadley Centre, ECMWF and LMD atmospheric climate models, *Clim. Dyn.*, 17, 905–922, doi:10.1007/s003820100157, 2001. (Cited on page 65.)
- Werner, F., Ditas, F., Siebert, H., Simmel, M., Wehner, B., Pilewskie, P., Schmeissner, T., Shaw, R. A., Hartmann, S., Wex, H., Roberts, G. C., and Wendisch, M.: Twomey effect observed from collocated microphysical and remote sensing measurements over shallow cumulus, *J. Geophys. Res.*, 119, doi:10.1002/2013JD020131, 2014. (Cited on page 5.)
- West, R. E. L., Stier, P., Jones, A., Johnson, C. E., Mann, G. W., Bellouin, N., Partridge, D. G., and Kipling, Z.: The importance of vertical velocity variability for estimates of the indirect aerosol effects, *Atmos. Chem. Phys.*, 14, 6369–6393, doi:10.5194/acp-14-6369-2014, 2014. (Cited on pages 6, 62, 68, and 74.)
- Wielicki, B. A. and Parker, L.: On the determination of cloud cover from satellite sensors: The effect of sensor spatial resolution, *J. Geophys. Res.*, 97, doi:10.1029/92JD01061, 1992. (Cited on page 18.)
- Wielicki, B. A., Barkstrom, B. R., Harrison, E. F., III, R. B. L., Smith, G. L., and Cooper, J. E.: *Clouds and the Earth’s Radiant Energy System (CERES): An Earth Observing*

- System Experiment, *Bull. Amer. Meteor. Soc.*, 77, 853–868, doi:10.1175/1520-0477(1996)077<0853:CATERE>2.0.CO;2, 1996. (Cited on page 58.)
- Williams, K. D. and Webb, M. J.: A quantitative performance assessment of cloud regimes in climate models, *Clim. Dyn.*, 33, 141–157, doi:10.1007/s00382-008-0443-1, 2008. (Cited on page 65.)
- Winker, D. M., Hunt, W. H., and Hostetler, C. A.: Status and performance of the CALIOP lidar, *Proc. SPIE*, 5575, 8–15, doi:10.1117/12.571955, 2004. (Cited on pages 17, 57, and 58.)
- Winker, D. M., Hunt, W. H., and McGill, M. J.: Initial performance assessment of CALIOP, *Geophys. Res. Lett.*, 34, doi:10.1029/2007GL030135, L19803, 2007. (Cited on pages 17, 57, and 58.)
- Winker, D. M., Vaughan, M. A., Omar, A., Hu, Y., Powell, K. A., Liu, Z., Hunt, W. H., and Young, S. A.: Overview of the CALIPSO mission and CALIOP data processing algorithms, *J. Atmos. Ocean. Technol.*, 26, 2310–2323, doi:10.1175/2009JTECHA1281.1, 2009. (Cited on pages 17, 57, 58, and 59.)
- Winker, D. M., Tackett, J. L., Getzewich, B. J., Liu, Z., Vaughan, M. A., and Rogers, R. R.: The global 3-D distribution of tropospheric aerosols as characterized by CALIOP, *Atmos. Chem. Phys.*, 13, 3345–3361, doi:10.5194/acp-13-3345-2013, 2013. (Cited on page 25.)
- WMO: International Cloud Atlas, Volume I - Manual on the Observation of clouds and other meteors, vol. WMO-No.407, URL https://wmoica-staticfile.s3.amazonaws.com/wmo_407_en-v1.pdf?javer=1607221219, ISBN:92-63-10407-7, 1975. (Cited on page 16.)
- Wood, R. and Bretherton, C. S.: On the Relationship between Stratiform Low Cloud Cover and Lower-Tropospheric Stability, *J. Clim.*, 19, 6425–6432, doi:10.1175/JCLI3988.1, 2006. (Cited on page 65.)
- Wood, R. and Hartmann, D. L.: Spatial variability of liquid water path in marine low cloud: The importance of mesoscale cellular convection, *J. Clim.*, 19, 1748–1764, doi:10.1175/JCLI3702.1, 2006. (Cited on page 133.)
- Wood, R., Leon, D., Lebsock, M., Snider, J., and Clarke, A. D.: Precipitation driving of droplet concentration variability in marine low clouds, *J. Geophys. Res.*, 117, doi:10.1029/2012JD018305, URL <http://dx.doi.org/10.1029/2012JD018305>, D19210, 2012. (Cited on page 71.)
- Xiong, X., Wenny, B. N., and Barnes, W. L.: Overview of NASA Earth Observing Systems Terra and Aqua moderate resolution imaging spectroradiometer instrument calibration algorithms and on-orbit performance, *J. Appl. Remote Sensing*, 3, 032501–032501–25, doi:10.1117/1.3180864, 2009. (Cited on page 59.)
- Yuan, T., Li, Z., Zhang, R., and Fan, J.: Increase of cloud droplet size with aerosol optical depth: An observation and modeling study, *J. Geophys. Res.*, 113, doi:10.1029/2007JD008632, URL <http://dx.doi.org/10.1029/2007JD008632>, D04201, 2008. (Cited on page 71.)

- Yum, S. S., Hudson, J. G., and Xie, Y.: Comparisons of cloud microphysics with cloud condensation nuclei spectra over the summertime Southern Ocean, *J. Geophys. Res.*, 103, 16 625–16 636, doi:10.1029/98JD01513, 1998. (Cited on pages 69 and 75.)
- Zeng, S., Riedi, J., Trepte, C. R., Winker, D. M., and Hu, Y.-X.: Study of global cloud droplet number concentration with A-Train satellites, *Atmos. Chem. Phys.*, 14, 7125–7134, doi:10.5194/acp-14-7125-2014, 2014. (Cited on pages 71, 78, 135, and 136.)
- Zhang, J. and Reid, J. S.: MODIS aerosol product analysis for data assimilation: Assessment of over-ocean level 2 aerosol optical thickness retrievals, *J. Geophys. Res.*, 111, doi:10.1029/2005JD006898, 2006. (Cited on page 27.)
- Zhang, J. and Reid, J. S.: A decadal regional and global trend analysis of the aerosol optical depth using a data-assimilation grade over-water MODIS and Level 2 MISR aerosol products, *Atmos. Chem. Phys.*, 10, 10 949–10 963, doi:10.5194/acp-10-10949-2010, 2010. (Cited on page 41.)
- Zhang, Z.: On the sensitivity of cloud effective radius retrieval based on spectral method to bimodal droplet size distribution: A semi-analytical model, *J. Quant. Spectrosc. Rad. Transfer*, 129, 79–88, doi:10.1016/j.jqsrt.2013.05.033, URL <http://www.sciencedirect.com/science/article/pii/S0022407313002410>, 2013. (Cited on page 71.)
- Zhang, Z. and Platnick, S.: An assessment of differences between cloud effective particle radius retrievals for marine water clouds from three MODIS spectral bands, *J. Geophys. Res.*, 116, doi:10.1029/2011JD016216, D20215, 2011. (Cited on pages 70, 71, and 78.)
- Zhang, Z., Ackerman, A. S., Feingold, G., Platnick, S., Pincus, R., and Xue, H.: Effects of cloud horizontal inhomogeneity and drizzle on remote sensing of cloud droplet effective radius: Case studies based on large-eddy simulations, *J. Geophys. Res.*, 117, doi:10.1029/2012JD017655, URL <http://dx.doi.org/10.1029/2012JD017655>, D19208, 2012. (Cited on page 70.)
- Zheng, Y. and Rosenfeld, D.: Linear relation between convective cloud base height and updrafts and application to satellite retrievals, *Geophys. Res. Lett.*, 42, 6485–6491, doi:10.1002/2015GL064809, 2015GL064809, 2015. (Cited on pages 69 and 70.)
- Zuidema, P., Westwater, E. R., Fairall, C., and Hazen, D.: Ship-based liquid water path estimates in marine stratocumulus, *J. Geophys. Res.*, 110, doi:10.1029/2005JD005833, URL <http://dx.doi.org/10.1029/2005JD005833>, D20206, 2005. (Cited on pages 70 and 134.)

Supplement: Cloud Condensation Nuclei

A.1 Validation of CCN relevant aerosol mass

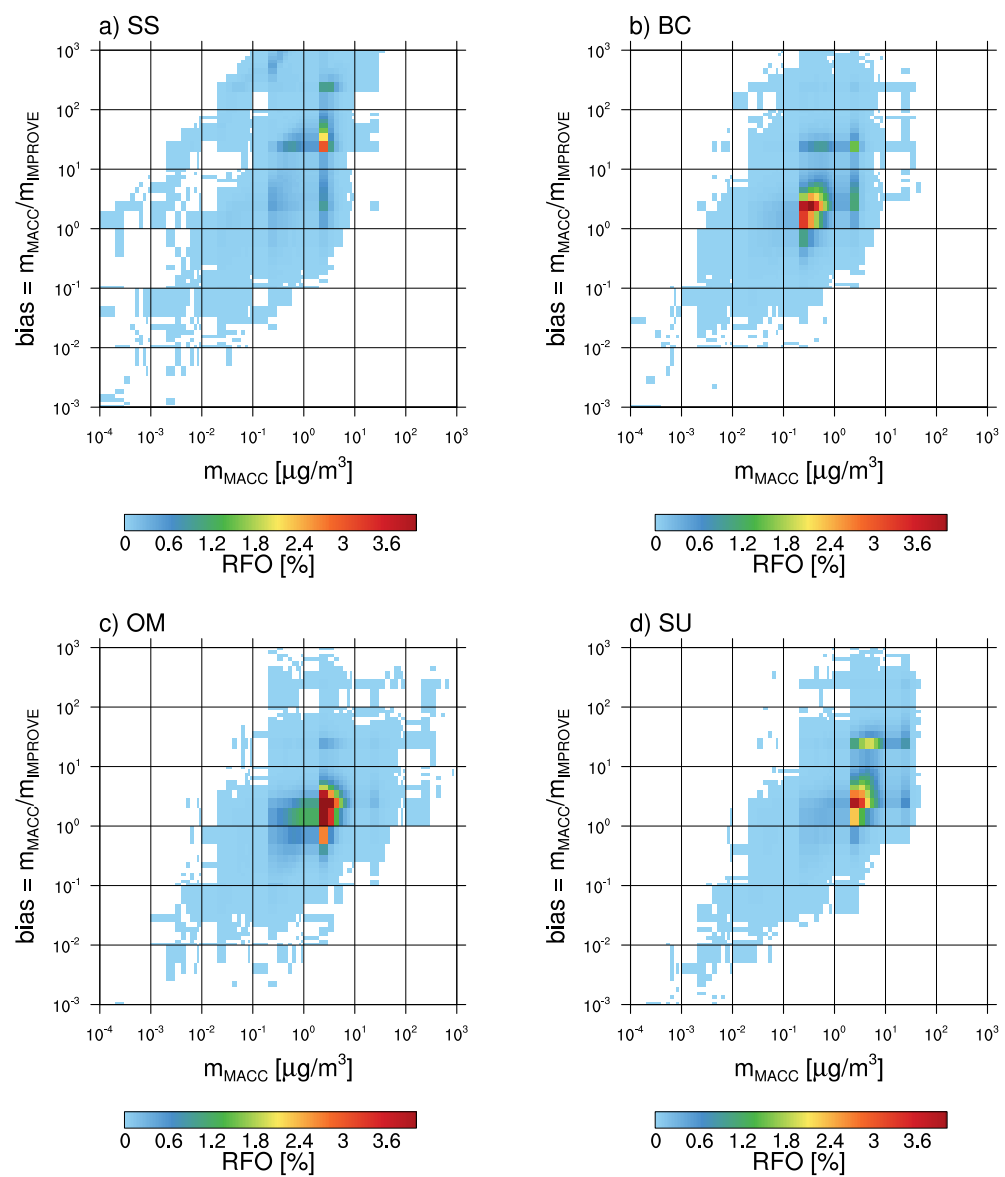


Figure A.1: MACC vs IMPROVE MCONC Bias Joint Histograms, for a) fine-mode sea salt, b) elemental/black carbon, c) organic matter and d) sulfate. The red line indicates a ratio of one. Data above represents an overestimation, data below an underestimation of MACC simulated mass concentrations in comparison to IMPROVE measurements.

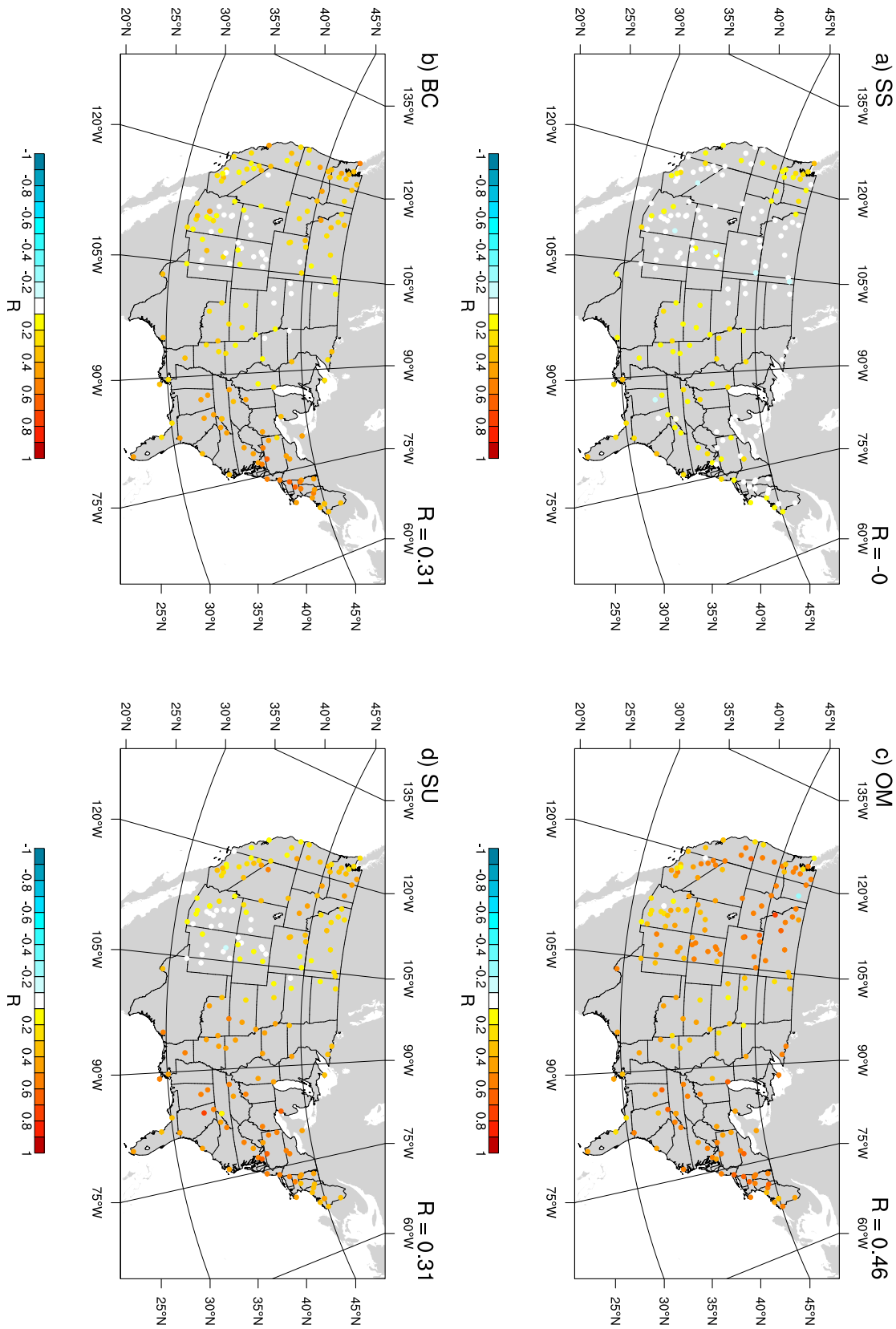


Figure A.2: Maps of Mass Correlation Coefficients, between IMPROVE and MACC-II mass concentrations. The average linear Pearson correlation coefficient R of the logarithmic values is given on the top of each panel for a) fine-mode sea salt, b) elemental/black carbon, c) organic matter and d) sulfate.

A.2 Seasonal variability of CCN contributions

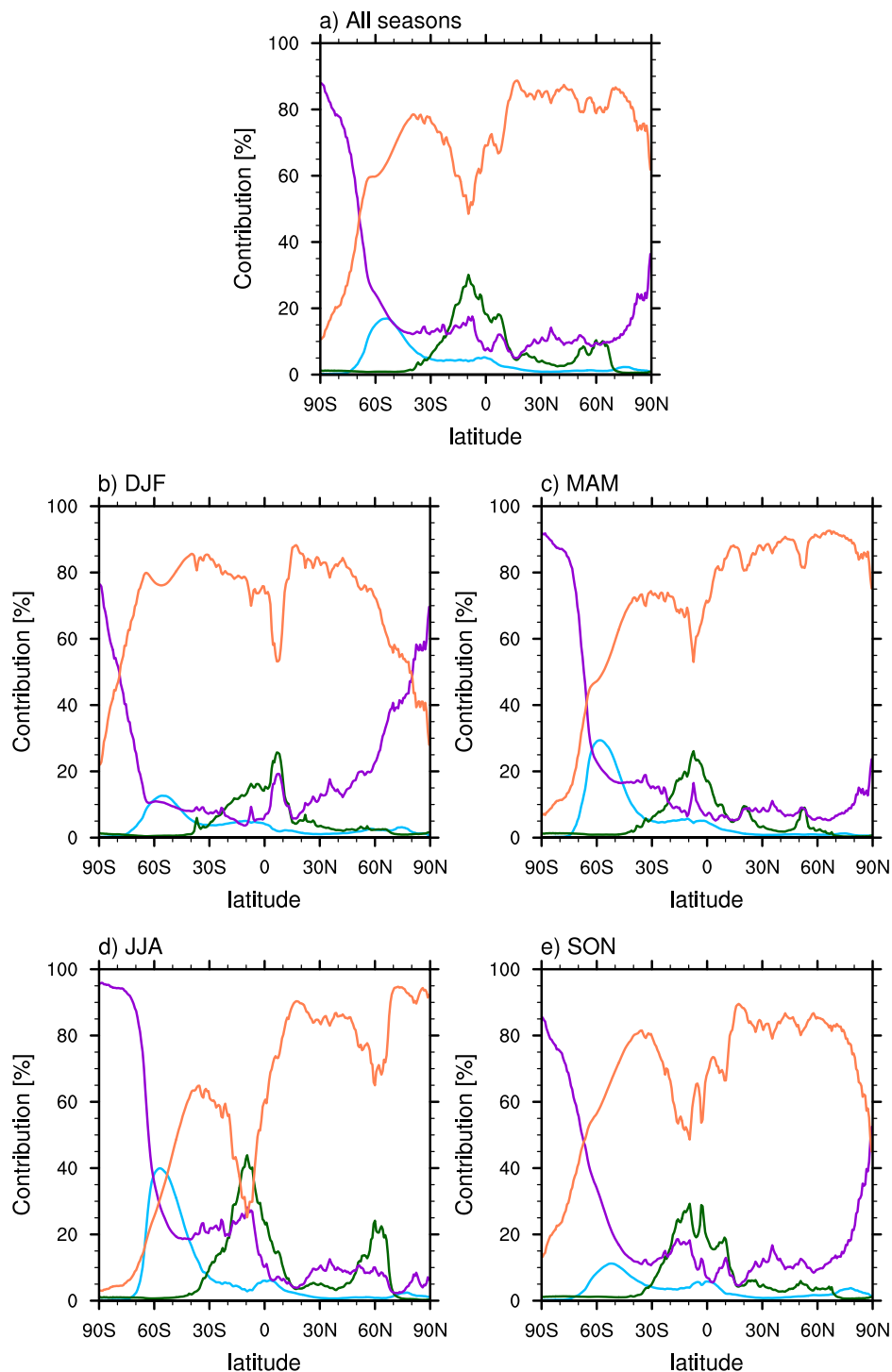


Figure A.3: Zonal and seasonal means of total CCN contributions at 0.4% Ssat. The near-surface CCN relevant species are SU (coral), the three SS modes which are taken together as one mode SS (blue), OM (green) and BC (purple) which are hydrophilic components only. Panels are sorted with a) All seasons, b) DJF, c) MAM, d) JJA and e) SON.

A.3 Bias distributions of CCN relevant aerosol masses

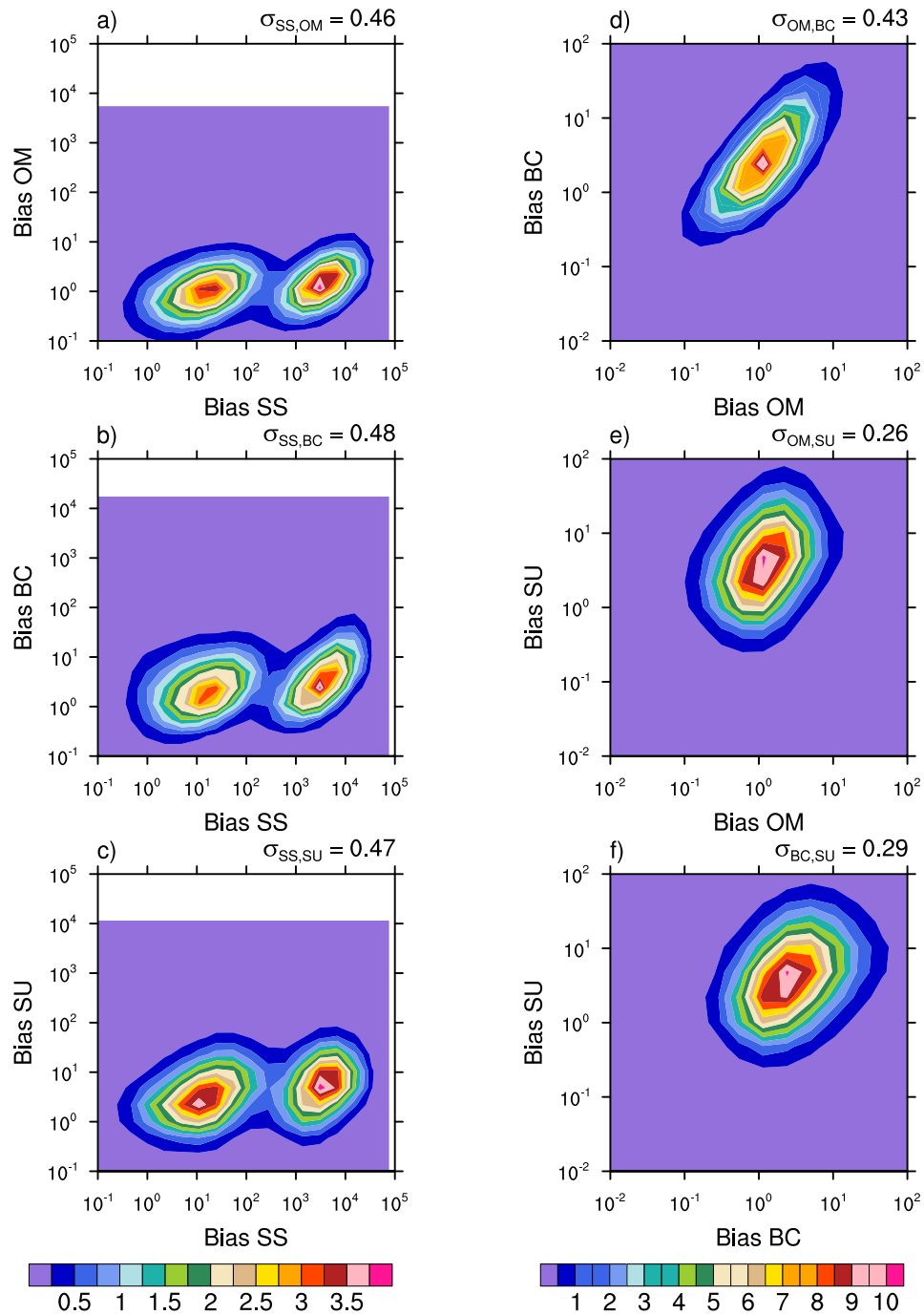


Figure A.4: Joint PDF of MACC MCONC bias distributions, for assessing the covariance of a) SS and OM, b) SS and BC, c) SS and SU, d) OM and BC, e) OM and SU and f) BC and SU. The computed square root of the covariance $\sigma_{m_x, y}$ is stated at the top of each panel.

Supplement: Cloud Droplet Number Concentration

B.1 Satellite retrieved cloud and aerosol microphysical properties

In this section, the most important satellite-retrieved cloud and aerosol microphysical properties which are used to determine CDNC and its sensitivity to aerosol perturbations should be introduced.

B.1.1 Satellite retrieved cloud microphysical properties determining CDNC

While CDNC cannot directly be retrieved from satellite observations, it can be estimated using the droplet effective radius r_{eff} and the cloud optical depth τ_c . They can be solely and independently determined from reflection functions of clouds as shown by Nakajima and King (1990). The reflection function R depends on the cloud's radiative properties assuming vertically homogeneous. It represents the albedo of a medium that would be obtained from directional reflectance measurement if the reflected radiation field were isotropic (Nakajima and King, 1990). Therefore, $R(\tau_c; \mu, \mu_0, \phi)$ depends also on μ_0 , the cosine of the solar zenith angle θ , on the absolute value of the cosine of the solar zenith angle μ , and on ϕ which is the relative azimuth angle between the direction of propagation of the emerging radiation and incident solar direction. τ_c is determined using a non-absorbing channel in the VIS while, independently from this, a water/ice absorbing channel in the NIR is used to determine r_{eff} , which itself is retrieved using the similarity parameter. An example of how this reflection function could look like is given in Figure B.1, which is taken from Nakajima and King (1990). Here, r_{eff} is derived from $\lambda = 2.16 \mu m$, while for optically thin clouds $\lambda = 3.7 \mu m$ is preferred, just like in this study.

Having determined r_{eff} and τ_c for a liquid water cloud, they can be used to determine the total extinction of this cloud. To determine how much light can pass through an attenuating medium, Beer's law is applied in a general form of

$$\frac{I}{I_0} = e^{-\tau_{total}} \quad (B.1)$$

with I being the attenuated radiative flux from the incoming total radiative flux I_0 and τ_{total} being the total optical depth of the medium.

If the medium is a cloud, τ_{total} can be replaced with τ_c if the extinction is considered between the cloud base and the cloud top. τ_c is then defined as the vertical integral of the

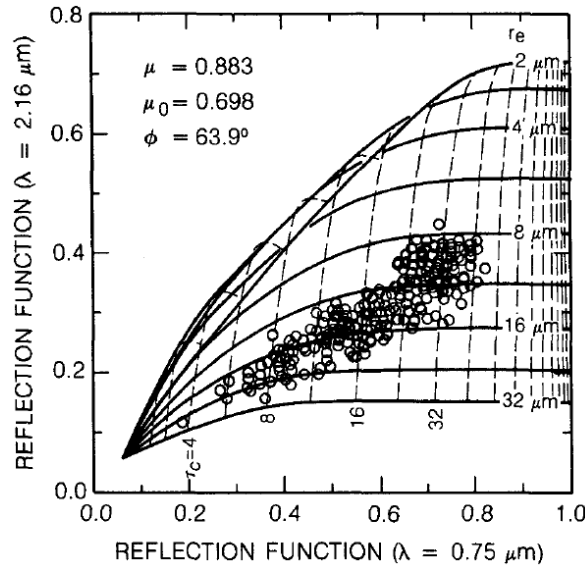


Figure B.1: Reflection function, taken from Nakajima and King (1990). It shows theoretical relationships between the reflection function at 0.75 and 2.16 μm for various values of τ_c (at $\lambda = 0.75 \mu\text{m}$) and r_{eff} (at $\lambda = 2.16 \mu\text{m}$) for the case when $\mu_0 = 0.698$ ($\theta_0 = 45.7^\circ$), $\mu = 0.883$ ($\theta = 28.0^\circ$), and $\phi = 63.9^\circ$. The superimposed circles represent data from measurements above marine stratocumulus clouds from the FIRE experiment on July 10th, 1987. © American Meteorological Society. Used with permission.

cloud extinction coefficient β_{ext} in the solar spectrum (absorption can be neglected, extinction \approx scattering) between the cloud base $h = CB$ and the cloud top $h = CT$

$$\tau_c = \int_{CB}^{CT} \beta_{ext}(h) dh \quad (\text{B.2})$$

Assuming spherical cloud droplets, $\beta_{ext}(h)$ can be determined from the droplet radius r , the droplet size distribution $n(r)$ within a cloud unit volume at height h and the extinction efficiency factor Q_{ext} which represents the ratio between the extinction and the geometric cross section $A = \pi r^2$ of a given droplet

$$\beta_{ext}(h) = \int_0^\infty Q_{ext}(r) \pi r^2 n(r) dr . \quad (\text{B.3})$$

Q_{ext} can be approximated to its asymptotic value of $Q_{ext} = 2$ as usually $r \gg \lambda$ for visible wavelengths so that the limit of geometrical optics is almost reached (van de Hulst, 1957; Hansen and Travis, 1974; Bennartz, 2007).

The droplet effective radius r_{eff} as well as the liquid water content L_c at height h are given as functions of the droplet radius r and the droplet size distribution $n(r)$, with (Hansen and Travis, 1974)

$$r_{eff}(h) = \frac{\int_0^\infty r^3 n(r) dr}{\int_0^\infty r^2 n(r) dr} \quad (\text{B.4})$$

which represents the ratio of the mean volume of a cloud particle to its mean surface area, and

$$L_c(h) = \frac{4\pi\rho_w}{3} \int_0^\infty r^3 n(r) dr \quad (\text{B.5})$$

which represents the amount of liquid water within a unit volume.

The vertical integral of the L_c between cloud base and top gives the liquid water path L_p of the respective cloud. Assuming adiabaticity, that is L_c and r_{eff} increase linearly with height within the cloud and N_d stay constant, the liquid water path may be written as (Wood and Hartmann, 2006; Painemal and Zuidema, 2011)

$$L_p = \frac{5}{9} \rho_w \tau_c r_{eff} \quad (\text{B.6})$$

Combining Equations B.4 and B.5 and inserting them into Equation B.3 gives the extinction coefficient as a function of the liquid water content and the effective radius

$$\beta_{ext}(h) = \frac{3Q_{ext}}{4\rho_w} \frac{L_c(h)}{r_{eff}(h)} \quad (\text{B.7})$$

r_{eff} is related to the mean volume radius introducing a factor k

$$k = \left(\frac{r_v}{r_{eff}} \right)^3 \quad (\text{B.8})$$

which is most commonly estimated as $k \approx 0.8$ as stated in several studies (e.g. Brenguier et al., 2000; Bennartz, 2007; Painemal and Zuidema, 2011). However this value can vary depending on the width of the droplet size distribution and therefore introduces uncertainties when set to a fixed value for several cloud types.

Using Equation B.5 and B.8, the mean volume radius can be written as

$$r_v^3(h) = \frac{1}{N_d(h)} \int_0^\infty r^3 n(r) dr = \frac{3L_c(h)}{4\pi\rho_w N_d(h)} \quad (\text{B.9})$$

Utilizing the assumption that CDNC is constant with height and LWC is a constant fraction (f_{ad}) of its adiabatic value, writing

$$L_c(h) = f_{ad} c_w h \quad (\text{B.10})$$

with c_w being the ‘‘condensation rate’’ (Brenguier et al., 2000) or ‘‘water content lapse rate’’ (Painemal and Zuidema, 2011), we can use Equation B.9 to substitute for r_{eff} in Equation B.7 and combine this with Equation B.10 and B.2 to obtain a new description of the cloud optical depth

$$\begin{aligned} \tau_c &= \int_{CB}^{CT} Q_{ext} \left(\frac{3f_{ad}c_w}{4\rho_w} \right)^{\frac{2}{3}} (N_d\pi k)^{\frac{1}{3}} h^{\frac{2}{3}} dh \\ &= \frac{3Q_{ext}}{5} \left(\frac{3f_{ad}c_w}{4\rho_w} \right)^{\frac{2}{3}} (N_d\pi k)^{\frac{1}{3}} H^{\frac{5}{3}} \end{aligned} \quad (\text{B.11})$$

which is only dependent on the number of droplets and the geometrical cloud thickness H .

The Equations B.9 and B.10 can be applied near the cloud top ($h = CT$) to specify H as a function of $r_{eff}(CT)$, N_d and other known parameters, which with some rearrangements

finally give CDNC as

$$N_d = \frac{2\sqrt{10}}{k\pi Q_{ext}^3} \left(\frac{f_{ad}c_w\tau_c}{\rho_w r_{eff}^5} \right)^{\frac{1}{2}}. \quad (\text{B.12})$$

wich can be also expressed as

$$N_d = \beta \tau_c^{0.5} r_{eff}^{-2.5} \quad (\text{B.13})$$

with β containing k , f_{ad} and c_w (see Equation 4.7).

Since r_{eff} is raised to the power of -2.5, while k , f_{ad} , c_w and τ_c is raised to a lesser extent, N_d is much more sensitive to changes but also to uncertainties in r_{eff} , although uncertainties from the other parameters are not to be neglected either.

The condensation rate c_w describes the amount of condensate (in kg/m⁴) as the air parcel rises under moist adiabatic conditions, in dependence on the excess of water vapor, and thus in dependence on pressure and temperature. It has been shown however that this dependency is relatively weak, and the error of assuming a value that is constant throughout the cloud, and simply derived from cloud top pressure (CTP) and cloud top temperature (CTT), only gives an underestimation of $\sim 2\%$ (Grosvenor and Wood, 2014). Uncertainties from CTP and CTT can still propagate onto estimations of N_d .

Futher uncertainties are related to the adiabatic fraction f_{ad} which describes possible departures from a full adiabatic behavior of the air parcel due to effects of entrainment or the formation of precipitation. Zuidema et al. (2005) states that the assumption of adiabaticity is suitable for marine non-precipitating stratiform liquid clouds, but for polluted continental clouds significant deviations can be found (Kim et al., 2005). Observations from aircraft campaigns over stratocumulus clouds however show a large variability of adiabatic fractions from 0.1 to 0.9 (e.g. Brenguier et al., 2000; Painemal and Zuidema, 2011; Min et al., 2012). Min et al. (2012) also found a dependence on cloud geometrical thickness with higher values of ~ 0.8 for thin clouds (< 200 m) and smaller values of ~ 0.5 for thicker clouds (~ 500 m). More systematic long-term observations with a ground-based cloud radar and lidar however give values of ~ 0.6 (e.g. Merk et al., 2016; Kim et al., 2008). Uncertainties in these estimates result from difficulties in retrieving the correct cloud boundaries to determine L_p and H which are used to estimate f_{ad} . Especially for thinner clouds this could lead to large uncertainties. Merk et al. (2016) determined the overall uncertainty of f_{ad} to be around 30%. Given the high spatial variability of f_{ad} , better constraints are necessary to reduce its uncertainty on CDNC. In this study $f_{ad} = 1$ for simplicity and comparability of the various cloud regimes.

Boers et al. (2006) summarizes the uncertainties contributing to the theoretical derivation of CDNC as four basic thermodynamic and microphysical items, namely (1) the sub-adiabatic character of the cloud, (2) the shape of the liquid water profile, (3) the link between the volume radius and the effective radius and (4) the character of the mixing processes (homogeneous/inhomogeneous mixing, see Chapter 2.3) which determines the vertical variation in L_c and its distribution between vertical variations in the CDNC and the volume radius.

All of these issues have been discussed here, and since it is difficult to account for all effects in a global analysis including several cloud types, I decided to follow an approximate

approach from Quaas et al. (2006), setting β to be constant as $\beta = 1.37 \cdot 10^{-5} m^{-0.5}$, which is derived from values given in Brenguier et al. (2000).

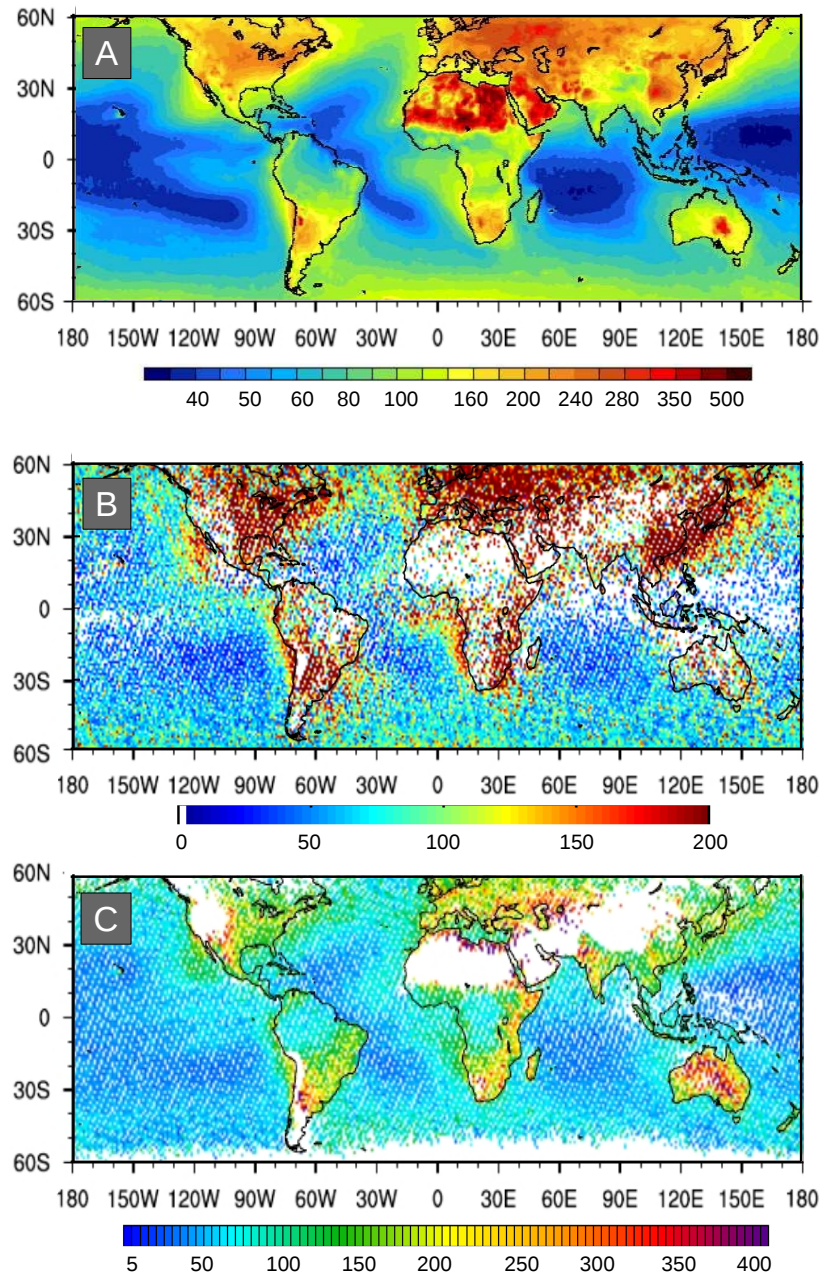


Figure B.2: References of global CDNC distributions, derived from MODIS data in A) Quaas et al. (2006), Figure 1a, in B) Zeng et al. (2014), Figure 1a, and C) in this study 4.12, lowest panel, for comparison. The figures are adopted from the respective figures given in the literature and compiled here for better comparison. Please note the different contour scales of each panel!

Due to different assumptions as well as different sampling and data usage, the distributions of CDNC, even if retrieved from the same instrument, can be very different as is presented in Figure B.2. It shows a compilation of two CDNC distributions from the literature (Quaas et al., 2006; Zeng et al., 2014) in comparison to the one retrieved in this study.

A rough comparison reveals that the CDNC distribution used in this study is in between the distributions from the other two studies. In this study, the same assumptions and

methodology are applied as by Quaas et al. (2006). However, they computed CDNC from joint histograms of τ_c retrieved at $0.86 \mu m$ and r_{eff} retrieved at $2.1 \mu m$ from TERRA (Level 3 data) between March 2000 and February 2005 at a $1 \times 1^\circ$ horizontal and daily temporal resolution. Only those data pixels are chosen, where the retrieval is supposed to be the most reliable with $4 \leq \tau_c \leq 70$ and $4 \mu m \leq r_{eff} \leq 30 \mu m$ and $CTT > 273 K$ to assure that only liquid water clouds are considered.

In this study, CDNC are computed from Aqua Level 2 Modis retrievals between 2007 and 2010, applying Equation 4.7 on each cloud group which contains valid τ_c and r_{eff} at $3.7 \mu m$ within a CERES footprint using nadir ground track data only. The sampling is further reduced in comparison to Quaas et al. (2006), as other filtering criteria for ideal case clouds are applied from CALIPSO and CloudSat retrievals (see Section 4.3.5 and Section 4.3.2). This reduced sampling can directly be seen when comparing Panel A and Panel C in Figure B.2, however the general distribution is similar. High altitude regions and desert regions are mostly eliminated in this analysis, and the high values of CDNC still seen in Panel A over the Sahara are gone, while larger values over Australia still remain. In Panel C some of the large values occur directly next to regions with missing (filtered out) values, these need to be seen critically.

Zeng et al. (2014) agrees with the choice of taking r_{eff} at $3.7 \mu m$, and they also use Aqua Level 2 MODIS retrievals from November 2007 to December 2008, which are however not on the CCCM statistical dimensions, but on a simple 1 km resolution along the CALIOP track. They derive CDNC using Equation B.12, for which they assume $f_{ad} = 0.8$, $Q_{ext} = 2$, a variable c_w (depending on CTT from MODIS, CTP from CALIOP cloud top altitude and a representation of water vapor saturation pressure) and a gamma distribution of CDNC for k . Furthermore, they filter for overcast water clouds with a combination of CALIOP, MODIS and POLDER cloud products, and remove thin clouds with $\tau_c < 5$ as detected by MODIS. Therefore, the resemblance of data sampling between Zeng et al. (2014) and this study is quite high, even though an additional list of other filtering criteria is applied here (see Section 4.3.5 and Section 4.3.2) which still leads to more gaps in the global picture. Comparable features between Panel B and C are e.g. the higher CDNC along the eastern coasts of South America and South Africa, while higher CDNC over Australia and India in Panel C do not agree with CDNC in Panel B.

Regarding the differences and uncertainties which can occur when using adiabatically retrieved CDNC from satellites, it is important to note that they must be handled with care when used as validation for models.

B.1.2 Satellite retrieved aerosol microphysical properties determining CDNC sensitivity

For estimating CDNC sensitivity from satellite retrievals, some information about the CCN-active aerosol content and variability is needed.

The aerosol optical depth AOD, or the aerosol index AI are often taken as proxies for CCN. However, problems with these estimates are manifold and described in the Introduction of Chapter 3. Here, I simply want to show how these parameters are defined and retrieved.

For the AOD retrieval, clearsky regions are used for the application of Beer's law (Equa-

tion B.1) with $\tau_{\text{total}} = \tau_{\text{scattering}} + \tau_{\text{absorption}}$ being the integral over the entire atmospheric column. Besides aerosols, also other atmospheric components can extinct light which must be considered when calculating the AOD. Therefore, to get τ they must be subtracted from τ_{tot} , namely as

$$\tau = \tau_{\text{total}} - \tau_{\text{Water Vapor}} - \tau_{\text{Rayleigh Scatt.}} - \tau_{\text{O}_3} - \tau_{\text{NO}_2} - \tau_{\text{CH}_4} - \tau_{\text{CO}_2} . \quad (\text{B.14})$$

Since aerosols can scatter as well as absorb radiation at various wavelengths, also in the VIS, one needs to account for assumptions in the single scattering albedo ω which is the ratio of scattering efficiency to total extinction efficiency to retrieve either one, the extinction by scattering only or the aerosol absorption optical depth (AAOD). This is a simple description of how the AOD can be derived in general, a more precise description for the MODIS algorithm for retrieving AOD is given in (e.g. Remer et al., 2005). They give an accuracy of MODIS AOD of $\sim 6\%$ over oceans and $\sim 10\%$ over land in comparison to collocated AERONET measurements.

It has been shown that AOD is a suitable proxy for CCN, as the aerosol light extinction is linearly related to CCN concentrations for aerosols of identical size, shape and composition in surroundings of similar humidity (Stier, 2015). However, since these assumptions do not apply in real conditions, the retrieval of CCN based on extinction measurements only becomes quite uncertain (Kapustin et al., 2006).

Different size distributions from different aerosol populations strongly impact measurable radiative properties such as the scattering phase function, the single scattering albedo and also the spectral variation of AOD. Retrievals of AOD at one wavelength, typically at 550 nm, therefore neglect variations of aerosol size distributions, especially from smaller aerosol particles (the fine mode).

This can be partly compensated by accounting for the spectral dependency of AOD using the Ångström exponent α (Ångström, 1929), which is retrieved from AOD at two (or more) different wavelengths, typically from 440 nm to 870 nm

$$\alpha = -\frac{d \ln \tau}{d \ln \lambda} = -\frac{\ln\left(\frac{\tau_2}{\tau_1}\right)}{\ln\left(\frac{\lambda_2}{\lambda_1}\right)} \quad (\text{B.15})$$

with α being the negative slope (using least squares fit) of the dependence of AOD with wavelength in logarithmic scales. Typical values of α range from nearly zero for high optical thickness Sahelian/Saharan desert dust cases dominated by coarse mode aerosols (Holben et al., 1991) to values > 2.0 for fresh smoke particles, which are dominated by accumulation mode aerosols (Kaufman et al., 1992; Eck et al., 1999).

α is then multiplied with τ to obtain the aerosol index AI (Deuzé et al., 2001), which is shown to be a superior proxy of CCN (e.g. Nakajima et al., 2001; Kapustin et al., 2006; Liu and Li, 2014), as it gives lower weight to large aerosols and reduces the impact of large but low number-concentration sea salt and dust particles (Stier, 2015). For a constant α , AI is proportional to AOD.

$$AI = \tau \cdot \alpha \quad (\text{B.16})$$

However, in this study for estimating the CDNC sensitivity from MODIS data only, the AOD

is used rather than the AI for three main reasons:

1. because AOD is also used in the MACC-II re-analysis from which radiative properties and aerosol characteristics, and CCN are determined, which enables a consistent and comprehensive analysis
2. because the focus of this study is to compare CDNC sensitivity of the various cloud regimes in relative terms, so that absolute differences are not as important
3. because even Stier (2015) shows that only a slight but not a significant improvement of CCN estimates results from using AI instead of AOD in a fully-self consistent model.

B.2 The supersaturation balance equation

This Section investigates the saturation balance equation. The equations are adapted from Abdul-Razzak et al. (1998) and Ghan et al. (2011). Again, we start with Equation 4.1 in Section 4.3.3,

$$\frac{dS_{sat}}{dt} = \alpha w - \gamma \frac{dW}{dt} , \quad (\text{B.17})$$

with α and γ being size-invariant coefficients (for derivation see Pruppacher and Klett (1997))

$$\alpha = \frac{gM_w L_e}{c_p R_G T^2} - \frac{gM_d}{R_G T} \quad (\text{B.18})$$

$$\gamma = \frac{R_G T}{e_s M_w} + \frac{M_w L_e^2}{c_p R_G T^2} . \quad (\text{B.19})$$

dW/dt denotes the water condensation rate during the aerosol activation and subsequent growth processes, with W being the liquid water mass mixing ratio. It is written as (Ghan et al., 2011)

$$\frac{dW}{dt} = \frac{4\pi\rho_w}{\rho_a} \cdot \int_0^\infty r^2 \frac{dN_a}{dr_d} \frac{dr}{dt} dr_d \quad (\text{B.20})$$

and can be expressed in terms of supersaturation as

$$\frac{dW}{dt} = \frac{4\pi\rho_w}{\rho_a} \cdot \int_0^\infty r^2 \frac{dN_a}{dS_c} \frac{dr}{dt} dS_c \quad (\text{B.21})$$

where $(dN_a/dS_c)dS_c = n(S_c)dS_c$ is the number concentration of particles activated between S_c and $S_c + dS_c$ (Abdul-Razzak et al., 1998). For an external mixture of N aerosols species, this equation needs to be generalized to (Abdul-Razzak and Ghan, 2000)

$$\frac{dW}{dt} = 4\pi\rho_w \sum_{i=1}^N \int_0^S r_i^2 \frac{dr_i}{dt} \frac{dn_i(S_c)}{dr_d} dS_c . \quad (\text{B.22})$$

The growth rate of droplet radius dr/dt is given by (Leitch et al., 1986; Abdul-Razzak et al., 1998)

$$\frac{dr}{dt} = \frac{G}{r} (S_{sat} - S_{sat,eq}) = \frac{G}{r} \left(S_{sat} - \frac{A}{r} + \frac{Kr_d^3}{r^3} \right) , \quad (\text{B.23})$$

using $S_{sat,eq}$ derived from Equation 2.9. G is the growth coefficient which describes the diffusion of heat and moisture to the particles and is written as

$$G = 1 / \left[\frac{\rho_w R_G T}{p_s D_v M_w} + \frac{L_e \rho_w}{K_a T} \left(\frac{L_e M_w}{T R_G} - 1 \right) \right] \quad (\text{B.24})$$

In contrast to Abdul-Razzak et al. (1998), instead of the modified diffusivity D'_v the size-independent water vapor diffusivity D_v is applied here. This is easier to compute and is justified since a correction of the continuum diffusion model for gas kinetic effects is not likely to make a significant quantitative difference in the prediction of droplet growth for natural conditions (Pruppacher and Klett, 1997). Therefore D_v is written as

$$D_v = 0.211 \left(\frac{T}{T_0} \right)^{1.94} \cdot \left(\frac{p_0}{p} \right) \quad (\text{B.25})$$

with $T_0 = 273.15 \text{ K}$ and $p_0 = 1013.25 \text{ mb}$. The water vapor transport to and from a cloud droplet is accompanied by a transport of heat owing to the release or absorption of heat of phase change. The resulting difference between the particle and its environment causes a flow of sensible heat by thermal diffusion or heat conduction. The thermal conductivity K_a of humid air which goes into Equation B.24 is computed as (Pruppacher and Klett, 1997)

$$K_a = k_a(T) \left(1 - \left(\gamma_1 - \frac{\gamma_2 k_v}{k_a} \right) x_v(q) \right), \quad (\text{B.26})$$

in which k_a depends on temperature T and x_v depends on specific humidity q and is the mole fraction for water vapor in moist air (Pruppacher and Klett, 1997). Here again, instead of applying the size-dependent modified thermal conductivity K'_a as in Abdul-Razzak et al. (1998), the normal conductivity is being used because the differences are of little consequence for the droplet growth, having then a size-independent growth coefficient G .

Applying Equation B.23 to Equation B.22 and implementing both into B.17, one can see that a rigorous derivation of an expression for S_{max} would involve a complex function of supersaturation with respect to supersaturation, which is in general not possible (Abdul-Razzak et al., 1998).

Neglecting curvature, solute, and gas kinetic effects in Equation B.23, leads to two expressions for S_{max} , one for small S_0 and one for large S_0 , which can then be combined to a single expression of S_{max} for all values of S_0 . Errors due to these simplifications are mostly eliminated by employing adjusting coefficients which are evaluated using results of detailed numerical simulations.

B.3 Regime-based cloud base parameters

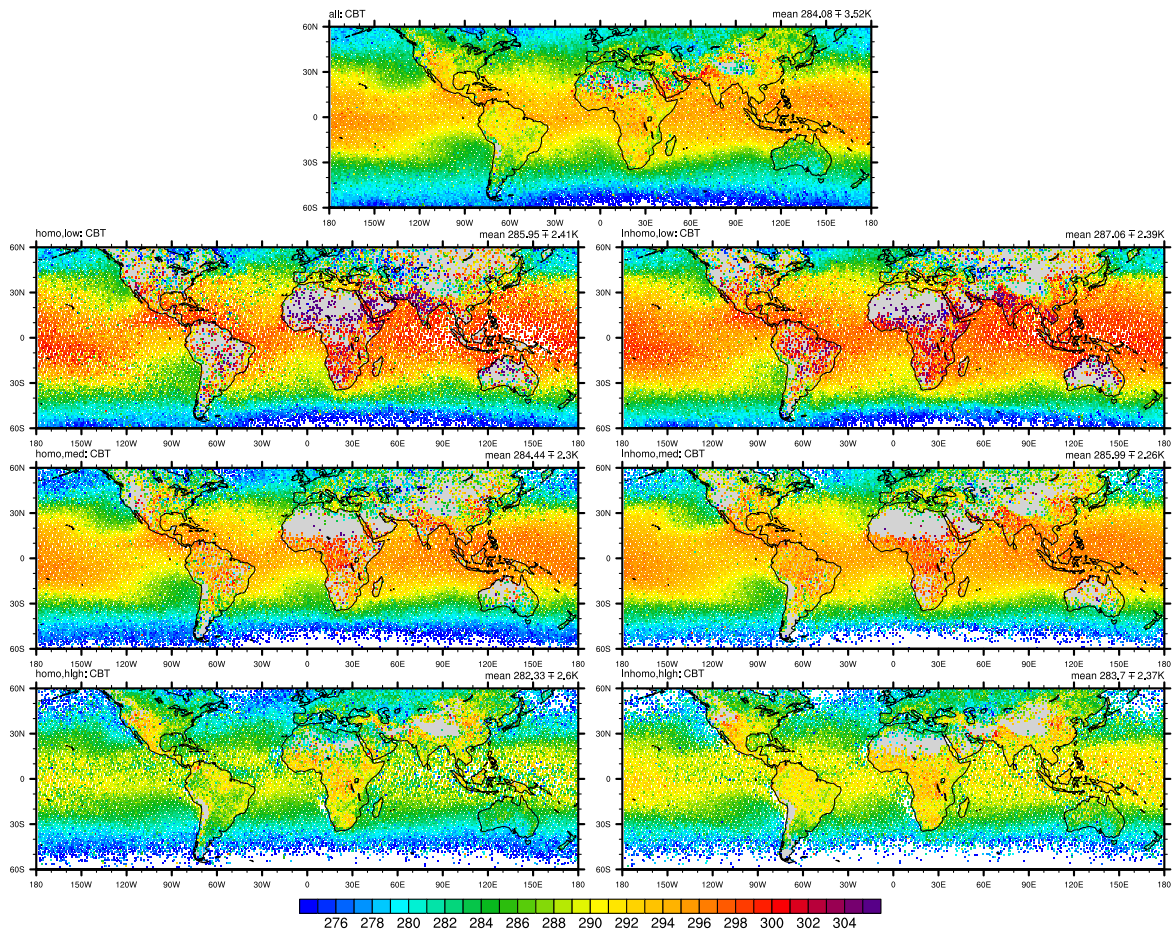


Figure B.3: Regime-based cloud base temperature

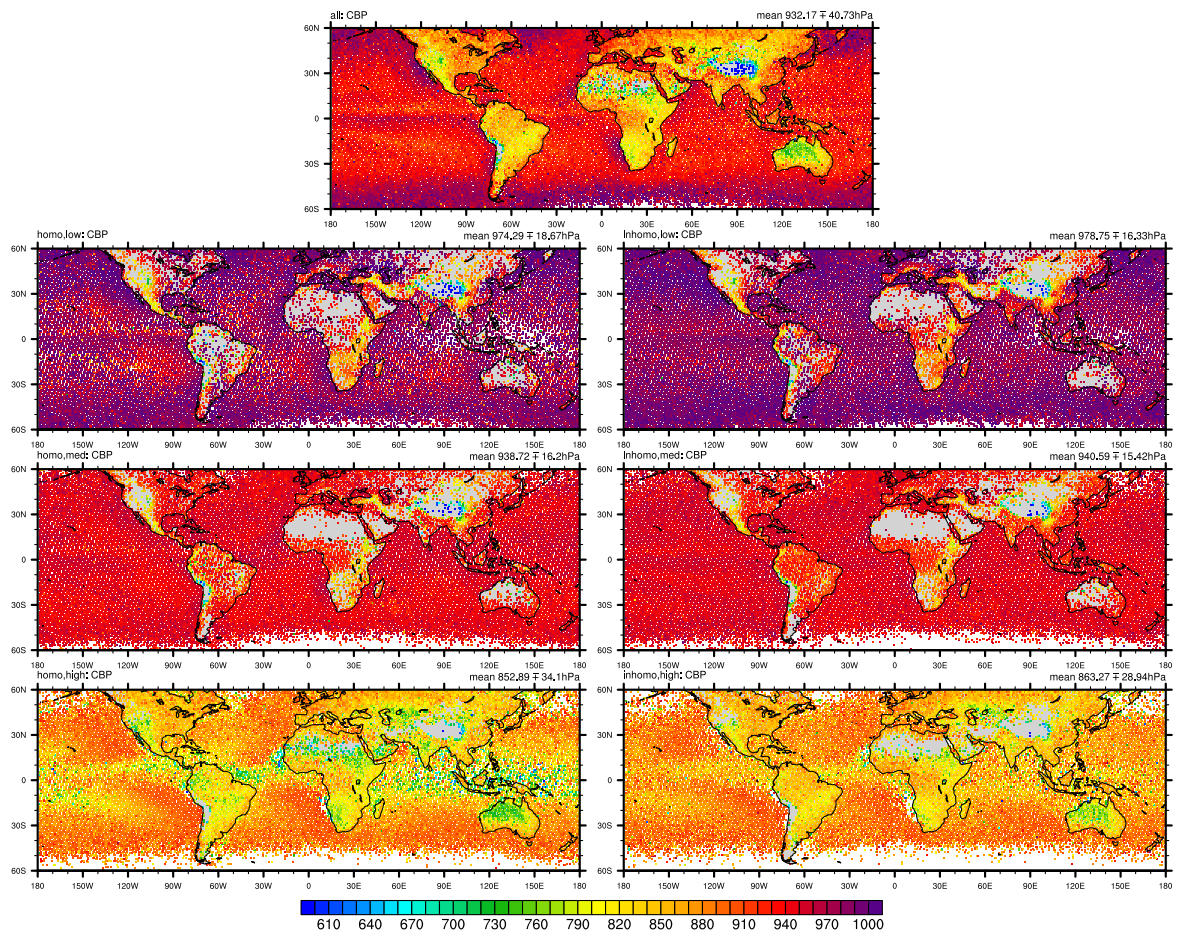


Figure B.4: Regime-based cloud base pressure

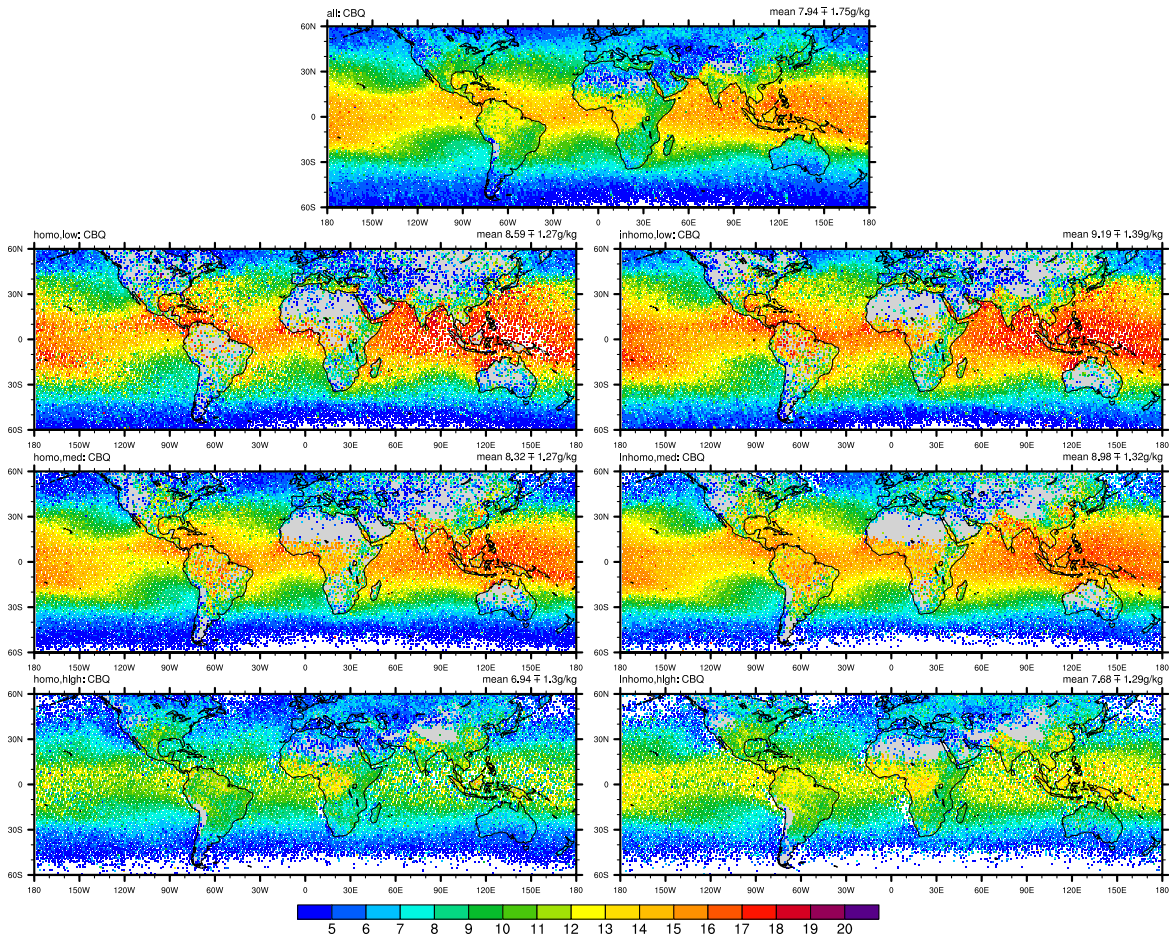


Figure B.5: Regime-based cloud base specific humidity

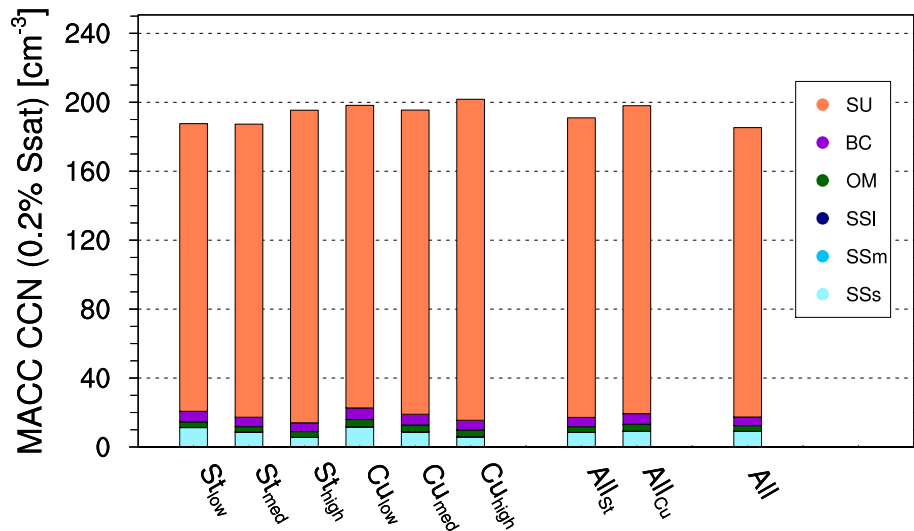


Figure B.6: Regime-based CCN at $0.2\% S_{sat}$ near cloud base

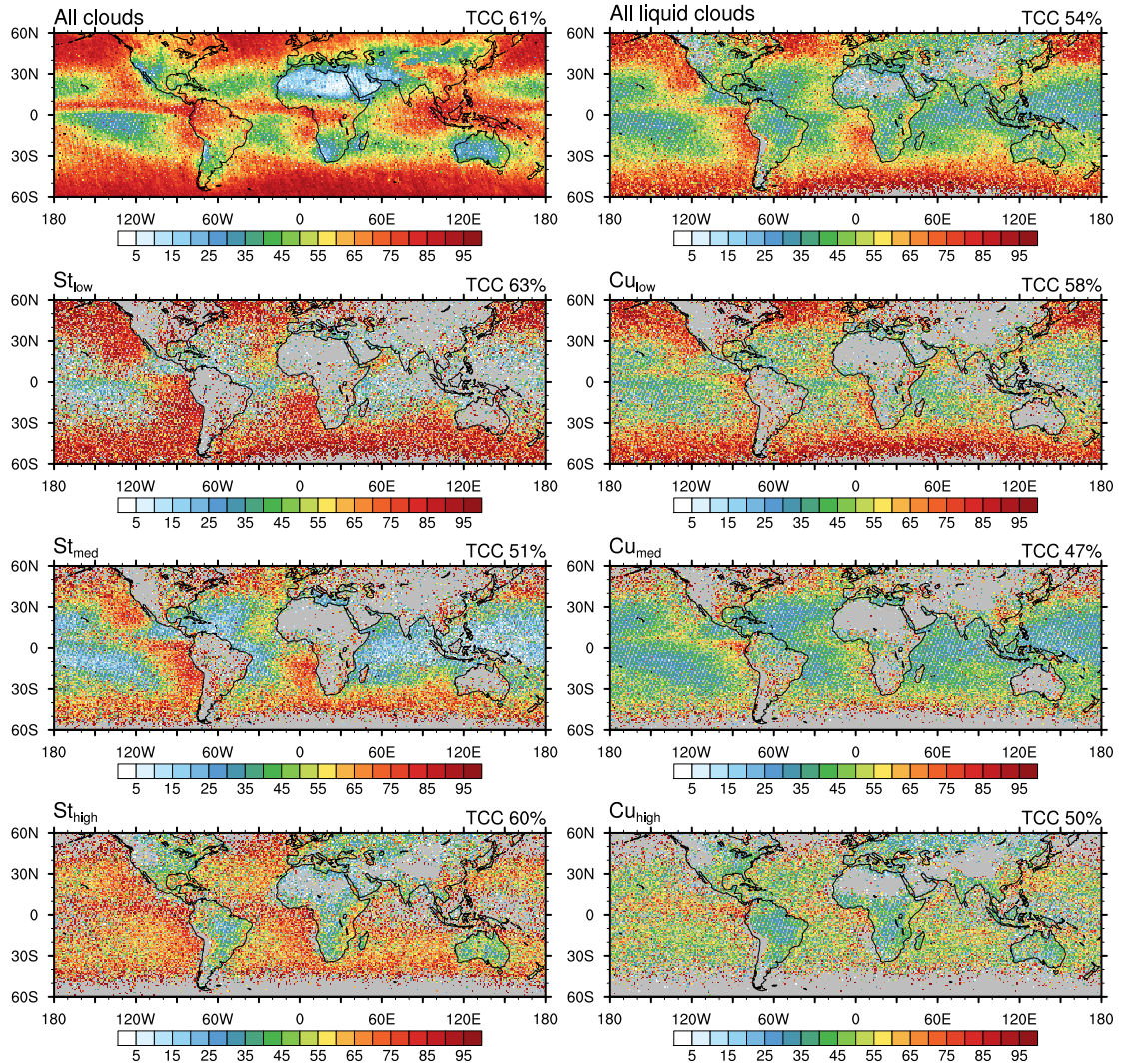


Figure B.7: Regime-based total cloud cover, for a) any clouds found, b) any filtered liquid clouds found, c-e) all stratiform clouds and f-h) all cumuliform clouds that fulfill the classification conditions. The mean value between 60S and 60N is written at the top of each panel. From all measured FOVs, in 84 % of the cases a cloud could be detected - their mean cloud fraction is 61 %. The total mean cloud fraction of 61 % (a) is related to the cases in which any type of cloud, no matter of liquid, mixed-phase or ice, is detected. This happens in 84 % of all measured cases. The mean cloud fraction of filtered liquid clouds (b) is related to all cases in which any liquid, single-layer, non-precipitating cloud is detected. This happens in 12 % of all measured FOVs, or in 14 % of the cases in which any type of cloud has been detected (see Figure 4.5, a). Its' total cloud fraction of 54 % is distributed among the individual regimes (see Figure 5.2).

B.4 Global distribution of regime-based maximum supersaturations

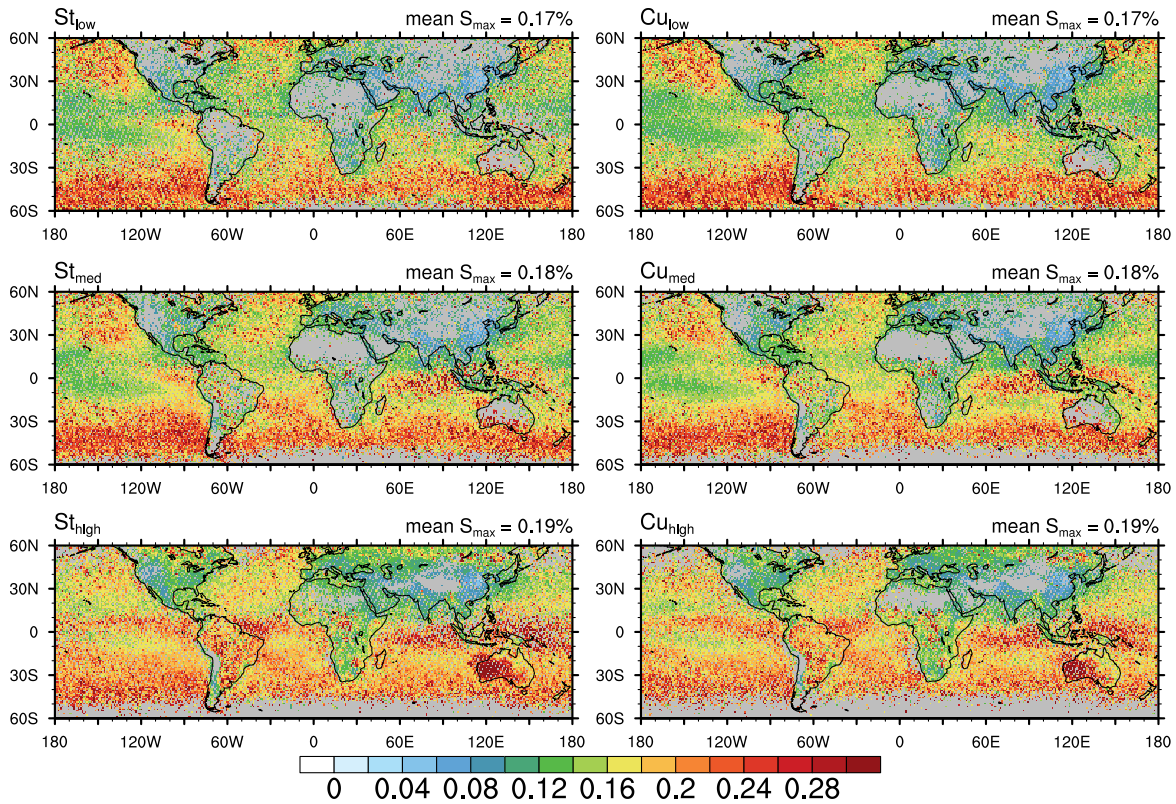


Figure B.8: Experiment 1: Global distribution of regime-based S_{max} , which is obtained from computed S_{max} integrated over the pre-described updraft PDF for each cloud regime. The global mean values are given on top of each panel.

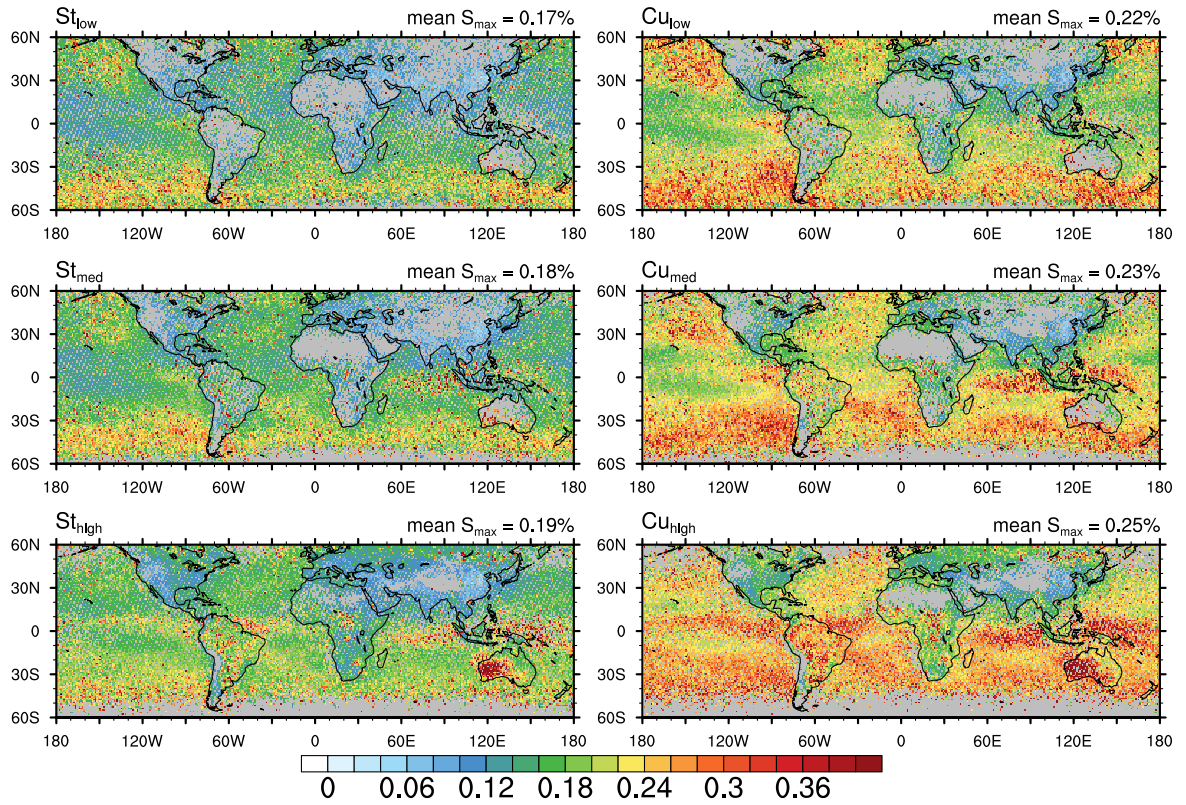


Figure B.9: Experiment 2: Global distribution of regime-based S_{max} , which is obtained from computed S_{max} integrated over the pre-described updraft PDF for each cloud regime. The global mean values are given on top of each panel.

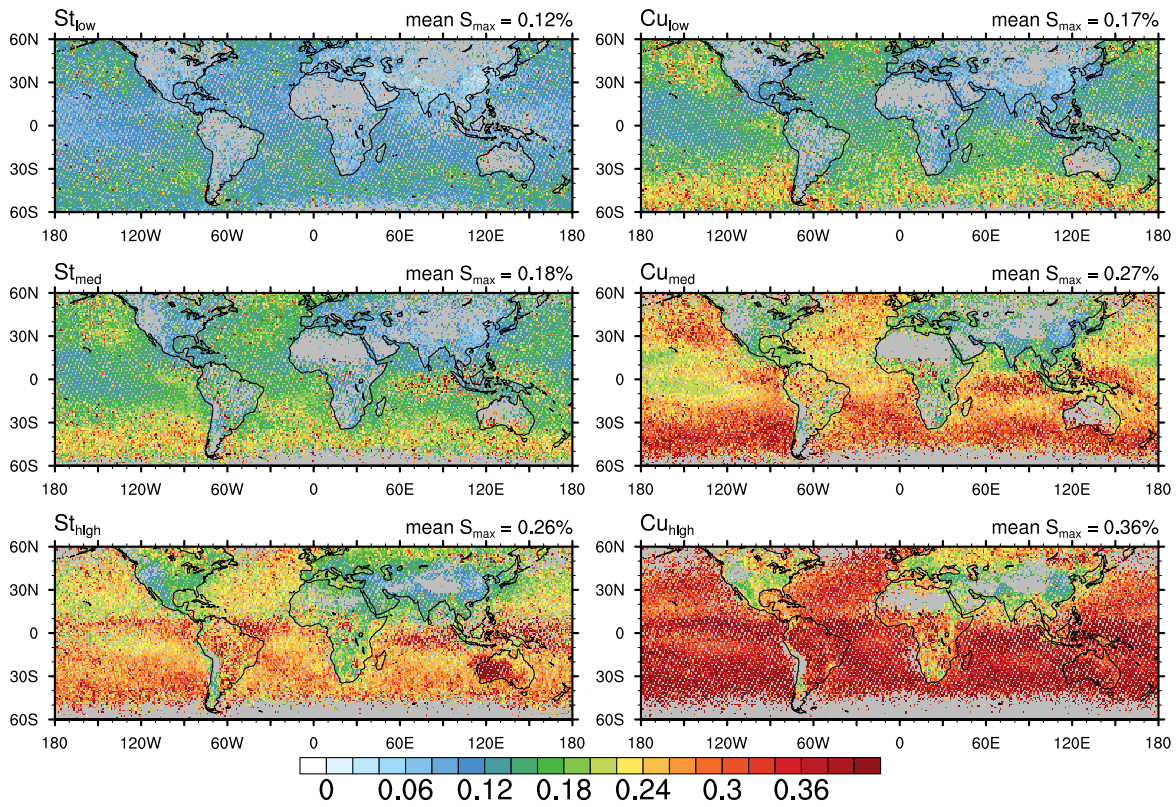


Figure B.10: Experiment 3: Global distribution of regime-based S_{max} , which is obtained from computed S_{max} integrated over the pre-described updraft PDF for each cloud regime. The global mean values are given on top of each panel.

Supplement: Radiative Forcing

C.1 RF_{aci} with fixed anthropogenic fraction

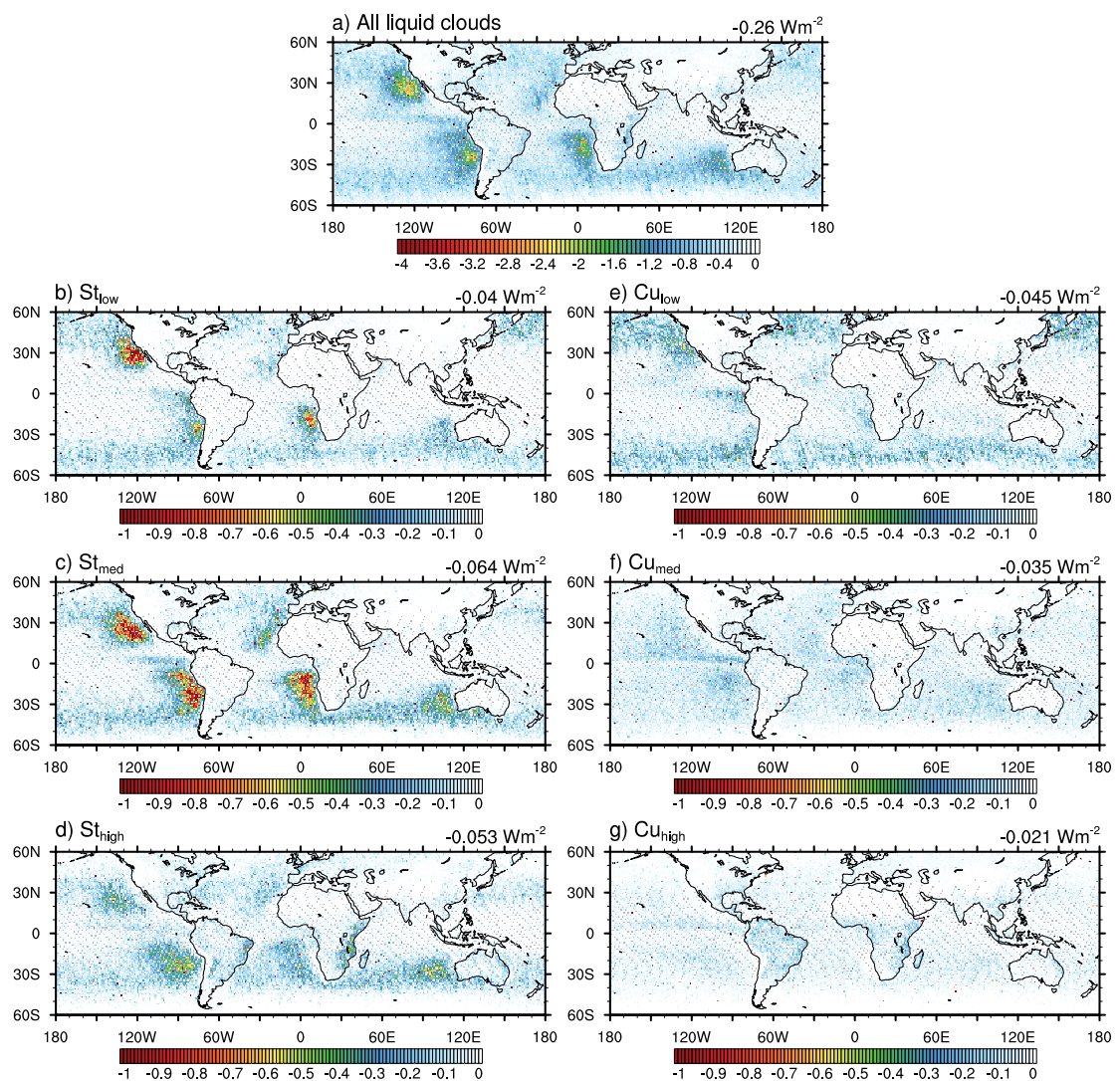


Figure C.1: RF_{aci} for regime-based CDNC from Exp1 and fixed anthropogenic fraction ($f_{anth} = 36\%$).

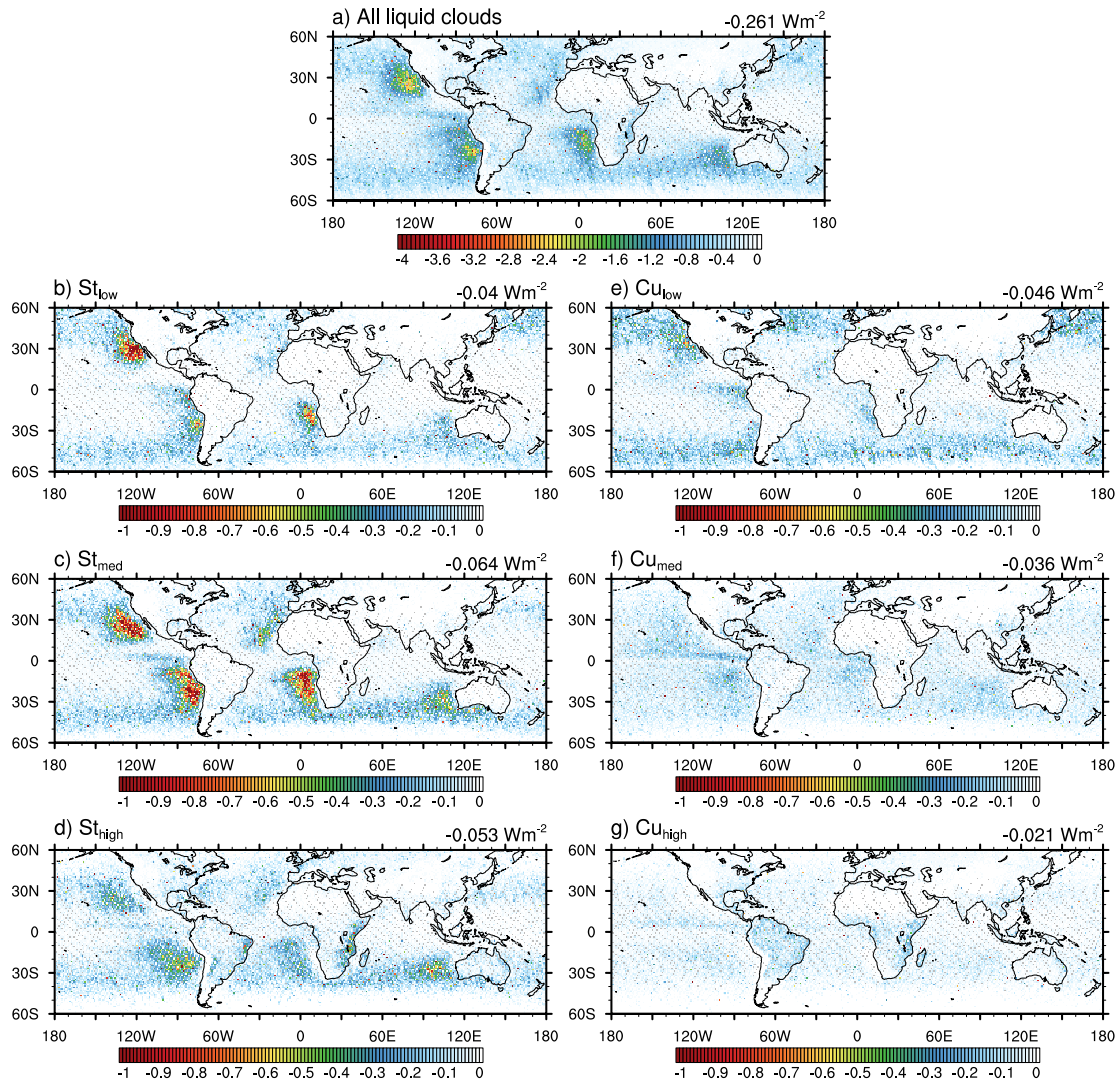
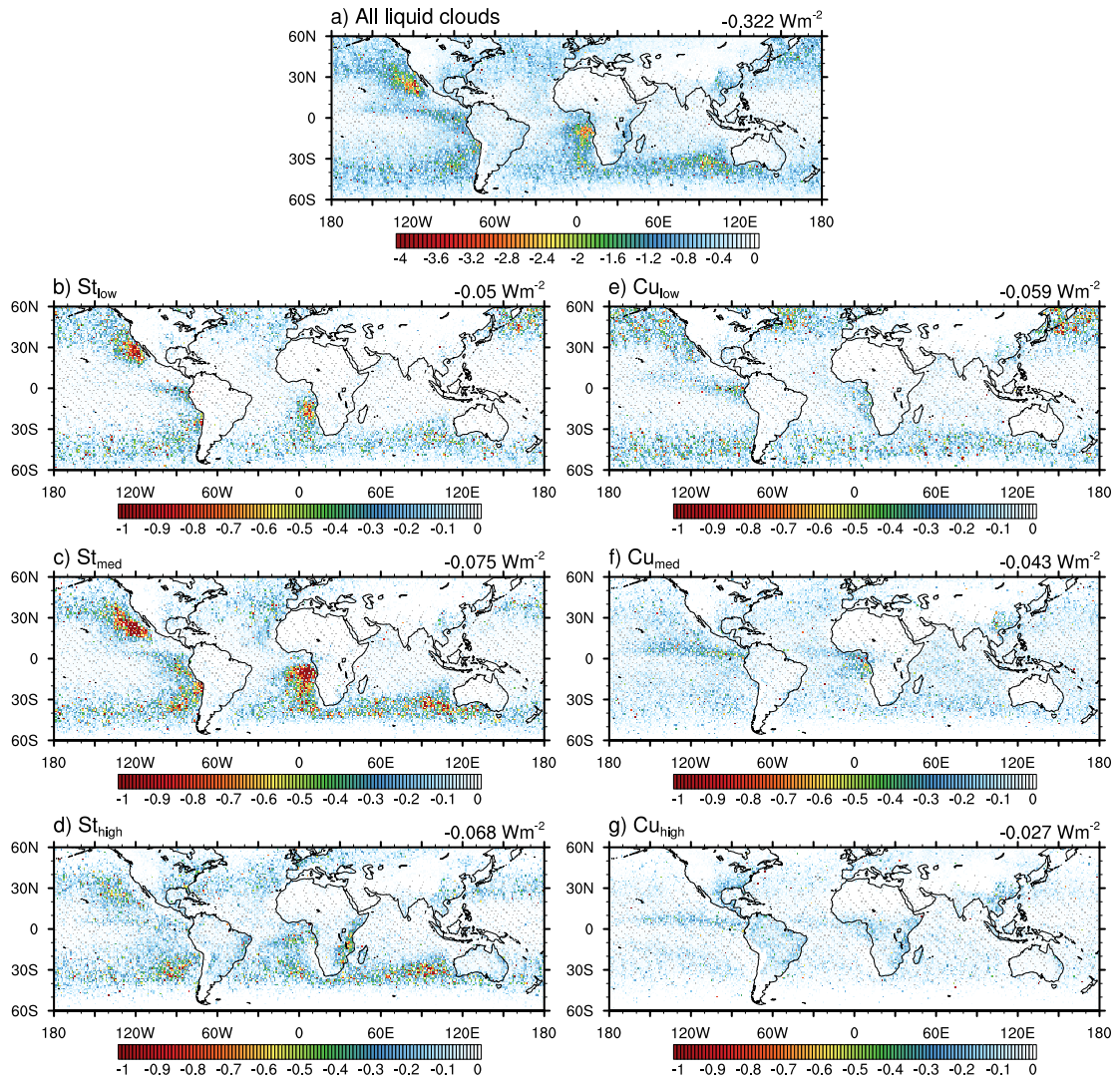


Figure C.2: RF_{aci} for regime-based CDNC from Exp2 and fixed anthropogenic fraction ($f_{anth} = 36\%$).

C.2 RF_{aci} with full anthropogenic fraction distributionFigure C.3: RF_{aci} for regime-based CDNC from Exp1 and full distribution of f_{anth} .

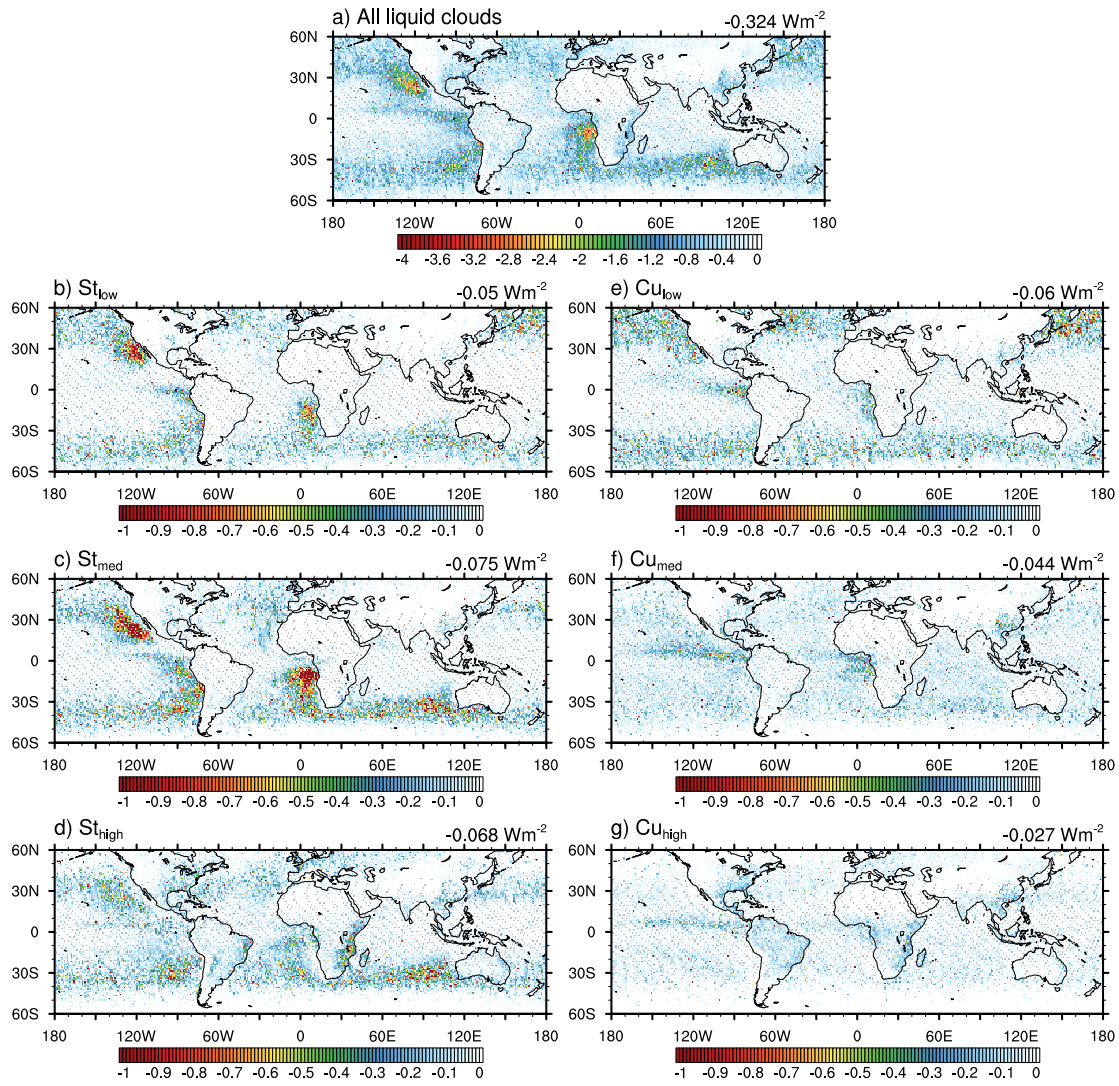


Figure C.4: RF_{aci} for regime-based CDNC from Exp2 and full distribution of f_{anth} .

Acknowledgements

Here, I would like to thank a number of people who helped me throughout the PhD time and made this dissertation possible.

Foremost, I would like to express my sincere gratitude to my supervisor Johannes Quaas for his outstanding support and constructive criticism during all the phases of the PhD.

Special thanks goes to the working group on Clouds and global Climate, especially to Claudia Unglaub, Johannes Mülmenstädt, Odran Sourdeval, Marc Salzmann, Tom Goren, Edward Gryspeerdt and Matthias Brueck, with whom I worked closely together and discussed many thoughts.

The same holds for the PhD candidates of the LGS-CAR graduate school, especially to Daniel Merk, Sebastian Bley and Henner Bieligk who made the dissertation time not just work but also fun.

Furthermore I would like to thank the working group on climate processes at the University of Oxford, especially Philip Stier and Daniel Partridge, for helping me to understand and work with the activation parameterization.

I am also very glad for the support that other scientists gave me. I am grateful for the contribution of anthropogenic aerosol fractions by Nicolas Bellouin, and for the discussion with Angela Benedetti, Jean-Jaque Morcrette and Olivier Boucher on the use of the MACC-II reanalysis assumptions and validation, for Robert Wood helping me out with a corrected ARM dataset for one of the stations, and for discussing marine aerosol size distributions with Alfred Wiedensohler.

Last but not least, I like to thank my family and friends who not just helped me through the nerve-racking and hard times of the writing process but also enjoyed with me the fun and productive times and appreciated my efforts.

Many people helped to improve this thesis, and I am very grateful to all of them.